# A High Fidelity Multiphysics Framework for Modeling CRUD Deposition on PWR Fuel Rods

by

Daniel John Walter

**A dissertation submitted in partial fulfillment**
**of the requirements for the degree of**
**Doctor of Philosophy**
**(Nuclear Engineering and Radiological Sciences)**
**in the University of Michigan**
**2016**

Doctoral Committee:

Associate Professor Annalisa Manera, Chair
Professor Thomas J. Downar
Brian K. Kendrick, Los Alamos National Laboratory
Professor William R. Martin
Assistant Professor Necmiye Ozay
Research Scientist Victor Petrov

# DEDICATION

for my wife Lauren, my son Ralph F, and my grandfather Ralph E

"*Always stick with the fundamentals; work from the fundamentals, whatever is involved with regard to the particular problem*," stated by an engineering student 25 years after their education at Ohio Northern University, in response to what they learned under the teaching of Ralph E Walter.

# ACKNOWLEDGMENT

Foremost, I am thankful to my wife, Lauren, who moved her life in Maryland to fit into my life at the University of Michigan. Her support and confidence in me kept us chugging through graduate school.

During my first year at UM, I had yet to focus on a subject area within the NERS department. Thanks to Professor Martin for advising me in that time. I eventually realized my interest in reactor analysis and deterministic methods, and Professor Downar encouraged me to learn the DeCART code. Soon after, Professor Downar and a newly appointed faculty member, Professor Manera, had me involved in a Department of Energy project called the Consortium for the Advanced Simulation of Light Water Reactors (CASL).

I transitioned to working with Professor Manera and Victor Petrov, who both encouraged me to gain experience with computational fluid dynamics (CFD) and the STAR-CCM+ code. For the remainder of my time at UM, Professor Manera's expertise, excitement, and involvement in our research projects maximized my academic development. Additionally, I am indebted to Victor Petrov for his expertise in CFD and the numerous explanations provided to me throughout the last four years. His commitment to this project has been a primary reason for its success.

None of this work would have been possible without the primary author of the MAMBA code, Brian Kendrick at Los Alamos National Laboratory. He provided a novel and robust computational tool that enabled state-of-the-art research and promoted collaboration among a multi-disciplinary team. CASL is also acknowledged for their role in the development of the MAMBA code. Special thanks to Jeff Secker from Westinghouse for his collaboration on the plant comparisons presented in Chapter VI; and, special thanks to Tim Grunloh and Michael Rose, who were always available to bounce ideas around with.

# TABLE OF CONTENTS

# LIST OF FIGURES

# LIST OF TABLES

# LIST OF APPENDICES

# ABSTRACT

Corrosion products on the fuel cladding surfaces within pressurized water reactor fuel assemblies have had a significant impact on reactor operation. These types of deposits are referred to as CRUD (Chalk River Unidentified Deposit or Corrosion Related Unidentified Deposit) and can lead to power shifts, as a consequence of the accumulation of solid boron phases on the surface of the fuel pins. Corrosion deposits can also lead to fuel failure resulting from localized corrosion, where the increased thermal resistance of the deposit leads to higher cladding temperatures. The prediction of these occurrences requires a comprehensive model of local thermal hydraulic and chemical processes occurring in close proximity to the cladding surface, as well as their driving factors. Such factors include the rod power level and distribution, the corrosion product concentration in the reactor coolant, as well as the feedbacks between heat transfer, fluid dynamics, chemistry, and neutronics.

To correctly capture the coupled physics and corresponding feedbacks, a high fidelity framework is developed that predicts three-dimensional CRUD deposition on a rod-by-rod basis. Multiphysics boundary conditions resulting from the coupling of heat transfer, fluid dynamics, coolant chemistry, CRUD deposition, neutron transport, and nuclide transmutation inform the CRUD deposition solver. Through systematic parametric sensitivity studies of the CRUD property inputs, coupled boundary conditions, and multiphysics feedback mechanisms, the most important variables of multiphysics CRUD modeling are identified. Moreover, the modeling framework is challenged with a blind comparison of plant data to predictions by a simulation of a sub-assembly within the Seabrook nuclear plant that experienced CRUD induced fuel failures during cycle 5. Such a comparison at this level of detail had previously never been attempted; therefore, this initial model validation demonstrates the modeling framework's capabilities by accurately reproducing localized corrosion deposit distributions.

The physics included within the suggested computational framework are *loosely* coupled via an operator-splitting technique. A common challenge among loosely coupled physics is the determination of the frequency of the solution data exchange, while maintaining the coupled solution accuracy and minimizing execution time. This is particularly crucial when computationally intensive codes are used. The problem of determining a suitable integration time stepsize is exacerbated when the time scales at which the individual physics develop, and respond to feedback, are disparate. In the present work, a control theory approach is adopted to determine the temporal discretization at which to execute a data transfer from one physics to another. Specifically, the coupled stepsize selection is viewed as a feedback control problem and a controller of the type *integral* is utilized. The temporal discretization is unknown *a priori* and adapts with the problem solution to maintain a user-prescribed tolerance of specified quantities, i.e. the $L^2$ relative error norm of physical parameters are monitored to control the stepsize. Predictor-corrector algorithms are leveraged to enable convergence error estimates.

The highly nonlinear precipitation rate of lithium tetraborate, a solid boron phase, and its dependence on the local thermal hydraulic conditions is the primary motivation for seeking an automated and adaptive stepsize selection algorithm. The evolution of the power distribution with fuel depletion drives the thermal hydraulic boundary conditions that strongly affect the boron precipitation rate. A coupled time stepsize that is too large may significantly affect the solution accuracy, while a uniform or fixed temporal discretization with an unnecessarily small stepsize would result in prohibitively high computational expense for the CFD solution.

# CHAPTER I
# Introduction

## 1.1 Reactor operation

Optimal pressurized water reactor (PWR) performance relies on the consideration of a variety of design parameters, risk assessments, constraints, and trade-offs. Maintaining sufficient safety margins while maximizing power output and cycle length is one example of balancing various aspects of reactor operation. Other design bases include sufficient shutdown margin, limited power peaking factors, limited (negative) fuel and moderator temperature coefficients, and limited departure from nucleate boiling ratio (DNBR). Furthermore, the ability of the reactor to safely respond to operational transients and accident scenarios is paramount. Examples of operational transients include withdrawal and insertion of rod cluster control assemblies, while accident scenarios include, among others, loss of coolant accidents (LOCA) and main steamline break (MSLB) events.

Furthermore, several in-core phenomena have been identified that have an impact on PWR operation, specifically on the integrity of the fuel rods, which includes the first barrier of the radioactive fuel—the cladding. Such phenomena include corrosion deposits forming on the cladding surface, cladding hydriding, pellet-cladding interaction, and grid-to-rod fretting. The focus of this dissertation is on the deposition and precipitation of corrosion products on fuel rods and the associated multiphysics modeling methodology. Corrosion deposits have proven to affect power distributions, leading to unplanned reductions of power and eventual shutdowns. Additionally, they have been responsible for accelerated cladding corrosion, leading to failed fuel rods and plant shutdown to replace the compromised rods.

## 1.2 Corrosion related unidentified deposit

Chalk River unidentified deposit (CRUD) was first identified in the late 1940s at the Canadian Chalk River Laboratories. Subsequently, two primary operating concerns were recognized: (i) CRUD induced power shift (CIPS) and (ii) CRUD induced localized corrosion (CILC). CIPS, historically known as axial offset (AO) or axial offset anomaly (AOA), refers to the shifting of the axial power distribution, often toward the bottom half of the core. This is due to CRUD buildup and the presence of solid boron phases, known as boron hideout, in the top half of the core where coolant temperatures are highest. Figure 1.1 shows heavy CRUD deposition on PWR fuel rods from the Palo Verde Nuclear Generating Station. CILC refers to the corrosion of the cladding due to increased thermal insulation of the cladding surface by the CRUD deposit, illustrated in Figure 1.1 (right). More recently, the acronym CRUD has been generalized to corrosion residual unidentified deposit or corrosion related unidentified deposit.

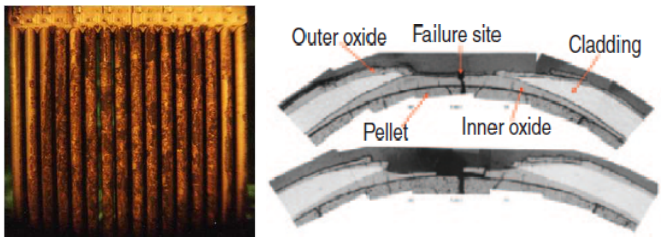


Figure 1.1: Heavy CRUD deposition on fuel rods at the Palo Verde Nuclear Generating Station [Station, 2004] (left), and CRUD induced localized corrosion of fuel cladding [Deshon et al., 2010] (right).

The risk of CIPS and CILC increases with power uprates and longer cycles due to the increased potential for thicker CRUD deposits. In the United States, 18 distinct reactors with a total of 37 cycles had reported CIPS by 2004 [EPRI, 2004]. CILC failures have primarily been an operating issue in boiling water reactors (BWRs) with copper-containing condenser tubes. Only a handful of PWR plants have experienced CILC fuel failures [IAEA, 2010]; nonetheless, the goal of zero fuel failures stands, and understanding and preventing such failures is necessary. Therefore, CIPS and CILC are important phenomena that require careful risk assessment because they impact core peaking factors, shutdown margin, and fuel integrity [Wang et al., 2010].

In PWRs, the primary CRUD source comes from corrosion of the steam generator tubing, which develops as oxygen diffuses into the base metal, transforming the alloy elements from the metallic state to the oxide state. Divalent metal ions are then released into the water as soluble metal ions [Castelli, 2010]. The metal ion release rate is dependent on the diffusion coefficient of oxygen, the oxide thickness and composition, and coolant conditions, among other contributors [EPRI, 2004]. Three coolant chemistry conditions that promote corrosion and release of the corrosion products are high oxygen content, low pH, and high temperature. As the oxygen content increases, the oxidation rate accelerates. Moreover, the corrosion product release rate is significantly affected by the coolant pH. Historically, increasing the pH in plants has decreased corrosion; however, a high pH requires a high lithium concentration in the coolant which may increase the probability of undesirable boron hideout in the CRUD layer [EPRI, 2004]. CRUD prevention techniques that were developed and implemented in the last forty years are illustrated in Figure 1.2.

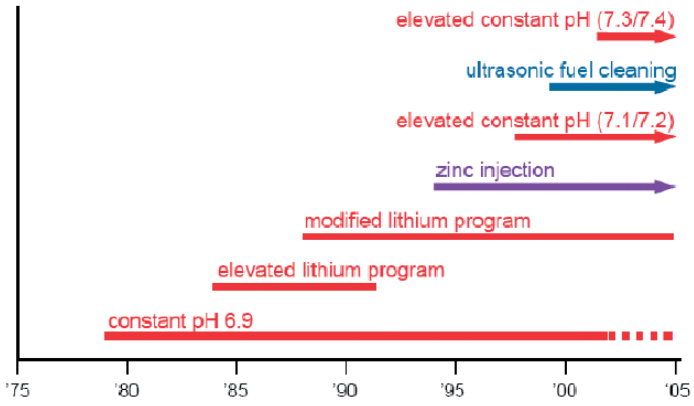


Figure 1.2: CRUD prevention techniques [IAEA, 2007].

The corrosion particulates release from the site of formation, circulate the primary loop, and deposit on core internals including the fuel rods. These CRUD deposits are composed mostly of nickel ferrite, nickel oxide, and nickel metal with other nickel-iron-chrome spinels [Deshon et al., 2010]. CRUD deposits are typically thicker on the upper regions of the fuel rods due to the higher temperature of the surrounding coolant and increased probability of subcooled nucleate boiling (SNB) [EPRI, 1997]. Boron hideout within the CRUD layer leads to an offset of the axial power distribution, i.e. CIPS. The asymmetry in the boron

concentration along the axial direction is directly correlated with the increase in the CRUD thickness and increased internal boiling along the axial direction. The internal boiling occurs within *chimneys* that develop in the CRUD, as shown in Figure 1.3. The coolant and its soluble species, such as boric acid and lithium, are drawn into the chimneys. As the coolant vaporizes, the soluble species concentrate along the cladding surface. For very thick CRUD deposits, the vapor produced and trapped within the chimneys may cause cladding surface dryout, leading to a dramatic increase in cladding temperature. A sample CRUD layer illustrating species concentration and solid boron precipitation is depicted in Figure 1.3.

The concentration of metaboric acid—present within the coolant for reactivity control—and a specific precipitate, lithium tetraborate ($Li_2B_4O_7$), within the CRUD deposit are believed to be the primary contributors to CIPS [EPRI, 1997, EPRI, 2004, Deshon et al., 2010]. The concentrated boron *hiding out* in the thicker CRUD layers reduces the neutron flux in those regions, leading to a redistribution of the power. The thermal neutron (of energy 0.00253 eV) cross section of boron is approximately 3840 barns, which is sufficient to have significant neutronics effects.

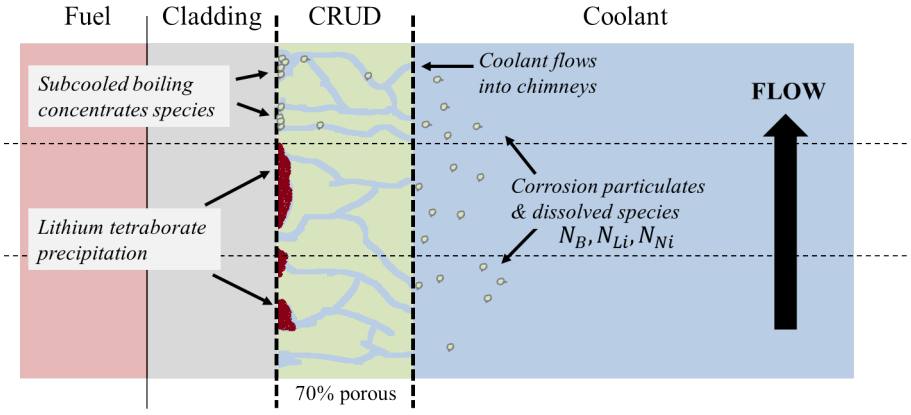


Figure 1.3: CRUD chimney and species concentration illustration (not to scale).

In addition to core conditions having an impact on the formation of CRUD, the core geometry, specifically, the fuel assembly support structures, known as spacer grids, strongly influence the deposition of corrosion particulates. The spacer grids contain mixing vanes to improve convective heat transfer between the fuel rod and coolant by inducing turbulent flow, which also improves the DNBR performance. Typically, between eight and ten spacer


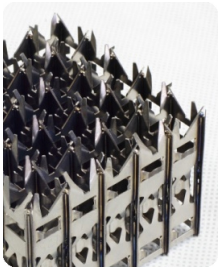

Figure 1.4: Fuel assembly spacer grid [AREVA, 2016] (left) and mixing vanes [KAERI, 2016] (right).

grids are used to support a PWR fuel assembly; Figure 1.4 depicts a spacer grid design. The axial region between two grids is referred to as a *span*. Optimization of the vane design in terms of size, shape, bend angle, and location is often performed in the interest of efficient reactor operation [In et al., 2001]. The spacer grid illustrated in Figure 1.4 contains split-vanes, which is the general type of vanes used in the computational models within this dissertation.

## 1.3 Reactor modeling

### 1.3.1 A partitioned approach

The governing physics of nuclear reactors are multi-scale and multi-disciplinary. Despite the interdependence among the different physics, reactor analysis has historically—prior to about 20 years ago—been decomposed into specific disciplines, each focusing on a singular physics solution. The motivation behind this approach is attributed to limited computational resources, specifically, a single workstation (desktop with a single or possibly several processors). In practice, repeated reactor analysis calculations are performed to optimize fuel loading patterns, ensure safety limits, etc.

The following lists the most important light water reactor (LWR) analysis disciplines and their solution fields:

- *neutronics* – steady state neutron flux distribution,

- *neutron kinetics* – time-dependent neutron flux distribution,
- *nuclide depletion/burnup* – time-development or transmutation of the radioactive nuclide composition,
- *hydraulics/fluid dynamics* – coolant density and temperature fields,
- *heat transfer* – fuel and cladding temperature fields,
- *fuel behavior* – fuel properties and fission gas release with burnup,
- *CRUD/coolant chemistry* – corrosion product deposition and boron hideout.

Steady state neutronics and time-dependent nuclide depletion may be combined to form the discipline of *fuel burnup*, or in the case of a pin array, *lattice burnup* or *lattice depletion*. Traditionally, lattice depletion analysis has been carried out using several different deterministic codes with varying fidelities. A typical reactor physics analysis methodology consists of three steps: multi-group cross section library generation, two-dimensional (2-D) lattice transport calculation, and three-dimensional (3-D) few-group diffusion calculation. CASMO [Knott, 1995], SIMULATE [Studsvik, 1995], and HELIOS [Studsvik, 2008], have been reliable neutronics tools for decades, originally developed by Studsvik Scandpower. Additionally, PARCS has been the primary diffusion solver used by the Nuclear Regulatory Commission (NRC) for licensing; and, ANC is used by Westinghouse. More recently, the latter two steps of the neutronics analysis methodology have been combined, and *direct* solutions are sought, e.g. DeCART [Joo et al., 2004,Hursin et al., 2008], nTRACER [Jung et al., 2013], LANCER02 [Knott and Wehlage, 2007], and MPACT [Kochunas et al., 2013]. This combined approach eliminates several assumptions involved in the traditional partitioned approach and is popular for high fidelity modeling and research efforts.

Often, fluid dynamics and heat transfer solvers are combined to form the discipline of *thermal hydraulic*s (TH). Moreover, thermal hydraulics exists in three primary approaches with varying fidelities: system, subchannel, and computational fluid dynamics (CFD) analysis. Both steady state and time-dependent formulations are utilized, depending on the specific application.

Popular system codes include RELAP5 [INL, 2005] and TRACE [NRC, 2010], which are used by the NRC to analyze loss of coolant accidents and system transients in both PWRs

and boiling water reactors (BWRs). Popular subchannel thermal hydraulics codes are VIPRE [CSAInc, 2015] and COBRA-TF [Salko, 2015], which were developed by the Electric Power Research Institute (EPRI) and Pennsylvania State University (PSU), respectively. These 3-D tools are used to evaluate reactor core safety limits including power peaking, minimum departure from nucleate boiling ratio (MDNBR), and critical power ratio (CPR). More recently, CFD has been used for high fidelity thermal hydraulics analysis, including spacer grid designs, where resolution of the 3-D flow field is necessary; ANSYS FLUENT [ANSYS, 2009b], ANSYS CFX [ANSYS, 2009a], and STAR-CCM+ [CD-adapco, 2012] are well recognized CFD simulation suites.

A popular fuel behavior tool is FRAPCON [Geelhood et al., 2011], which was developed by the NRC to calculate the steady state response of LWR fuel rods during long-term burnup. A more advanced, high fidelity, time-dependent fuel performance and analysis tool is BISON [Hales, 2013], which is currently under development at the Idaho National Laboratory (INL). In BISON, material heat conduction and equilibrium mechanics equations are coupled through the temperature and displacement variables.

Of the physics mentioned above, the most important physics for high fidelity CRUD deposition prediction and evaluation of CIPS and CILC are neutronics/depletion, thermal hydraulics via CFD, and CRUD/coolant chemistry. However, the spatial discretization (mesh) resolution—often used in practical industry simulations—needs refinement in order to achieve the resolution necessary to predict CIPS and CILC on the fuel rod scale. The specific coupling of these physics is discussed in detail in Chapter II.

### 1.3.2 A coupled approach

As computational power increases, so does the ability to perform more complex simulations based on first principles, which require less assumptions. Thus, the reactor simulation paradigm has shifted toward a coupled approach, where the existing legacy simulation tools are modified to improve their solution accuracy by exchanging data during the simulation, i.e. more accurate solutions are obtained by replacing fixed boundary conditions with dynamic boundary conditions provided by coupled physics. Examples include the coupling of:

- subchannel and system TH methods to simulate a large break LOCA transient [Zhang et al., 1998],
- neutron kinetics and system thermal hydraulics to simulate a main steam line break transient [Kozlowski et al., 2004],
- neutronics, subchannel or CFD, and fuel performance to simulate pellet-clad interaction [Clarno et al., 2015] and cladding hydriding [Mankosa et al., 2016],
- and, neutronics, CFD, and coolant chemistry to simulate CRUD deposition [Walter et al., 2015b].

Mathematically, this decomposed coupling technique is known as operator-splitting (OS). The term *fractional step* and *loose* coupling has also been used to describe the OS technique. Recently, the Consortium for Advanced Simulation of LWRs (CASL) project has focused on the development of an all-encompassing reactor analysis and simulation suite, known as Virtual Environment for Reactor Analysis (VERA). VERA adopts a *plug-and-play* approach, where each physics may be used independently or coupled to the other physics in an OS-fashion.

On the other hand, a different approach is adopted with the MOOSE computational framework [Gaston et al., 2009], in which computational efficiency is traded for accuracy by providing implicit fully-coupled solutions exploiting Jacobian-free Newton-Krylov (JFNK) methods. This alternative is often described as a *mono-block, monolithic*, or *tight* coupling strategy, which involves developing the coupled field equations and often employing a Newton-type iteration method to decrease the nonlinear residual until the converged solution is found. This approach is the most accurate, but the implementation is much more intense and cumbersome; in addition, it is challenging to apply this type of method to existing codes. Depending on the coupled physics and the strength of the respective feedback mechanisms, tight coupling may reduce the computational cost. A hybrid approach, where OS and monolithic schemes are both utilized for highly nonlinear and strongly coupled problems, was adopted by [Vijalapura and Govindjee, 2005].

[Ragusa and Mahadevan, 2009] compares monolithic and OS solutions for select coupled neutron kinetics and thermal hydraulics problems including a SCRAM accident; it is concluded that the normally reduced accuracy of an OS approach may be fully restored, and

comparable to the monolithic scheme, by using predictor-corrector (P-C) and fixed-point iteration (FPI) schemes. Moreover, a predictor-corrector approach alone (without FPIs) may serve to sufficiently converge the coupled solution, thus saving computation time. Ragusa points out that reformulating the nonlinear problem to solve as a mono-block allows implementation of adaptive time stepping strategies of numerical integration methods; however, there is no mention of an adaptive stepsize approach to the OS technique.

The OS strategy offers a straightforward approach to the coupling of existing computational physics tools, especially where a practical balance of computational efficiency and solution accuracy is sought. However, the stronger the two-way feedback between the coupled physics, the more of a concern numerical stability becomes and the slower a converged solution is obtained. [Fellipa et al., 2001] is a useful historical reference of the development of partitioned multiphysics analysis, which summarizes relevant terminology and temporal coupling schemes. Additionally, [Piperno et al., 1995] and [Piperno and Farhat, 2001] applied partitioned solution procedures to a fluid-structure interaction (FSI) problems and describe the implementation of unconditionally stable staggered time-integrators, including the utilization of a P-C and trapezoidal rule scheme. A similar P-C approach is adopted within the present modeling framework to obtain time-consistent solutions to the coupled CRUD deposition problem; details may be found in Section 2.3.

## 1.4 State-of-the-art CRUD modeling

In general, modeling of CRUD deposition may be separated into three primary domains: (i) ex-core, (ii) in-core off-cladding, and (iii) in-core on-cladding. All three of these domains must be considered to enable accurate deposition predictions. The first domain includes calculation of the source term, resulting from the corrosion of steam generator tubing and other primary loop internals; the dissolved and particulate species concentrations within the reactor coolant are determined. The second domain includes calculation of the coolant flow conditions that drive CRUD deposition and erosion, e.g. the turbulent kinetic energy, and thermal hydraulic boundary conditions at the cladding interfaces. The third domain includes the deposition of the CRUD on the cladding surface, including species diffusion and chemical reactions.

## Legacy

In the last decade, the state-of-the-art of CRUD deposition prediction in PWRs has been primarily developed by EPRI and in collaboration with Westinghouse Electric Company (WEC). An assessment methodology utilizing the thermal hydraulic code VIPRE and the coolant chemistry code BOA (Boron-induced Offset Anomaly Risk Assessment Tool) has been the primary CRUD prediction capability within industry [EPRI, 2003].

As mentioned in Subsection 1.3.1, VIPRE is a 3-D subchannel analysis code designed to model steady state and transient conditions of LWRs. A two-fluid representation is utilized, where the mass, momentum, and energy equations are solved for each phase. A typical radial discretization for a quarter-core calculation is to divide each assembly into four nodes, i.e. 2x2 quarter-assembly array, as shown in Figure 1.5. For a typical full-height PWR, the axial mesh in VIPRE consists of 30-60 planes of uniform or varying thickness depending on the required solution resolution.

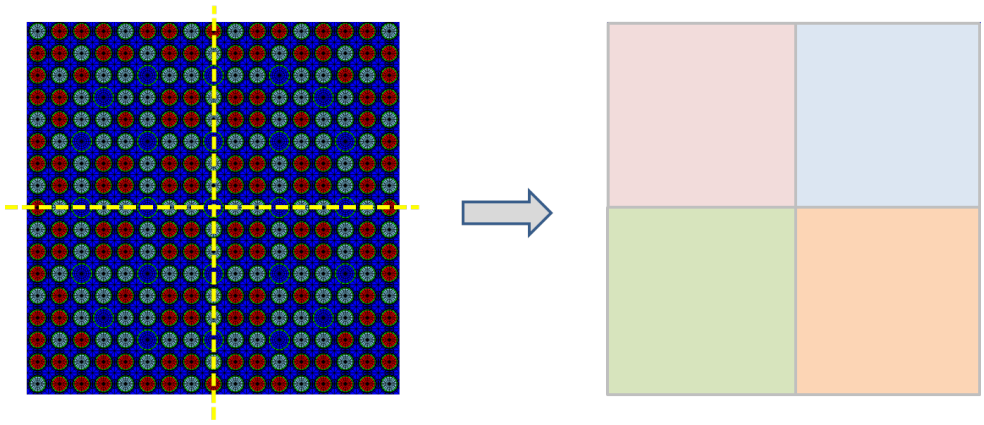

Figure 1.5: Illustration of explicit fuel assembly geometry homogenization to four nodes.

BOA is a risk assessment tool used to predict the release of corrosion products, e.g. CRUD, from the out-of-core surfaces of a PWR and the eventual deposition of these products on the (in-core) fuel rods. Corrosion, physical chemistry, and thermal hydraulic models are combined to facilitate the CRUD deposition predictions. A similar 2x2 radial mesh per assembly is typically used; this level of detail means that, for a 17x17 fuel assembly, 66 fuel rods are averaged together. Clearly, with this mesh fidelity, variations in rod power and local coolant conditions are not modeled.

## Recent

More recently, under the CASL program, the industry-standard CRUD prediction capability was improved through the coupling of BOA and VIPRE with a neutron diffusion and depletion code [Secker et al., 2011, Secker et al., 2012, Kendrick et al., 2013]. The neutronics code used in this coupling effort was ANC, a 3-D neutron diffusion tool that uses cross sections generated by the 2-D lattice code PARAGON. A consistent radial mesh of 2x2 quarter-assemblies was used in all three codes. A typical ANC axial mesh consists of approximately 24 uniform-thickness nodes; it is assumed that the axial resolution was also consistent with up to 60 uniform thickness planes.

**Algorithm 1.1** ANC/VIPRE/BOA time-consistent coupling formulation for a given time step from $n$ to $n+1$.

1. Initialize solution at time $n$
   (a) Steady state neutronics/TH at $n$
2. Obtain predictor solutions using initial solution
   (a) Deplete nuclide composition from $n$ to $n+1$
   (b) Deposit CRUD from $n$ to $n+1$
3. Obtain corrector solutions using most recent solutions
   (a) Steady state neutronics/TH at $n+1$
   (b) Deplete nuclide composition from $n$ to $n+1$; average P-C solutions
   (c) Deposit CRUD from $n$ to $n+1$; average P-C solutions
   (d) Converged? If not, repeat (3); if so, exit

The coupling between VIPRE and ANC featured a two-way data exchange interface, which used FPI to converge the nonlinear solution. The three way coupling with BOA was completed by a one-way data transfer from VIPRE to BOA and another from BOA to ANC. A time-consistent solution was eventually obtained by embedding the FPI within a predictor-corrector method, e.g. a type of Crank-Nicolson time advancement [Schmidt, 2012], as summarized in Algorithm 1.1. It is noted that the feedback mechanisms of boron destruc-

tion due to transmutation of boron-10 to lithium-7 and that of the thermal resistance within the thermal hydraulic and heat transfer solver are not included. Without including the thermal insulation of the cladding due to CRUD within the thermal hydraulic (heat transfer) solver, CILC predictions based on cladding temperature changes are not possible.

A higher fidelity capability was developed and investigated by using CFD to predict heat transfer coefficients (HTC) within a representative fuel assembly [Secker et al., 2012]. The CFD-predicted HTCs were extracted following a spacer grid and scaled by the standard Dittus-Boelter forced convection HTCs predicted within VIPRE. The HTC ratios were binned in 10 unique intervals, which then represented 10 unique surfaces within each BOA node. The resultant CRUD deposition using the higher fidelity mesh model, which included various sub-cooled boiling magnitudes, showed significant reduction in CRUD and boron mass, thus demonstrating the importance of mesh refinement and inclusion of CFD-scale physics. It is noted that only the HTC was varied within the BOA node; variations in rod power, heat flux, and coolant temperatures were not explicitly considered.

AREVA has also developed a CRUD risk assessment methodology, which acknowledges the need for high resolution models [Jones et al., 2013, Bhatt et al., 2015]. Four risk assessment levels were identified that include both low and high fidelity analysis; three relevant levels are: Level II corresponds to the legacy analysis fidelity of quarter-assemblies, Level III uses higher fidelity subchannel and neutronics methods to quantify CIPS and CILC risk, and Level IV includes CFD modeling to more accurately assess the CILC risk.

## Current

In the present dissertation, a new state-of-the-art, higher fidelity framework for the modeling of CRUD deposition is introduced and analyzed. The objective of this work is to improve CIPS and enable CILC predictions on a rod-by-rod basis, which previously have not been possible.

In the proposed framework, the individual fuel rods are explicitly modeled in each of the coupled physics, allowing calculations more closely based on first principles. A 3-D CRUD deposition tool, MAMBA, which was jointly developed by Los Alamos National Laboratory and CASL, is used. The addition of 3-D computational fluid dynamics and 3-D neutron

transport with depletion complete the multiphysics framework. Refer to Table 1.1 for a comparison of the methods and resolution of the suggested computational framework to the previous CRUD deposition modeling approaches.

Of course, a coupled simulation of such a high fidelity is significantly more computationally expensive and will be constrained to the sub-assembly level, e.g. pin array, for the computational model size. Consequently, it is the author's expectation that coarser mesh models, such as ANC/VIPRE/BOA, may be used to identify regions of the full-core that should be further investigated and analyzed using the high fidelity framework presented in Chapter II. Moreover, CFD-informed correlations to model the enhanced heat transfer effects (downstream of spacer grids) within existing subchannel analysis codes are another option for reducing the computational expense.

Table 1.1: Comparison of methods/resolution of suggested computational framework to previous CRUD deposition modeling approaches.

| Physics | Method previously used | Method currently used |
|---|---|---|
| Neutronics | 3-D nodal diffusion | 3-D neutron transport |
| Thermal hydraulics | 1-D subchannel | 3-D fluid dynamics |
| CRUD/chemistry | lumped parameter | 3-D finite element |

## Model validation

Two options of validating physics models are:

1. existing plant operating data,
2. and a controlled experiment.

As an initial validation of the high fidelity CRUD deposition modeling framework presented in this dissertation, both sources of data are utilized. The Seabrook nuclear power plant experienced both CIPS and CILC; upon shutdown CRUD and oxide measurement data were taken via both visual and scraping techniques. Simulation and plant data comparisons are performed in Chapter VI.

Additionally, experiments at the WALT loop, a high pressure flow loop that allows accelerated CRUD growth along a heated rod, have allowed the tuning of several input parameters of the present CRUD deposition model [Deshon, 2011, Kendrick and Barber, 2012, Wang et al., 2013]. To date, a controlled experiment used to validate the present multiphysics CRUD deposition model has not been performed.

## 1.5 Objectives and original contributions

The primary objective of this dissertation is:

***To advance the CRUD deposition modeling state-of-the-art by developing a high fidelity multiphysics framework to enable improved CIPS and CILC prediction capabilities on a rod-by-rod basis.***

Additional objectives and original contributions are identified as follows:

- identification and quantification of the most important CRUD structure properties, boundary conditions, and multiphysics feedback mechanisms from a modeling standpoint,
- development of spatial and temporal modeling requirements for inclusion of CRUD deposits within neutronics and thermal hydraulics,
- application of control theory methods to automate and adapt time stepsize selection for lattice depletion and other loosely coupled multiphysics simulations relevant to CRUD deposit on modeling,
- demonstration of the capability of the modeling framework through an initial validation with plant data,
- and identification of areas of future research that will most significantly and quickly improve CIPS and CILC predictions.

## 1.6 Dissertation outline

In the present introductory chapter, the physics of nuclear reactors and the various modeling approaches were summarized. Moreover, the operational effects of CRUD deposits on fuel rods and how this dissertation aims to improve model predictions was detailed. In the subsequent chapters, the computational framework for modeling CRUD deposition on a rod-by-rod basis is detailed.

An outline of the topics contained with each remaining chapter follows:

**II** the physics involved in the suggested modeling framework are introduced from a partitioned and a coupled viewpoint,

**III** the sensitivity of CRUD deposition predictions to CRUD property inputs and to the coupled boundary conditions provided by neutronics and thermal hydraulics are compared,

**IV** the feedback effects due to neutronics and thermal hydraulics are investigated to determine the dominating feedback mechanisms,

**V** an adaptive coupled time stepsize method based on control theory is developed and applied within the computational framework to optimize the multiphysics time stepping without sacrificing solution accuracy,

**VI** an initial model validation using Seabrook plant data is performed through a subassembly cycle simulation,

**VII** and the dissertation's conclusions, proposed future work, and similar modeling applications of the framework are summarized.

# CHAPTER II
# Governing physics

The multiphysics approach to high fidelity CRUD deposition modeling is described in this section. First, in Section 2.1, the governing equations of each of the physics are introduced. Then, in Section 2.2, simplified coupled equations are detailed using operator notation. In Section, 2.3, loose temporal coupling methods and their specific implementation within the CRUD deposition modeling framework are detailed. Last, in Section 2.4, the simulation models used in this dissertation are introduced with details contained in Appendix A.

## 2.1 Governing equations

Three partitioned physics of neutronics with fuel depletion, thermal hydraulics in the form of computational fluid dynamics, and CRUD/coolant chemistry are simulated using the computational tools of DeCART (Deterministic Core Analysis based on Ray Tracing), STAR-CCM+, and MAMBA (MPO Advanced Model for Boron Analysis), respectively. The specific methods and models used within these three codes are described in this section. After introducing the governing equations in this section, the variables directly involved in the coupling between the physics are discussed in Section 2.2.

### 2.1.1 Neutronics and fuel depletion

DeCART is a whole core neutron transport code capable of direct sub-pin level flux calculation at power generating conditions of a light water reactor. It requires neither *a priori* cross

section homogenization nor group condensation as needed in conventional reactor physics calculations, i.e. DeCART serves as a combined 2-D lattice physics and 3-D nodal diffusion tool. DeCART solves the 3-D neutron transport problem employing a 2-D/1-D method in which each planar (2-D) solution is performed using the Method of Characteristics (MOC), and the axial (1-D) solution is performed using the Nodal Expansion Method (NEM) based kernel [Joo et al., 2004, Hursin et al., 2008]. A 3-D consistent solution is obtained through coupling the transverse leakage terms; moreover, coarse mesh finite difference (CMFD) is used to accelerate convergence of the 2-D/1-D solution iteration.

The MOC solution is obtained by tracing discrete rays through the problem geometry. The number of characteristic rays is user-defined through three inputs of uniform ray spacing, number of rays in the polar direction within a quadrant, and number of rays in the azimuthal direction within a quadrant. Each ray represents a discretized volume, which is defined as the product of the ray's track length and spacing, within the problem domain. Very thin material layers, especially those that are strongly neutron absorbing, such as IFBA (integral fuel burnable absorber) or CRUD, may impose a stronger dependence of the solution on the ray tracing parameters [Walter and Manera, 2016b].

The DeCART code has various computational capabilities to solve both steady state eigenvalue problems and transient fixed source problems. The steady state calculation can be performed in various modes, which may consist of a criticality search, branch, restart, and/or depletion calculation. The depletion calculation is performed using the predictor-corrector method and has been well validated for a wide range of pressurized and boiling water reactor applications [Zhong et al., 2004].

### Methods of characteristics

The DeCART model domain is divided into a user-specified number of flat source regions (FSR), which are sufficiently small so that the sources, as well as the material properties, are regarded uniform in each region. Within each FSR, the angular flux and the corresponding scalar flux are determined and used to resolve the global spatial flux distribution. Another user-specified computational discretization is that of the cross section regions (XSR), which may be coarser than FSR, but not finer. The XSR mesh defines the coarsest discretization where material properties are constant. A relevant (assumed constant) material property

within each XSR is the macroscopic cross section, which is given as the product of the microscopic cross section $\sigma_x$ with reaction type $x$ and the material number density $N$,

$$\Sigma_x = \sigma_x N. \tag{2.1}$$

It is also noted that the microscopic cross section is a function of temperature, which is another material property assumed constant within each XSR during the neutronics calculation. Material temperatures and densities may be assumed or obtained from a thermal hydraulics calculation, typically by a subchannel or CFD solution.

The steady state Boltzmann transport equation is a function of six variables including three spatial $\vec{r}$, two angular $\vec{\Omega}$, and one energy $E$. The equation is expressed as,

$$\Omega \cdot \nabla \varphi(\vec{r}, \vec{\Omega}, E) + \Sigma(\vec{r}, E)\varphi(\vec{r}, \vec{\Omega}, E) = q_s(\vec{r}, \vec{\Omega}, E) + q_f(\vec{r}, \vec{\Omega}, E), \tag{2.2}$$

with the source term composed of the scattering source and an assumed isotropic fission source,

$$q_s(\vec{r}, \vec{\Omega}, E) = \int_0^\infty dE' \int_{4\pi} d\Omega' \Sigma_s(\vec{r}, \vec{\Omega}' \to \vec{\Omega}, E' \to E)\varphi(\vec{r}, \vec{\Omega}', E'), \tag{2.3}$$

$$q_f(\vec{r}, \vec{\Omega}, E) = \frac{1}{4\pi} \frac{\chi(\vec{r}, E)}{k} \int_0^\infty dE' \nu\Sigma_f(\vec{r}, E')\phi(\vec{r}, E). \tag{2.4}$$

The angular and scalar flux are related by integration over the solid angle,

$$\phi(\vec{r}, E) = \int_{4\pi} \varphi(\vec{r}, \vec{\Omega}, E). \tag{2.5}$$

As mentioned, DeCART is based on the MOC solution, which is obtained for 2-D *slices* of the 3-D geometry; these slices are referred to as *planes*. Equation 2.2 is integrated in the axial direction across a plane with a given thickness, and then the partial derivatives are replaced by total derivatives to obtain the characteristic equation,

$$\frac{d}{ds}\bar{\varphi}(\vec{r}_{\vec{r},0} + s\vec{\Omega}_{\vec{r}}, \vec{\Omega}, E) + \frac{\bar{\Sigma}(\vec{r}_{\vec{r},0} + s\vec{\Omega}_{\vec{r}}, \vec{\Omega}, E)}{\sin\theta}\bar{\varphi}(\vec{r}_{\vec{r},0} + s\vec{\Omega}_{\vec{r}}, \vec{\Omega}, E)$$

$$= \frac{1}{\sin\theta}\tilde{q}(\vec{r}_{\vec{r},0} + s\vec{\Omega}_{\vec{r}}, \vec{\Omega}, E), \tag{2.6}$$

where $\vec{r}_{\vec{r}}$ is the position vector in 2-D space with $\theta$ as the polar angle of $\vec{\Omega}$.

Under the assumption that the material properties and source term are constant within a given FSR, the solution of Equation 2.6 for the angular flux is,

$$\bar{\varphi}(\vec{r}_{\vec{r}}, \vec{\Omega}_{\vec{r}}, E) = \bar{\varphi}(\vec{r}_{\vec{r},0}, \vec{\Omega}_{\vec{r}}, E)\exp\left(-\frac{\bar{\Sigma}(E)s}{\sin\theta}\right) + \frac{\tilde{q}(\vec{\Omega}_{\vec{r}}, E)}{\bar{\Sigma}(E)}\left[1 - \exp\left(\frac{\bar{\Sigma}(E)s}{\sin\theta}\right)\right] \tag{2.7}$$

The axial integration transforms the axial leakage into a source term, which is used to couple the planes. Therefore, a 1-D coupling of each planar MOC solution is realized, resulting in the 2-D/1-D method solution of the 3-D transport equation.

**Fuel depletion**

The transmutation of nuclides during reactor operation is a time-dependent process that is coupled with the steady state neutronics solution of the neutron flux field. The coupling of these physics enables accurate fuel depletion calculations. A general expression for the change in the concentration $N$ of a nuclide $i$ by neutron interaction and radioactive decay is given as,

$$\frac{dN_i(t)}{dt} = \sum_{j=1}^{M} l_{ij}\lambda_j N_j + \bar{\phi}\sum_{k=1}^{M} f_{ik}\sigma_k N_k - (\lambda_i + \sigma_i\bar{\phi})N_i, \tag{2.8}$$

where the coefficients including the microscopic reaction rate are assumed constant for the XSR, and for a given depletion time step. The macroscopic reaction rate $R$ for a nuclide $i$ in a given XSR is given by,

$$R_i = \sigma_i N_i \bar{\phi}, \tag{2.9}$$

where the multi-group cross section and scalar flux have been collapsed to a single energy group. The multi-group cross section is collapsed to one group using weighting factors calculated from the multi-group fluxes. The coefficients in Equation 2.8 are summarized as:

- $l_{ij}$ is the fraction of radioactive disintegrations by nuclide $j$ leading to the formation of nuclide $i$,
- $\lambda_i$ is the radioactive disintegration for nuclide $i$,
- and $f_{ik}$ is the fraction of neutron reactions by nuclide $k$ leading to the formation of nuclide $i$.

A system of coupled first-order ordinary differential equations describes the nuclide transmutation of several nuclides; this system is written in vector-matrix form as,

$$\frac{d\vec{N}(t)}{dt} = \vec{\vec{A}}\vec{N}, \tag{2.10}$$

where $\vec{\vec{A}}$ is an $NxN$ matrix, often referred to as the *transition matrix*. An efficient solution algorithm is used in DeCART, which was originally employed within ORIGEN-2.2. This approach relies on the matrix exponential method for the long-lived nuclides and on a Gauss-Seidel iteration for the short-lived nuclides [Croff, 1980]. Separation of the long- and short-lived nuclides is necessary to reduce the stiffness of the transition matrix to allow calculation of the matrix exponential.

Recently, several other methods have been suggested including Krylov subspace methods [Yamamoto et al., 2007], CRAM [Pusa and Leppanen, 2010], and a new two-block decomposition method [Lee and Nam, 2013]. Moreover, comparisons of the various methods have been performed [Saadi et al., 2012,Isotalo and Aarnio, 2011a]. It is noted that numerical integration methods may also be used to solve the nuclide transmutation problem as performed in the ALEPH code [Fiorito et al., 2013], where an implicit multi-stage Runge Kutta method is utilized.

The removal of the nonlinear dependence of the microscopic reaction rate on the nuclide concentration is partially recovered through the use of a predictor-corrector method as described in Algorithm 2.2. Consequently, several methods have been developed and used in practice in many lattice physics codes. In general, the P-C methods are all of the type where the predictor step utilizes a forward Euler method, while the corrector step is essentially the trapezoidal rule.

**Algorithm 2.2** A typical predictor-corrector algorithm for fuel depletion where averaging the predictor and corrector nuclide concentrations is performed.

1. calculate the beginning-of-step (BOS) microscopic reaction rate, $R_{n-1}$, using the BOS nuclide inventory $N_{n-1}$,
2. deplete $N_{n-1}$ to the end-of-step (EOS) using $R_{n-1}$ to obtain the predicted EOS nuclide inventory, $N_n^p$,
3. calculate $R_n^p$ using $N_n^p$,
4. re-deplete $N_{n-1}$ to EOS using $R_n^p$ to obtain $N_n^c$,
5. and, average the predictor and corrector nuclide inventories to obtain the final nuclide inventory, $N_n = \frac{1}{2}(N_n^p + N_n^c)$.

For additional details on the 2-D/1-D solution scheme or the depletion methods employed within DeCART, including their practical implementation, please refer to [Hursin et al., 2008].

### 2.1.2 Fluid dynamics and heat transfer

STAR-CCM+ is a commercial computational fluid dynamics code that solves the balance equations for continuity, momentum, and fluid enthalpy on a 3-D finite-volume mesh. STAR-CCM+ is capable of modeling conjugate heat transfer (CHT), such that the conduction process is modeled within the fuel pellet and cladding and the convective heat transfer is modeled in the cooling fluid that surrounds the fuel pin. In the simulations presented in this dissertation, the Reynolds-Averaged Navier-Stokes (RANS) approach for the solution of the standard $k$-$\varepsilon$ transport equations is used for the turbulence modeling for a single phase fluid [Launder and Spalding, 1974]. In the current computational framework, two-phase fluid modeling is not included in the CFD solution; rather, localized subcooled boiling is only assumed to occur within the CRUD deposit pores, and such a model is included within the MAMBA code. Typically, the volumetric pore boiling rate is much larger than the surface boiling rate.

While the standard $k$-$\varepsilon$ turbulence model is known to be deficient when applied to compli-

cated flows involving strong streamline curvature, rotating flows, or turbulent anisotropy, past efforts have shown reasonable predictions when applied to flow velocity downstream of spacer grids with mixing vanes. Based on the results of recent benchmarks [NEA, 2013, Yan et al., 2014, EPRI, 2014, EPRI, 2015], the $k$-$\varepsilon$ model appears to be a good choice for the modeling effort presented herein. Next, the equations relevant to this type of flow modeling are introduced.

**Fluid flow**

The *continuity*, also known as *mass-conservation*, equation[1] is,

$$\frac{\partial \rho}{\partial t} + \nabla \cdot (\rho \vec{U}) = 0, \tag{2.11}$$

where $\rho$ is the fluid density and $\vec{U}$ is the velocity field. In the case of constant density flows, the continuity equation reduces to the *divergence-free* condition of,

$$\nabla \cdot \vec{U} = 0. \tag{2.12}$$

The incompressible *Navier-Stokes*, also known as the momentum balance, equation is,

$$\rho \frac{D\vec{U}}{Dt} = -\nabla p + \mu \nabla^2 \vec{U}, \tag{2.13}$$

where $\mu$ is the dynamic viscosity and $p$ is the pressure. Together, the continuity and Navier-Stokes equations govern the flow of constant-property Newtonian fluids.

The RANS equations are obtained by decomposing the instantaneous velocity and pressure fields into a mean value and a fluctuating component. This process is known as the *Reynolds decomposition*, and for velocity, it is given as,

$$\vec{U} = \left\langle \vec{U} \right\rangle + \vec{u}'. \tag{2.14}$$

[1] In the interest of generality, the time-dependent forms of the mass, momentum, and energy equations are shown; however, all CFD simulations documented in this dissertation were performed in steady state.

The decomposition results in an additional term, $\nabla \cdot \bar{\bar{T}}$, within the momentum transport equation, where $\bar{\bar{T}}$ is known as the *Reynolds stress tensor* and is given as,

$$\bar{\bar{T}} \equiv -\rho \left\langle \vec{u}'\vec{u}' \right\rangle = -\rho \begin{bmatrix} \langle u'u' \rangle & \langle u'v' \rangle & \langle u'w' \rangle \\ \langle u'v' \rangle & \langle v'v' \rangle & \langle v'w' \rangle \\ \langle u'w' \rangle & \langle v'w' \rangle & \langle w'w' \rangle \end{bmatrix}, \tag{2.15}$$

where the velocity components of $\vec{u}'$ are denoted by $u'$, $v'$, and $w'$ for the x-, y-, and z-directions, respectively. Another relevant quantity is the *turbulent kinetic energy* (TKE), which is computed as half the trace of the Reynolds stress tensor,

$$k = \frac{1}{2} \left\langle \vec{u}' \cdot \vec{u}' \right\rangle, \tag{2.16}$$

which physically is the mean kinetic energy per unit mass in the fluctuating velocity field [Pope, 2000].

**Turbulence modeling**

Modeling the Reynolds stress tensor and bringing closure to the governing equations is the primary challenge in turbulence modeling. Consequently, various models are available that attempt to predict the turbulent flow as accurately as possible, despite the assumptions associated with the RANS approach. Two fundamental classes of RANS modeling include eddy viscosity models and Reynolds stress transport models. The eddy viscosity approach is adopted in this work; however, Reynolds stress transport models have also been used as a basis for comparison (see Appendix B). The most common eddy viscosity model is the *Boussinesq approximation*, or the *turbulent-viscosity hypothesis*, which computes the Reynolds stress tensor as,

$$\bar{\bar{T}} = 2\mu_t \bar{\bar{S}} - \frac{2}{3}(\mu_t \nabla \cdot \vec{u}' + \rho k)\bar{\bar{I}}, \tag{2.17}$$

where the $\bar{\bar{S}}$ is the strain tensor given by,

$$\bar{\bar{S}} = \frac{1}{2}(\nabla \vec{u}' + \nabla \vec{u}'^{T}). \tag{2.18}$$

Essentially, the small-scale vortices, or eddies, are not resolved and a large-scale motion is calculated instead. The standard $k$-$\varepsilon$ turbulence model utilizes the Boussinesq approximation to provide closure to the flow equations. The turbulent viscosity $\mu_t$ is given by,

$$\mu_t = C_\mu \frac{k^2}{\varepsilon}, \tag{2.19}$$

with $C_\mu = 0.09$ for the $k$-$\varepsilon$ model.

Additional treatments in the viscous near-wall region of the standard $k$-$\varepsilon$ turbulence model are necessary to approximate the steep profiles of the velocity and the turbulent dissipation. These treatments are generally known as *wall functions*, and are implemented as boundary conditions a set distance away from the wall to ensure that the turbulence model equations are not solved within this region. An important parameter for defining wall functions is called *y-plus,* $y^+$, and is the distance from the wall measured in viscous lengths,

$$y^+ \equiv \frac{y}{\delta_\nu} = \frac{u_\tau y}{\nu}, \tag{2.20}$$

where $y$ is the distance from the wall, $\delta_\nu$ is the viscous length scale, and $u_\tau$ is the friction velocity defined as,

$$u_\tau \equiv \sqrt{\frac{\tau_w}{\rho}}, \tag{2.21}$$

with the wall shear stress given by,

$$\tau_w \equiv \rho\nu \left( \frac{d\langle \vec{U} \rangle}{dy} \right)_{y=0}. \tag{2.22}$$

The $y^+$ value is useful in differentiating the regions of near-wall flow. Closest to the wall, $y^+ <\sim 5$, referred to as the *viscous sublayer*, the Reynolds shear stress is negligible compared with the viscous stress. The *viscous wall region* is defined for $\sim 5 < y^+ <\sim 50$, where the Reynolds shear stress is affected by changes in molecular viscosity. In the *outer layer*, $y^+ >\sim 50$, viscosity effects are negligible [Pope, 2000].

In the viscous sublayer, where the mean velocity profile completely depends on the viscosity effects, a linear relationship is adopted,

$$u^+ \equiv \frac{\langle \vec{U} \rangle}{u_\tau}. \tag{2.23}$$

Alternatively, the *log law* is valid in regions with $y^+ > 30$,

$$u^+ = \frac{1}{\kappa} \ln y^+ + B, \tag{2.24}$$

where $\kappa$ is the von Karman constant and $B$ is a general constant. The region with $\sim 5 < y^+ <\sim 30$ is called the *buffer layer*, which is the transition region between viscosity- and turbulence-dominated regions of the boundary layer. Most CFD codes offer blended wall functions, where the transition region is represented by a continuous function that connects the laws given by Equations 2.23 and 2.24 [Rodi, 1991]. In STAR-CCM+ the blended wall function is referred to as the *two-layer* model.

### Conjugate heat transfer

In addition to using STAR-CCM+ for the solution of the flow equations, 3-D heat conduction and the associated heat removal through convection is solved, i.e. the simultaneous solution of heat transfer in both the solid (fuel, cladding, etc.) and fluid (coolant) is sought. This coupled solution is known as conjugate heat transfer; continuous boundary conditions of temperature and heat flux are imposed on the solid/fluid interface. Within the fluid and solid regions, the *Segregated Fluid Enthalpy* and *Segregated Solid Energy* models, respectively, in STAR-CCM+ are utilized. The total energy, $e$, conservation equation for the fluid is given as,

$$\rho \frac{De}{Dt} = -\nabla \vec{q}'' + q_f''' - p \nabla \cdot \vec{U} + \Phi, \tag{2.25}$$

where the heat flux vector out of the cladding is $\vec{q}''$ and the volumetric heat generation rate within the fluid is $q_f'''$, which is zero in this case. The dissipation function $\Phi$ is given as,

$$\Phi = (\bar{\bar{\tau}} : \nabla \vec{U}), \tag{2.26}$$

with the friction tensor as $\bar{\bar{\tau}}$; the associated rate of heat addition due to viscous effects is

typically small compared to the other terms in Equation 2.25. By applying thermodynamic relations and introducing the volumetric thermal expansion coefficient $\beta$ to Equation 2.25, a typical form for solving heat transfer problems is obtained,

$$\rho c_p \frac{DT}{Dt} = -\nabla \vec{q}'' + q_f''' + \beta T \frac{Dp}{Dt} + \Phi. \tag{2.27}$$

For each solid region $s$, e.g. the fuel and cladding materials, the heat equation takes the form of,

$$\rho c_p \frac{\partial T}{\partial t} = \nabla \cdot (k_{th}^s \nabla T) + q_s''', \tag{2.28}$$

where Fourier's law of heat conduction has been applied,

$$\vec{q}'' = -k_{th}^s \nabla T, \tag{2.29}$$

with $k_{th}^s$ as the solid thermal conductivity for region $s$. The volumetric heat generation rate $q_s'''$ within the solid is provided by the neutronics solution for the fuel material; there is not heat generation within the cladding. The fluid and solid heat solutions are coupled through the temperature and heat flux variables at the solid/fluid interface.

The use of conjugate heat transfer allows direct calculation of the wall temperature and heat flux without the need to estimate the heat transfer coefficient through a Nusselt-type correlation, e.g. Dittus-Boelter.

### 2.1.3 Coolant and CRUD chemistry

MAMBA simulates 3-D CRUD growth along the surface of a single fuel rod. MAMBA does not solve for the transport of corrosion particulates from their release site to the fuel rod; instead, such calculations are reserved for a system-level code like BOA.

The primary physics and chemistry associated with CRUD formation currently treated in MAMBA include:

- solving a general nonlinear, 3-D heat transport equation for the CRUD layer, including localized heat sinks due to internal boiling within the deposit,
- an adaptive grid which grows radially in time as mass deposits on the surface of the CRUD,
- time evolving microstructure (porosity) of the CRUD layer, due to localized deposition and precipitation of nickel ferrite and lithium tetraborate within the pores,
- time evolving lithium and boric acid coolant chemistry at the CRUD surface and inside the pores of the CRUD,
- mass transport of various soluble coolant species into the interior of the CRUD, due to boiling induced Darcy flow,
- diffusion of various soluble species inside the CRUD, due to the flow induced concentration gradients within the CRUD layer,
- and mass evaporation in the form of steam vapor, due to the localized boiling inside the CRUD layer.

The coolant chemistry conditions are supplied by the user, or an ex-core model, and consist of the following coolant concentrations: boron ($B$), lithium ($Li$), dihydrogen ($H_2$), soluble nickel ($Ni$), soluble iron ($Fe$), and particulate $NiFe_2O_4$. The external boundary conditions needed by the 3-D heat transport solver include the heat flux at the cladding surface and the temperature or heat transfer coefficient at the CRUD/coolant interface. The various CRUD properties used by MAMBA are based on the Westinghouse WALT loop studies [Kendrick and Barber, 2012], which include porosity, CRUD solid density and thermal conductivity. Additionally, the average CRUD chimney properties, including radius $r_{chim}$, density $\rho_{chim}$, and heat transfer coefficient $h_{chim}$, were optimized by fitting the MAMBA-computed CRUD temperature to the WALT loop data. The CRUD porosity $\eta$ and solid density $\rho_c$ may be combined to express the *bulk CRUD density*,

$$\rho_{bulk} = \rho_c(1 - \eta(\vec{r})), \tag{2.30}$$

where $\vec{r}$ is the position vector. Refer to Section 3.1 in Chapter III for a sensitivity study of the previously mentioned CRUD properties.

**Heat transfer**

The 3-D general, time-dependent, nonlinear heat equation for the CRUD layer with local heat sinks is,

$$\frac{\partial T(\vec{r},t)}{\partial t} = \nabla \cdot [D_t(\vec{r},t)\nabla T(\vec{r},t)] - T_{sink}(T, T_{sat}, \eta(\vec{r})), \tag{2.31}$$

where $T$ is the CRUD temperature field, $t$ is the time, and $T_{sat}$ is the saturation temperature of the coolant. The saturation temperature is dependent on the local soluble boric acid concentration—added to the coolant for reactivity control.

MAMBA's boiling correlation is best described as a generalized *Cohen-type* thermal hydraulics model [Henshaw et al., 2006, Cohen, 1974] with the boiling heat flux leaving a given CRUD volume element is expressed as,

$$q'' = h_{chim}\rho_{chim}A_{chim}\kappa(\eta)(T - T_{sat}), \tag{2.32}$$

where the effective bulk chimney boiling surface area is $A_{chim}$. The local heat sinks $T_{sink}$ are proportional to the chimney boiling by,

$$T_{sink} \propto \frac{q''}{h_{chim}\rho_{chim}}. \tag{2.33}$$

If the CRUD temperature is less than the saturation point, then the boiling heat flux is set to zero. The boiling heat flux acts as a localized *sink* in the heat transport calculation, thus resulting in a decreased thermal resistance across the deposit. The boiling model has been benchmarked against the models used in BOA and successfully validated against the WALT loop experiments [Deshon, 2011, Kendrick and Barber, 2012].

It should be clarified that the two-phase fluid models are implemented within MAMBA, while single-phase CFD calculations are performed to provide the CRUD layer boundary

conditions; i.e. subcooled nucleate boiling is assumed to only occur *within* the CRUD deposit and not within the coolant immediately outside the CRUD.

The thermal diffusivity $D_t$ is given by,

$$D_t(\vec{r},T) = \frac{k_{th}^{eff}(\vec{r},T)}{C_v(\vec{r},T)}, \tag{2.34}$$

where the effective thermal conductivity $k_{th}^{eff}$ is calculated as a standard mixing fraction where the conductivities of water $k_{th}^{w}$ and the CRUD $k_{th}^{c}$ are weighted by the CRUD porosity,

$$k_{th}^{eff}(\vec{r},T) = \eta(\vec{r})k_{th}^{w}(T) + [1-\eta(\vec{r})]k_{th}^{c}. \tag{2.35}$$

The solid CRUD thermal conductivity is fixed at 1.1 W/m-K, which was determined based on experimental CRUD growth studies using the WALT loop [Deshon, 2011, Kendrick and Barber, 2012]. The effective heat capacity is similarly determined, but is also weighted by the densities of water $\rho_w$ and the CRUD $\rho_c$,

$$C_v(\vec{r},T) = \eta(\vec{r})\rho_w(T)c_v^{w}(T) + [1-\eta(\vec{r})]\rho_c c_v^{c}(T). \tag{2.36}$$

The water properties are a function of pressure and temperature; standard NIST correlations are utilized. For reference, the thermal conductivity at standard operating temperature and pressure is approximately 0.6 W/m-K. Whereas, the specific heat capacity of the solid CRUD, $c_v^c$, composed primarily of nickel ferrite (a.k.a. trevorite), is calculated as a function of temperature from a correlation developed in [Ziemniak et al., 2007].

### Surface deposition kinetics

MAMBA models both surface and volumetric (pore fill) deposition of CRUD; let the CRUD layer be denoted by $c$ and its solid and porous components denoted by $s$ and $p$, respectively. The species $i$ that are available to deposit on the surface of the CRUD are nickel ferrite ($NiFe_2O_4$), nickel oxide ($NiO$), and iron oxide ($Fe_3O_4$). The CRUD surface deposition rate for each species is governed by two Arrhenius rate parameters associated with the porous regions inside the CRUD layer: (i) for boiling regions, $\tilde{a}_i^p$, which is multiplied by the local

mass evaporation rate $q_c''$, i.e. the steaming flux leaving the boiling chimneys, and (ii) for non-boiling regions, $a_i^p$. In boiling regions, the CRUD growth rate is enhanced due to the boiling-induced flow of coolant into the CRUD, which increases the flux of particulates onto the CRUD's surface. Moreover, competition between the advective flux of soluble species due to boiling-induced flow and concentration gradient-induced diffusive flux strongly affects the surface deposition rate.

Equation 2.37 gives the deposition kinetics rate equation for each surface element,

$$\frac{dN_i^c}{dt} = a_i^p N_i^p + \tilde{a}_i^p q_c'' N_i^p - N_{erosion}^c, \tag{2.37}$$

where $N_i^c$ and $N_i^p$ are particulate concentrations in the solid and porous CRUD regions, respectively. The Arrhenius rate coefficient is given as,

$$a_i^p = A_i^p \exp[-E_i^p/RT], \tag{2.38}$$

where $A_i^p$ and $E_i^p$ are the Arrhenius rate prefactor and activation energy, respectively, and $R$ is the universal gas constant. The CRUD loss due to turbulent flow is given as the product of the TKE $k_{CFD}$ and an adjustable constant $x_e$,

$$N_{erosion}^c = x_e k_{CFD}. \tag{2.39}$$

The constant $x_e$ was correlated with CRUD deposition patterns from plant data, where immediately downstream of the spacer grids very little to no CRUD exists, then it builds up throughout the span until just upstream of the next grid [EPRI, 2010]. Equation 2.37 is solved numerically used Gear's method with automatic time step refinement [Gear, 1969].

**Pore fill kinetics**

The species $j$ that are available to deposit within the CRUD include $NiFe_2O_4$, $NiO$, and $Fe_3O_4$, lithium tetraborate ($Li_2B_4O_7$), lithium metaborate ($LiBO_2$), bonnacordite ($Ni_2FeBO_5$), and metaboric acid ($HBO_2$).

The precipitation of various solid phase boron compounds, such as $Ni_2FeBO_5$, $LiBO_2$, and $Li_2B_4O_7$ is governed by equilibrium thermodynamics and is a function of temperature. The

temperature dependence of the equilibrium constants $K$ are typically fit to experimental data using a three-term correlation of the general form,

$$\log K = A + \frac{B}{T} + C \log T, \tag{2.40}$$

where $A$, $B$ and $C$ are fitting constants [Byers et al., 2000]. Byers details the development of a solubility correlation for lithium monoborate, which is implemented within MAMBA with coefficients of $A = -11.19885$, $B = 2531.638$, and $C = 5.1128$. Similar proprietary correlations are implemented for lithium tetraborate and bonnacordite. The relevant reaction of precipitation of lithium tetraborate is given as,

$$2Li^+ + 4B(OH)_3 \rightarrow Li_2B_4O_7 + 5H_2O + 2H^+. \tag{2.41}$$

Because lithium tetraborate is the least soluble and precipitates out of solution first (in comparison to the other boron-containing compounds of interest), this particular compound is the dominating *solid* boron phase within the CRUD deposit modeled by MAMBA. The dominant *soluble* boron phase is metaboric acid, which is added to the coolant within pressurized water reactors to control reactivity. The combination of the presence of lithium tetraborate and metaboric acid within CRUD deposits is believed to be the strongest contributor to CIPS.

The presence of solid boron phases also impacts the CRUD induced localized corrosion condition of the plant due to changes in the specific heat capacity and thermal conductivity of the CRUD layer. In general, the introduction of solid boron phases within the porous CRUD structure increases the thermal resistance and temperature of the corrosion deposit. This behavior is attributed to less convective cooling because the porous CRUD layer, including chimneys, are filled by the solid boron phases, thus restricting the flowing water's ability to remove heat. However, there is a trade-off between convective and conductive heat transfer as boron phases fill the CRUD pores. The thermal conductivity of the water present in the porous structure is lower than that of the solid CRUD/boron mixture, so heat conduction will be more efficient as the CRUD layer densifies.

The pore fill kinetics is governed by,

$$\frac{dN_j^c}{dt} = a_j^s A(\eta)[N_j^s - \underbrace{N_j^*(T, N_{Ni}^s, N_{Fe}^s, pH)}_{solubility}], \tag{2.42}$$

where $a_j^s$ is the Arrhenius rate coefficient and $A(\eta)$ is the pore surface area. The second term on the right side of Equation 2.42 is calculated through thermodynamics and solubility models. The time evolution of the CRUD porosity is described by,

$$\rho_{bulk}\frac{d\eta(\vec{r})}{dt} = -N_j^c m_j, \tag{2.43}$$

where the mass $m$ of species $j$ is calculated as the product of the molecular mass $M_j$, concentration $N_j$, and volume $V_j$.

**Species transport**

The soluble transport equation for species $j$ is,

$$\frac{dN_j^s}{dt} = \frac{(F_{boiling}^j - F_{diffusion}^j - F_{vapor}^j)}{\Delta r}, \tag{2.44}$$

where the local fluxes are defined as,

$$F_{boiling}^j = v_b N_j^s, \tag{2.45}$$

$$F_{diffusion}^j = \frac{D_j(T)\Delta N_j^s}{\Delta L}, \tag{2.46}$$

and,

$$F_{vapor}^j = v_s N_j^v, \tag{2.47}$$

where $\Delta L$ is the radial path length and $v_s$is the streaming velocity. The streaming and boiling velocities are related through mass conservation by,

$$\rho_s v_s = \rho_w v_b. \tag{2.48}$$

The local boiling velocity is,

$$v_b = \frac{q'''\Delta r}{H_v \rho_w}, \tag{2.49}$$

where $q'''$ is the volumetric heat generation rate, $\Delta r$ is the MAMBA cell radial thickness, and $H_v$ is the heat of vaporization of the water.

## 2.2 Coupled equations

In this section, simplified forms of the coupled equations are presented to emphasize the coupling variables within each solution field. Because the high fidelity prediction of CRUD deposition involves several complex and coupled solution methods, the most useful form to express the coupled equations is through the use of a specific physics operator that take inputs and transforms them to outputs. Of course, the inputs and outputs are not exhaustive of all solution variables, but are only included if relevant to the present modeling framework. Moreover, a simplistic conformal mesh (*one-to-one*) solution transfer between the physics is assumed for this discussion; however, in the actual coupled simulations, non-conformal solution transfers are performed, which include global conservation of quantities such as power and nuclide inventory.

The nuclide concentration $N$ is a vector that includes all relevant isotopes $j$, including, specific CRUD and boron concentrations provided from the CRUD physics, e.g. nuclides $Fe$, $Ni$, $O$, $Li$, and $B$. All remaining quantities discussed in this section are scalars values for a single cell within the respective physics' spatial discretization at an instant in time. Also, the scalar neutron flux and cross section represent collapsed, single energy group values.

For the steady state neutronics physics, the inputs consist of the nuclide concentration, nuclide microscopic cross section $\sigma$, nuclide temperature $T$, and the nuclide (coolant) density $\rho_{cool}$. The neutronics operator $\mathcal{N}$ represents the solution of the 3-D transport equation via the 2-D/1-D method, resulting in the local flux distribution $\phi$ and the critical coolant boron concentration $N_B^{cool}$,

$$(\phi, N_B^{cool}) = \mathcal{N}(\sigma, N, T, \rho_{cool}). \tag{2.50}$$

The cross sections are dependent on their temperatures $T$. For the coolant isotopes, their number densities are calculated based on the coolant density $\rho^{cool}$.[2]

The power density distribution $q'''$ is extracted and scaled to the flux distribution through the power density operator $\mathcal{P}$,

$$q''' = \mathcal{P}(\phi). \tag{2.51}$$

The neutron reaction rate with boron-10, also referred to as the boron destruction rate, within the CRUD layer is calculated as,

$$R_{B10} = \phi \sigma_{B10} N_{B10}. \tag{2.52}$$

The nuclide depletion, often in the form of Equation 2.8, is more simply represented using the depletion operator $\mathcal{D}$, which is a function of the flux and cross section,

$$N = \mathcal{D}(\phi, \sigma, N). \tag{2.53}$$

The steady state neutronics and nuclide depletion physics are coupled through $N$, $\phi$, and $\sigma$.

The CFD physics is represented by two primary equations, the Navier-Stokes equations as shown in Equation 2.13, denoted by the fluid operator $\mathcal{F}$, and the temperature equation as shown in Equation 2.28, denoted by the heat transfer operator $\mathcal{H}$. Together, these operators describe the conjugate heat transfer calculation. The fluid operator has a single coupled input of cladding surface heat flux $q''$, and its outputs are the coolant temperature $T^{cool}$, density $\rho^{cool}$, and turbulent kinetic energy near the cladding surface $k_{CFD}$:

[2] In practice, inclusion of the thermal hydraulic feedback ($T$ and $\rho_{cool}$) to the neutronics is crucial for realistic predictions of the neutron flux distribution and transmutation of nuclides during reactor operation. As a result, a fixed-point iteration of the neutronics and thermal hydraulics is recommended in this modeling framework. However, in the analyses contained within this dissertation, a one-way coupling from neutronics to CFD is utilized and the TH feedback is neglected. The rationale behind this approach stems from the importance of providing a typical (realistic) power distribution to the CFD solver, so that realistic thermal hydraulic boundary conditions may be provided to the CRUD deposition solver. A neutronics model domain of a single, radially-reflective pin cell does not adequately represent this heterogeneity of a fuel assembly, let alone a full core. As a result, maintaining a typical power distribution evolution with (high power) depletion and a typical coolant boron letdown is nearly impossible for such a small model when thermal hydraulic feedback is present.

$$(T^{cool}, \rho^{cool}, k_{CFD}) = \mathcal{F}(q''). \tag{2.54}$$

The heat transfer operator provides the cladding heat flux and solid temperatures, on the basis of the heat generation rate (power density) within the solid, coolant temperature, and CRUD thermal resistance $\Gamma$:

$$(T^{solid}, q'') = \mathcal{H}(q''', T^{cool}, \Gamma). \tag{2.55}$$

The neutronics, fuel depletion, and CFD physics are coupled through $q'''$, $T^{solid}$, $T^{cool}$, and $\rho^{cool}$.

The CRUD chemistry physics is represented by the operator $\mathcal{C}$, where inputs include the cladding heat flux, CRUD/coolant interface temperature, TKE, coolant boron concentration, and the neutron reaction rate with boron-10. The outputs include the CRUD thermal resistance and the CRUD composition $N_j^{CRUD}$, where $j$ may be $Fe$, $Ni$, $O$, $Li$, and $B$:

$$(N_j^{CRUD}, \Gamma) = \mathcal{C}(q'', T^{cool}, k_{CFD}, N_B^{cool}, R_{B10}). \tag{2.56}$$

The CFD and CRUD chemistry physics are coupled through $\Gamma$, $q''$, $T^{cool}$ and $k_{CFD}$; whereas, the neutronics and CRUD chemistry physics are coupled through $N_B^{cool}$, $R_{B10}$, and $N_j^{CRUD}$. The coupled variables between each of the physics is illustrated in Figure 2.6 for neutronics, fuel depletion, CFD with conjugate heat transfer, and CRUD deposition.

Figure 2.7 illustrates the CRUD modeling domain and its coupled boundary conditions, as shown in Equation 2.56, utilized by the MAMBA code. The fuel region generates heat $q'''$ within each axial spatial element, or plane, $z$. The thermal hydraulic solver calculates the heat transfer through the fuel and cladding to provide a heat flux as a Neumann boundary condition and a coolant temperature as a Dirichlet boundary condition for the CRUD deposition solver. Additionally, the turbulent kinetic energy is calculated and available to the CRUD solver to calculate erosion of the CRUD layer. The neutronics provides the destruction rate of boron-10 within the CRUD, and it provides a global coolant boron concentration. The radial and azimuthal distributions of all of the variables, excluding the coolant boron concentration, are also provided to MAMBA, but are not shown in Figure 2.7.

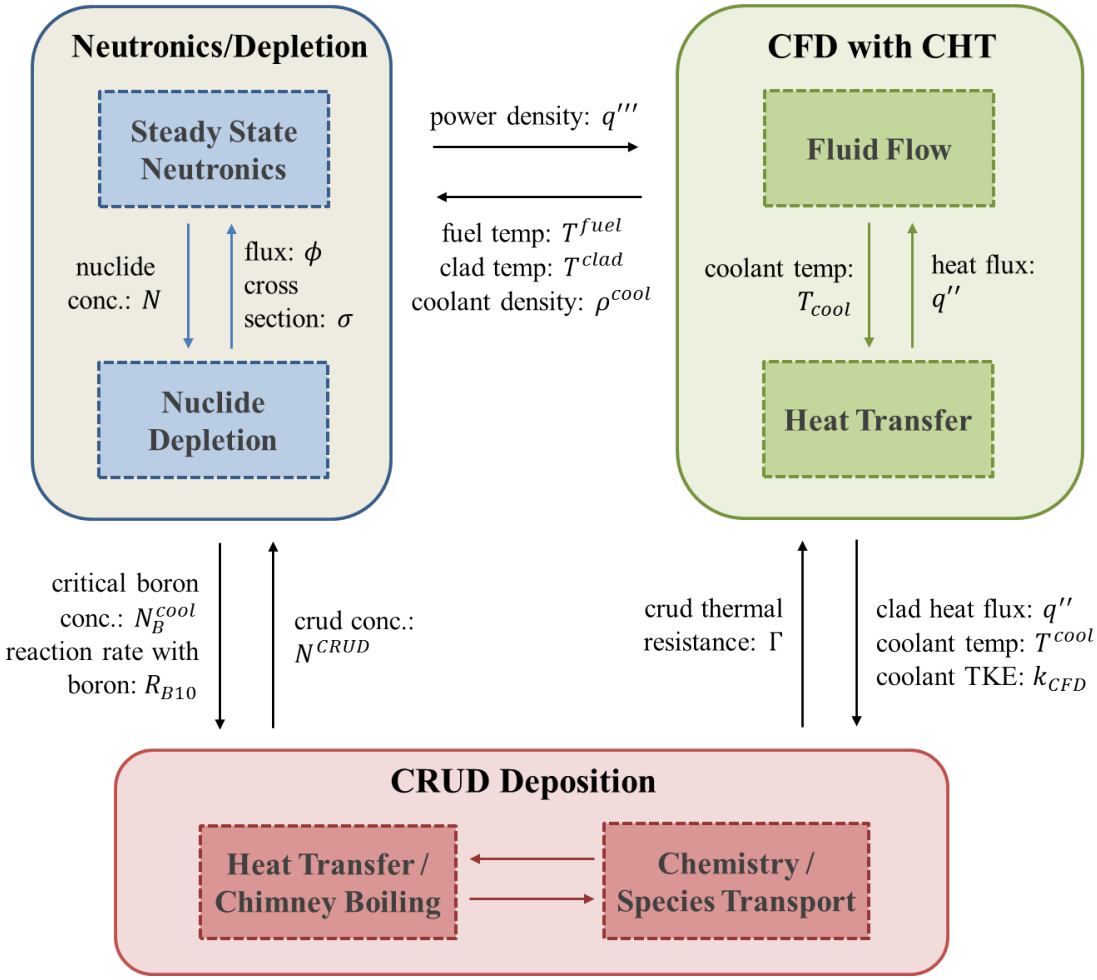


Figure 2.6: Multiphysics coupling and data exchange framework for high fidelity CRUD deposition modeling.

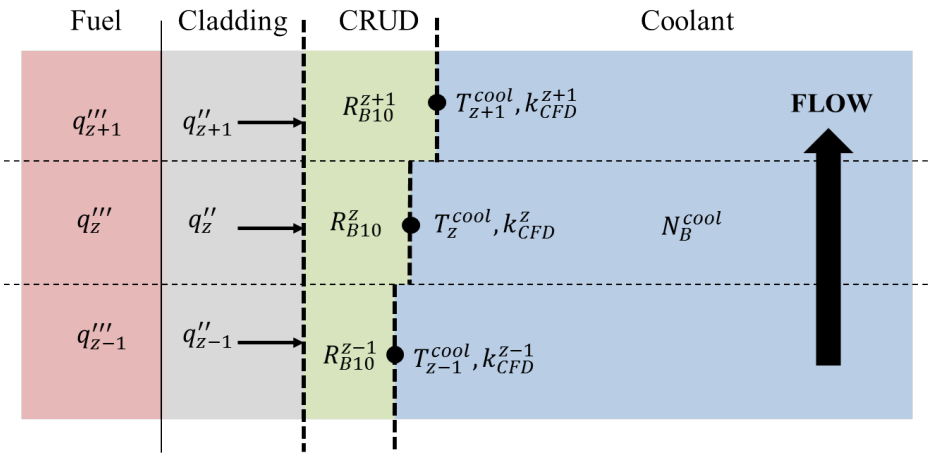


Figure 2.7: CRUD modeling domain and coupled boundary conditions provided to MAMBA (not to scale).

## 2.3 Loose temporal coupling approaches

Several loose temporal coupling methods are introduced in this section for the physics included within the modeling framework. Refer back to Section 2.2 and Figure 2.6 for a description of the coupled variables. Both one-way and two-way coupling approaches, as well as lagged and predictor-corrector methods, are utilized within this dissertation. Table 2.2 summarizes the physics components and their respective time scales.

Table 2.2: Summary of each physics' time scales.

| Physics | Temporal description | Time scale |
|---|---|---|
| Neutronics | steady | – |
| Fuel depletion | time-dependent | days |
| CFD | steady | – |
| CRUD deposition | time-dependent | hours |

## Coupled STAR-CCM+ and MAMBA

Consider the coupling of time-dependent CRUD deposition with steady state CFD, where the frequency at which to update the thermal hydraulic boundary conditions $T$ within the CRUD solver is controlled by the coupled time stepsize. The power distributions $q'''_n$ at each time step $n$ are calculated offline and assumed to be available to the CFD solver. Figure 2.8 (left) illustrates a method where the CFD solution lags the CRUD deposition solution; as the coupled stepsize approaches zero, so should the error in the coupled solution. Thermal resistance $\Gamma$ feedback to the CFD solver is also shown. In Figure 2.8 and all other figures in this section, the blue color indicates the beginning of the step and the red color indicates the end of the step.

Rather than explicitly lagging the CFD solution, a middle-of-step (MOS) approach is also considered, where the thermal hydraulic boundary conditions are interpolated between points $n$ and $n+1$. Figure 2.8 (right) illustrates the MOS scheme. To achieve a time-consistent solution, a predictor-corrector method is considered, as shown in Figure 2.9. Using this approach, two CFD and two CRUD deposition calculations are performed for each coupled time step; however, longer stepsizes are expected. Both the temporal dependence of the power distribution and the thermal resistance is considered in the corrector step by linearly interpolating the thermal hydraulic boundary conditions.

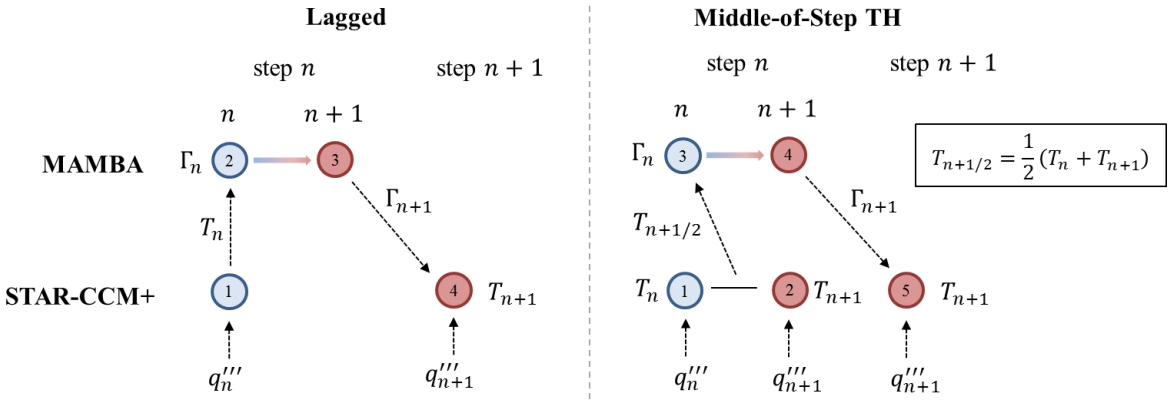


Figure 2.8: Lagged temporal (left) and middle-of-step thermal hydraulic (right) coupling between CFD and CRUD deposition models with offline calculation of power distributions.

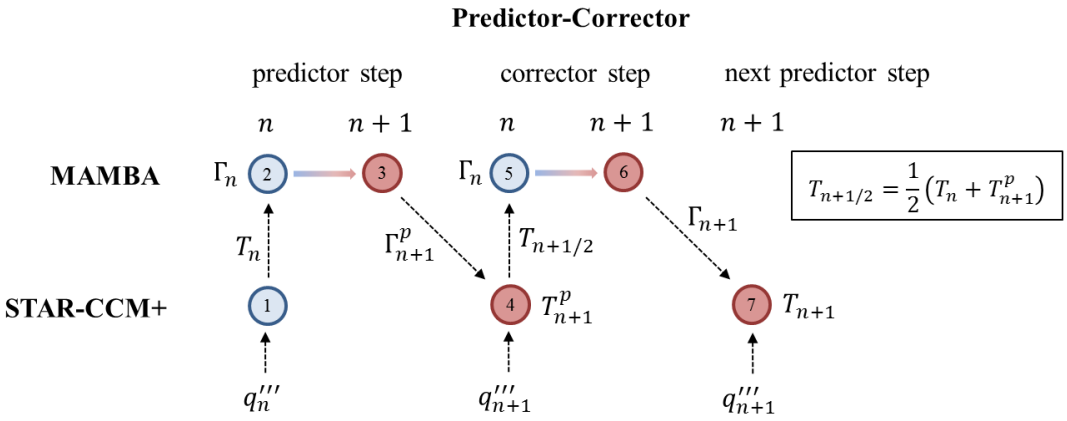


Figure 2.9: Predictor-corrector temporal coupling between CFD and CRUD deposition models with offline calculation of power distributions.

Because the power distribution evolution, e.g. $q'''_n$ and $q'''_{n+1}$, drive the cost of converging the CFD solution, each predictor step leverages the previous corrector step's converged solution. Therefore, the computational cost of the additional CFD simulation in the predictor-corrector method increases the CFD computational expense by about 10-20%, not 100%. On the other hand, the computational cost of the CRUD deposition solution when using a P-C approach is increased by 100% because the time-dependent solution starts at the beginning of the time step on both the predictor and corrector steps.

## Coupled DeCART, STAR-CCM+ and MAMBA

Introducing two additional physics components, namely steady state neutronics and time-dependent fuel depletion, to the coupling of CFD and CRUD deposition considerably complicates the temporal coupling method. As detailed in Subsection 2.1.1, a P-C approach is often adopted to enable larger neutronics/depletion stepsizes; a P-C method is always used for the neutronics/depletion calculation, even if a lagged approach is used for coupling with other physics.

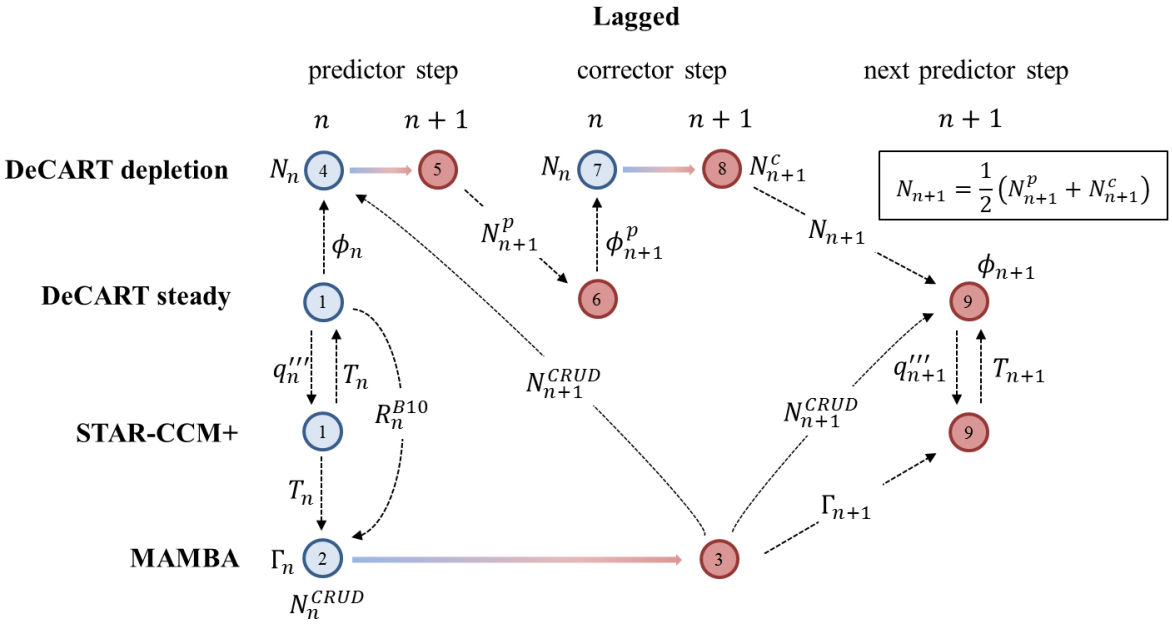


Figure 2.10: DeCART neutronics/depletion coupled with steady state STAR-CCM+ thermal hydraulics and time-dependent CRUD deposition via lagged approach.

Combining these physics with CRUD deposition via a time-lagged approach is illustrated in Figure 2.10. The end-of-step, $n+1$, CRUD composition is provided to the beginning of step, $n$, of the current depletion calculation and the beginning step, $n+1$, of the next steady state neutronics calculation. Moreover, the power distribution is provided to the CFD solver at the beginning of each time step. A fixed-point iteration is illustrated in Figure 2.10; however, a one-way coupling from neutronics to CFD is utilized in this dissertation. See Footnote 2 in Section 2.2 for rationale behind neglecting TH feedback to the neutronics.

To clarify, the approach shown in Figure 2.10 is still considered a lagged method because the CFD solution is only converged at the beginning and end of the time step; moreover, the feedback between the neutronics and the CRUD deposition is also only considered at the beginning and end of the time step. For small stepsizes, such a lagged approach will provide a sufficiently converged solution. To fully resolve the nonlinearity of the coupled systems, a time-consistent predictor-corrector approach must be considered for all of the physics, as shown in Figure 2.11. In this approach, all four of the physics are converged on both the

predictor and corrector steps.[3]

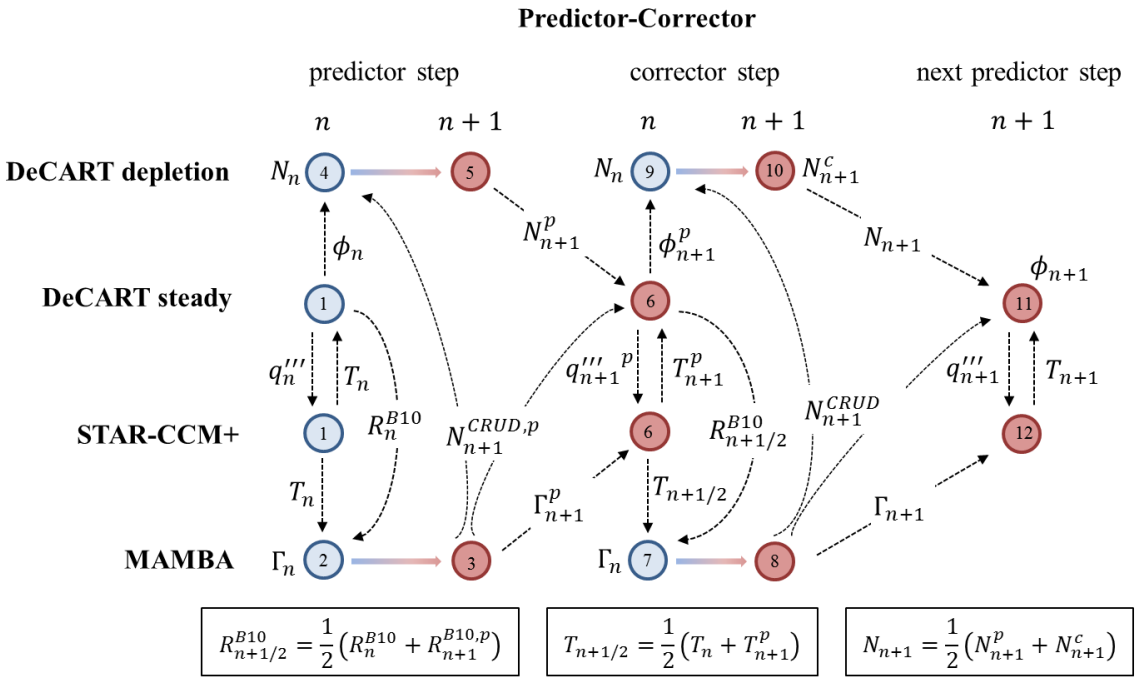


Figure 2.11: DeCART neutronics/depletion coupled with steady state STAR-CCM+ thermal hydraulics and time-dependent CRUD deposition via P-C approach.

[3]Regarding the temporal coupling shown in Figure 2.11, the predictor CRUD composition, $N^{CRUD,p}_{n+1}$, instead of the beginning-of-step composition, $N^{CRUD}_n$, is provided to the depletion solver. This modeling choice is based on the implementation requirements of an adaptive coupled stepsize algorithm, detailed in Subsection 5.2.2. Basically, better coupled time stepsize control is obtained by keeping the CRUD composition fixed during the depletion P-C calculation.

## 2.4 Simulation models

In the present modeling framework includes three primary physics:

1. neutronics with depletion,
2. computational fluid dynamics with conjugate heat transfer,
3. and CRUD deposition with coolant chemistry.

Because each physics is modeled by separate computational tools (e.g. DeCART, STAR-CCM+, and MAMBA), for each coupled simulation, three models must be described. Therefore, in this section, a high level summary of the models is included; whereas, details of the models are found in Appendix A.

Then, an overview of the coupling implementation and code structure is included. Finally, this section concludes with a discussion on the lateral boundary conditions used within the CFD models, specifically, symmetric vs. periodic. Additional sensitivity studies of the CFD turbulence model and meshing are contained in Appendix B and C, respectively.

### Plant conditions

Unless otherwise noted, the plant conditions for cycle 5 of the Seabrook Nuclear Power Plant are used in all of the simulation models. The dissolved species, including boron, lithium, and nickel concentrations are shown in Figures 2.12 and 2.13. These coolant conditions are assumed spatially constant and vary in time according to the reported plant data [WEC, 2011]. Around 50 effective full-power days (EFPD), a plant shutdown occurs, resulting in an instantaneous increase in the particulate and soluble nickel concentration within the coolant, i.e. a *CRUD burst* occurs following a power transient. The dissolution of the primary constituents of CRUD, such as nickel ferrite and lithium tetraborate, occurs due to their characteristic of retrograde solubility. In other words, as the temperature decreases, the solubility increases.[4]

[4]The occurrence of CRUD bursts leads to substantial difficulty in obtaining accurate solid boron and other CRUD constituent measurements because the species dissolve following a reactor shutdown.

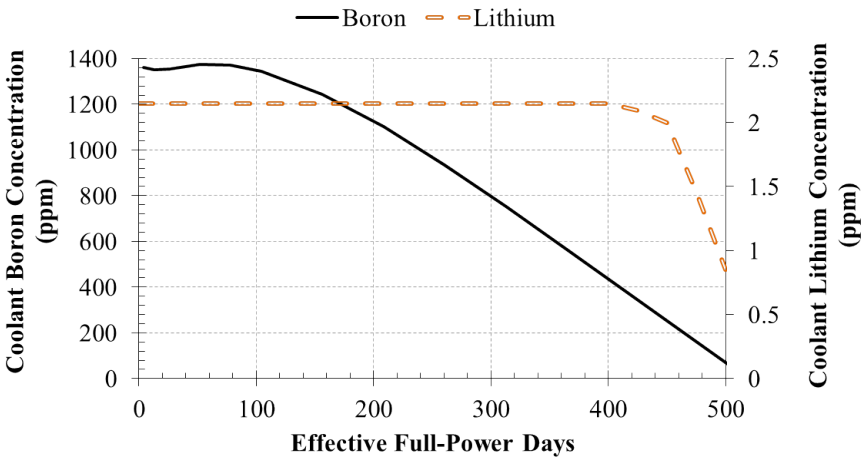


Figure 2.12: Coolant boron and lithium concentrations during cycle 5 of Seabrook plant.

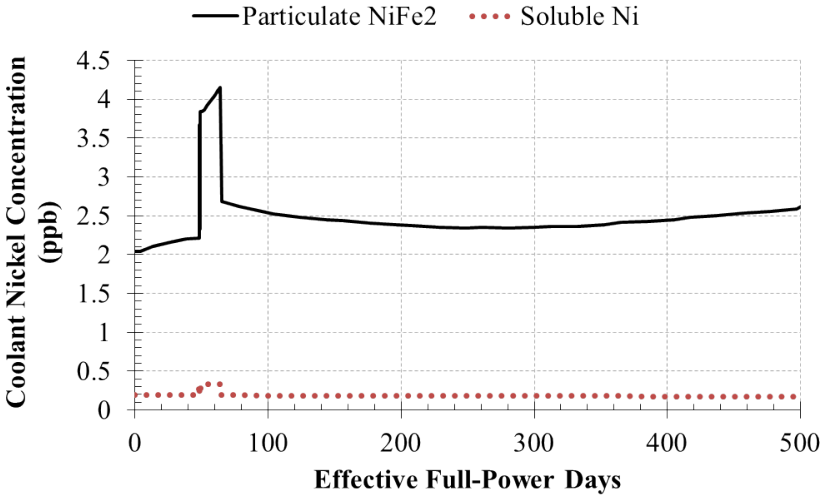


Figure 2.13: Coolant soluble and particulate nickel concentrations during cycle 5 of Seabrook plant.

## Model domains

To facilitate various sensitivity studies and model analyses, a total of three different modeling domains are utilized in this dissertation:

1. 2-D assembly,
2. 3-D pin cell,
3. and 3-D sub-assembly.

It is noted that the MAMBA model domain is no larger than a single fuel rod surface that grows CRUD in the radial direction; therefore, for multi-pin models, an instance of MAMBA is used for each fuel rod.

In Chapter III, a coupled STAR-CCM+ and MAMBA 3-D pin cell model is used. Two variations of the CFD model are considered: one with spacer grids and mixing vanes and one without. When the spacer grids are modeled, only three out of the typical eight grids are included to reduce the computational expense. The grids toward the top of the core, where coolant temperatures are highest, are included.

In Chapter IV, two neutronics models are introduced. The first model is a 3-D 5x5 pin array model that is used to assess the power shifting effect resulting from a boron-containing CRUD deposit. The second model is a 3-D pin cell model used to quantify the effects of the neutronics and thermal hydraulics feedback mechanisms on CRUD deposition predictions.

In Chapter V, 2-D assembly models are used to parameterize a depletion stepsize controller to facilitate automated and adaptive time stepsize selection. Three fuel loadings, including fresh fuel, IFBA, and gadolinium-bearing rods, are considered. Then, an additional stepsize controller is parameterized for a 3-D pin cell model to enable coupled DeCART, STAR-CCM+, and MAMBA cycle simulations.

In Chapter VI, a 3-D sub-assembly model consisting of a 5x5 pin array with a central guide tube is used to perform an initial validation with plant data. The CFD model includes three spacer grids with mixing vanes. A DeCART 3-D sub-assembly model is not used in this chapter because power distributions, precomputed by ANC, are used throughout the cycle simulation.

## Driver routine

Because STAR-CCM+ is a closed-source code, in-memory coupling with other physics is more complicated than with an open-source code. A capability, referred to as *user code*, is available within STAR-CCM+. Essentially, external code in C or FORTRAN may be compiled as a shared object library to be loaded at runtime. Access to STAR-CCM+ data in raw form, in-memory, is available through the user code. This capability is utilized to efficiently couple STAR-CCM+ with DeCART and MAMBA.

Moreover, user control of STAR-CCM+ is possible through a JAVA API; for example, a JAVA program can be written and used to drive coupled physics simulations with STAR-CCM+. Figure 2.14 illustrates the interaction of the JAVA driver, STAR-CCM+, and a user code shared object library.

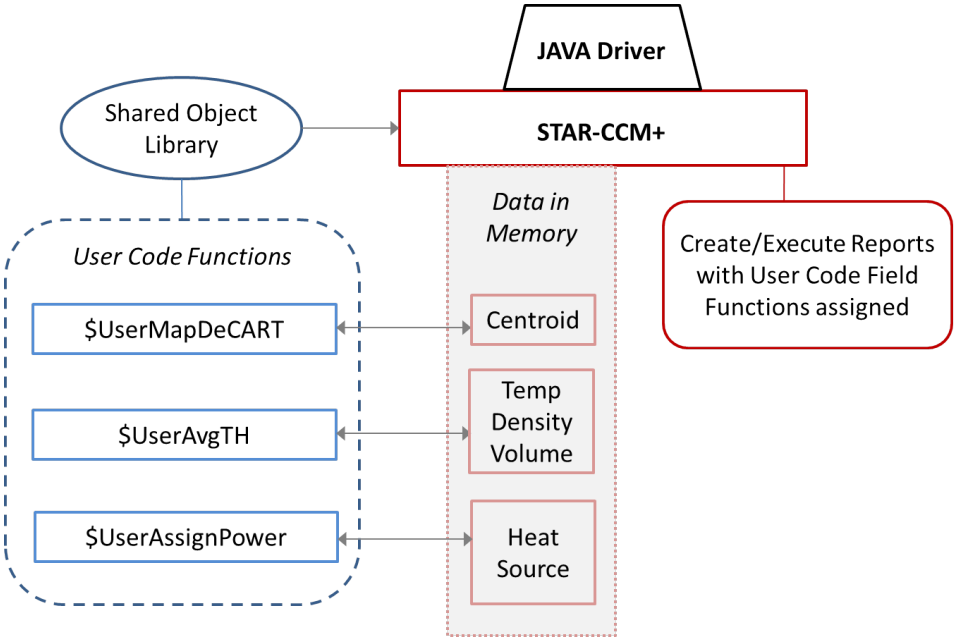


Figure 2.14: Interaction of JAVA driver, STAR-CCM+, and user code to enable multiphysics simulations.

## STAR-CCM+ lateral boundary conditions

Because of the significant computational expense of CFD, a single 3-D pin cell model (rather than a multi-pin model) containing three spacer grids with mixing vanes is repeatedly used in this dissertation. It is acknowledged that this is a *synthetic* model that cannot reproduce the exact turbulent flow patterns that would be present within a single pin cell within a reactor core; this is primarily due to the lateral boundary conditions. In reality, the number of vanes surrounding a fuel rod and the orientation of the vanes from one pin cell to the next varies significantly. For example, refer to Figure 7.96 in Appendix A.

Both symmetric and periodic lateral boundary conditions have been considered, and the differences of each models' thermal hydraulic predictions are briefly discussed herein. To best demonstrate the boundary condition effects when simulating a single pin cell domain, the azimuthal temperature variation of the outer cladding surface, as predicted by the conjugate heat transfer calculation, is compared for several axial elevations in Figure 2.15. The first spacer grid begins at an elevation of 203.28 cm, and the tips of the vanes reach an elevation of approximately 208 cm. In Figure 2.15, elevations of 200 cm, 208 cm, and 230 cm are compared.

In general, symmetric lateral boundary conditions should exhibit *quadrant-symmetry*; however, spatial discretization (meshing) effects in the present model results in minor asymmetries. On the other hand, the periodic boundary conditions result in similar behavior immediately downstream of the spacer grid, but further downstream, the quadrant-symmetry disappears and the periodic boundary effects are revealed.

Based on the asymmetry in the azimuthal cladding temperature distribution of an interior fuel rod in a sub-assembly model (see Figure 6.77 in Chapter VI), periodic lateral boundary conditions are adopted in the single pin cell CFD model in this dissertation. The quadrant-symmetry resulting from the symmetric boundary conditions is less representative of the flow patterns within an actual fuel assembly. That being said, the solution accuracy of the single pin cell CFD model is not crucial to draw accurate conclusions regarding the sensitivity of multiphysics CRUD deposition simulations.

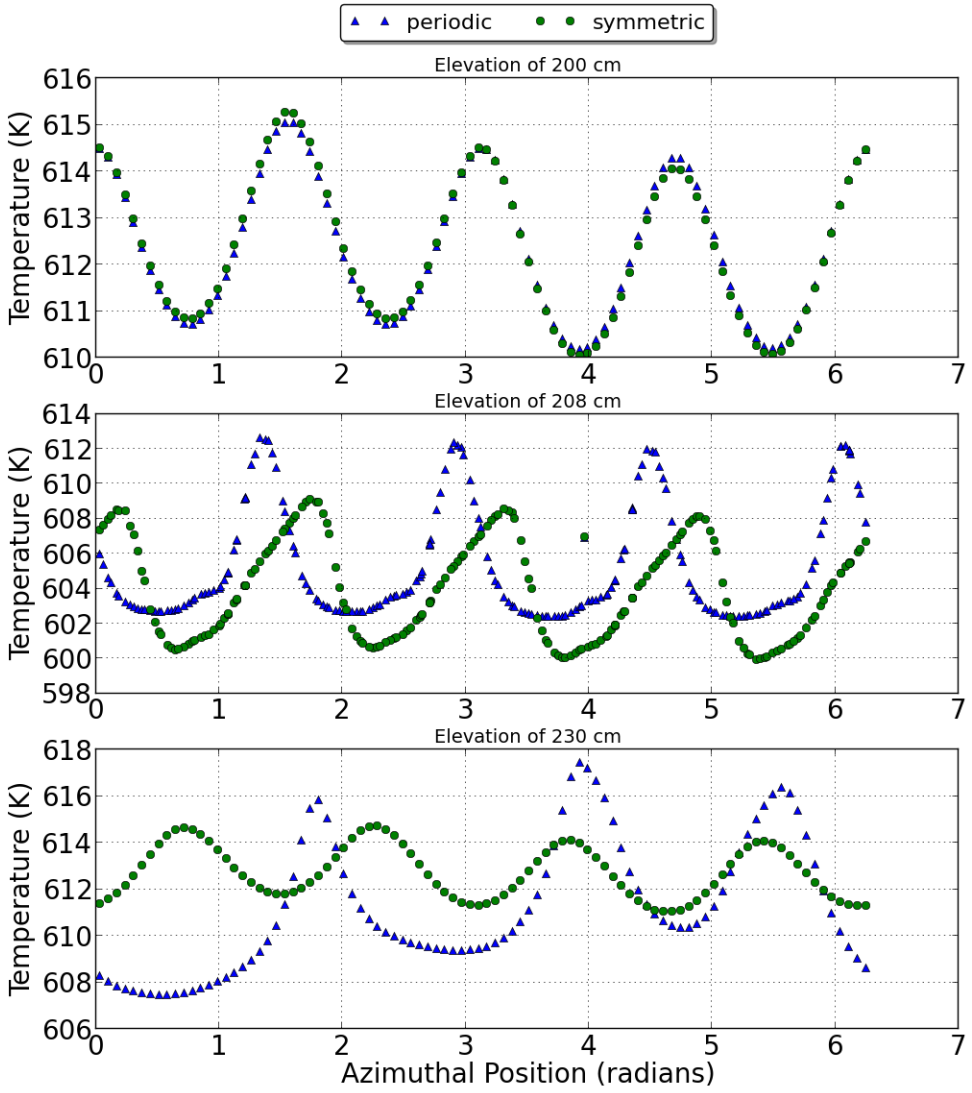


Figure 2.15: Comparison of outer cladding temperature for symmetric and periodic lateral boundary conditions in STAR-CCM+ single 3-D pin cell model with spacer grids.

# CHAPTER III

# Sensitivity of CRUD deposition predictions

In this chapter, the coolant and CRUD chemistry solver MAMBA is systematically analyzed to determine the solution sensitivity to changes in the input parameters and coupled boundary conditions. In the present framework, there are two types of inputs that should be distinguished from one another: *stand-alone* and *coupled*. The distinction between these types is that coupled conditions/parameters are those that are calculated by one of the coupled physics of neutronics or CFD.

The stand-alone conditions and input parameters that are considered are:

- particulate and soluble nickel concentration within coolant,
- CRUD solid density and porosity,
- CRUD chimney radius, chimney heat transfer coefficient, and chimney density,
- Arrhenius rate coefficient,
- and Arrhenius boiling rate coefficient (or SNB multiplier).

On the other hand, the coupled boundary conditions include:

- rod power magnitude and distribution,
- coolant boron concentration,

- cladding/CRUD interface heat flux distribution,
- CRUD/coolant interface temperature distribution,
- turbulent kinetic energy near CRUD surface distribution,
- and boron destruction rate within CRUD due to neutron capture reactions.

Additionally, the pin power distribution is not an explicit coupled boundary condition of the MAMBA code, but is used in the CFD solver to perform a conjugate heat transfer calculation between the heat generating fuel and the coolant flow. Therefore, the thermal hydraulic boundary conditions are strongly coupled with the power distribution, so it is included in the coupled conditions.

The coolant lithium concentration is also a stand-alone plant condition, but the CRUD prediction sensitivity to the lithium variability is not directly investigated. It is known that the lithium concentration directly impacts the precipitation of lithium tetraborate; however, the present analysis focuses on conditions that are modeled by one of the coupled physics, e.g. the critical coolant boron concentration is predicted by the neutronics/depletion solver.

First, a parametric study of the stand-alone inputs to MAMBA, with the exception of the Arrhenius rate parameters, is completed in Section 3.1. In Sections 3.2 and 3.3, an introduction of the 3-D pin cell model and a brief mesh convergence study are performed. Then, the effect of the non-boiling and boiling Arrhenius rate coefficients are analyzed. In Section 3.5, the coupled boundary conditions are systematically investigated for CRUD deposition simulations, where feedbacks from the coupled physics of neutronics, fuel depletion, and thermal hydraulics are not considered. Refer to Chapter IV for an analysis of the feedback mechanisms from the coupled physics.

## 3.1 Analysis of input parameters

A parametric study on MAMBA's stand-alone input parameters is completed using Latin hypercube sampling (LHS). Wilks formula states that approximately 100 samples—and therefore 100 simulations—are needed to ensure a two-sided limit of 95%/95% [Wilks, 1941, Nutt

and Wallis, 2004]. In other words, 95% of the design space is represented within the sample space to a 95% confidence level; and, the input parameters are assumed to be independent of one another. In case some of the sample simulations cannot complete or experience stability issues, 130 samples are simulated to ensure at least 100 samples will be available for data processing. If all 130 sample simulations are completed, then the confidence level is increased to 99% The software package DAKOTA is used to perform the sampling [Adams, 2015].

### 3.1.1 A simplified MAMBA model

To facilitate an efficient parametric study, a simplified MAMBA model is utilized; effectively, a 2-D model is realized by fixing the axial discretization to a single 1 cm thick region. This nodalization guarantees spatial convergence. The fuel rod radius is 0.4759 cm with a spatial domain outside the cladding surface that is discretized into 16 azimuthal regions and grows radially in 5 $\mu m$ increments.

Table 3.3: MAMBA input parameters that are fixed during the LHS parametric study.

| Parameter | Value | Units |
|---|---|---|
| Arrhenius rate coefficient | 130.0 | none |
| Boiling rate coefficient | $0.94\text{x}10^{-3}$ | none |
| Dissolved hydrogen concentration | 32.0 | $cm^3/kg$ |
| Nickel diffusion coefficient | $0.719\text{x}10^{-5}$ | $cm^2/s$ |
| Iron diffusion coefficient | $0.712\text{x}10^{-5}$ | $cm^2/s$ |
| Boric acid diffusion coefficient | $1.07\text{x}10^{-5}$ | $cm^2/s$ |
| Lithium diffusion coefficient | $1.03\text{x}10^{-5}$ | $cm^2/s$ |
| Deuterium diffusion coefficient | $4.80\text{x}10^{-5}$ | $cm^2/s$ |

Several input parameters and plant conditions remain fixed during this study, as detailed in Table 3.3. The coolant boron and lithium concentrations vary during the cycle according to Figure 2.12, but remain the same for all sample sets. Because the precipitation of solid boron phases is very sensitive to whether local subcooled nucleate boiling is occurring, two LHS cases are considered with different thermal hydraulic boundary conditions. Table 3.4

compares the cladding heat flux and coolant interface temperature for the cases, which were extracted from CFD with conjugate heat transfer simulations. The TH boundary conditions are spatially and temporally uniform, and erosion of the CRUD deposit due to the flow turbulence is not considered. This study was designed with the intent that the majority of parameter sets simulated using case A will not precipitate boron, whereas those associated with case B will. All 130 parameters sets are simulated for both case A and B.

Table 3.4: LHS cases with fixed thermal hydraulic boundary conditions used in MAMBA parametric study.

| LHS Case | Cladding heat flux ($MW/m^2$) | CRUD outer temperature (K) |
|---|---|---|
| A | 0.800 | 609 |
| B | 1.00 | 619 |

### 3.1.2 Latin hypercube sampling of design space

The lower and upper bounds of the stand-alone input parameters that are *uniformly* sampled are summarized in Table 3.5. A base case with values suggested by the WALT loop comparisons is also identified [Kendrick and Barber, 2012]. Defining distributions of the input parameters based on experiments is crucial to enable accurate uncertainty quantification; however, such distributions were not considered in this investigation.

The particulate and soluble nickel concentration ranges are based on the bounds associated with the Seabrook plant shown in Figure 2.13. The range of values for the porous CRUD properties is based on plant data [Byers and Wang, 2006] and experimental WALT loop studies [Deshon, 2011, Kendrick and Barber, 2012, Wang et al., 2013].

An upper limit of $1.0x10^6$ chimneys per $cm^2$ was suggested in [Short et al., 2013] by referencing [Deshon, 2011]; however, such chimney densities of this magnitude are uncommon based on the data reported in [Deshon, 2011, Kendrick and Barber, 2012, Wang et al., 2013]. In order to set realistic bounds on the chimney surface density, a metric known as the *chimney area fraction* is introduced,

$$f_{chim} = \rho_{chim} \pi r_{chim}^2. \tag{3.57}$$

Data reported in [Deshon, 2011] suggest lower and upper bounds of approximately 1% and 10%, respectively, on the chimney area fraction. In Table 7.37 within Appendix D [Byers and Wang, 2006, Wang, 2009], chimney densities of $\sim 1.0x10^6$ are reported, however, the associated average chimney radius is approximately 2 $\mu m$, resulting in a chimney area fraction approaching 15%. In Table 7.38 within Appendix D [Wang et al., 2013], the chimney densities from the WALT loop do not exceed $2.0x10^5$ and are, again, associated with radii of 2 $\mu m$, resulting in a chimney area fraction of 2.5%. A lower limit of 0.5% is also reported. Considering all of the reported data, a fractional area range of 0.5% to 15% is used in the present investigation.

Table 3.5: MAMBA input parameters and associated bounds used in Latin hypercube sampling study; suggested (base) values shown.

| Parameter | Lower Bound | Upper Bound | Base | Units |
|---|---|---|---|---|
| Particulate nickel concentration | 1.5 | 4.0 | 2.2 | ppb |
| Soluble nickel concentration | 0.2 | 0.35 | 0.22 | ppb |
| CRUD solid density | 4.6 | 5.5 | 5.33 | g/cm$^3$ |
| CRUD porosity | 0.55 | 0.72 | 0.7 | none |
| Chimney radius | 2.0 | 4.1 | 4.0 | $\mu m$ |
| Chimney heat transfer coeff | 1.0x10$^6$ | 1.0x10$^7$ | 6.7x10$^6$ | W/m$^2$-K |
| Chimney density | 4.5x10$^4$ | 3.0x10$^5$ | 1.0x10$^5$ | cm$^{-2}$ |

The CRUD porosity and solid density may be combined to express the *bulk CRUD density*,

$$\rho_{CRUD}^{bulk} = \rho_{CRUD}(1 - \eta). \tag{3.58}$$

Based on the WALT loop data reported in Table 7.38, a 60% porous deposit with solid density of 5.9 g/cm$^3$ gives an upper limit of the bulk density of 2.36 g/cm$^3$. A lower limit of 1.30 g/cm$^3$ is given by a porosity of 76% and solid density of 5.4 g/cm$^3$. The bounds of

the solid density, of 4.6 $g/cm^3$ and 5.5 $g/cm^3$, and porosity, of 55% and 72%, are used to respect similar bulk density limits.

The chimney heat transfer coefficient value of 6.7x10$^6$ W/m$^2K$ has previously been optimized by fitting the MAMBA-computed CRUD temperature to the WALT loop data [Kendrick and Barber, 2012]; a variation between 1.0x10$^6$ and 1.0x10$^7$ W/m$^2K$ was chosen based on initial validation experiments.

### 3.1.3 Correlation coefficients

The Pearson product-moment correlation coefficient [Pearson, 1895] is used to measure the linear correlation between the input variables and three output metrics of maximum CRUD mass, thickness, and boron mass during the cycle. The possible range of the coefficient is -1 to 1, where -1 is linear negative correlation, 0 is no correlation, and 1 is linear positive correlation.

Consider a scalar output $y$, which is obtained through $k$ inputs, or factors, $x_i$ according to the function,

$$y = f(x_1, x_2, ..., x_k). \tag{3.59}$$

Pearson's correlation coefficient is used for each factor $x_i$ and is expressed as the covariance of the input variable and output metric divided by the product of their respective standard deviations,

$$Corr(x_i, y) = \frac{\sum_n (x_{i,n} - \bar{x})(y_n - \bar{y})}{\sqrt{\sum_n (x_{i,n} - \bar{x})^2 \sum_n (y_n - \bar{y})^2}}. \tag{3.60}$$

The mean for a sample size of $N$ is given by,

$$\bar{x} = N^{-1} \sum_{n=1}^{N} x_n. \tag{3.61}$$

In the subsequent subsections, the correlation coefficients of each input factor are tabulated and compared for three output metrics of total CRUD mass, thickness, and total boron mass.

Then, the correlation scatter plots for the most strongly correlated inputs are reported. All 130 sample simulations are included in the calculation of the correlation coefficients, i.e. no sample simulations are discarded.

### Case A: Heat flux of 0.8 MW/m$^2$

An average correlation coefficient, calculated by considering the Pearson correlation coefficients for the end-of-cycle CRUD characteristics of CRUD mass, thickness, and boron mass, is utilized. In Table 3.6, the most correlated input factors are:

1. particulate nickel concentration with 0.84,
2. CRUD porosity with 0.34,
3. and CRUD solid density with -0.11.

The particulate nickel concentration has the highest sensitivity on all three metrics considered. Regarding the total CRUD mass, the particulate nickel concentration is 98% correlated with all the other six input factors less than 10% correlated. The CRUD thickness and boron mass predictions are also strongly correlated with the CRUD porosity and solid density, where a more porous and less dense CRUD structure results in thicker CRUD deposits with more boron hideout.

The correlation plots for these three parameters are shown in Figures 3.16, 3.17, and 3.18 for the CRUD mass, thickness, and boron mass, respectively. The remaining parameters of soluble nickel concentration, chimney radius, chimney density, and chimney heat transfer coefficient are, on average, less than 10% correlated with the output metrics. In Figure 3.19, the CRUD mass, thickness, and boron mass are plotted during the cycle for all 130 samples. The base case, described in Table 3.5, is also shown as a point of reference. A wide range of CRUD characteristics are predicted; the CRUD mass ranges from approximately $0.4x10^{-2}$ to $1.2x10^{-2}$ g, the thickness from 5 to 35 $\mu m$, and the boron mass from $0.1x10^{-3}$ to $1.5x10^{-3}$ mg.

Table 3.6: Pearson's correlation coefficients of LHS of MAMBA inputs for case A.

| Input parameter | Pearson's correlation coefficient | | | Average coefficient |
|---|---|---|---|---|
| | CRUD mass | Thickness | Boron mass | |
| Particulate nickel concentration | 0.98 | 0.80 | 0.74 | 0.84 |
| CRUD porosity | 0.088 | 0.48 | 0.46 | 0.34 |
| CRUD solid density | -0.038 | -0.19 | -0.11 | -0.11 |
| Soluble nickel concentration | 0.013 | 0.031 | 0.021 | 0.02 |
| Chimney radius | 0.0076 | 0.0035 | -0.063 | -0.02 |
| Chimney density | -0.026 | -0.033 | -0.0091 | -0.02 |
| Chimney heat transfer coeff | 0.015 | 0.0059 | -0.054 | -0.01 |

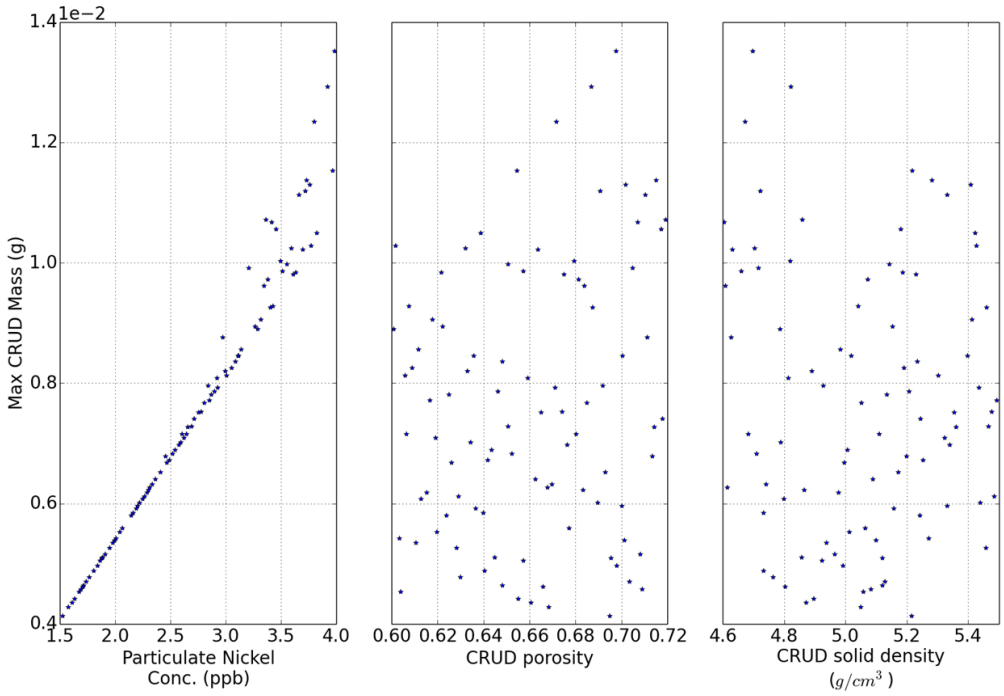


Figure 3.16: Maximum CRUD mass during cycle for LHS of MAMBA inputs for case A.

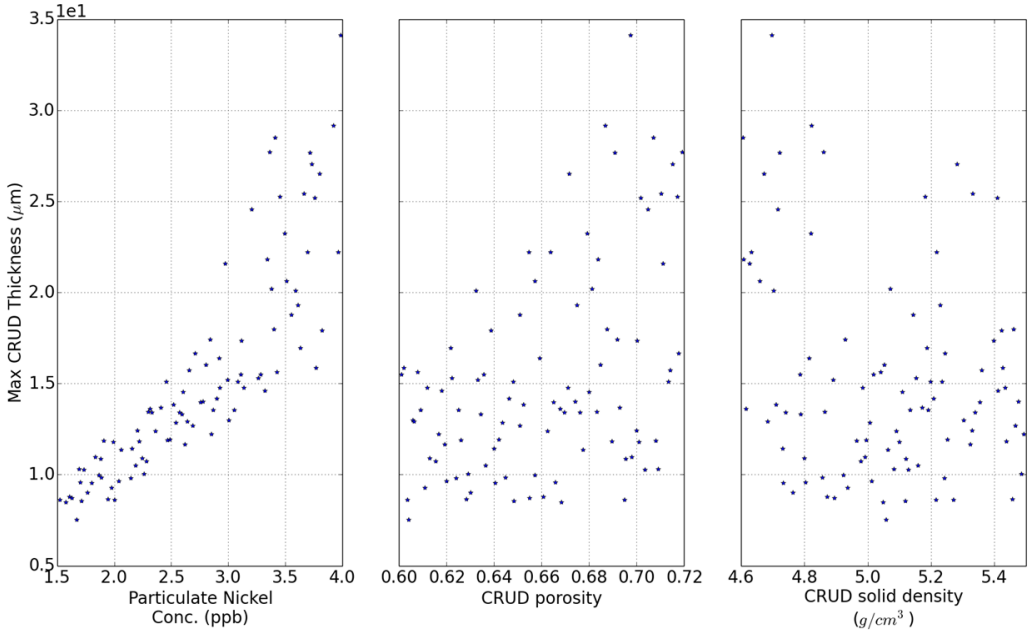


Figure 3.17: Maximum CRUD thickness during cycle for LHS of MAMBA inputs for case A.

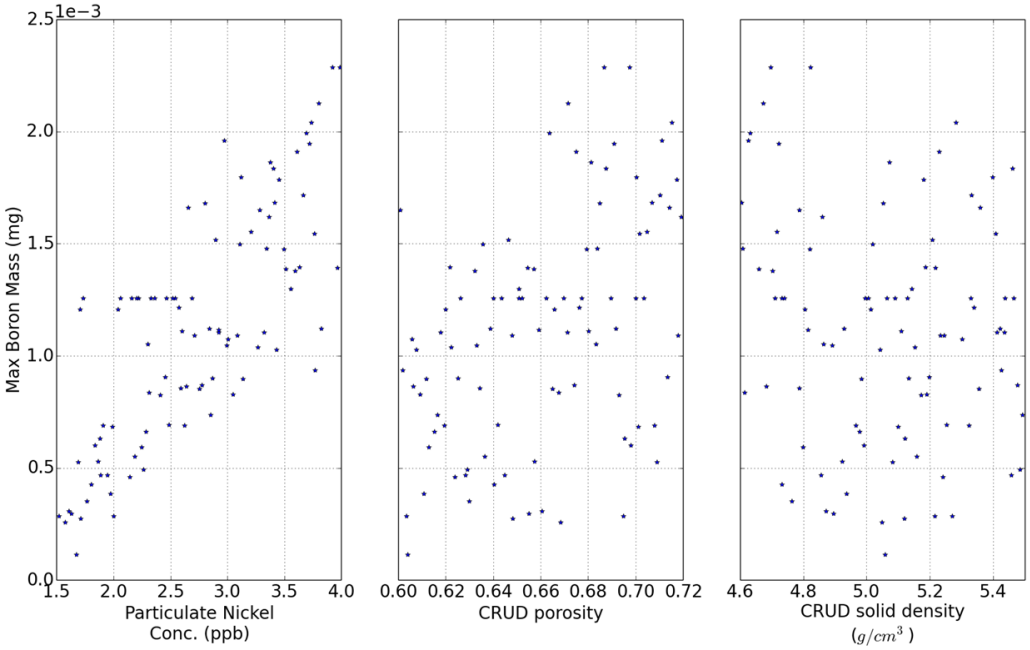


Figure 3.18: Maximum boron mass during cycle for LHS of MAMBA inputs for case A.

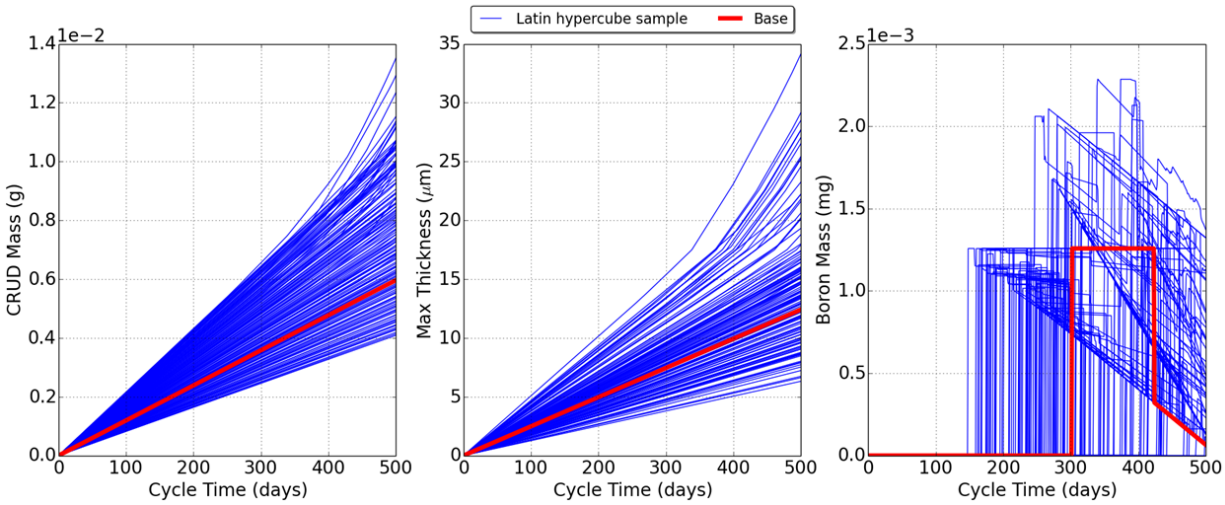


Figure 3.19: CRUD mass, thickness, and boron mass during the cycle for LHS of MAMBA inputs for case A.

### Case B: Heat flux of 1.0 MW/m$^2$

According to Pearson correlation coefficients summarized in Table 3.7, the most correlated input factors are:

1. particulate nickel concentration with 0.70,
2. CRUD porosity with 0.37,
3. chimney heat transfer coefficient with 0.15,
4. and chimney density with 0.13.

The correlation plots for these four parameters are shown in Figures 3.20, 3.21, and 3.22 for the CRUD mass, thickness, and boron mass, respectively. The remaining parameters of CRUD solid density, soluble nickel concentration, and the chimney radius are, on average, less than 10% correlated with the output metrics. However, for the metric of CRUD thickness, the CRUD solid density is correlated with a coefficient of -0.15, and the boron mass is correlated with soluble nickel concentration by 0.10.

Table 3.7: Pearson's correlation coefficients for LHS of MAMBA inputs for case B.

| Parameter | Pearson's correlation coefficient | | | Average coefficient |
|---|---|---|---|---|
| | CRUD mass | Thickness | Boron mass | |
| Particulate nickel concentration | 0.95 | 0.79 | 0.36 | 0.70 |
| CRUD porosity | 0.13 | 0.50 | 0.48 | 0.37 |
| Chimney heat transfer coeff | 0.077 | 0.095 | 0.28 | 0.15 |
| Chimney density | 0.041 | 0.064 | 0.28 | 0.13 |
| CRUD solid density | -0.029 | -0.15 | 0.0022 | -0.06 |
| Soluble nickel concentration | 0.023 | 0.028 | 0.10 | 0.05 |
| Chimney radius | 0.037 | 0.024 | 0.035 | 0.03 |

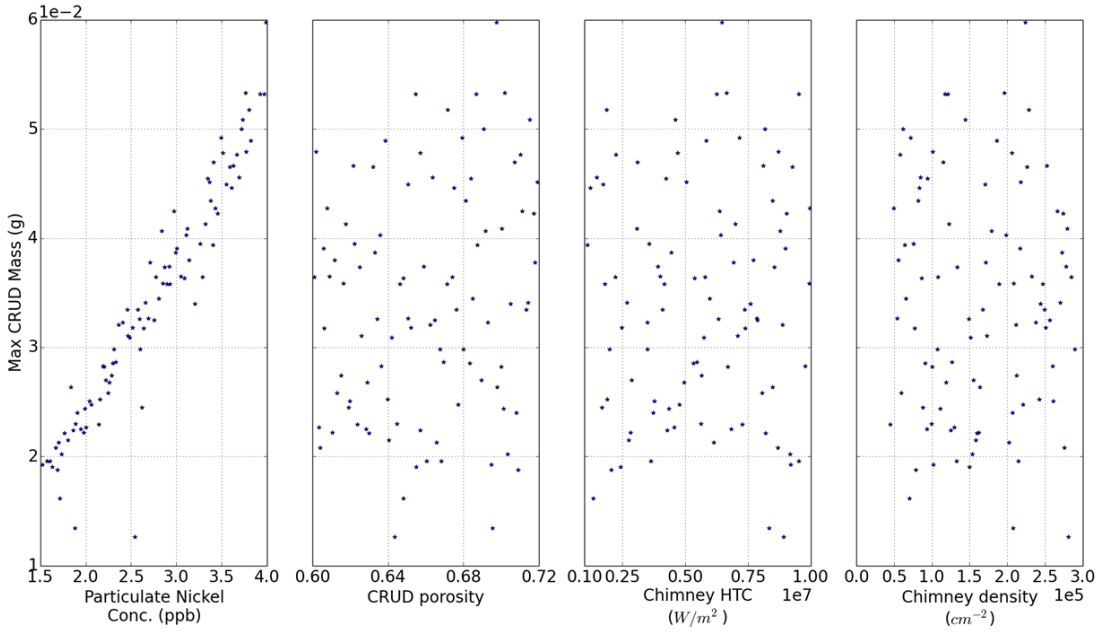


Figure 3.20: Maximum CRUD mass during cycle for LHS of MAMBA inputs for case B.

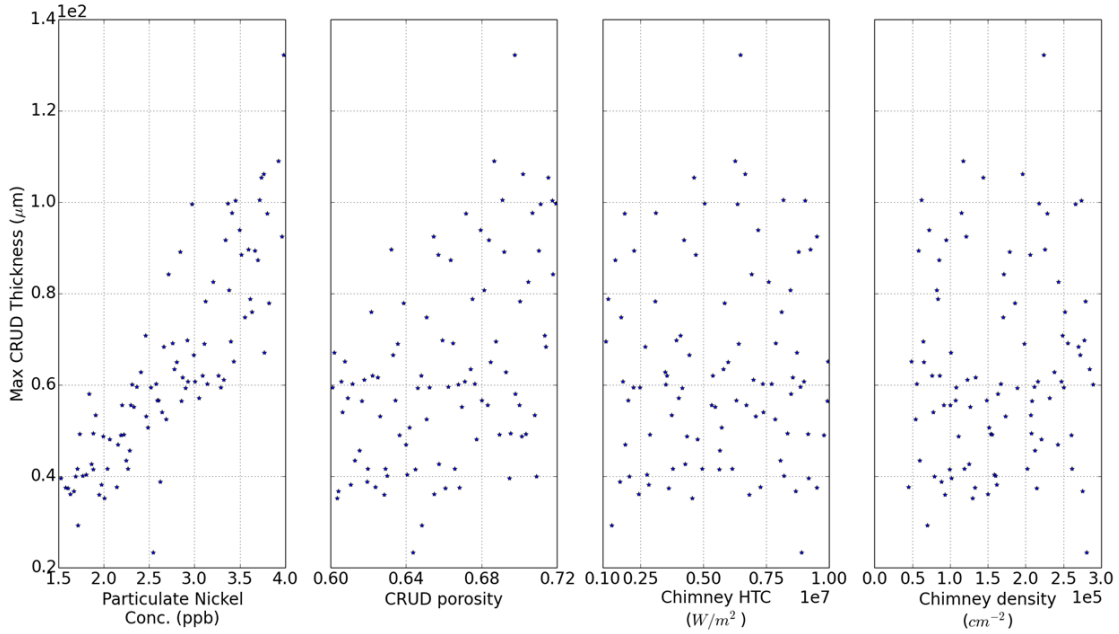


Figure 3.21: Maximum CRUD thickness during cycle for LHS of MAMBA inputs for case B.

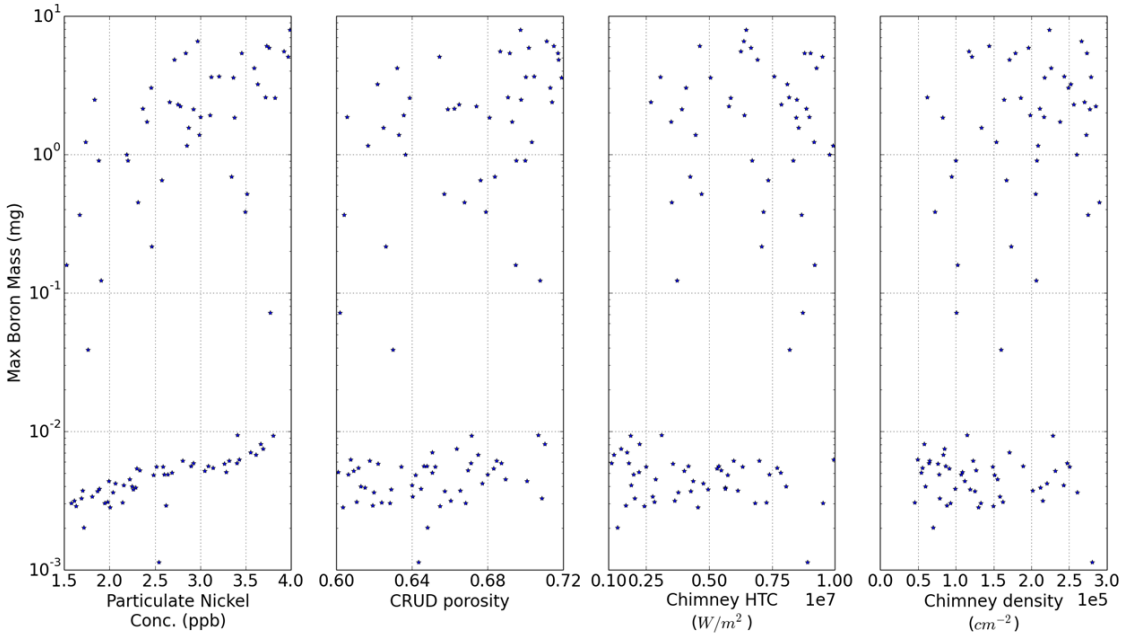


Figure 3.22: Maximum boron mass during cycle for LHS of MAMBA inputs for case B.

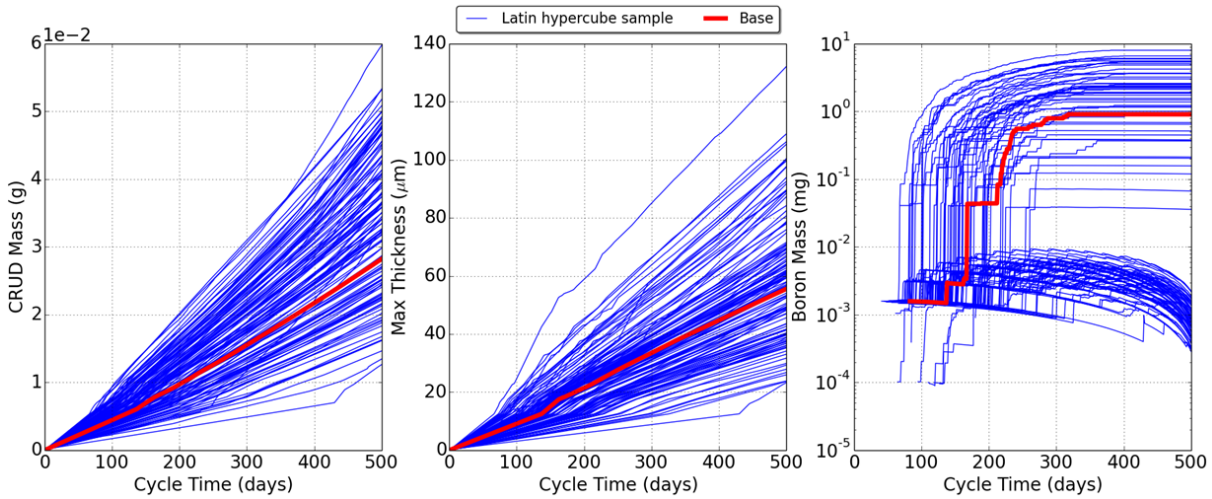


Figure 3.23: Maximum integral CRUD mass, thickness, and boron mass during the cycle for LHS of MAMBA inputs for case B.

In Figure 3.23, the 130 samples are separated into two distinct classes, where boron has precipitated in approximately half of the sample sets. The correlation coefficients for the end-of-cycle (EOC) boron mass are re-calculated by separating the samples using a cutoff of $10^{-2}$ mg. To determine if the input factor correlation changes with the onset of solid boron precipitation, the average parameter values belonging to each class as well as the correlation coefficients are calculated and summarized in Table 3.8.

Considering the correlation coefficients for the two classes of samples below and above $10^{-2}$ mg of boron at EOC, it is revealed that select input parameters are correlated similarly, and others very differently, when boron is precipitating. The particulate nickel concentration and CRUD porosity are unquestionably the most important input factors regardless of whether boron precipitation is occurring. The soluble nickel concentration, CRUD solid density, and chimney density are all negatively correlated by approximately 10% when boron precipitation is not occurring. On the other hand, during boron precipitation, the CRUD solid density and chimney density have reduced effects, and the effect of the chimney radius becomes relevant with 13% correlation. Moreover, the soluble nickel concentration is positively correlated with boron precipitation.

Table 3.8: Average value parameter and Pearson's correlation coefficients of EOC boron mass separated into two classes using cutoff of $10^{-2}$ mg for LHS of MAMBA inputs for case B.

| Parameter | Units | Below $10^{-2}$ mg | | Above $10^{-2}$ mg | |
|---|---|---|---|---|---|
| | | Avg. value | Coefficient | Avg. value | Coefficient |
| Particulate nickel conc. | ppb | 2.63 | 0.80 | 2.95 | 0.48 |
| CRUD porosity | none | 0.619 | 0.30 | 0.662 | 0.38 |
| Soluble nickel conc. | ppb | 0.273 | -0.12 | 0.278 | 0.15 |
| Chimney radius | $\mu m$ | 2.99 | -0.011 | 3.15 | -0.13 |
| CRUD solid density | g/cm$^3$ | 5.04 | -0.12 | 5.06 | -0.043 |
| Chimney density | cm$^{-2}$ | 1.49x10$^5$ | -0.11 | 2.06x10$^5$ | 0.029 |
| Chimney HTC | W/m$^2$-K | 4.66x10$^6$ | -0.060 | 6.88x10$^6$ | -0.016 |

## 3.2 3-D simulation model

Generally, the model domain used in the remainder of this chapter is a full-length single pin cell, consisting of fuel, cladding, and coolant. The active fuel length is 365.76 cm with a fuel rod radius of 0.4579 cm. Unless otherwise noted, the plant conditions described in Section 2.4 are used. The stand-alone conditions and input parameters are set to the values shown in Table 3.9.

Table 3.9: Summary of stand-alone input parameters used in MAMBA simulations.

| Parameter | Value | Units |
|---|---|---|
| CRUD solid density | 5.33 | $g/cm^3$ |
| CRUD initial porosity | 70 | % |
| Chimney radius | 4.0 | $\mu m$ |
| Chimney heat transfer coeff. | $6.7x10^6$ | $W/m^2K$ |
| Chimney density | $4.8x10^4$ | $cm^{-2}$ |
| Arrhenius rate coeff. | 130.0 | none |
| Boiling rate coeff. | $0.94x10^{-3}$ | none |

Table 3.10: Summary of cases used to assess spacer grid and mixing vanes effects.

| Case descriptor | Spacer grid and vanes | Cladding temperature and heat flux variation due to grid and vanes | Erosion |
|---|---|---|---|
| no grid | no | no | no |
| grid | yes | yes | no |
| grid + erosion | yes | yes | yes |

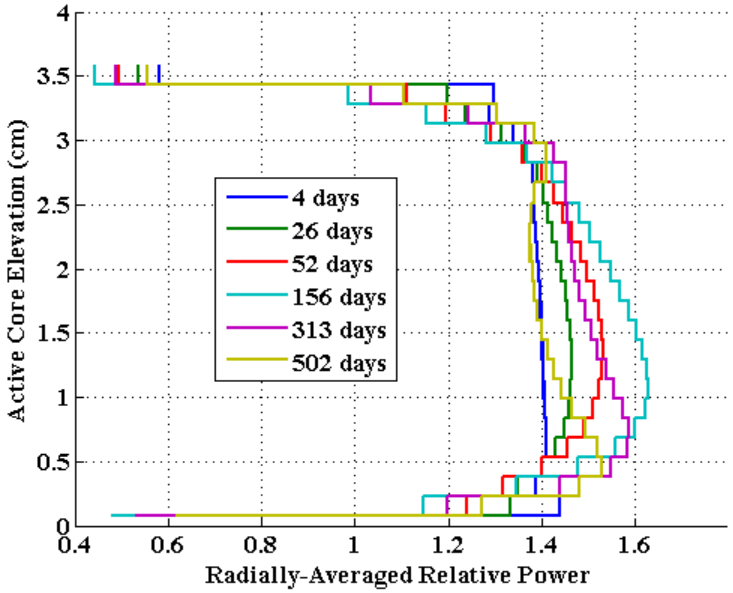


Figure 3.24: Axial power distribution at select burnup states for assembly G70 of Seabrook plant, cycle 5.

The CFD model domain includes three spacer grids, each with four mixing vanes, modeled around the upper half of the rod at axial locations of 203.28 cm, 249.00 cm, and 294.72 cm. However, a CFD model that does not include the spacer grids is also used to generate CRUD predictions without the effects of grids/vanes. The CFD models are documented in detail in Appendix A. Table 3.10 summarizes three distinct variations of the thermal hydraulic boundary conditions that are relevant in the subsequent analyses.

DeCART is not used to predict a power distribution in this chapter, instead an axial power

distribution, corresponding with the end of cycle 5, is extracted from an ANC simulation of the Seabrook core provided by WEC. This power distribution is used as the heat source within the CFD model, where conjugate heat transfer calculations are performed. Figure 3.24 shows the radially-integrated axial power distributions for a specific fuel assembly (G70, see Chapter VI for additional Seabrook plant details) at select burnup states, as predicted by the nodal neutron diffusion code ANC. The length of cycle 5 was 502 EFPD, corresponding to core burnup of 19.242 MWd/kgHM.

## 3.3 MAMBA mesh sensitivity

In this section, a mesh sensitivity analysis of MAMBA is completed using the end-of-cycle power distribution in Figure 3.24, corresponding to 502 EFPD; no radial or azimuthal power variation is considered. The power level is normalized to the nominal core operating power of 3,322 $MW_{th}$, then a spatially-uniform peaking factor of 1.5 is applied. In Figure 3.24, localized power peaking exceeding 1.6 was predicted for the fuel assembly with localized rod power peakings exceeding 1.7. For the present model, a rod power peaking of 1.5 is sufficient to cause boron precipitation, which strongly influences the required fidelity of the mesh to achieve convergence. For each CRUD deposition simulation, a 500 day cycle is completed with fixed thermal hydraulic conditions, resulting from the EOC power distribution. Recall that the thermal hydraulic boundary conditions include cladding surface heat flux and temperature at the CRUD/coolant interface; turbulent kinetic energy may also be used if erosion of the CRUD is modeled.

### Axial

First, an axial discretization sensitivity study is performed. Planar thicknesses of approximately 5 cm to 0.5 cm are considered. A radially adaptive mesh that *grows* in 5 $\mu m$ increments is used for all cases. Table 3.11 summarizes the effect of the axial discretization of the CRUD solver on the total nickel ferrite and boron masses at the EOC. The azimuthal discretization is fixed at 16 equal-angle sectors. Figure 3.25 compares the pin's integral boron mass during the cycle. Based on the comparisons, planar thicknesses approaching 5 cm is

much too coarse with relative errors in the boron mass of more than 40%. Using a relative error cutoff of 20%, sufficient mesh convergence is achieved with a uniform planar thickness of 1.143 cm. Unless otherwise noted, all subsequent MAMBA simulations will use this axial discretization.

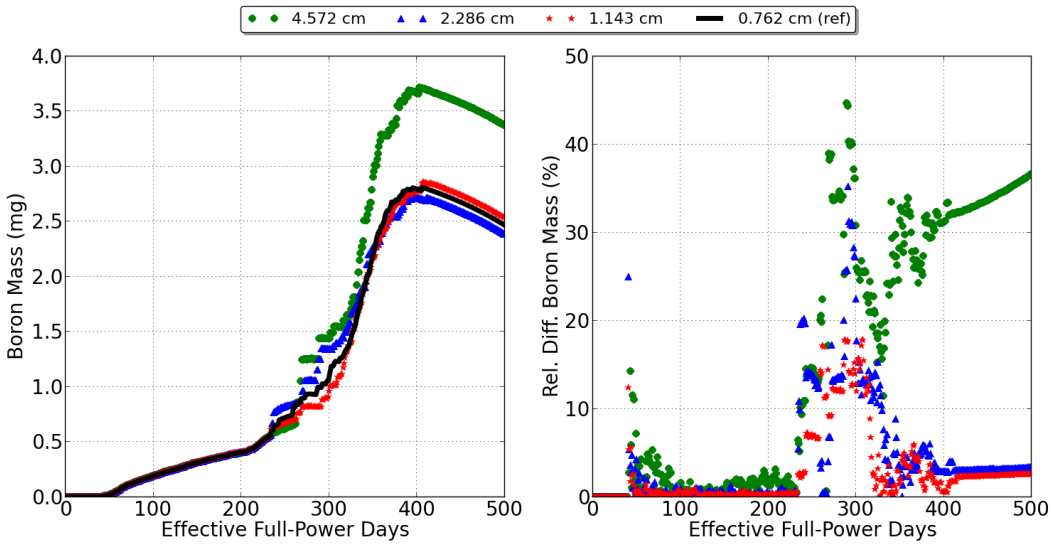


Figure 3.25: Integral boron mass and relative difference comparison for various axial plane thicknesses within MAMBA; 480 planes used as reference.

Table 3.11: MAMBA axial mesh sensitivity study cases showing total nickel ferrite and boron mass at the EOC with grid and erosion.

| Number of planes | Plane thickness (cm) | Total $NiFe_2O_4$ mass (g) | Total boron mass (mg) |
|---|---|---|---|
| 80 | 4.572 | 3.651 | 3.372 |
| 160 | 2.286 | 3.666 | 2.386 |
| 320 | 1.143 | 3.663 | 2.532 |
| 480 | 0.7620 | 3.667 | 2.469 |

## Azimuthal

The azimuthal dependence of the CRUD deposition is driven by the thermal hydraulic boundary conditions. The variation of the three boundary conditions, cladding heat flux, coolant temperature, and turbulent kinetic energy, are strongly correlated with the turbulent-flow induced by the spacer grid and mixing vanes. Investigations to support the previous assertion are completed in Section 3.5.

Table 3.12 compares the EOC nickel ferrite and boron mass for four azimuthal discretizations of 4, 8, 16, and 32 sectors. In Figure 3.26, the integral boron mass and relative difference from the 32 azimuth reference case are compared. The next highest resolution case of 16 azimuths still has difficulty capturing the point in time when boron precipitation begins; errors of more than 60% persist during the middle-of-cycle.

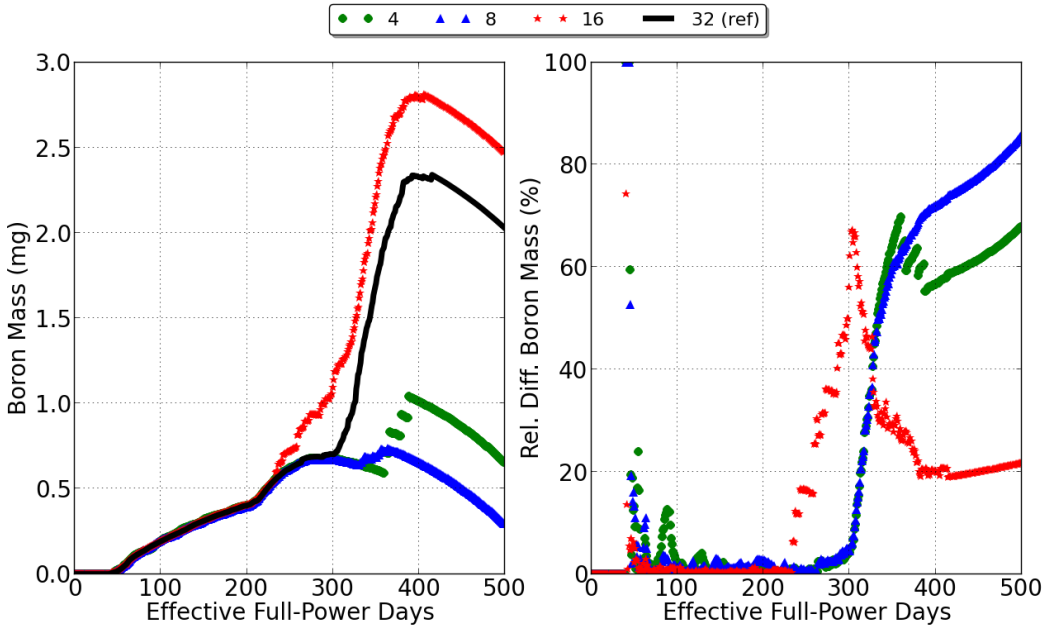


Figure 3.26: Integral boron mass and relative difference comparison for various azimuthal discretizations with 32 azimuths as reference.

When using 4 and 8 azimuths in the MAMBA model, the boron mass predictions are highly inaccurate due to averaging of the high fidelity thermal hydraulic boundary conditions. To determine which boundary condition(s) is causing this significant effect, erosion is turned

off and only the heat flux and temperature variation caused by the turbulent flow is used within the CRUD solver. Table 3.13 compares the same azimuthal discretizations, and it is revealed that without erosion, the effect of the azimuthal discretization, particularly when using 4 or 8 azimuths, is diminished.

Table 3.12: Azimuthal mesh sensitivity study cases showing total nickel ferrite and boron mass at the EOC with erosion.

| Number of azimuths | Azimuth angle (radians) | Total $NiFe_2O_4$ mass (g) | Total boron mass (mg) |
|---|---|---|---|
| 4 | $\pi/2$ | 3.696 | 0.654 |
| 8 | $\pi/4$ | 3.649 | 0.293 |
| 16 | $\pi/8$ | 3.667 | 2.469 |
| 32 | $\pi/16$ | 3.630 | 2.030 |

Table 3.13: Azimuthal mesh sensitivity study cases showing total nickel ferrite and boron mass at the EOC with the grid, but without erosion.

| Number of azimuths | Azimuth angle (radians) | Total $NiFe_2O_4$ mass (g) | Total boron mass (mg) |
|---|---|---|---|
| 4 | $\pi/2$ | 5.733 | 7.379 |
| 8 | $\pi/4$ | 5.627 | 5.046 |
| 16 | $\pi/8$ | 5.616 | 6.694 |
| 32 | $\pi/16$ | 5.609 | 5.583 |

To balance computational efficiency and solution accuracy, all subsequent MAMBA calculations will be performed with an axial discretization of 320 uniform thickness planes of 1.143 cm and 16 equal angle azimuths. Despite higher boron mass errors in the middle-of-cycle, this mesh discretization allows end-of-cycle predictions within approximately 20% of the highest fidelity mesh tested of 480 planes and 32 azimuths. That being said, it is clear that the spatial dependence of the erosion of the CRUD deposit is very strong. If computation-

ally attainable, an azimuthal mesh discretization of 32 or more sectors should be considered when coupled with a high fidelity CFD model.

## 3.4 Arrhenius rate parameters

As detailed in Subsection 2.1.3, the surface deposition kinetics is governed by a three-term equation with two sources and one sink, as shown in Equation 2.37. The Arrhenius rate coefficients for boiling and non-boiling porous ($p$) regions are given by $\tilde{a}_i^p$and $a_i^p$, respectively, where $i$ is a specific species, e.g. nickel ferrite. In non-boiling regions within the CRUD layer, the rate coefficient is calculated by an exponential decay law, shown in Equation 2.38.

The Arrhenius rate prefactor $A_i^p$ and activation energy $E_i^p$ are input parameters, whereas the average kinetic energy is the product of the universal gas constant $R$ and the temperature $T$. Increasing the temperature causes the rate coefficient to increase as well. In boiling regions, the exponential decay law is directly replaced by an input parameter, $\tilde{a}_i^p$. The rate of surface deposition is enhanced in boiling regions, and the current approach is to take the product of the rate coefficient and the heat flux. Table 3.14 summarizes the Arrhenius rate parameter combinations considered in this study. Because of the strong effect that the flow turbulence has on the CRUD deposition distribution, spacer grids and erosion is included in all cases.

Table 3.14: Summary of non-boiling and boiling Arrhenius rate parameters for nickel ferrite used in MAMBA model sensitivity study.

| Case Descriptor | $A^p_{NiFe_2O_4}$ | $\tilde{a}^p_{NiFe_2O_4}$ |
|---|---|---|
| 100; 0.72 | 100.0 | $0.72\text{x}10^{-3}$ |
| 115; 0.72 | 115.0 | $0.72\text{x}10^{-3}$ |
| 130; 0.72 | 130.0 | $0.72\text{x}10^{-3}$ |
| 130; 0.94 | 130.0 | $0.94\text{x}10^{-3}$ |
| 130; 1.16 | 130.0 | $1.16\text{x}10^{-3}$ |

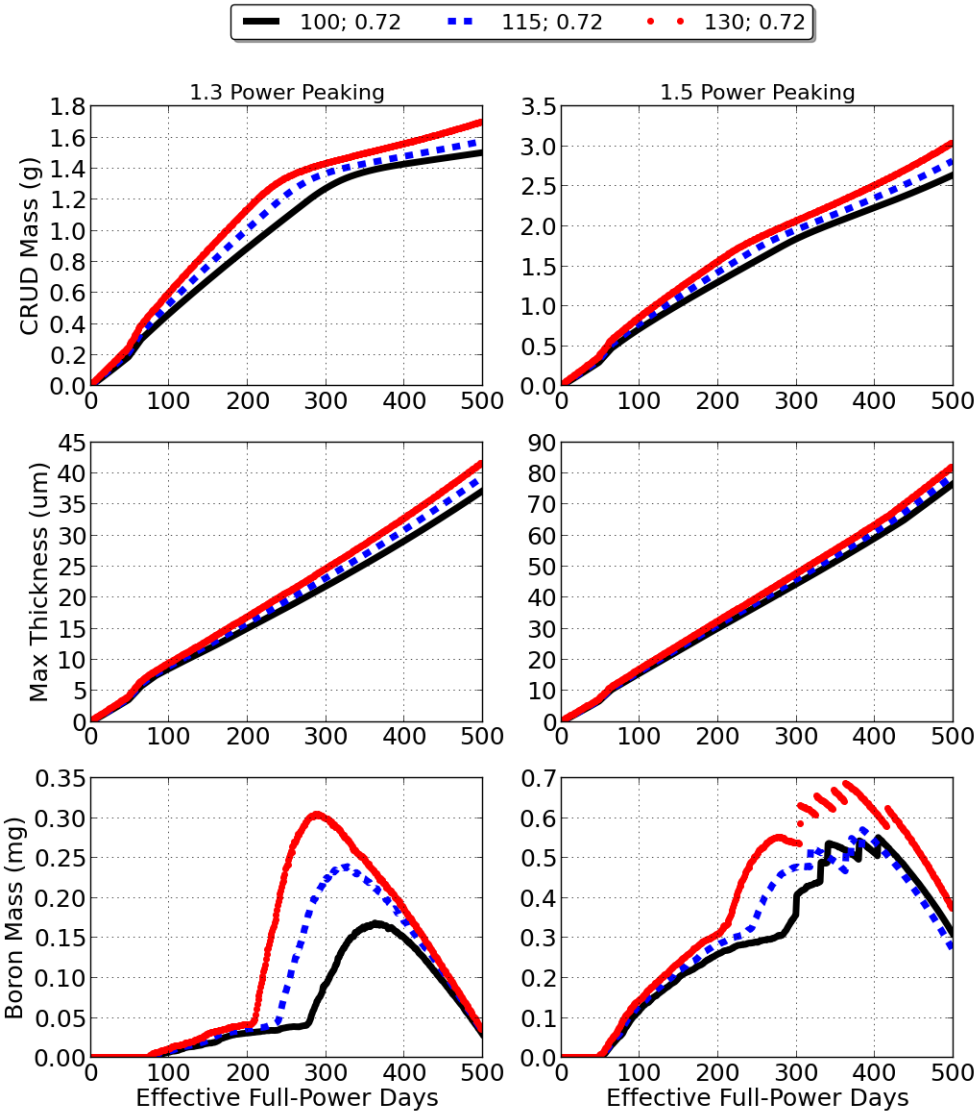


Figure 3.27: Comparison of various non-boiling Arrhenius rate prefactors with $0.72\text{x}10^{-3}$ boiling coefficient for the 1.3 (left) and 1.5 (right) power levels.

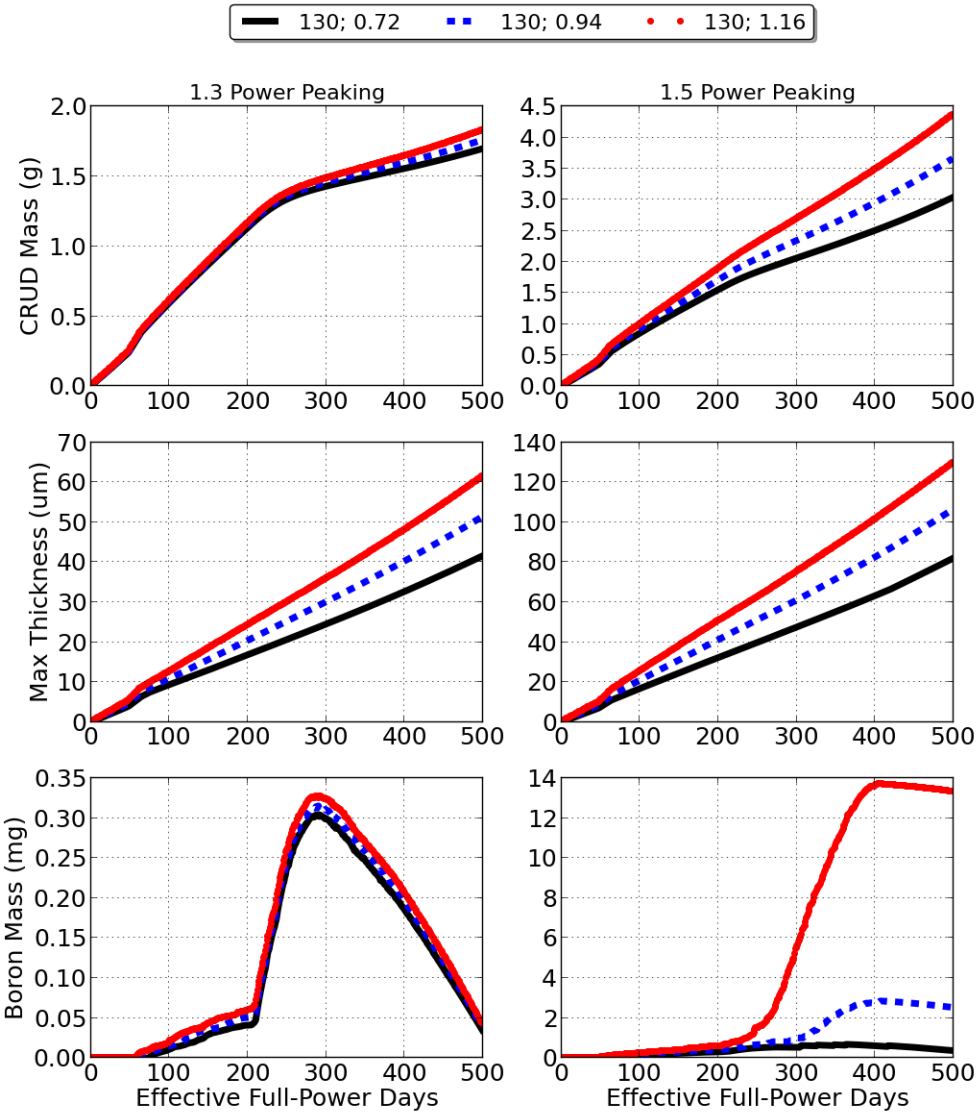


Figure 3.28: Comparison of various boiling Arrhenius rate coefficients with 130.0 non-boiling prefactor for the 1.3 (left) and 1.5 (right) power distributions.

Figure 3.27 compares the integral CRUD characteristics for two power levels of 1.3 and 1.5 for three non-boiling Arrhenius rate prefactors. The boiling rate coefficient is low enough, at $0.72\text{x}10^{-3}$, that even in the 1.5 power level case, boron precipitation does not occur. A higher non-boiling prefactor leads to a quicker increase in the CRUD and boron mass; essentially,

the rate at which species deposit within the pores of the CRUD is accelerated.

Similarly, Figure 3.28 compares the cases for varying boiling rate coefficients when the non-boiling rate prefactor is fixed to 130.0. For the lower power level of 1.3, the CRUD thickness is most sensitive to the boiling coefficient. At the higher power level of 1.5, the effect of the boiling rate coefficient is dramatic with variations in the boron mass of more than one order of magnitude. An increase in the coefficient from $0.94\text{x}10^{-3}$ to $1.16\text{x}10^{-3}$ causes nearly a 600% increase in the boron mass; the relationship between the Arrhenius boiling coefficient and the boron mass is highly nonlinear.

## 3.5 Analysis of coupled boundary conditions

In this section, the thermal hydraulic boundary conditions are varied to understand the associated sensitivity of the CRUD predictions. First, an axial power distribution from Figure 3.24 (in Section 3.2) is used to perform an investigation of the effect of various power levels. Second, spacer grid and mixing vanes effects are considered, including erosion of the CRUD deposit. Then, the azimuthal variation of the sub-pin power level is considered. In Subsection 3.5.4, the fidelity of the thermal hydraulic boundary conditions is reduced to a subchannel-like mesh to analyze the effects on CRUD predictions. In the remaining subsection, variation in the coolant boron concentration is investigated.

### 3.5.1 Rod power level

Based on the power magnitudes experienced during cycle 5 in the Seabrook plant, the assembly-average relative power levels considered in this study are 1.1, 1.3, and 1.5 peaking compared to nominal power. These peakings are applied to the distribution associated with 502 EFPD, as this is a typical power profile that develops with depletion. Figure 3.29 compares the axial distributions; radial and azimuthal variation is not considered. Based on the ANC simulation data provided by WEC, pin power reconstruction calculations predicted axial power distributions with maximums for relative power of more than 1.7 at select burnup steps for select rods in the Seabrook G70 assembly. Therefore, the three magnitudes of power considered in this study well represent various rods in the core.

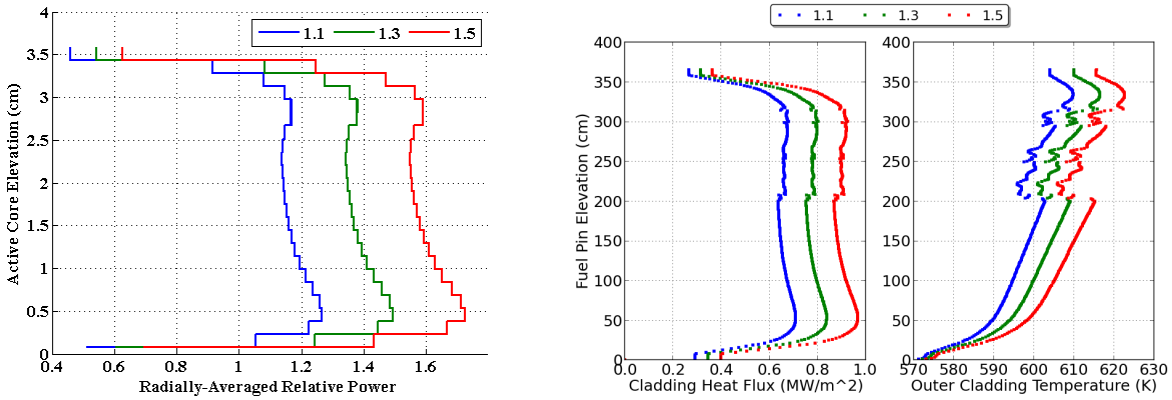


Figure 3.29: Axial power levels of 1.1, 1.3, and 1.5 peaking, applied to EOC Seabrook distribution (left), and axial distribution of cladding heat flux (middle) and outer cladding temperature (right), used to assess effects on MAMBA predictions.

For each power distribution, a computational fluid dynamics simulation is converged using a single pin cell with spacer grids and vanes model. Then, the thermal hydraulic boundary conditions required by the CRUD solver are extracted; the axial distribution of cladding heat flux and coolant temperature is shown in Figure 3.29. A summary of the rod power level and associated thermal hydraulic conditions is shown in Table 3.15. The maximum heat flux in the top half of the pin is quoted in the table; in general, the coolant temperatures in the bottom half of the core are not high enough to cause significant CRUD deposition.

Table 3.15: Summary of thermal hydraulic parameters predicted by STAR-CCM+, resulting from various magnitudes of pin power.

| Pin power peaking | Total pin power (kW) | Temperature rise (K) | Max heat flux in top half of rod ($MW/m^2$) |
|---|---|---|---|
| 1.1 | 69.3 | 32.7 | 0.680 |
| 1.3 | 81.9 | 37.9 | 0.803 |
| 1.5 | 94.5 | 42.8 | 0.926 |

Three MAMBA simulations are completed for a 500 day cycle using each pair of thermal hydraulic boundary conditions, resulting from each power level. Figure 3.30 compares the integral CRUD characteristics during the cycle. All other input parameters are held constant;

erosion of the CRUD layer based on the CFD-computed TKE is not included. Refer to Subsection 3.5.2 for flow turbulence effects on erosion of the CRUD layer. The significant difference between the 1.1 and 1.3 power results compared to the 1.5 power case is due to precipitation of lithium tetraborate. The power density and resulting heat flux out of the cladding causes subcooled boiling in select regions; Figure 3.31 shows a 2-D distribution of the boron surface density within the CRUD deposit in the axial and azimuthal directions.

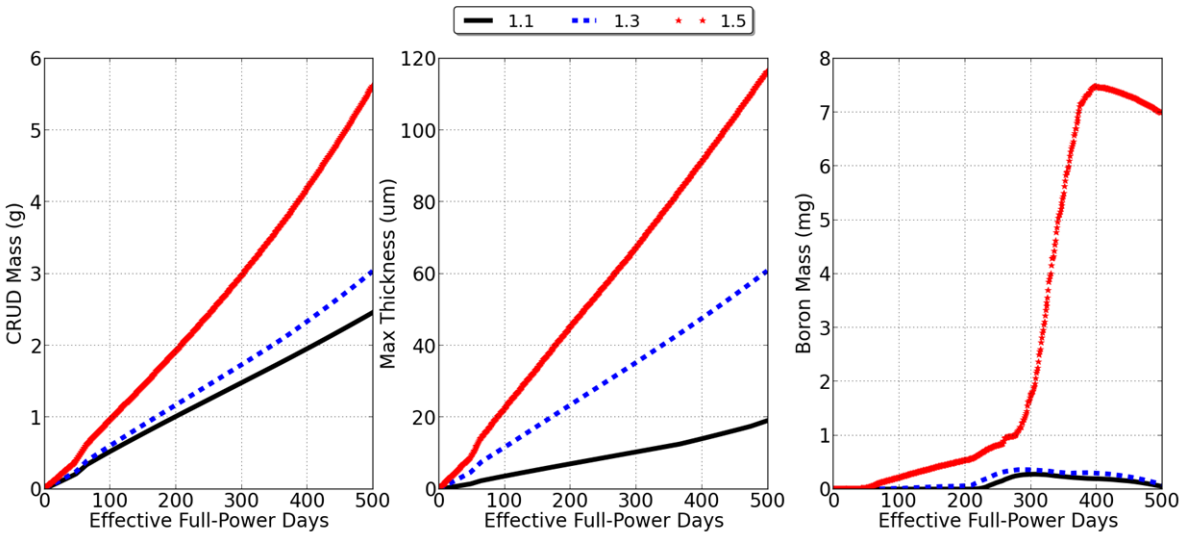


Figure 3.30: Effect of power level and thermal hydraulic boundary conditions on the integral CRUD characteristics; no erosion.

The precipitation of various solid phase compounds, such as lithium tetraborate, is governed by equilibrium thermodynamics and is a function of the compound concentration and temperature. The temperature dependence of the equilibrium constants are fit to experimental data using a three-term correlation as shown in Equation 2.40 in Subsection 2.1.3. Because lithium tetraborate is the least soluble and precipitates out of solution first (in comparison to the other boron-containing compounds of interest), this particular compound is the dominating *solid* boron phase within the CRUD layer modeled by MAMBA. The dominant *soluble* boron species is metaboric acid, referred to as coolant boron. The combination of the presence of lithium tetraborate and metaboric acid within CRUD deposits is believed to be the strongest contributor to CIPS [EPRI, 1997, EPRI, 2004, Deshon et al., 2010].

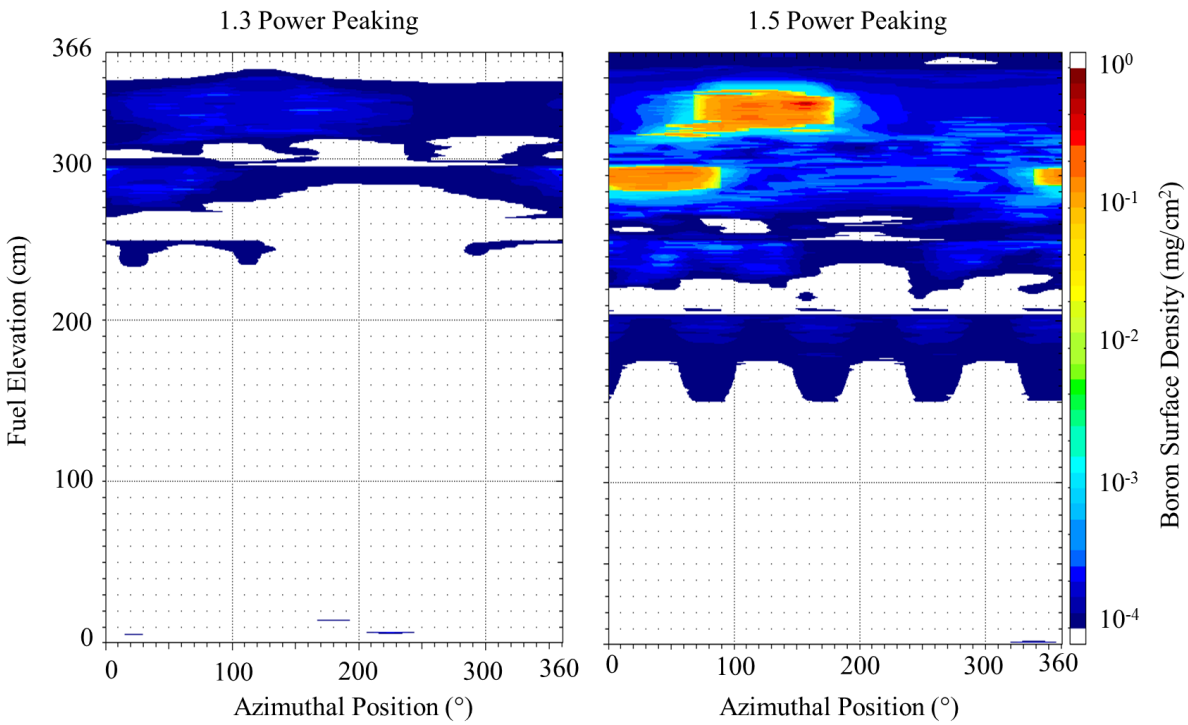


Figure 3.31: Boron surface density (interpolated) in the axial and azimuthal directions at 500 days as predicted by MAMBA for 1.3 (left) and 1.5 (right) power peaking cases; no erosion.

In the previous simulations, the power distribution has remained the same and only the power peaking level has been changed as a means of comparison. To demonstrate the effect of the axial power distribution itself, an additional distribution from Seabrook cycle 5, assembly G69 is used, as calculated by ANC. The previously used distribution *G70* and the newly introduced distribution *G69* are compared in Figure 3.32. The G69 distribution exhibits higher power in the top half of the assembly, resulting in higher cladding heat flux and temperature boundary conditions provided to the CRUD deposition solver. Table 3.16 summarizes the maximum heat flux for two power levels applied to each fuel assembly power distribution. An increase in heat flux of only a couple percent has an enormous effect on the boron precipitation rate, leading to more than three times the amount of boron hideout mass. If conditions are conducive to solid boron precipitation, accurate prediction of the localized heat flux distribution is crucial.

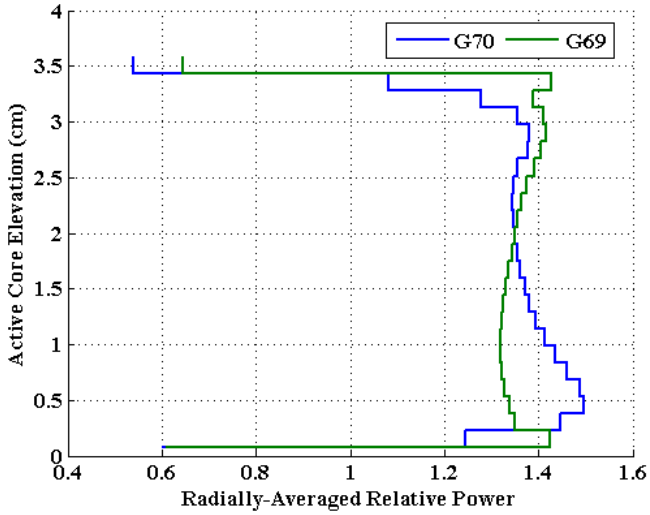


Figure 3.32: Axial power distributions from Seabrook assemblies G69 and G70 with 1.3 power peaking.

Table 3.16: Summary of thermal hydraulic parameters for the two axial power distributions from the G70 and G69 Seabrook assemblies.

| Assembly | Pin power peaking | Max heat flux in top half of rod ($MW/m^2$) |
|---|---|---|
| G70 | 1.3 | 0.845 |
| G69 | 1.3 | 0.867 |
| G70 | 1.5 | 0.974 |
| G69 | 1.5 | 0.993 |

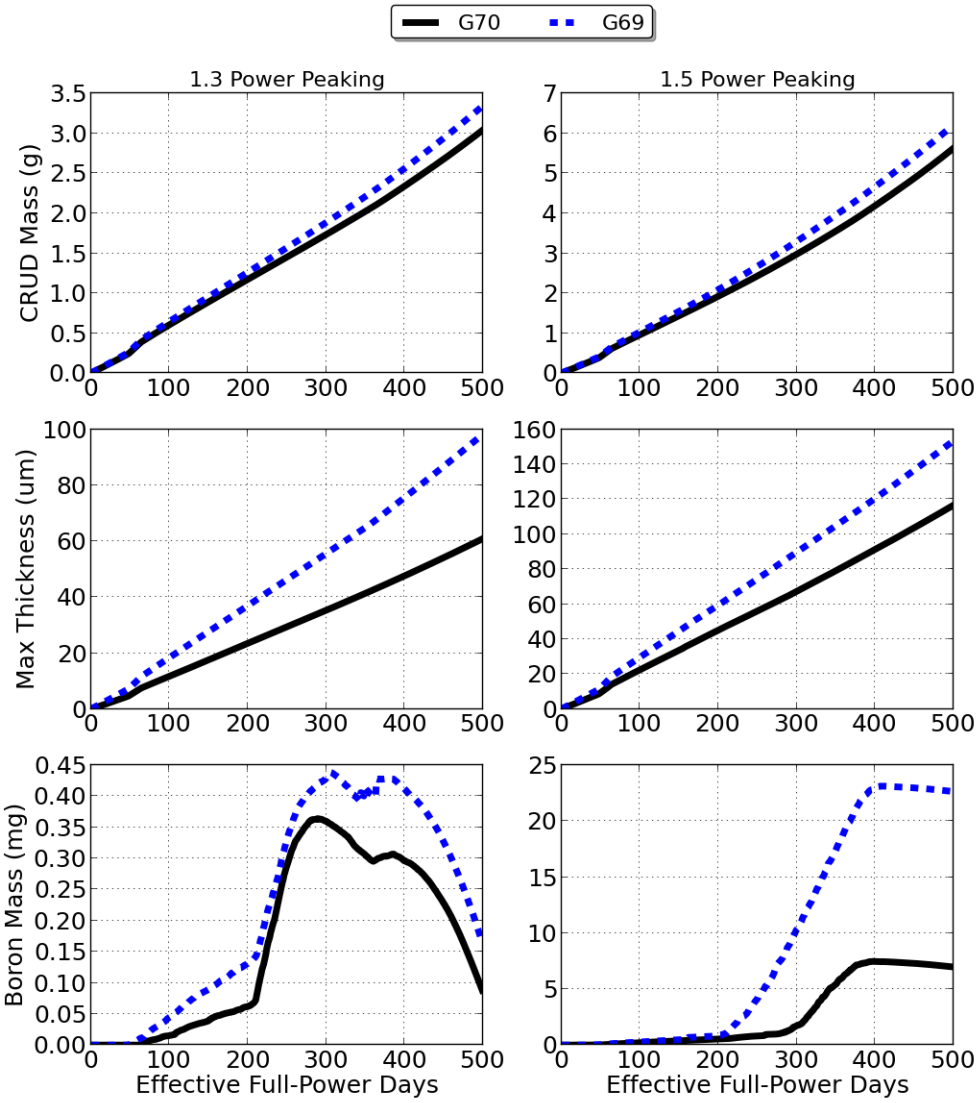


Figure 3.33: Effect of axial power distribution from two different Seabrook assemblies on the integral CRUD characteristics; no erosion.

### 3.5.2 Spacer grid effects

Turbulent flow patterns are predictable through the use of computational fluid dynamics. The fuel bundle support structures, known as spacer grids, typically contain mixing vanes, which improve convective heat transfer by increasing the turbulence of the flow. Such flow characteristics are primarily controlled by the geometry of spacer grid, its mixing vanes, and the fuel lattice. Significant temporal variation (during the operating cycle) in the flow is not expected unless a plant shutdown or other operational event occurs.

All of the boundary conditions provided to the CRUD deposition solver by CFD, which include coolant temperature, cladding heat flux, and turbulent kinetic energy, are strongly influenced by the spacer grid and mixing vanes. The outer cladding surface temperature upstream and downstream of the first spacer grid is shown in Figures 3.34 and 3.36 (top), respectively. The azimuthal temperature variation upstream of the grid results from asymmetric cooling of the fuel pin.

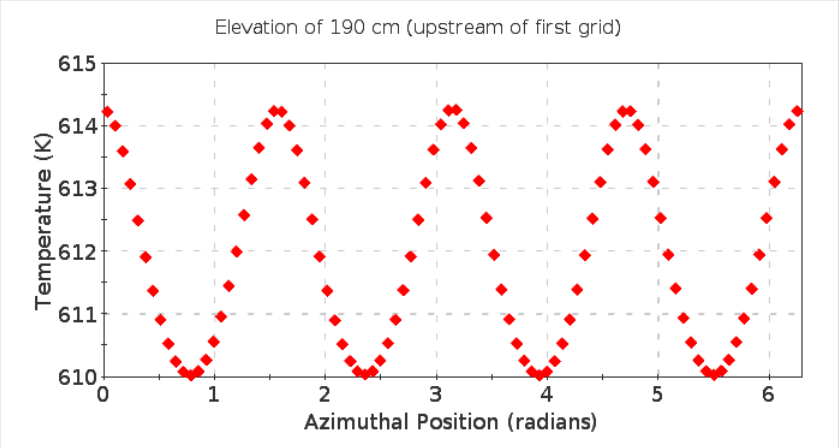


Figure 3.34: Outer cladding surface temperature upstream of first spacer grid at an elevation of 190 cm.

Downstream of the grid, the nominal four degree variation in the azimuthal cladding temperature increases to more than ten degrees as a direct result of the mixing vanes. Additionally, the cladding heat flux and turbulent kinetic energy near the cladding surface are shown in Figure 3.36 (middle and bottom). Another view of the outer cladding surface temperature, heat flux, and turbulent kinetic energy is shown in Figure 3.35 near the third spacer grid,

ranging from 290 cm to 315 cm in axial elevation. The striped, swirling pattern of the thermal hydraulic properties is evident; this spatial variation drives the CRUD deposition distribution.

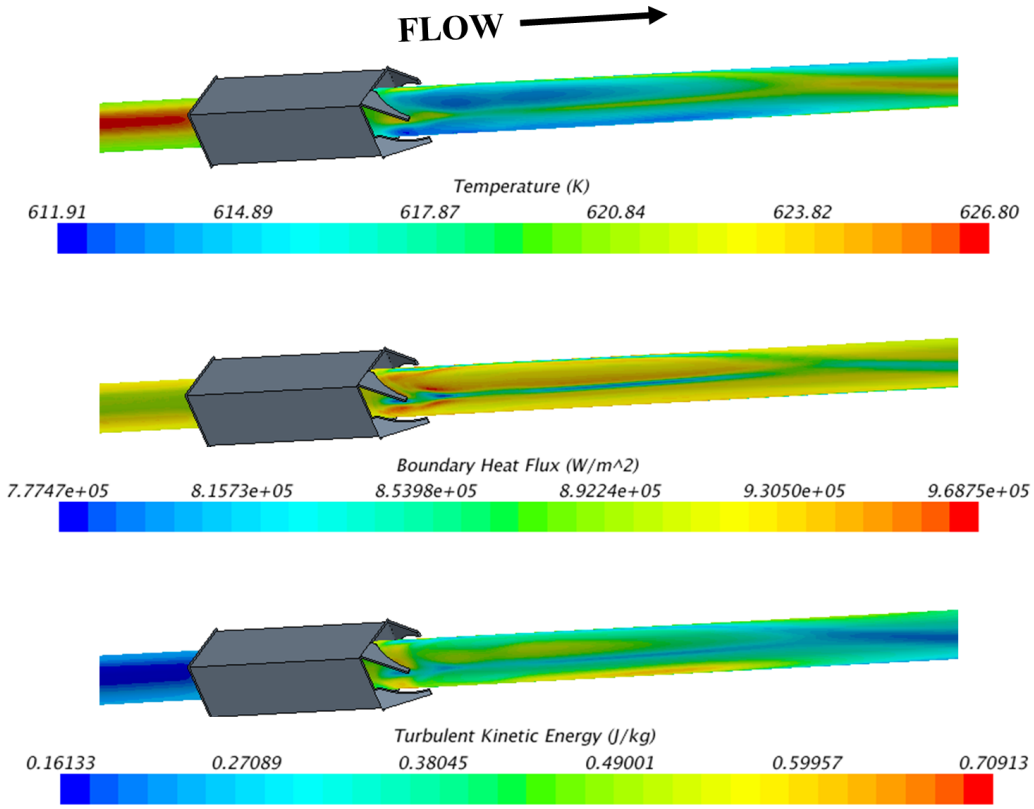


Figure 3.35: Outer cladding surface temperature (top), heat flux (middle), and TKE (bottom) upstream and downstream of the third spacer grid when using the 1.5 power distribution.

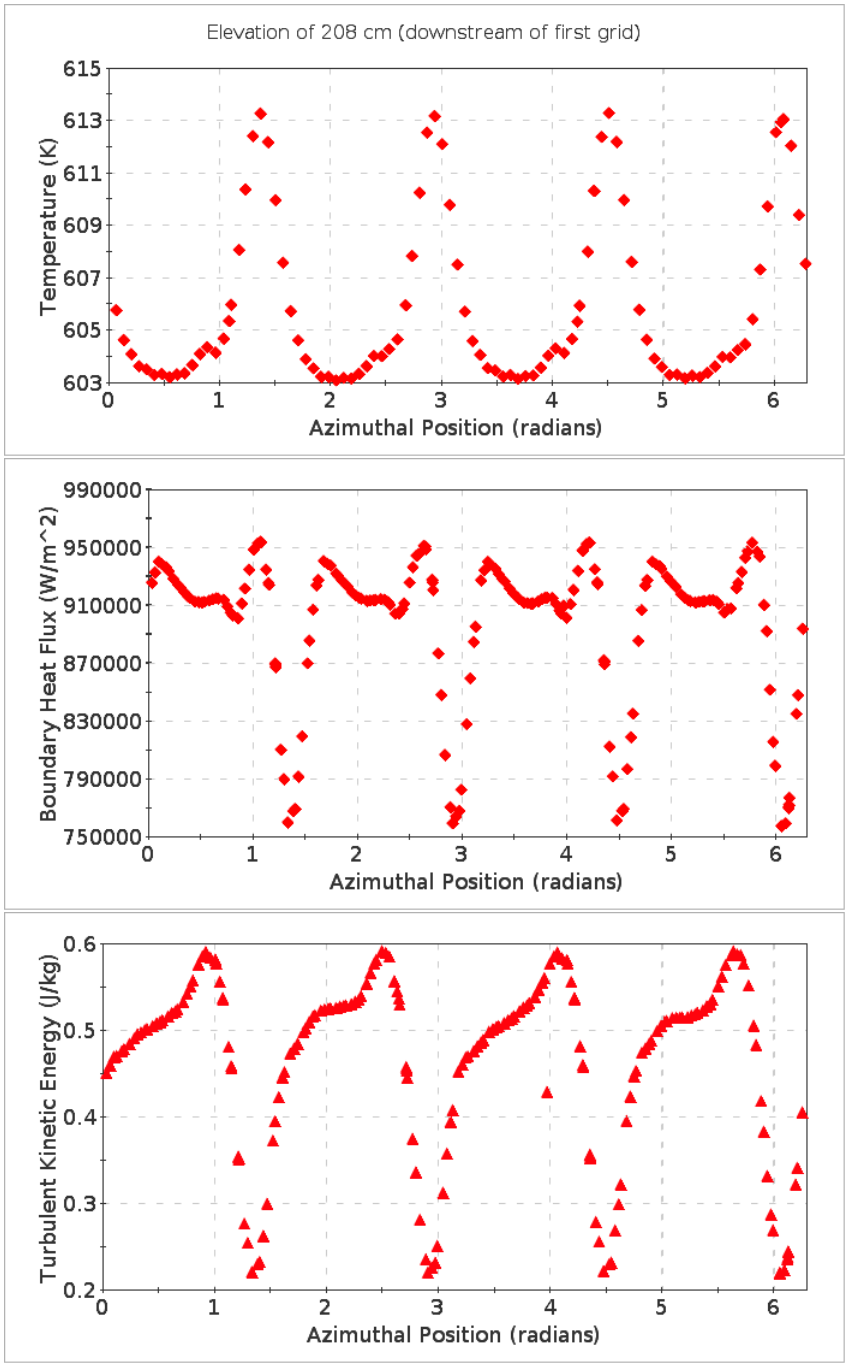


Figure 3.36: Outer cladding surface temperature (top), heat flux (middle), and turbulent kinetic energy (bottom) downstream of first spacer grid at an elevation of 208 cm.

Currently, MAMBA models the CRUD deposit erosion by weighting the turbulent kinetic energy, $k_{CFD}$, of the coolant close to the CRUD's surface with an adjustable constant $x_e$, which acts as a sink in the surface deposition kinetics. This constant has been tuned according to plant data [EPRI, 2003]. The surface deposition kinetics is governed by a three-term equation with two sources and one sink as shown in Equation 2.37 in Subsection 2.1.3, with the solid CRUD loss due to erosion given by Equation 2.39. Refer back to Subsection 2.1.3 for additional details regarding the modeling of the CRUD deposition kinetics.

Table 3.10 in Section 3.2 summarizes the cases used to assess the effects the spacer grids have on CRUD deposition. The first case, *no grid*, completely removes the spacer grid and mixing vanes in the CFD model, so that any temperature and heat flux gradient resulting from the vanes is no longer considered. The second case, *grid*, includes the spacer grid and vanes, but does not use the TKE to calculate the CRUD deposit erosion, whereas the third case, *grid+erosion*, does. It is important to note that even though the second case is not using the TKE to erode the CRUD, the spatially-dependent temperature and heat flux distributions resulting from the flow turbulence in the CFD calculation is considered.

In Figure 3.37, the CRUD characteristics of three MAMBA cycle simulations for the 1.3 (left) and 1.5 (right) power levels are compared. Ignoring the thermal hydraulic variation included by the grid and vanes causes the integral CRUD and boron mass to be dramatically overpredicted by more than 50% and 200%, respectively. Furthermore, inclusion of the CRUD deposit erosion is nearly as important in order to obtain accurate boron hideout mass predictions. Previously, it was shown that varying the axial power distribution (the localized thermal hydraulic boundary conditions) significantly affected the rate of boron precipitation. Again, the nonlinear behavior and sensitivity to the thermal hydraulic boundary conditions is demonstrated.

Figure 3.38 shows the CRUD thickness (top) and mass evaporation flux (bottom) within the axial and azimuthal directions for the three spacer grid cases using the 1.5 power level. Inclusion of the spacer grid effects—both improved convective heat transfer and turbulence-induced CRUD erosion—are necessary to predict accurate CRUD deposit distributions. Figure 3.39 shows the boron density in the axial and radial directions and correlates the turbulent kinetic energy in the vicinity of the space grids with erosion of the CRUD deposit. The 2-D distributions are reported for the radial or azimuthal cell closest to the cladding surface.

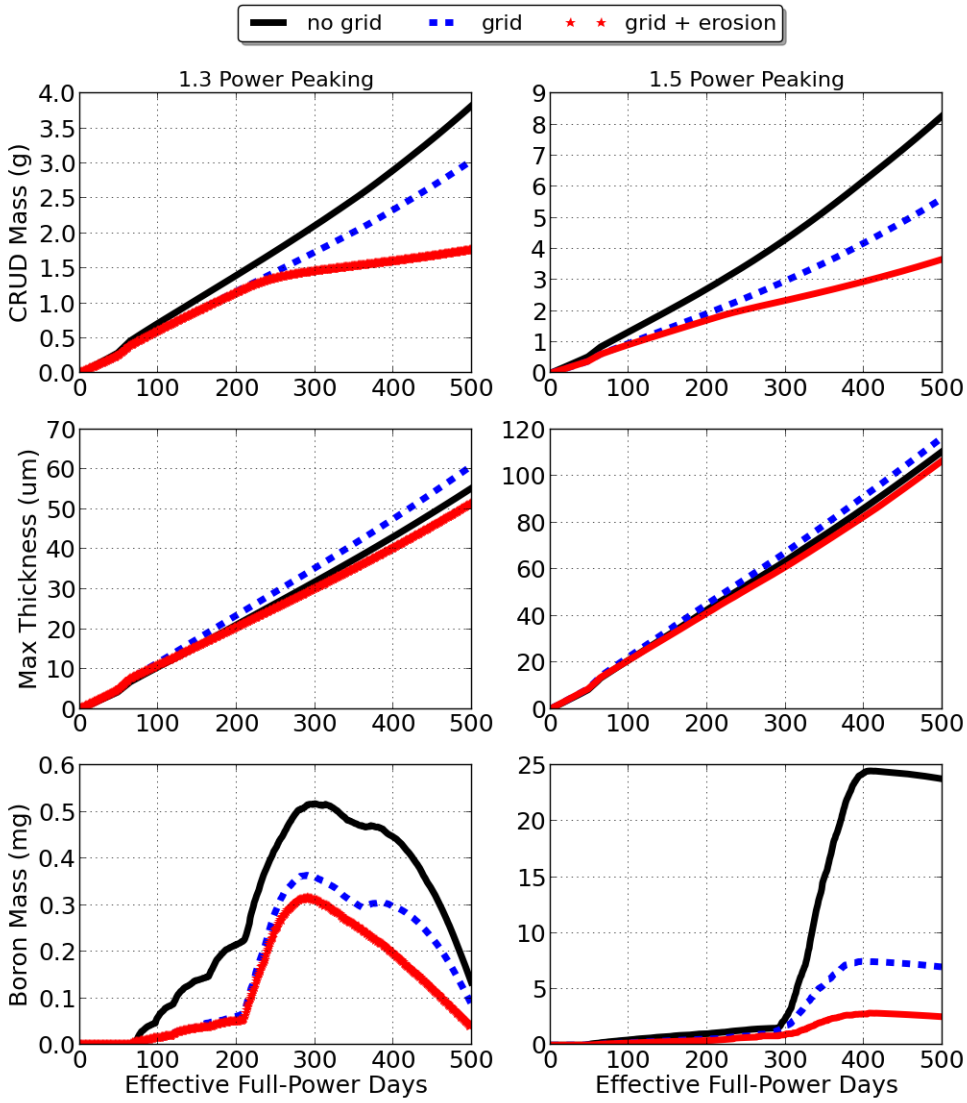


Figure 3.37: Comparison of including spacer grid and mixing vane effects on the CRUD deposit characteristics for the 1.3 (left) and 1.5 (right) power levels.

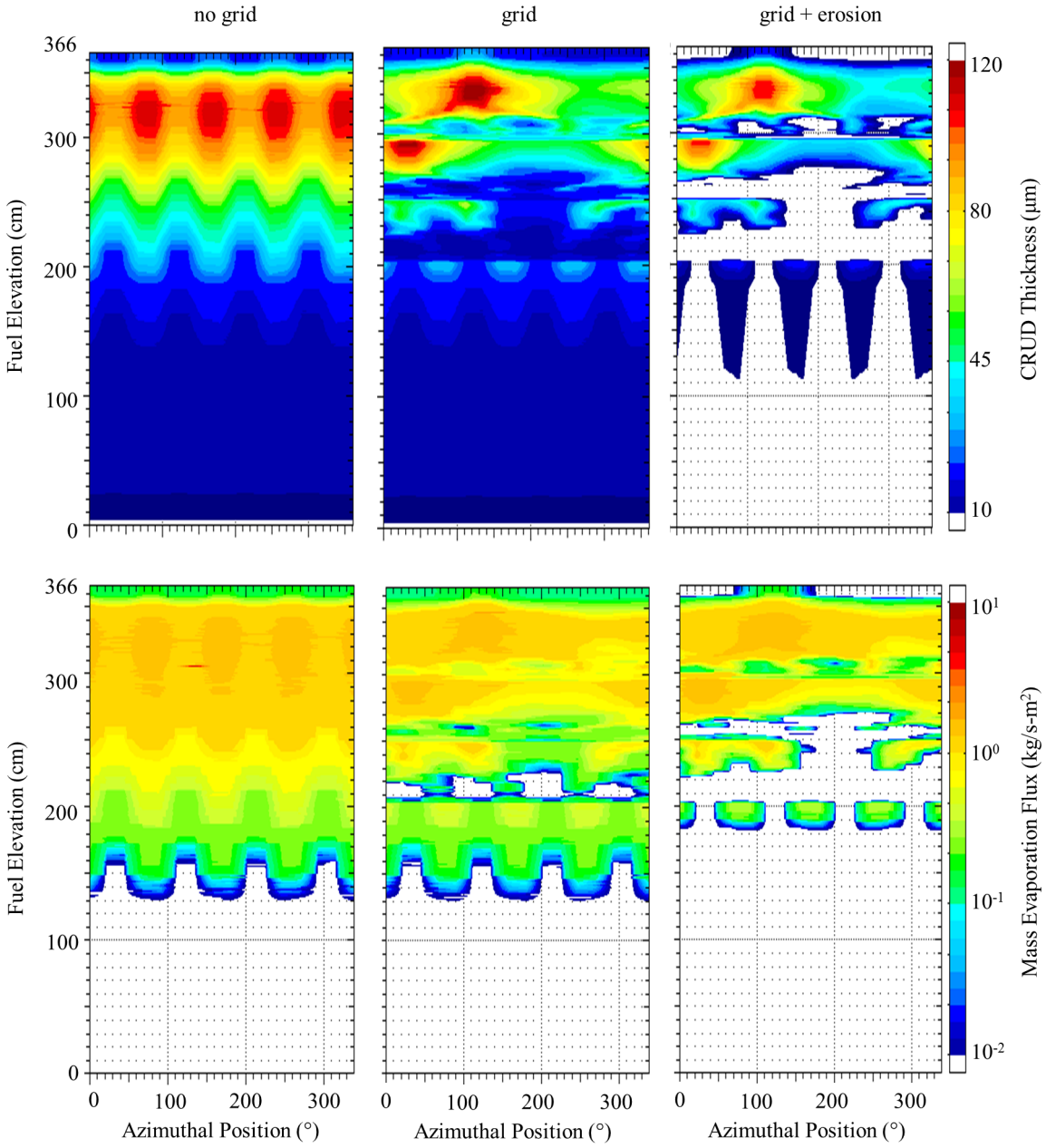


Figure 3.38: Interpolated CRUD thickness (top) and interpolated mass evaporation flux (bottom) in the axial and azimuthal directions for the no grid (left), grid (middle), and grid+erosion (right) cases; predicted by MAMBA at 500 days using 1.5 power level.

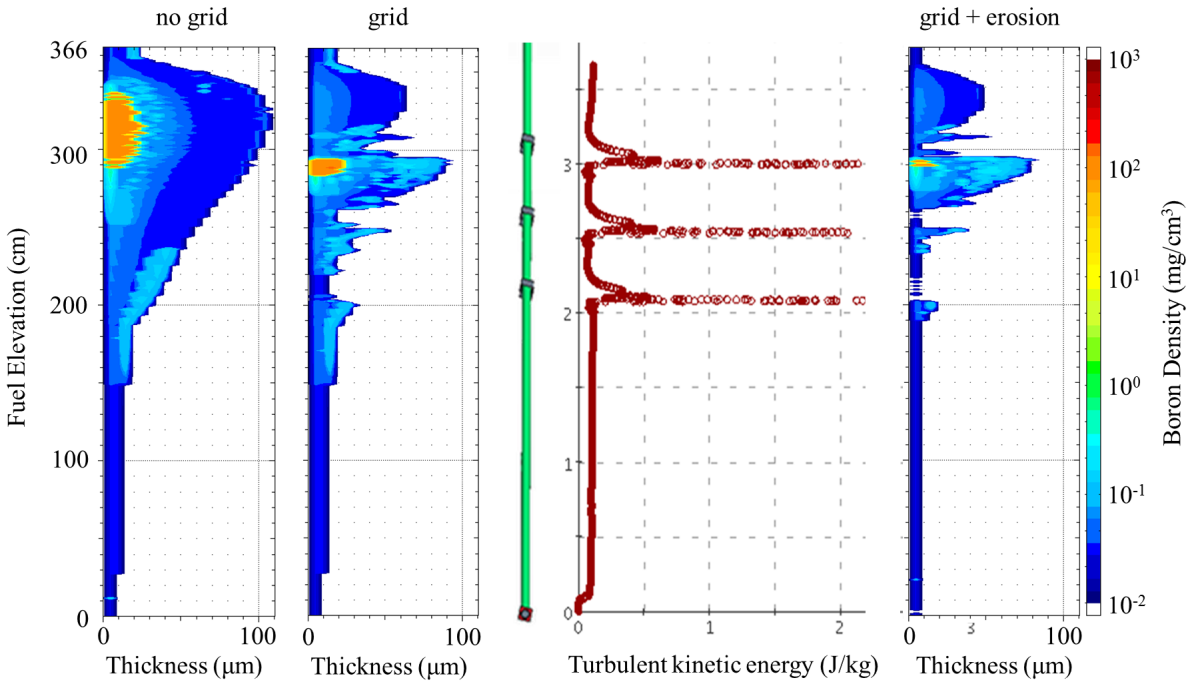


Figure 3.39: Boron density (interpolated) within the axial and radial CRUD distribution, and turbulent kinetic energy along the length of the rod and its correlation with erosion of the CRUD deposit in the grid+erosion model; predicted by MAMBA at 500 days using 1.5 power level.

### 3.5.3 Azimuthal power variation

All previous studies have assumed a uniform power distribution in the radial and azimuthal directions, i.e. the heat generation rate only varied in the axial direction. A previous investigation determined that the coolant temperature and heat flux resulting from radial power variations were negligible [Walter et al., 2014], and from a neutronics standpoint, only affected the fuel temperature predictions. On the other hand, azimuthal power variations of 3% resulted in heat flux variations on the same order. Therefore, the effects of azimuthal power variations on CRUD deposition are investigated further.

In commercial reactor operation, a variety of conditions and operating events may cause a circumferential variation of the heat generation rate within a fuel pin. In particular, two

situations are identified:

1. a fuel pin neighboring a guide tube (water rod)
2. and a fuel pin neighboring an inserted control rod.

In the second case, despite a strong circumferential variation of the power, a significant power reduction also occurs, thus reducing the likelihood of sufficient heat flux to result in subcooled nucleate boiling (and enhanced CRUD deposition). Therefore, the first case is the focus of this study because the presence of a water rod typically causes enhanced neutron moderation and increased power.

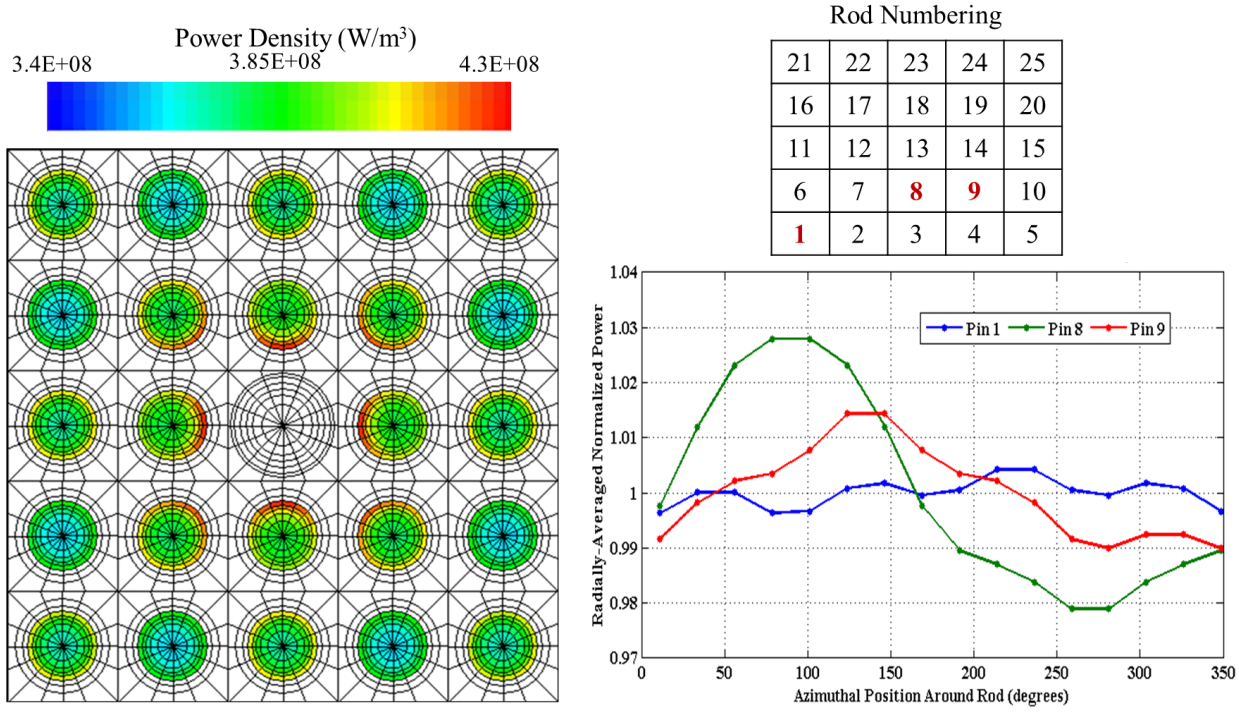


Figure 3.40: DeCART 5x5 pin cell model azimuthal power variation in the vicinity of a guide tube at an elevation of 255 cm (left), rod numbering (top, right), and azimuthal power variation for rods 1, 8, and 9 (bottom, right).

Lattice transport calculations performed by DeCART show an azimuthal power variation of approximately 3% is expected for a fuel pin neighboring a guide tube; however, a variation

of up to 6% is not unrealistic. Figure 3.40 shows the azimuthal power effects for all rods (left), and a comparison of three pins (right) is shown at an elevation of 255 cm. Pin 1 is far from the water rod, pin 8 is closest to the water rod, and pin 9 is diagonal to the water rod.

To determine the sensitivity of the CRUD deposition predictions to changes in the azimuthal power, two cases of 3% and 6% variation are simulated and compared with the uniform power with 1.5 peaking case previously completed in Subsection 3.5.1. The CFD model without spacer grids or mixing vanes, previously referred to as the *no grid* model, is used to ensure that the flow turbulence and power variation effects are independently analyzed. The first variation considered is the pin 8 distribution shown in Figure 3.40 (right), which is simplified to a cosine distribution with 3% amplitude. The second case increases the amplitude variation to 6%. Then, the same cases are re-run with the CFD model that includes the spacer grids and mixing vanes; erosion of the CRUD layer is also considered.

Figure 3.41 compares the integral boron mass along the rod for the three power variation cases for the no grid (left) and grid + erosion (right) model. In the case of no grid, significant boron precipitation is occurring, so changing the local thermal hydraulic conditions has less of an effect than in the case of grid + erosion.

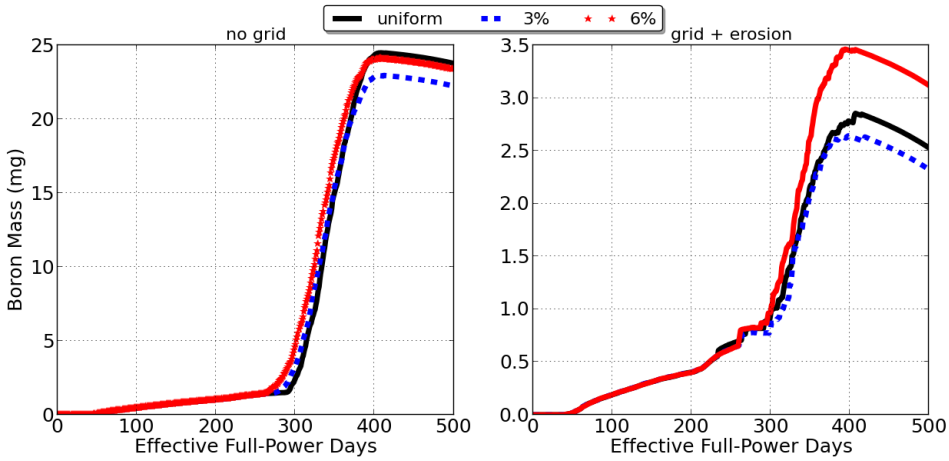


Figure 3.41: Comparison of azimuthal power variation of 3% and 6% on the integral boron mass for the 1.5 power level distributions with no grid (left) and with grid+erosion (right); note scale of boron mass or each plot.

Figure 3.42 compares 2-D boron surface density distributions for the two azimuthal power

variation cases for the no grid (top) and grid + erosion (bottom) CFD models. The modulated power cases clearly affect the boron precipitation locations; whether a net decrease or increase in the boron mass results is dependent on the local conditions. For example, consider the boron density predictions for the grid + erosion cases in Figure 3.42 (bottom). Between positions of 0 and 100 degrees at an elevation between 280 and 295 cm, a heavy boron deposit has formed. As the azimuthal power is modulated, the aforementioned boron deposit is less prevalent, and the boron deposit at a higher elevation of 325 cm is more significant. This is due to the location, where convective heat transfer is minimized, being in phase with the modulated power.

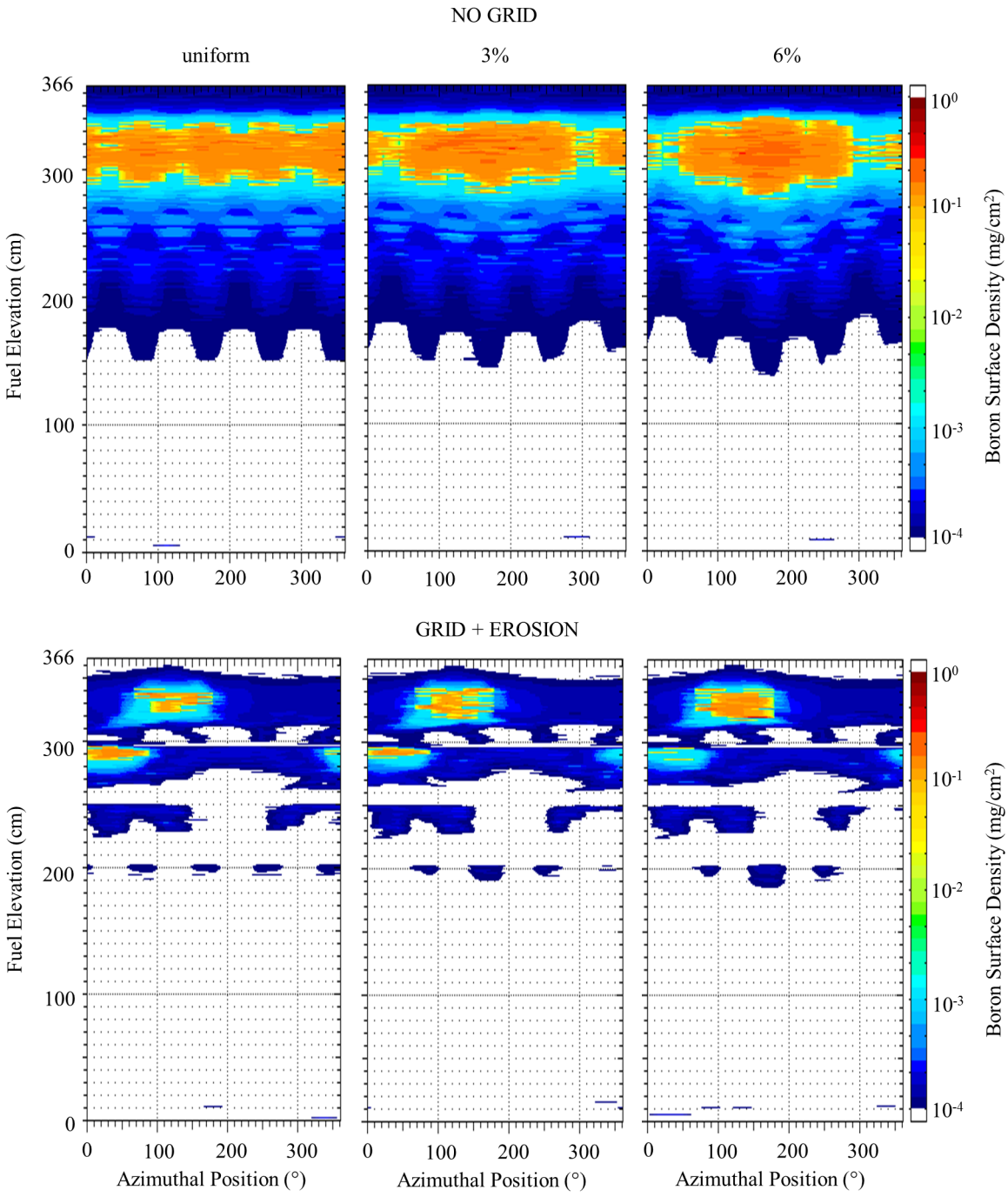


Figure 3.42: Comparison of azimuthal power variation of 3% and 6% on the boron surface density (interpolated) axial and azimuthal distribution for the 1.5 power level distributions without (top) and with (bottom) spacer grid and erosion in CFD model.

### 3.5.4 Fidelity of TH boundary conditions

The resolution of the thermal hydraulic boundary conditions that are provided to the MAMBA model is investigated in this section. The motivation for such an analysis stems from the industry-standard subchannel analysis approach, which calculates the cladding heat flux and temperature according to four azimuthal sectors, or quadrants; see Figure 3.43 for comparison of subchannel and CFD meshes. In the axial direction, a typical subchannel analysis planar discretization is approximately 5 cm, but may be finer or coarser depending on the fidelity of the model. In a sufficiently meshed CFD model, the axial discretization is on the order of millimeters in regions of complex flow, and may be on the order of one centimeter further downstream of spacer grids.

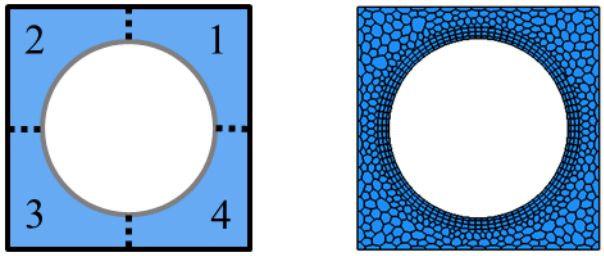


Figure 3.43: Subchannel analysis mesh consisting of quadrants for each pin cell (left), and CFD mesh with three prism layers and polyhedral cells (right).

The MAMBA azimuthal and axial discretization remains fixed at 16 sectors and 320 planes with thickness of 1.143 cm. The CFD model mesh with and without spacer grids also remains fixed. However, once the TH boundary conditions are extracted from CFD, they are averaged to 4 azimuthal sectors and to a specified planar discretization. Specifically, four axial discretizations are investigated: 320 planes of 1.143 cm (no loss of axial fidelity), 80 planes of 4.572 cm, and 40 planes of 9.144 cm. Table 3.17 summarizes the four cases of varying fidelity; considering the three different spacer grid models in Table 3.10 (Section 3.2), a total of twelve cases are compared to conclude which conditions are most sensitive to the decrease in axial and azimuthal resolution.

Table 3.18 compares the end-of-cycle values of CRUD mass, maximum thickness, and boron mass for the twelve cases. The relative difference in the boron mass is also tabulated. Generally, reducing the azimuthal fidelity to quadrant-variation introduces at least 10% of boron

Table 3.17: Summary of cases used to assess impact of the fidelity of TH boundary conditions provided to MAMBA.

| Case descriptor | Azimuthal averaging | Axial averaging | Number of planes | Axial plane thickness (cm) |
|---|---|---|---|---|
| reference | no | no | 320 | 1.143 |
| avg-320 | yes | no | 320 | 1.143 |
| avg-80 | yes | yes | 80 | 4.572 |
| avg-40 | yes | yes | 40 | 9.144 |

mass error. Depending on the local conditions, averaging of the thermal hydraulic boundary conditions in the axial directions may or may not introduce additional error because cancellation of error is occurring.

Figure 3.44 compares the cases in terms of the integral CRUD and boron masses during the 500 day cycle. As shown in Subsection 3.5.2, inclusion of the spacer grid effects is vital to accurate CRUD and boron mass predictions. Exclusion of the grids' enhancement of convective heat transfer results in overpredictions of the CRUD and boron mass by 25% and 200%, respectively. Moreover, inclusion of the CRUD erosion using the erosion model presented within this framework, further cuts the boron mass prediction in half.

Figure 3.45 focuses on the boron mass prediction of the grid + erosion model for the three averaged cases. Once the onset of boron precipitation occurs, relative errors of 30% are introduced by averaging the high fidelity CFD solution to quadrants. By the EOC, the errors have been reduced to 10% for the 320 and 40 plane cases. Depending on the axial distribution of the thermal hydraulic boundary conditions, including the turbulent kinetic energy, and the locations that are most susceptible to boron precipitation, cancellation of error is possible; for example, compare the 80 and 40 plane cases.

Table 3.18: End-of-cycle CRUD characteristics predicted for all combinations of the cases shown in Tables 3.10 and 3.17.

| Case descriptor | CRUD mass (g) | Maximum CRUD thickness ($\mu m$) | Boron mass (mg) | Rel. diff. boron mass (%) |
|---|---|---|---|---|
| | | *grid + erosion* | | |
| reference | 3.823 | 120.9 | 5.232 | – |
| avg-320 | 3.727 | 112.1 | 4.672 | -10.7 |
| avg-80 | 3.693 | 112.0 | 4.184 | -20.0 |
| avg-40 | 3.665 | 110.0 | 4.693 | -10.3 |
| | | *grid* | | |
| reference | 5.741 | 131.42 | 10.553 | – |
| avg-320 | 5.689 | 124.2 | 8.986 | -14.8 |
| avg-80 | 5.686 | 123.8 | 9.063 | -14.1 |
| avg-40 | 5.652 | 122.0 | 9.414 | -10.8 |
| | | *no grid* | | |
| reference | 8.321 | 124.1 | 29.87 | – |
| avg-320 | 8.110 | 116.1 | 21.26 | -28.82 |
| avg-80 | 8.115 | 115.6 | 22.14 | -25.88 |
| avg-40 | 8.114 | 115.5 | 23.05 | -22.83 |

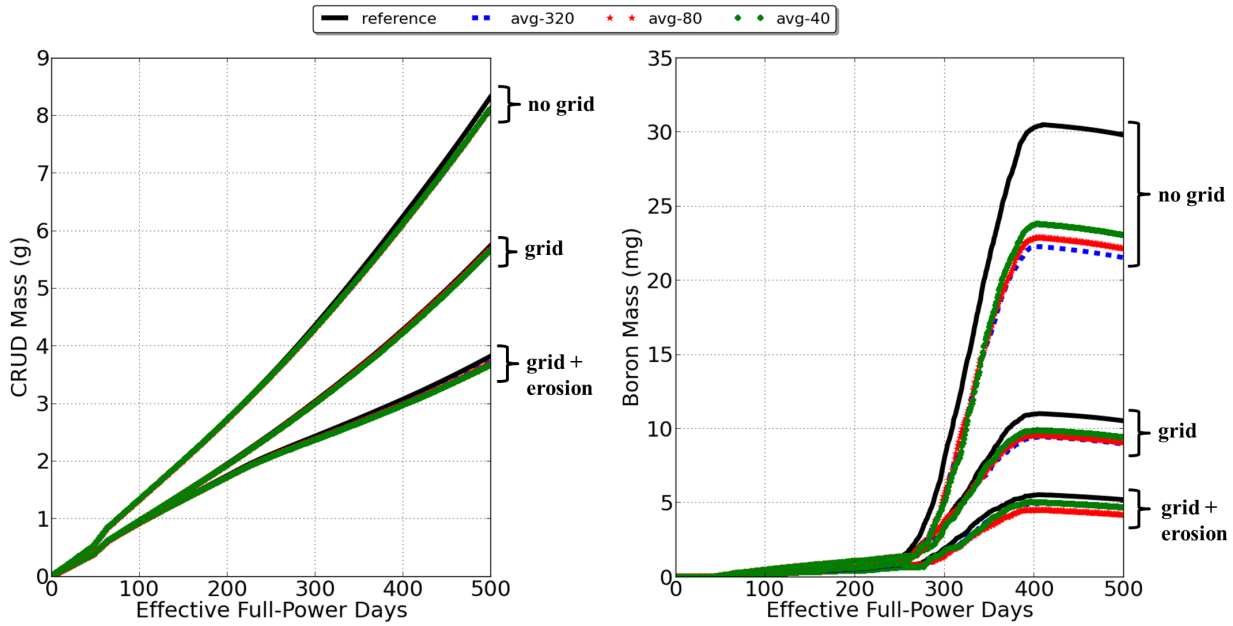


Figure 3.44: Comparison of CRUD characteristics when varying solution transfer fidelity of thermal hydraulic boundary conditions for various spacer grid models.

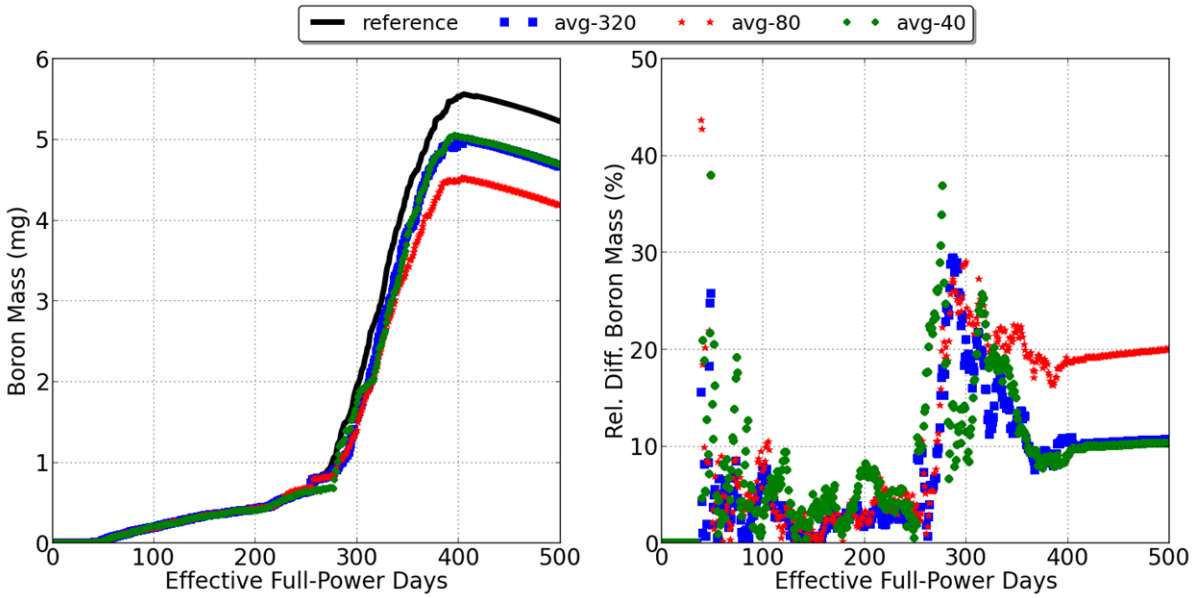


Figure 3.45: Comparison of boron mass when varying solution transfer fidelity of thermal hydraulic boundary conditions for grid + erosion model.

### 3.5.5 Coolant boron concentration

Three coolant boron curves are considered in this subsection; Figure 3.46 compares the Seabrook coolant boron concentration over a depletion cycle with an *upper limit* letdown [Cochran and Tsoulfanidis, 1999] and one fixed concentration of 500 ppm. The thermal hydraulic conditions resulting from the 1.5 power level are used; erosion is included. Two boiling Arrhenius rate coefficients are considered, $0.72x10^{-3}$ and $0.94x10^{-3}$; all other input parameters and boundary conditions remain fixed. The non-boiling Arrhenius rate coefficient is fixed at 130.0.

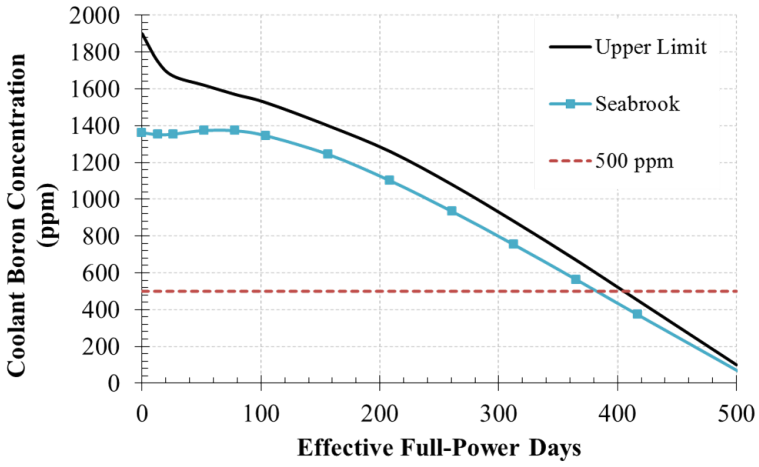


Figure 3.46: Coolant boron concentrations used in CRUD deposition sensitivity study.

Figure 3.47 shows the integral CRUD mass (top), maximum CRUD thickness (middle), and boron mass (bottom) along the fuel rod for the boiling coefficients of $0.72x10^{-3}$ (left) and $0.94x10^{-3}$ (right). The coolant boron concentration does not affect the nickel ferrite mass or the CRUD thickness, but is a significant factor in the boron hideout mass. The evolution of the coolant boron concentration during the cycle, combined with diffusion of metaboric acid out of the CRUD layer, leads to a reduction in the integral boron mass toward the middle and end of the cycle. For the fixed 500 ppm concentration, such behavior is not predicted because the 500 ppm source of metaboric acid dominates the loss due to diffusion. The upper limit coolant boron concentration case results in more than 100% more boron mass than the Seabrook curve, despite an average difference in coolant boron concentration of

only a couple hundred ppm throughout the cycle. The boron precipitation rate dependence on the coolant boron concentration is highly nonlinear.

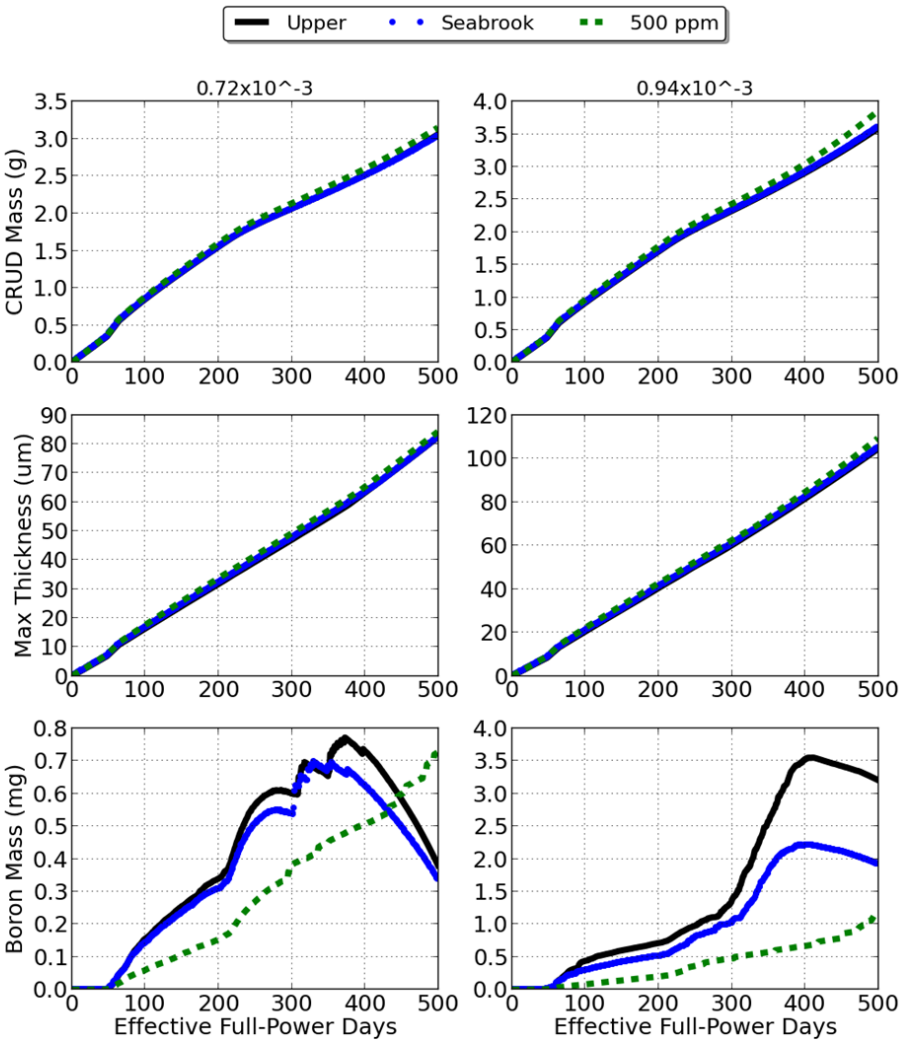


Figure 3.47: Coolant boron concentration comparison of CRUD characteristics when the Arrhenius boiling coefficient is $0.72x10^{-3}$ (left) and $0.94x10^{-3}$ (right).

## 3.6 Chapter III conclusions

In this chapter, both stand-alone and coupled input parameters to the MAMBA code were investigated to determine the CRUD deposition prediction sensitivity. Specifically, the total CRUD mass, maximum thickness, and total boron mass were used as figure of merits.

### Stand-alone inputs

Based on the parameter study in Section 3.1, the parameters that were found to affect the figure of merits the most are:

1. particulate nickel concentration
2. and CRUD porosity.

Regarding the boron mass prediction, the next two most important parameters are:

1. chimney heat transfer coefficient
2. and chimney density.

Despite fixed thermal hydraulic boundary conditions (for case B), variation of the stand-alone input parameters results in CRUD deposit predictions with and without boron precipitation

Regarding the CRUD thickness prediction, the CRUD solid density is the only other parameter that appears to be correlated. Overall, the chimney radius and soluble nickel concentration are the least correlated with the CRUD predictions. The CRUD thermal conductivity is an important parameter that was not considered in this stand-alone input sensitivity analysis. As detailed in Subsection 2.1.3, the solid CRUD thermal conductivity is fixed at 1.1 W/m-K, and the effective conductivity is calculated as a mixing fraction based on the porosity; see Equation 2.35.

## Coupled conditions

In Section 3.5, several plant and boundary conditions relevant to the multiphysics framework presented in this dissertation were investigated. In Figure 3.48, all of the CRUD predictions are anonymously compared to demonstrate the spread of the predictions. A base case is identified that uses the Seabrook coolant boron letdown, 1.5 power level, includes spacer grid effects and erosion, and has Arrhenius coefficients of 130.0 and $0.94x10^{-3}$. A different (inconsistent) power distribution was used in Subsection 3.5.4, so the results are neglected from Figure 3.48. Table 3.19 summarizes the ranges of the end-of-cycle CRUD predictions for all cases varying the coupled plant and boundary conditions.

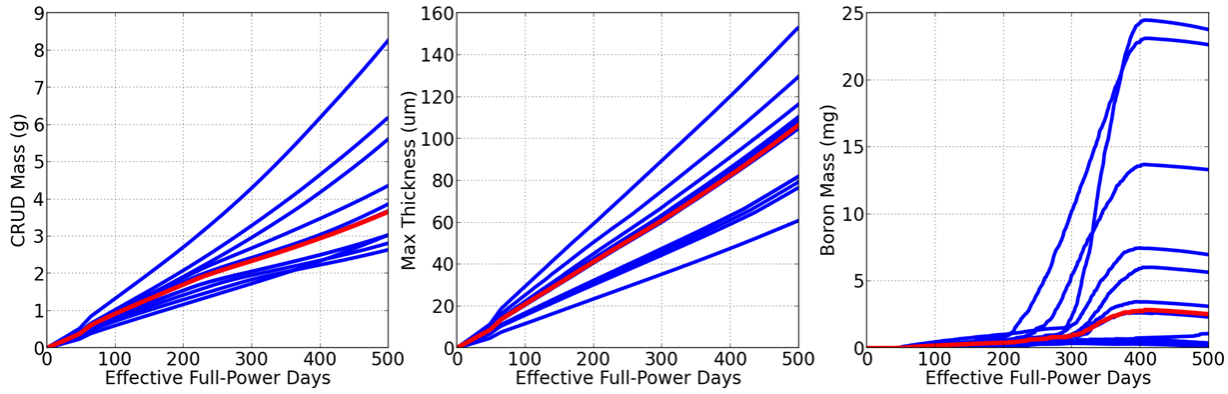


Figure 3.48: CRUD characteristics predicted for several different plant and boundary conditions; base case shown in red.

Table 3.19: Ranges of end-of-cycle CRUD deposition output metrics resulting from variations in the coupled boundary conditions.

| Output metric | Minimum | Maximum | Base |
|---|---|---|---|
| CRUD mass (g) | 2.64 | 8.27 | 3.66 |
| Max thickness ($\mu m$) | 60.8 | 153 | 106 |
| Boron mass (mg) | 0.0880 | 23.8 | 2.53 |

## Stand-alone and coupled conditions comparison

The CRUD characteristics predicted from the coupled condition parameter study, as shown in Figure 3.48, are compared with the stand-alone input parameter study predictions, as shown in Figure 3.23. Because different models (2-D and 3-D) were used in the respective studies, the predictions are normalized by their respective base cases and compared in Figure 3.49.

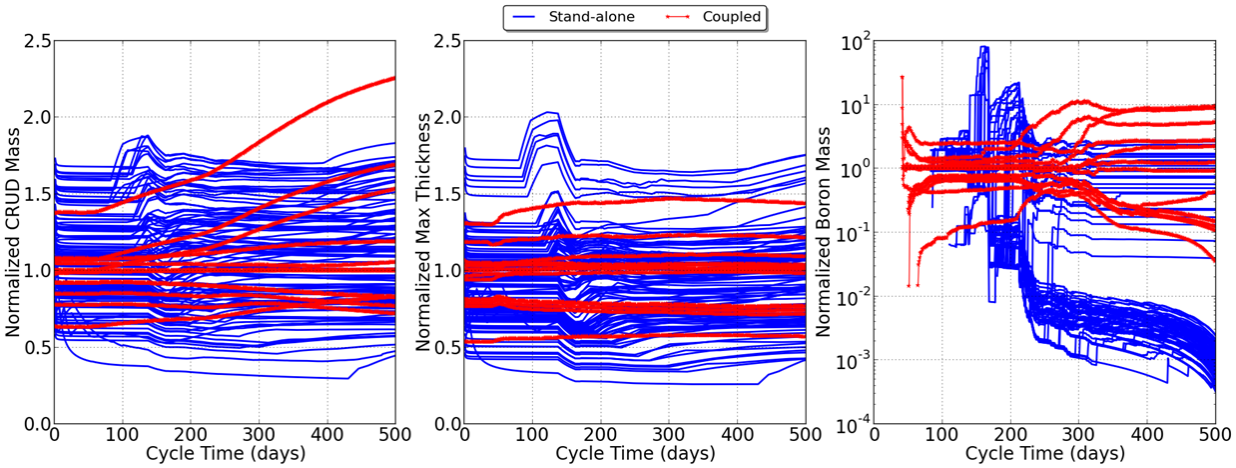


Figure 3.49: Normalized CRUD characteristics predicted for stand-alone and coupled MAMBA parameter studies.

Overall, the deviation of the output metrics are comparable for the stand-alone and coupled conditions, i.e. the variance of the metrics are on the same order of magnitude when comparing the standalone and coupled conditions. Therefore, the importance of inclusion of the high fidelity multiphysics boundary conditions within the CRUD deposition model is confirmed. Specifically, both the fuel rod power level, axial distribution of the power, and the spacer grid/vanes effects are critical to the CRUD growth model. The CRUD deposit distribution is clearly driven by the effects of the spacer grid and mixing vanes, including the convective heat transfer rate and the CRUD erosion rate. On the other hand, the rod power and its axial distribution strongly influence whether enhanced CRUD deposition due to subcooled boiling-induced Darcy flow, is occurring.

# CHAPTER IV

# Multiphysics feedback effects

In the analyses presented in Chapter III, the power distribution remained fixed throughout the cycle simulations, and only the effect of the power level was considered. Moreover, no feedbacks between the physics were considered, i.e. the effects of the CRUD deposit on the neutron flux distribution and conjugate heat transfer solution were neglected. In this chapter, both the evolution of the power distribution with fuel depletion and the presence of a CRUD deposit within the neutronics and thermal hydraulic models is investigated. The two primary operational issues of CIPS and CILC motivate the analyses in this chapter.

The neutronics effects of a boron-containing CRUD deposit include:

1. localized redistribution of power due to increased neutron absorption,
2. reduced coolant boron concentration required to maintain criticality,
3. and boron destruction due to neutron reactions within the CRUD deposit.

Changes in the power distribution directly affect the thermal hydraulic boundary conditions (heat flux and temperature) calculated by CFD, which are provided to the CRUD deposition solver.

The thermal hydraulic effects resulting from inclusion of an additional thermal resistance representing the CRUD deposit include:

1. localized increases in the cladding temperature

2. and localized redistribution of the heat flux.

The effect of the roughness of the CRUD deposit on the fluid dynamics is not considered in the present framework.

## 4.1 Power distribution evolution with depletion

In Section 3.5 of Chapter III, the strong effect of the power level and axial distribution on CRUD deposition and boron hideout predictions was demonstrated. In order to parse out effects in the previous simulations, the power distribution remained fixed during the cycle. Consequently, consistent comparisons were made which enabled identification of some of the most important coupled physics impacting CRUD deposition.

However, the effects of the power distribution evolution with depletion on the subsequent evolution of the thermal hydraulic boundary conditions provided to the CRUD deposition model need investigated. Because both fuel depletion and CRUD deposition are time dependent, an appropriate temporal coupling method must be adopted. Therefore, it is the aim of this section to analyze two classes of temporal coupling methods, e.g. lagged and predictor-corrector, with various fixed stepsizes, in order to conclude which method balances solution accuracy and computational efficiency.

In the present study, the calculation of the 3-D power distributions are decoupled from the CFD and CRUD deposition simulations. Using this approach, feedback effects from the latter physics on the neutronics/depletion are neglected, and only temporal effects of the power distribution on the TH and CRUD deposition are considered. A single fuel pin cell as described in Appendix A is depleted in 5 day increments under hot conditions; two models are considered, one with a 1.45 and one with a 1.5 peaking of nominal power. The axial power distribution evolution is shown in Figure 4.50 for the 1.45 peaking model.

### Lagged temporal coupling

The power distribution is provided to the CFD solver at discrete points during the depletion cycle; then, the CFD model is converged and the TH boundary conditions are provided to the CRUD deposition solver. Simply, a one-way coupling between three physics is utilized:

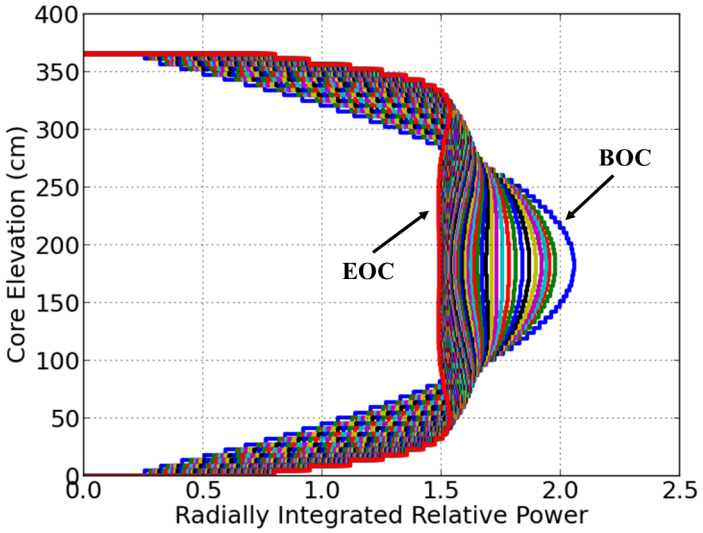


Figure 4.50: Axial power distribution evolution with depletion from BOC to EOC for single fuel pin cell with 1.45 peaking applied to power.

$$Neutronics \rightarrow CFD \rightarrow CRUD\ deposition.$$

Because both the fuel depletion and CRUD deposition physics are time dependent, a time-lagged temporal coupling approach is used, as illustrated in Figure 2.8 (left); the resistance feedback is not included. To determine what fidelity of temporal discretization is necessary to obtain a converged CRUD deposition solution, the power distributions, which are calculated every 5 EFPD, are linearly interpolated in one day increments.

Four uniform stepsizes of 1, 5, 25, and 50 days are simulated and the resulting integral boron mass predictions are compared in Figure 4.51 for the 1.45 (left) and 1.5 (right) power peaking levels. To explain the behavior of the boron mass prediction for the 1.45 power level, Table 4.20 details important points during the cycle. Throughout the cycle, competition between in-flux of soluble boron and diffusion of boron out of the CRUD deposit exists. As the coolant boron concentration is decreased during the cycle, the integral effect of diffusion dominates the competing physics. However, localized precipitation of lithium tetraborate occurs between 315 and 340 days; essentially, at a specific location on the rod, the CRUD thickness was high enough to enable continued concentration of soluble boron until the pre-

cipitation threshold is exceeded. The integral behavior of the boron hideout in the 1.5 power model is similar, but exhibits significant boron precipitation beginning around 275 days and ending around 400 days. At this point in the cycle, the dissolved boron concentration is low enough to allow diffusion of boron to decrease the total boron mass.

Table 4.20: Behavior of the boron hideout during the cycle for 1.45 power level model.

| Time range (days) | Integral boron mass behavior | Physics behavior |
|---|---|---|
| 0-50 | none | CRUD thickness too small to concentrate soluble boron |
| 50-275 | increasing | Concentration of soluble boron within CRUD near cladding interface |
| 275-315 | decreasing | Diffusion of boron out of CRUD dominates in-flux of soluble boron |
| 315-340 | increasing | Localized precipitation of lithium tetraborate |
| 340-500 | decreasing | Diffusion of boron out of CRUD dominates in-flux of soluble boron |

As boron begins to precipitate around 315 EFPD in the 1.45 power model, the coupled stepsize is significantly more important. The 1 and 5 day fixed stepsizes differ by more than 25% at the EOC. On the other hand, for the 1.5 peaking model, 1 and 5 day stepsizes result in nearly identical predictions, and only the 50 day result is poor. Other CRUD characteristics, such as the nickel ferrite mass and thickness of the CRUD, are negligibly affected by the degree of change of the thermal hydraulic boundary conditions during an operating cycle.

It is concluded that a coarse time stepsize of 50 days or greater is sufficient when boron precipitation is not occurring. However, to capture the evolution of the power, and subsequently the thermal hydraulic boundary conditions, within the CRUD deposition solver, during boron precipitation, a stepsize between 1 and 25 days is necessary. The optimal stepsize is physics-dependent and will vary depending on the local conditions driving boron precipitation. Moreover, the point at which boron precipitation begins is unknown *a priori*. Therefore, in Chapter V, an automatic and adaptive methodology based on control theory is introduced to facilitate the coupled time stepsize selection.

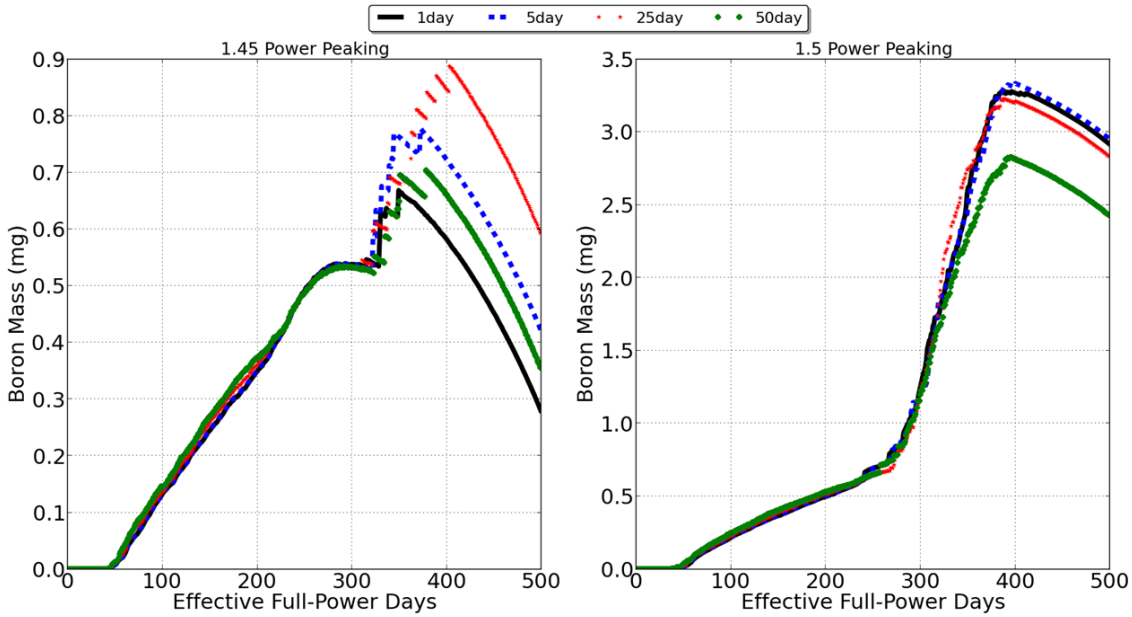


Figure 4.51: Comparison of integral boron mass for one-way TH boundary condition coupling at fixed stepsizes of 1, 5, 25, and 50 days for 1.45 power (left) and 1.5 power (right).

## Predictor-corrector temporal coupling

In the previous subsection, the importance of capturing the evolution of the TH boundary conditions as the power distribution changes with depletion was demonstrated. A one-way lagged temporal coupling investigation was completed by considering fixed stepsizes of 1, 5, 25, and 50 days. In this subsection, the analysis is continued by considering an additional loose temporal coupling method, namely a predictor-corrector (P-C) approach. Figure 2.9 details the time-consistent solution sequence.

The P-C method requires two CFD and two CRUD deposition calculations for each coupled time step. Once the CFD solution is converged on the corrector step using the EOS power distribution, the TH boundary conditions are averaged and used as the CRUD deposition boundary conditions for its corrector step. There is no thermal resistance feedback in this investigation; therefore, the P-C approach reduces to a middle-of-step approach, as shown in Figure 2.8 (right).

Figure 4.52 compares the boron hideout predictions of the lagged and P-C methods when

the stepsize is fixed at 50 days. A fixed stepsize of 1 day is used as the reference case. As expected, improved predictions are realized for the P-C approach. Recall that only changes in the 3-D power distribution are driving the temporally coupling effects reported in this section; therefore, additional effects due to the feedback mechanisms will be investigated in Section 4.4. Furthermore, an added benefit of using a predictor-corrector method to facilitate adaptive coupled time stepsize selection is investigated in Chapter V.

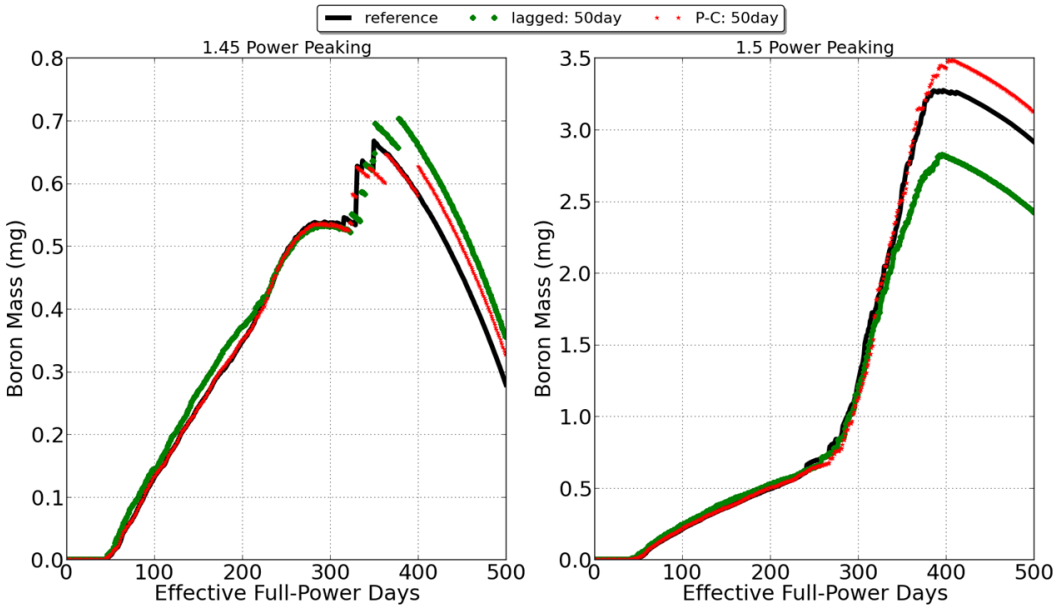


Figure 4.52: Comparison of integral boron mass for P-C TH boundary condition coupling for fixed stepsize of 50 days for 1.45 power (left) and 1.5 power (right).

## 4.2 Boron hideout within neutronics

From a neutronics viewpoint, boron hideout has two primary effects:

1. localized redistribution of power due to increased neutron absorption,
2. and reduced coolant boron concentration required to maintain criticality.

It is worth noting that the first point of power redistribution includes both localized power suppression in the immediate vicinity of the boron deposit and a power increase elsewhere, i.e.

power is conserved for the core (model). As mentioned in Chapter I, this condition is known as CRUD induced power shift. The power shifts *within* the rod containing the CRUD deposit and *to* neighboring rods. Consequently, the power shift feeds back through the thermal hydraulic solver to the CRUD deposition solver; local CRUD and boron deposition decreases due to the reduced heat flux, but the integral rod deposition may increase depending on local conditions.

The second point of reduced coolant boron concentration is a consequence of introducing negative reactivity into the reactor system, thus decreasing the necessary amount of negative reactivity from the coolant boron. This subsection aims to quantify the degree to which these effects feedback to the CRUD deposition predictions.

### 4.2.1 Modeling requirements

Modeling a very thin neutron-absorbing layer within MOC neutron transport is briefly discussed herein. Refer to Appendix E for an in depth analysis of the 2-D modeling requirements of CRUD deposits residing on the outer cladding surface [Walter and Manera, 2016b]. The axial dimension is not included in the investigation.

Two aspects of modeling CRUD within MOC neutron transport were identified:

1. ray tracing parameters including spacing and number of azimuthal angles,
2. and mesh refinement including spatial homogenization.

Ray tracing parameters with spacing of 300 $\mu m$, 16 azimuthal angles, and 4 polar angles are determined to be sufficiently converged for modeling of CRUD deposits with significant boron hideout mass. This is dependent on the MOC transport implementation, including flat source region approximation and ray volume correction; the investigation was performed using DeCART.

Generally, elimination of the radial and azimuthal spatial dependencies of the CRUD distributions results in approximately 50 pcm lower eigenvalues – see Table 7.45 in Appendix E. Specifically, radial mesh refinement including homogenization of the CRUD layer with the coolant is acceptable, provided the amount of coolant is restricted to approximately a

300 μm thick region. In this dissertation, because the CRUD grows in time, a radial region of thickness 150 μm—just outside the cladding—is fixed in the neutronics model, and all CRUD deposition is uniformly homogenized with the coolant in this region.

Azimuthal mesh refinement including smearing of the CRUD layer circumferentially around the rod is acceptable for most CRUD loadings that would be encountered during reactor simulation. However, significant reactivity differences should be expected if the azimuthal dependence is eliminated on a fuel rod experiencing heavy boron hideout. In the context of modeling multiple assemblies, likely only a handful of rods would experience enough boron hideout for the azimuthal variation to have an impact. In this dissertation, the azimuthal dependence of the CRUD deposit is included by using 16 azimuthally-dependent cross section regions within DeCART.

Inclusion of the CRUD structure porosity has reactivity effects ranging from -50 to +100 pcm, depending on the coolant boron concentration. Therefore, in this dissertation, the additional coolant within the CRUD structure is included to reduce multiplication factor prediction errors.

### 4.2.2 CRUD induced power shift

As briefly mention in the introduction to this section, in addition to power shifting within the CRUD-containing rod, power shifts to neighboring rods as well. In order to determine the amount of power *lost* to other rods, a 3-D 5x5 pin array (sub-assembly) neutronics model with 1.45 power peaking is utilized, as described in Appendix A.

To reduce the computational expense, a single pin cell with spacer grids CFD model is coupled with one fuel pin from the sub-assembly. Pin 8, as shown in Figure 7.94 is chosen. The 3-D power distribution is extracted from pin 8 at 4 EFPD and used as the heat source within the fuel in the CFD model; then, the thermal hydraulic boundary conditions required by the CRUD deposition solver are extracted.

A cycle simulation is performed using MAMBA, then the CRUD composition at two points during the cycle is extracted to be *deposited* on pin 8 within the neutronics model. In this way, two degrees of CRUD deposition and boron hideout are considered. Table 4.21

Table 4.21: Summary of pin 8 CRUD characteristics at various times during the CRUD deposition cycle simulation.

| CRUD distribution | Cycle time (days) | Max CRUD thickness ($\mu m$) | $NiFe_2O_4$ mass (g) | Boron mass (mg) |
|---|---|---|---|---|
| A | 300 | 71.07 | 2.432 | 1.718 |
| B | 420 | 101.2 | 3.208 | 5.359 |

summarizes the characteristics of the CRUD for the two points in time; the boron mass includes both isotopes boron-10 and boron-11.

Table 4.22: CRUD effects on the neutronics at 4 EFPD using various CRUD distributions.

| CRUD distribution | 5x5 array $k_\infty$ | 5x5 array $\delta k_\infty$ (pcm) | 5x5 array axial offset (%) | Pin 8 total power (kW) | Pin 8 axial offset (%) |
|---|---|---|---|---|---|
| none | 1.12224 | – | -0.246 | 93.96064 | -0.245 |
| A | 1.12222 | -2 | -0.448 | 93.93998 | -0.448 |
| B | 1.12217 | -7 | -0.886 | 93.91754 | -0.885 |
| Bx4 | 1.12192 | -32 | -2.795 | 93.92113 | -2.800 |

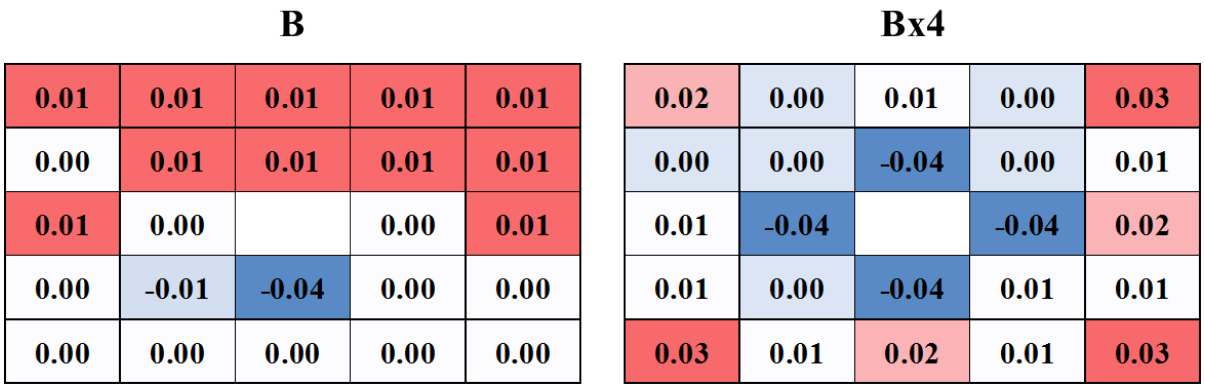


Figure 4.53: Absolute pin power difference (%) for 5x5 pin array when including CRUD distribution B on pin 8 (left) and on pins 8, 12, 14, and 18 (right).

For the extracted CRUD distributions, A and B, a steady state neutronics calculation is performed. One additional simulation, Bx4, is also run where CRUD is deposited on the

four pins, 8, 12, 14, and 18, surrounding the water rod. A porosity of 70% is assumed within each CRUD deposit. Table 4.22 summarizes changes in the multiplication factor, pin power, and axial offset of the 5x5 pin array and pin 8, when applicable. The radial pin power redistribution is shown in Figure 4.53. The axial shifting of the pin 8 power distribution is shown in Figure 4.54 (left) for each CRUD distribution. In Figure 4.54 (right) the azimuthal power variation spanning an elevation of 320 to 329 cm is shown.

Based on the changes in total power of pin 8, only a couple tenths of a percent of the total power redistributes to other pins within the sub-assembly. Most of the power shifting occurs within the pin itself; for distribution B applied to the four pins surrounding the guide tube, more than 2.5% of the power is shifted from the top toward the bottom of the pin. Based on the small amount of power that shifts to neighboring fuel rods, restricting the (neutronics) modeling domain to a single pin cell is assumed to be reasonable.

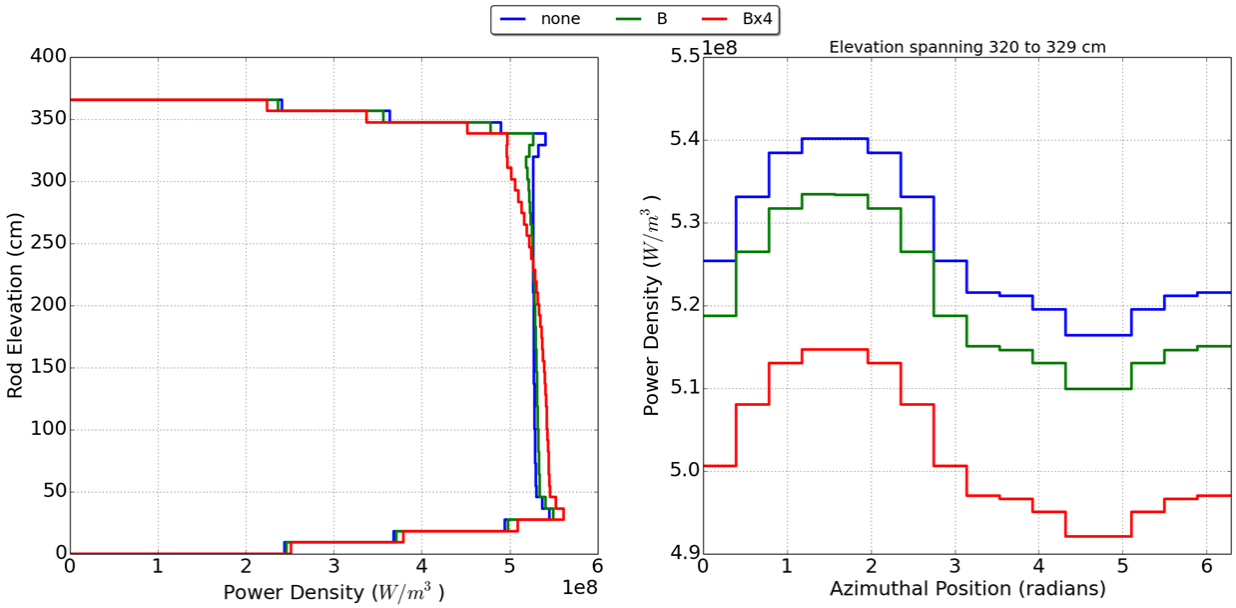


Figure 4.54: Axial (left) and azimuthal (right) power distributions for pin 8 before and after inclusion of the CRUD distribution B and Bx4.

### 4.2.3 Coolant boron concentration

To investigate the feedback effect of boron hideout through the prediction of the critical coolant boron concentration by the neutronics/depletion solver, standalone CRUD deposition simulations are performed. Ideally, the boron hideout composition and distribution would be directly modeled within the lattice depletion solver, and the associated feedback through the critical coolant boron concentration would be assessed. However, modeling of a larger domain would be necessary to accurately predict the sensitivity of the critical boron concentration prediction due to localized CRUD deposition. A 3-D problem domain of this size proves to be very computationally expensive on its own, especially when including CFD.

To get a ball park value for changes in the critical coolant boron concentration, due to CRUD buildup, the results from Subsection 4.2.2 that used the 5x5 pin array model with 1.45 peaking are leveraged. When four of the 24 fuel rods experienced significant boron hideout (e.g. case Bx4), a reactivity difference on the order of tens of pcm was encountered. It is assumed that a 10 pcm change in reactivity corresponds to a 1 ppm change in coolant boron concentration required to maintain criticality.

Therefore, the coolant boron concentration within the MAMBA model, as shown in Figure 3.46, is perturbed by 10, 50, and 100 ppm reductions at 350 EFPD. Figure 4.55 shows the effect of the coolant boron perturbations on the boron hideout mass predictions. Overall, the effect of the coolant boron concentration is quite significant, where a 50 ppm reduction causes a 20% decrease in the predicted boron mass.

### 4.2.4 Boron destruction

#### Theory

A secondary feedback mechanism from neutronics is the depletion of the boron concentrated within the CRUD and the associated production of lithium via the reaction,

$$^{10}B +^{1} n \rightarrow^{7} Li + \alpha. \tag{4.62}$$

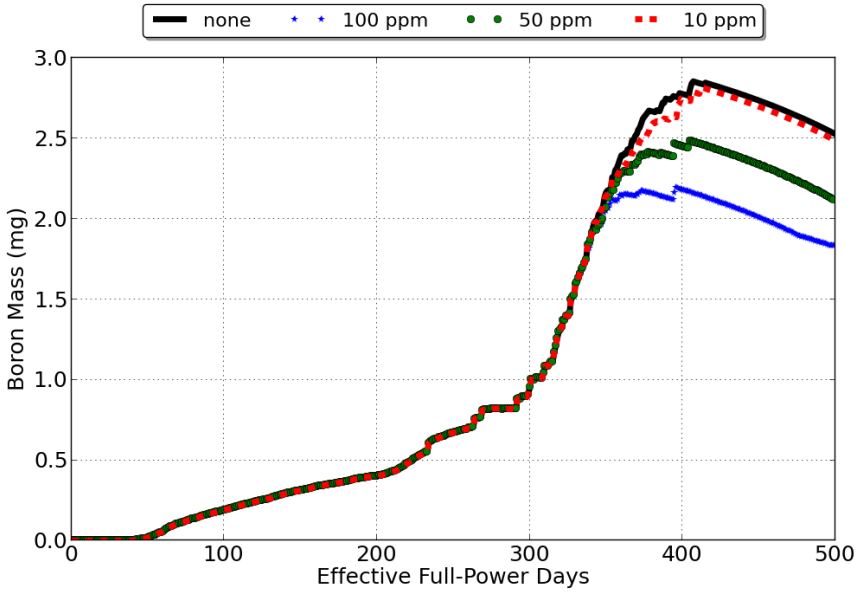


Figure 4.55: Boron hideout mass comparisons due to coolant boron concentration perturbations of 10, 50, and 100 ppm introduced at 350 days.

Recall, lithium tetraborate precipitation is the primary contributor to boron hideout and CIPS; therefore, both the boron and lithium, as seen in Equation 4.63, are important factors,

$$2Li^{+} + 4B(OH)_3 \rightarrow Li_2B_4O_7 + 5H_2O + 2H^{+}. \tag{4.63}$$

In the present framework, the destruction rate of the boron is considered by using the neutron flux distribution and associated absorption reaction rate predicted within the neutronics and fuel depletion solvers. The boron destruction rate is calculated as a normalized neutron capture reaction rate of boron-10 within each cross section region by the neutronics solver,

$$\tilde{R}_{B10} = \frac{R_{B10}}{N_{B10}}. \tag{4.64}$$

The boron-10 particle number density is $N_{B10}$, and the total macroscopic reaction rate, $R_{B10}$, is given by the sum of the reaction rates for each energy group, $g$,

$$R_{B10} = \sum_g \phi_g \Sigma_{a,g}^{B10}, \tag{4.65}$$

where $\phi_g$ is the scalar flux and $\Sigma_{a,g}^{B10}$ is the macroscopic absorption cross section. Then, the normalized reaction rates within the CRUD layer are mapped to the MAMBA domain and used to reduce the boron-10 concentration by,

$$N_{B10} = N_{B10} - N_{B10}\delta t \tilde{R}_{B10}, \tag{4.66}$$

where $\delta t$ is the time stepsize of the numerical integration method used within MAMBA to solve the deposition kinetics equations.

### Modeling results

A 3-D single pin cell model using coupled neutronics, CFD, and CRUD chemistry is used to investigate the effect of the boron destruction. A lagged coupling, similar to that shown in Figure 2.10, with fixed 5 day stepsizes is used; resistance feedback through the CFD solver is not included, and a one-way coupling from neutronics to CFD is utilized (not FPI).

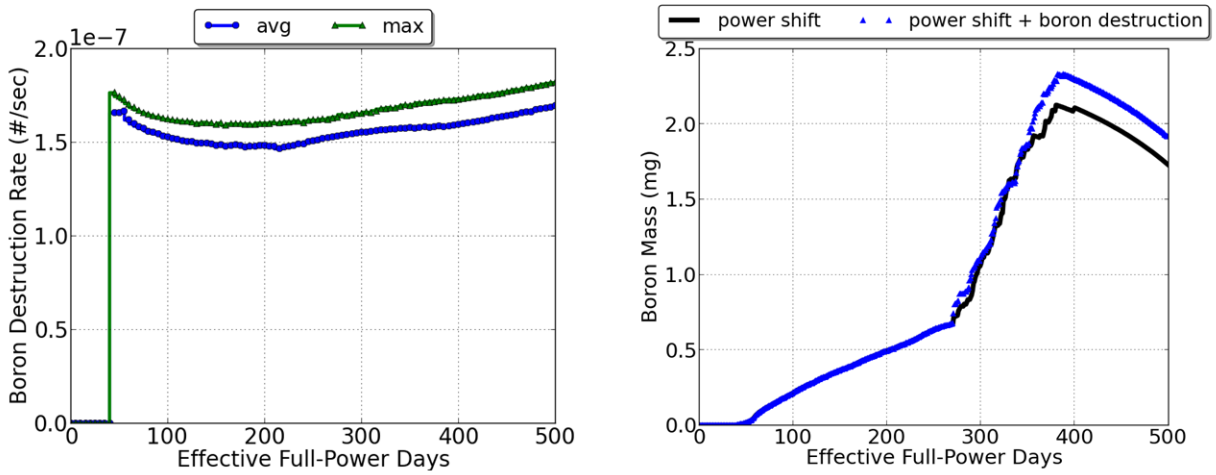


Figure 4.56: Average and maximum normalized boron destruction rate within the CRUD deposit (left), and integral boron mass comparisons of neutronics feedback mechanisms (right).

The average and maximum boron destruction rate are shown in Figure 4.56 (left). The destruction rates are calculated only for DeCART cross section regions that contain CRUD. Figure 4.56 (right) compares the integral boron mass along the rod for the case with and without boron destruction. Both cases include neutronics feedback in the form of power shift. Interestingly, the boron destruction feedback, when coupled with power shift feedback, results in a higher boron mass prediction. The strength of the power shift feedback dominates the decrease in boron due to destruction by neutron interactions. In other words, the negative feedback effect of the shifting of power is diminished by less boron deposited to cause the power shift.

#### Lithium production

The production of lithium, as shown in Equation 4.62, is not yet considered; however, it is not expected to have a significant effect on subsequent lithium tetraborate precipitation. To justify this assumption, let the production of lithium due to boron destruction be denoted by $N_{Li}^{prod}$.

$N_{Li}^{prod}$ occurs within the solid CRUD species, namely $Li_2B_4O_7$ and $NiFe_2O_4$. Because the precipitation of $Li_2B_4O_7$ occurs due to local species concentration within the coolant (within the CRUD pores), the $N_{Li}^{prod}$ must diffuse through the CRUD and into the coolant contained within the pores/chimneys. The diffusion process occurs on a time scale of days; whereas, the boiling-induced flow of the lithium and boron species dissolved in the coolant into the CRUD chimneys occurs on a time scale of milliseconds. Such a disparity in the time scales leads to the assumption that the production of lithium due to boron transmutation is a negligible effect, and thus it is not included in this multiphysics framework.

## 4.3 CRUD induced localized corrosion

Modeling the CRUD deposit as a thermal resistance within the thermal hydraulics model enables improved CILC predictions. Specifically, the increased cladding temperature resulting from the deposit is captured and may be used to inform the boundary conditions required by a corrosion model; such a model is presently not included in the framework described in this

dissertation. Nonetheless, the relative increase in cladding temperature may be used as an indicator of accelerated corrosion. Specifically, correlations between temperature and water-side oxidation rate of cladding materials (e.g. Zircaloy-2 and -4) may be used to approximate the CILC risk.

The thermal resistance $\Gamma$ is calculated within MAMBA as the ratio of the temperature difference across the CRUD and the heat flux entering the CRUD,

$$\Gamma = \frac{\Delta T}{q''}. \tag{4.67}$$

This definition of the thermal resistance accounts for the heat deposited within the chimneys of the CRUD due to vaporization. The presence of CRUD on the cladding surface increases the thermal resistance of the fuel rod, which has two effects which feedback to the CRUD deposition:

1. the cladding temperature increases,
2. and the heat flux redistributes.

The 3-D power distribution extracted from pin 8 of the 5x5 pin array at 4 EFPD is used. Two power peaking factors of 1.3 and 1.45 are considered to produce CRUD deposition predictions that do not precipitate solid boron species and that do, respectively. The single pin cell CFD model with spacer grids is coupled with the CRUD deposition solver for a 500 day cycle simulation; erosion of the CRUD deposit is included. The thermal resistance of the CRUD layer is updated using a lagged approach—as shown in Figure 2.8 (left)—at a fixed interval of 5 days from the beginning to the end of the cycle.

For the two power peaking levels, the maximum outer cladding temperature is compared before and after inclusion of the CRUD distributions' thermal resistances in Table 4.23. Figure 4.57 (top) compares the integral CRUD characteristics during the cycle simulation for each power level. Then, in Figure 4.57 (bottom), the total and maximum thermal resistance and maximum cladding temperature predicted during the cycle for each power level are compared. The significant increase in the thermal resistance of the CRUD deposit during boron precipitation is due to the solid boron phases reducing the convective heat transfer

Table 4.23: Maximum thermal resistance and cladding surface temperatures predicted during 500 day cycle for 1.3 and 1.45 power levels.

| Power peaking | CRUD present | Max thermal resistance ($m^2K/W$) | Max cladding temperature (K) |
|---|---|---|---|
| 1.3 | no | 0.00 | 624.20 |
| 1.3 | yes | $3.9275x10^{-6}$ | 624.76 |
| 1.45 | no | 0.00 | 629.31 |
| 1.45 | yes | $2.0604x10^{-5}$ | 646.32 |

within the chimneys. Therefore, accurate boron precipitation prediction is not only necessary for accurate CIPS predictions, but also for accurate CILC predictions.

To illustrate the increase in cladding temperature, the azimuthal variation at the cladding / CRUD and at the CRUD / coolant interface are compared in Figure 4.58 (left); an elevation of 335 cm is used because the CRUD's thermal resistance is at a maximum along the length of the rod. In general, the local heat flux decreases when the temperature of the cladding and CRUD increase due to the additional resistance, i.e. heat follows path of least resistance. Therefore, when providing the Dirichlet (temperature) and Neumann (heat flux) boundary conditions to the heat solver within MAMBA, a positive or negative feedback effect may result depending on local conditions and how the heat flux redistributes. Results presented in Section 4.4 demonstrate a negative feedback effect from the thermal resistance on the boron mass predictions.

In Section 2.4, the effects of the lateral boundary conditions of the single pin cell CFD model predictions were discussed. The previous coupled simulation is repeated using symmetric boundary conditions, and the azimuthal temperature variation of the cladding/CRUD and CRUD/coolant interfaces at an elevation of 335 cm is shown in Figure 4.58 (right). Clearly, the CFD model boundary conditions affect the flow patterns, temperature predictions, and subsequent CRUD deposit distributions.

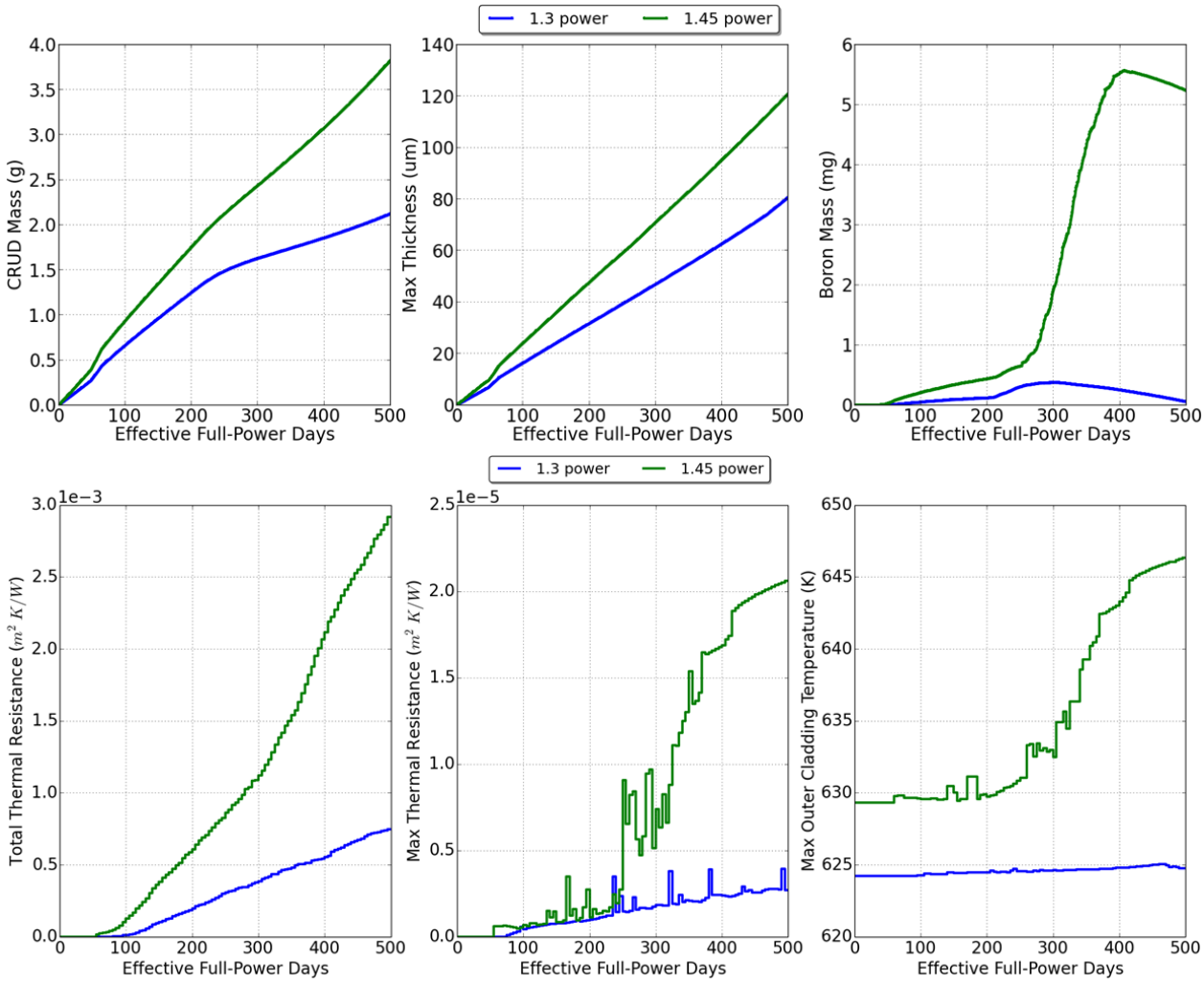


Figure 4.57: Comparison of integral CRUD characteristics (top), and total and maximum thermal resistance and maximum outer cladding temperature (bottom) for 1.3 and 1.45 fixed power simulations.

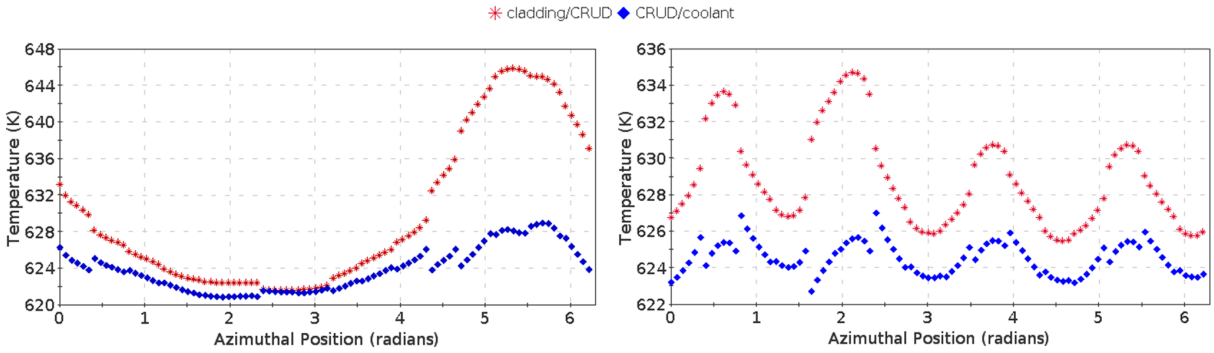


Figure 4.58: Azimuthal variation of cladding/CRUD and CRUD/coolant interface temperature at an elevation of 335 cm at EOC with periodic (left) and symmetric (right) lateral boundary conditions in CFD model.

## 4.4 Comparison of feedback mechanisms

A 3-D single pin cell model using coupled neutronics, CFD, and CRUD chemistry is used to perform the feedback mechanism analysis. Details of this model may be found in Appendix A. To consistently compare the feedbacks investigated in the previous sections, five cycle simulations are performed:

1. no feedback by neutronics or thermal hydraulics,
2. heat flux and temperature feedback due to thermal resistance within CFD,
3. power shift feedback due to boron hideout in neutronics,
4. boron destruction feedback due to neutron interactions,
5. and **all** feedback mechanisms**.**

All five cases are simulated using a fixed 5 day stepsize within the lagged coupling approach shown in Figure 2.10; however, thermal hydraulic feedback is not provided to neutronics, and the fuel temperature and coolant density remain fixed at hot conditions during the depletion cycle. See Footnote 2 in Section 2.2 for additional details.

Table 4.24: Feedback mechanism ranking in terms of EOC boron mass prediction.

| Feedback | EOC boron mass (mg) | Relative difference (%) |
|---|---|---|
| none | 2.955 | – |
| all | 1.752 | -40.7 |
| power shift | 1.733 | -41.4 |
| boron destruction | 3.140* | +6.26 |
| resistance | 2.884 | -2.41 |

* power shift feedback effect subtracted

Figure 4.59 (left) compares the feedback effects in terms of the integral CRUD characteristics for both temporal coupling approaches. Based on the feedback mechanism comparison, each mechanism is ranked in Table 4.24 by the relative change in the EOC boron mass. Because the power shift feedback is also included in the boron destruction case, an effective EOC boron mass is calculated by considering the effect that the power shift has on the prediction.

Cases 1 and 5 are repeated using a predictor-corrector coupling approach, as shown in Figure 2.11, to show the effect of using a time-consistent method. Figure 4.59 (right) compares the boron mass prediction for cases 1 and 5 when using the lagged and P-C coupling methods. Despite using a fixed coupled stepsize of 5 days in both lagged and P-C approaches, a relative difference in the EOC boron mass prediction of approximately 15% persists when the neutronics and thermal hydraulics feedback mechanisms are or are not included. This indicates that a 5-day lagged stepsize is not fully converged when considering all of the coupled feedback mechanisms. Moreover, the total effect of including feedbacks increases for the P-C method, where the EOC prediction is reduced by nearly 60% once all of the feedback mechanisms are considered. On the other hand, when using the lagged approach, a reduction of approximately 40% was realized once feedbacks were included.

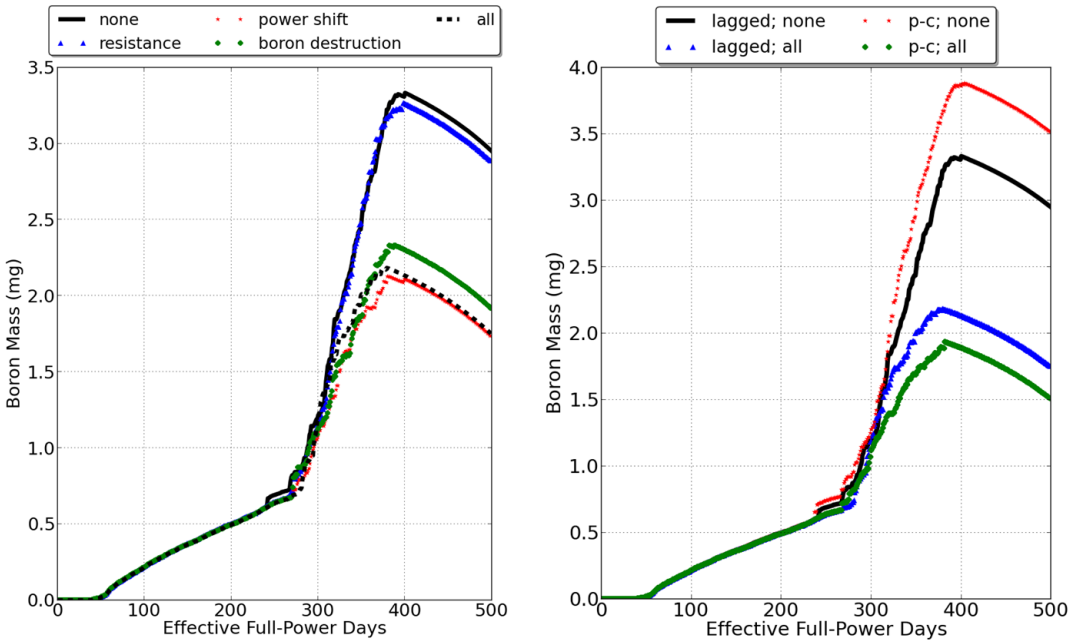


Figure 4.59: Boron mass comparison of feedback mechanisms from neutronics and thermal hydraulics when using lagged temporal coupling (left), and boron mass comparison of cases 1 and 5, no feedback and all feedbacks, for the lagged and P-C temporal coupling methods (right); fixed coupled stepsize of 5 days.

## 4.5 Chapter IV conclusions

The multiphysics feedback effects due to neutronics and thermal hydraulics on fuel rod CRUD deposition predictions were analyzed in this study. Both lagged and predictor-corrector temporal coupling methods were investigated. Based on the comparisons, six conclusions are drawn:

1. a model whose power distribution changes appreciably throughout the depletion cycle requires frequent updates to the thermal hydraulic boundary conditions provided to the CRUD deposition solver in order to accurately predict the boron hideout mass,

2. resolving the azimuthal temperature variation of the cladding surface, resulting from both the spacer grid and CRUD deposit effects, is vital to accurate CILC predictions,

3. accurate prediction of boron precipitation is necessary for accurate CILC predictions because of the significant increase in the thermal resistance,

4. the power shifting feedback through the neutronics dominates the CRUD deposition feedback mechanisms (thermal resistance and boron destruction feedback are negligible),

5. the feedback due to the thermal resistance present within the CFD model is negative in the present model due to localized redistribution of the heat flux,

6. and optimizing the temporal coupling (method and stepsize) between the three primary physics is important to balance solution accuracy and computational efficiency.

In the present study, the feedback due to the presence of the CRUD's thermal resistance within the CFD model showed little effect on CRUD deposition because increased cladding/coolant temperature are offset by heat flux redistribution. However, inclusion of the thermal resistance is necessary to quantify the cladding temperature increase and subsequent acceleration of localized corrosion.

Despite the predictor-corrector approach only showing minor improvement over the lagged approach, an additional benefit of the P-C method is that a natural extension to an automated and adaptive coupled stepsize algorithm may be realized. In fact, the increase in computational cost of using a P-C approach in comparison to a lagged approach is approximately 20%. Typically, the power distribution in the current corrector step and the next predictor step is only slightly different; therefore, the CFD solution is rapidly converged in the latter step.

Furthermore, when considering an adaptive approach, the computational benefit of reducing the overall number of time steps, while maintaining solution accuracy, is acknowledged. For fuel rods that are experiencing more significant boron precipitation, the nonlinear dependence on the thermal hydraulic boundary conditions is stronger, and more frequent updating is necessary. Adaptation of the coupled time stepping ensures a converged solution, despite differing behavior among the fuel rods in the model.

# CHAPTER V

## Adaptive time stepsize selection using control theory

In this chapter, fundamental elements of control theory and its application to time stepsize control is introduced. The works of Soderlind and Gustafsson makeup the majority of the literature on control theory applications to automate stepsize control of numerical integration methods. Gustafsson states the objective of stepsize control is that of an optimization problem where,

"*Given a method and an initial value problem, minimize the computational effort to construct an approximate solution in accordance with a user-specified accuracy requirement*," [Gustafsson et al., 1988].

Gustafsson, Lundh, and Soderlind originally viewed the stepsize selection in the numerical solution of ordinary differential equations (ODE) as an automatic control problem [Gustafsson et al., 1988]. Subsequently, Gustafsson focused on stepsize control techniques for explicit and implicit Runge-Kutta methods [Gustafsson, 1991, Gustafsson, 1994]. Additional works expand on the topic and introduce the application of digital filters [Gustafsson and Soderlind, 1997, Soderlind, 1998, Soderlind, 2002, Soderlind, 2003].

To introduce adaptive time stepsize control, Section 5.1 closely draws upon the discussions in the latter Soderlind references; a similar notation is adopted. Then, Section 5.2 details the application of stepsize controllers for coupling of multiphysics simulations whose time scales are different, and where optimization of the temporal discretization of data exchanges is of interest to reduce the high computational expense of obtaining a coupled high fidelity solution. Stepsize controllers are parameterized for the coupled physics involved in the CRUD

deposition modeling framework.

Once time stepsize controllers are developed for each of the physics, the 3-D single fuel pin cell cycle simulation previously performed in Section 4.4 is repeated in Section 5.3 using the adaptive approach.

## 5.1 Numerical integration stepsize control

This section introduces stepsize control in the context of numerical integration. First, in Subsection 5.1.1, a well-known elementary error controller based on heuristics is derived. Then, in Subsection 5.1.2, relevant control theory terms are defined, and the discrete-time integral (I) controller is discussed from a feedback control point of view. The controllers described in Subsections 5.1.2 and 5.1.3 form the basis for parameterizing controllers for each of the coupled physics of (i) neutronics and fuel depletion and (ii) CRUD deposition and CFD.

### 5.1.1 Elementary error control

The introduction of stepsize control of numerical integration is best achieved by considering the ODE,

$$\frac{dy}{dt} = f(y), \qquad y(t_0) = y_0, \qquad t \geq t_0, \tag{5.68}$$

where the numerical solution at discrete time steps is sought. The stepsize, $h$, is used to advance the solution of the ODE from one state in time $y(t)$ to the next $y(t+h)$, according to a prescribed error tolerance, $\varepsilon$. The global error is the accumulation of the local errors introduced in the current and all preceding time steps. The global error is given by,

$$g_{n=} \left\| y_n - y(t_n) \right\|, \tag{5.69}$$

which is the norm of the difference in the numerical and true solution at a given time. The numerical method is considered convergent if the global error approaches zero as the stepsize decreases,

$$\lim_{h \to 0} \max_{n} g_n = 0. \tag{5.70}$$

Controlling the global error is much more complex and computationally expensive than controlling the local error. Therefore, the (local) error committed in a single time step is controlled by the stepsize, which, in-turn, ensures a bound on the global error.

An elementary local error controller is given as

$$h_{n+1} = \left( \frac{\varepsilon}{\hat{r}_{n+1}} \right)^{\frac{1}{k}} h_n, \tag{5.71}$$

where $k$ depends on the order of the method and $\hat{r}_{n+1}$ is the local error estimate [Hairer et al., 1993]. The heuristic derivation of this control algorithm is given in [Soderlind, 2002]; the important aspects are now summarized. Consider the ODE in Equation 5.68 with a measure for the local error defined as,

$$\hat{e}_{n+1} = y_{n+1} - \hat{y}_{n+1}, \tag{5.72}$$

where $\hat{y}_{n+1}$ is the discrete reference solution. The local error is assumed to depend on the stepsize asymptotically as,

$$\hat{e}_{n+1} \sim h^{\hat{p}+1}, \tag{5.73}$$

where $\hat{p}$ is the order of the error estimate. Therefore, Equation 5.73 is expanded in an asymptotic series as,

$$\hat{e}_{n+1} = \hat{\Phi}_n h^{\hat{p}+1} + \mathcal{O}(h^{\hat{p}+2}), \tag{5.74}$$

where $\hat{\Phi}_n$ is the principal error function at time step $n$ and is dependent on the ODE solution. The order of the error estimate $\hat{p}$ is the largest integer for which $\hat{e}_{n+1} = \mathcal{O}(h^{\hat{p}+1})$ for all $n$.

Depending on the control objectives, the local error is controlled by either the error per step (EPS) with,

$$\hat{r}_{n+1} = \left\| \hat{e}_{n+1} \right\|, \tag{5.75}$$

and $k = \hat{p} + 1$, or by the error per unit step (EPUS) with $k = \hat{p}$ and,

$$\hat{r}_{n+1} = \left\| \frac{\hat{e}_{n+1}}{h_n} \right\|. \tag{5.76}$$

The above derivation suggests that the difference between the tolerance, $\varepsilon$, and error estimate, $\hat{r}_{n+1}$, will be eliminated by the controller, in Equation 5.71, in a single step, thus decreasing the local error to the set tolerance. This ideal control is dependent on two assumptions. The first assumption is that the local error estimate varies asymptotically according to the relation,

$$\hat{r}_{n+1} = \left\| \hat{\Phi}_n \right\| h_n^k. \tag{5.77}$$

The second assumption is that the norm of the principal error function varies slowly,

$$\left\| \hat{\Phi}_n \right\| \approx \left\| \hat{\Phi}_{n-1} \right\|. \tag{5.78}$$

In practice, explicit calculation of the principal error function is not necessary. In the extension of this methodology to loosely coupled multiphysics solution control, the principal error function cannot be known *a priori*.

### 5.1.2 Discrete-time integral controller

In this subsection, the interaction of the *process* and *controller*, known as *closed loop dynamics*, is developed. In the case of stepsize control of numerical integration, the process is the combination of the equation being solved and the integration method utilized. The controller is the means by which the local error estimate and prescribed tolerance is used to control the stepsize.

The elementary error controller, Equation 5.71, is written as a linear difference (recurrence) equation by taking logarithms,

$$\log h_{n+1} = \log h_n + \frac{1}{k}(\log \varepsilon - \log \hat{r}_{n+1}). \tag{5.79}$$

In this form, relevant control theory terminology is readily introduced using the terms in Equation 5.79:

- *control* is defined by $\log(h)$,
- *integral gain* by $1/k$,
- *setpoint* by $\log(\varepsilon)$,
- *error estimate* by $\log(\hat{r}_{n+1})$,
- and *control error* by $\log \varepsilon - \log \hat{r}_{n+1}$.

The controller's objective is to seek an equilibrium where the control of the current time step $n$ does not change in the next time step $n+1$. This is achieved by forcing the error estimate equal to the setpoint. The closed-loop feedback system is illustrated in Figure 5.60.

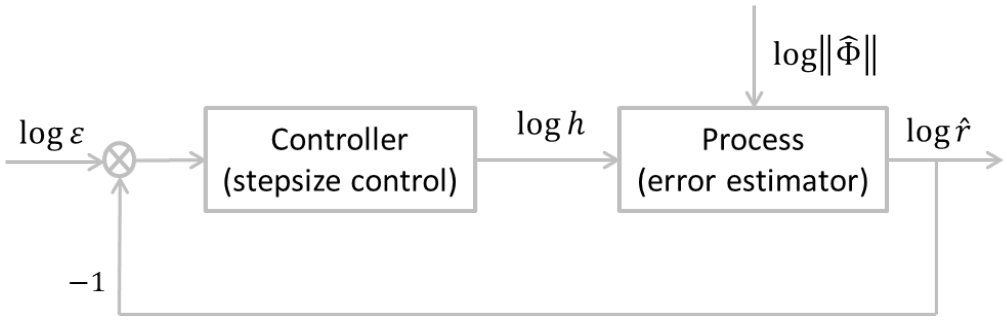


Figure 5.60: Feedback control loop for stepsize selection.

The solution of 5.79 is found as the sum of all past control errors,

$$\log h_n = \log h_0 + \frac{1}{k} \sum_{m=1}^{n} (\log \varepsilon - \log \hat{r}_m). \tag{5.80}$$

The assumption that the error evolves asymptotically according to Equation 5.77 is again employed; taking the logarithm gives,

$$\log \hat{r}_{n+1} = k \log h_n + \log \left\| \hat{\Phi}_n \right\|. \tag{5.81}$$

Inserting Equation 5.81 into Equation 5.79 to eliminate the error estimate and replacing the $1/k$ factor with the integral gain, $k_I$, gives,

$$\log h_{n+1} = (1 - kk_I) \log h_n + k_I \left( \log \varepsilon - \log \left\| \hat{\Phi}_n \right\| \right). \tag{5.82}$$

The integral gain should be viewed as a design parameter—no longer fixed based on the process—with the purpose of affecting the closed loop dynamic behavior. Therefore, the designer/user of the controller should determine proper gain values that produce *good* controller behavior. The process of determining an appropriate setpoint and gain value(s) is known as *controller parameterization*.

The root of Equation 5.82 is,

$$\lambda = 1 - kk_I. \tag{5.83}$$

[Soderlind, 2002] explains that the choice of $kk_I$ is a trade-off between the controller's response time and sensitivity to changes in $\log \left\| \hat{\Phi}_n \right\|$. The controller behavior resulting from various stable values of $kk_I \in [0, 2]$ is summarized by:

- $kk_I \in (1, 2]$ results in fast, oscillatory control,
- $kk_I \in 1$ results in deadbeat control,
- and $kk_I \in [0, 1)$ results in slow, smooth control.

Clearly, slow and smooth control is advantageous, so the range of $kk_I$ for integral control is between 0 and 1. The I controller is written as,

$$h_{n+1} = \left( \frac{\varepsilon}{\hat{r}_{n+1}} \right)^{k_I} h_n. \tag{5.84}$$

Comparison of the I controller to the elementary controller shows the singular difference is the substitution of $1/k$ for $k_I$, which results in smoother stepsize predictions, while still obeying the asymptotic error model given by Equation 5.77. The assumption of Equation 5.78 is no longer required.

### 5.1.3 PI and PID controllers

Despite the I controller's smooth stepsize sequence, more advanced controllers may be used to improve performance and increase the range of applicability. Such controllers utilize the benefits of integral control, but modify the behavior with additional proportional (P) and/or derivative (D) error components.

The proportional-integral (PI) controller includes two terms: (i) proportional to the control error, and (ii) proportional to the summation (discrete integral) of the control error. The PI controller is written in a form similar to difference equation of the integral controller,

$$\log h_n = \log h_0 + k_I \sum_{m=1}^{n} (\log \varepsilon - \log \hat{r}_m) + k_P (\log \varepsilon - \log \hat{r}_n). \tag{5.85}$$

Therefore, the recursion relation may be used to write the PI controller in a more useful form,

$$h_{n+1} = \left( \frac{\varepsilon}{\hat{r}_{n+1}} \right)^{k_I} \left( \frac{\hat{r}_n}{\hat{r}_{n+1}} \right)^{k_P} h_n. \tag{5.86}$$

The additional proportional component accounts for error trends and considers the local error estimate of the previous time step. Specifically, a quicker reduction of stepsize is achieved for increasing errors, and a quicker increase of stepsize is realized for decreasing errors. As with the I controller, the gains, $k_I$ and $k_P$, associated with the PI controller should be determined based on the controller's objective and required behavior. Choosing $k_I$ and $k_P$ is a compromise between stability and response time.

The addition of derivative action projects the previous errors' rates of change, which often allows larger integral and proportional gains, leading to a faster response. The combination of all three of the discussed actions suggests the proportional-integral-derivative (PID) controller given as,

$$h_{n+1} = \left( \frac{\varepsilon}{\hat{r}_{n+1}} \right)^{k_I} \left( \frac{\hat{r}_n}{\hat{r}_{n+1}} \right)^{k_P} \left( \frac{\hat{r}_n^2}{\hat{r}_{n+1} \hat{r}_{n-1}} \right)^{k_D} h_n. \tag{5.87}$$

## 5.2 Multiphysics solution control

Gustafsson and Söderlind focused on automatic and adaptive stepsize selection applied to numerical integration methods. However, a natural extension of their application is the control of the temporal discretization of data exchange between loosely coupled physics.

There have been only a handful of applications of control theory to automate and adapt the temporal coupling between the multiphysics simulations. Valli and others have utilized PID controllers, Equation 5.87, to select the time stepsize of the exchange of data between nonlinear iterations for coupled reaction-convection-diffusion and coupled viscous flow / heat transfer problems [Valli et al., 2002, Valli et al., 2005]. Stepsize control was achieved by monitoring normalized changes in solution variables of interest, such as velocity and temperature. Other interesting applications of adaptive stepsize selection may be found in Refs. [Burrage et al., 2004, Geiser and Fleck, 2009].

The previously mentioned works motivate the present research to apply control theory to automate and adapt the coupled time stepsize associated with physics of the CRUD deposition framework, as shown in Figure 2.6. Specifically, a unique stepsize controller will be chosen, parameterized, and implemented for the coupled physics of:

1. neutronics and fuel depletion,
2. and CFD and CRUD chemistry.

Parameterization of the each controller involves the identification of one or more control variables, the value of said variable(s), and the gain value(s). A balance of response time and damping to an external disturbance is often sought in order to parameterize a well-behaved controller. Several general controllers, including I, PI, and PID, are considered in the subsequent stepsize controller parameterizations. Latin hypercube sampling (LHS) is sometimes used in the subsequent subsections to ensure sufficient coverage of the parameter space; the DAKOTA code package is used to perform the LHS [Adams, 2015].

Adaptive time stepsize control hinges on the ability to compute an error estimate. For the loosely coupled multiphysics models presented within this CRUD deposition framework, predictor-corrector methods are leveraged to enable computation of said error estimate.

Consider physics A to be time-dependent and physics B to be steady state; these physics are coupled through solution variables $\alpha$ and $\beta$, respectively. Algorithm 5.3 summarizes a predictor-corrector method applied to the two physics, where a stepsize prediction is computed:

---

**Algorithm 5.3** A generalized adaptive predictor-corrector algorithm for loosely coupling a time-dependent physics A to a steady state physics B.

---

1. begin step $n$ with stepsize $h_n$ from $n-1$ to $n$ with $\beta_{n-1}$ known from previous step,
2. in physics A, using $\beta_{n-1}$ proceed in time from $n-1$ to $n$ to obtain $\alpha_n^p$,
3. in physics B, calculate $\beta_n^p$ using $\alpha_n^p$,
4. in physics A, using $\beta_n^p$ proceed in time from $n-1$ to $n$ to obtain $\alpha_n^c$,
5. in physics A, average the predictor and corrector solutions, $\alpha_n = \frac{1}{2}(\alpha_n^p + \alpha_n^c)$,
6. in physics B, calculate $\beta_n$ using $\alpha_n$,
7. compute next stepsize $h_{n+1}$ using error estimate $\hat{r}_{n+1}$,
8. and proceed to next step $n+1$.

---

Typically, an $L^2$ relative error norm is used to compute the error estimate,

$$\hat{r}_{n+1} = \left(\frac{1}{h_n}\right)\sqrt{\frac{\sum_V(\beta_n - \beta_n^p)^2}{\sum_V(\beta_n)^2}}, \tag{5.88}$$

where the EPUS method in Equation 5.76 is employed to normalize the error by the current stepsize. In Equation 5.88, $n$ represents the time step, $p$ denotes a predictor step value, and $\sum_V$ denotes summation over the model domain.

### 5.2.1 2-D lattice depletion

The application of adaptive stepsize control for two-dimensional assembly depletion simulations has been documented in detail in [Walter and Manera, 2016a]. A summary is presented within this subsection; and, in the interest of readability, additional details may be found in Appendix F. The 2-D fuel assembly models used in the DeCART simulations are documented in Appendix A.

Refer to Subsection 2.1.1 for details on steady state neutronics coupled with time-dependent nuclide transmutation. Traditionally, the temporal discretization used in the neutronics / depletion calculation is fixed by the user. A typical rule of thumb (ROT) is shown in Table 5.25, where smaller stepsizes are often used at the BOC and are increased as the EOC is approached [Cacuci, 2010, Collins et al., 2014]. The presence of burnable absorbers (BAs), such as IFBA or gadolinium, impacts the stepsizes necessary to ensure that the solution is no longer affected by stepsize refinement. Specifically, the gadolinium isotopes Gd-155 and Gd-157 are very strong neutron absorbers, and modeling the depletion of these isotopes requires stepsizes approximately four to five times smaller than fuel without these burnable absorbers. Recently, several new modeling methods for treatment of gadolinium fuels have been developed [Yamamoto et al., 2009,Isotalo and Aarnio, 2011b,Carpenter, 2009,Carpenter and Wolfill, 2010, Lee and Nam, 2013]. These methods are based on extrapolating the predictor and/or corrector solutions as a function of time or neutron reaction rate.

To enable depletion stepsize predictions, the traditional P-C approach is complemented with an adaptive stepsize algorithm based on control theory, where the one-group scalar neutron flux is used as the control variable. Specifically, the $L^2$ relative error norm of the scalar flux is utilized to calculate the error (per unit step) estimate,

$$\hat{r}_{n+1} = \left(\frac{1}{h_n}\right)\sqrt{\frac{\sum_V(\phi_n - \phi_n^p)^2}{\sum_V(\phi_n)^2}}. \tag{5.89}$$

Besides the neutron flux, consideration of the neutron cross section and/or nuclide concentrations may also be of interest, but are not considered in this study. For neutron transport solutions realized through the method of characteristics, calculation of the $L^2$ norm of the flux includes all depletable cross section regions.

Table 5.25: Typical rule of thumb depletion stepsize sequence for lattice calculations [Collins et al., 2014].

| Depletion step | Burnup stepsize (MWd/kgHM) | Burnup (MWd/kgHM) |
|---|---|---|
| 1 | 0.1 | 0.1 |
| 2 | 0.4 | 0.5 |
| 3 | 0.5 | 1.0 |
| 4 | 1.0 | 2.0 |
| ⋮ | ⋮ | ⋮ |
| 14 | 1.5 | 12.5 |
| 15 | 2.5 | 15.0 |
| ⋮ | ⋮ | ⋮ |
| 21 | 2.5 | 30.0 |

No additional depletion or transport calculations are necessary to utilize the stepsize controller; however, depending on each specific code's lattice depletion implementation, additional data may be required to be stored in memory. At minimum, both the predicted and corrected (end-of-step) one-group scalar neutron flux for each depletable cross section region must be accessible at the end of the depletion step. As a point of reference, in DeCART's implementation, an additional vector with length of the number of depletable cross section regions is kept in memory so that the predictor flux $\phi_{n+1}^{p}$ is accessible once the EOS flux $\phi_{n+1}$ is calculated.

To begin the depletion cycle, an initial depletion stepsize must be set; then, using the solution information from the initial step, an I controller allows a stepsize prediction for the second depletion step. Each predicted stepsize is rounded up to the nearest hundredth of a burnup unit (MWd/kgHM). If higher order controllers, such as PI or PID, are used, additional information must be available in memory. For a PI controller, the previous depletion step's error norm must be available; and for a PID controller, the previous two depletion steps' error norms must be available.

The stepsize controller parameterization process was performed using Latin hypercube sampling of the flux tolerance and integral gain ranges for an I controller. Additional error com-

ponents, such as proportional and derivative, were also considered, and the recommended parameter values are reported in Table 5.26. The details of the stepsize controller parameterization and controller analyses may be found in Appendix F. The range of parameterization balances solution accuracy and stepsize efficiency for the class of problems tested. That being said, a purely integrating controller provides robust behavior and no significant benefits of the addition of proportional or derivative control were realized for lattices without BAs or with IFBA. Therefore, an I controller, in the form of Equation 5.84, is recommended with the parameterization of,

$$h_{n+1} = \left(\frac{3 \times 10^{-4}}{\hat{r}_{n+1}}\right)^{0.10} h_n. \tag{5.90}$$

For gadolinium-bearing lattices, an integral controller with the following parameterization performed very well,

$$h_{n+1} = \left(\frac{7 \times 10^{-4}}{\hat{r}_{n+1}}\right)^{0.03} h_n. \tag{5.91}$$

However, the ability of the controller in Equation 5.91 to quickly increase the stepsize once the gadolinium burns out was lacking. Therefore, a PID controller of the form of Equation 5.87 should be investigated further. Additional error components should allow the integral gain to be increased, which would improve the controller response time. For all fuel types, an initial stepsize of 0.2 MWd/kgHM is recommended.

Table 5.26: Recommended 2-D lattice depletion stepsize controller parameterization ranges that result in acceptable behavior.

| Parameter | Lower bound | Upper bound |
|---|---|---|
| Initial stepsize (MWd/kgHM) | 0.10 | 0.30 |
| Flux tolerance | $1 \times 10^{-4}$ | $7 \times 10^{-4}$ |
| $k_I$ | 0.03 | 0.10 |
| $k_P$ | 0.05 | 0.12 |
| $k_D$ | 0.05 | 0.08 |

The integrating controllers shown in Equations 5.90 and 5.91 were implemented within DeCART. The three full-assembly lattice fuel types are simulated over a cycle length of 30.0 MWd/kgHM, which corresponds to approximately 800 EFPD. Figure 5.61 shows the predicted stepsize sequence for each fuel lattice type and the rule of thumb sequence. As expected, smaller stepsizes are required for the models with BAs because the impact of the transmutation of the nuclides on the neutron flux is stronger; thus, the stepsize is adjusted to ensure the prescribed flux tolerance is respected. The relatively constant stepsize of 0.2 MWd/kgHM predicted for the gadolinium fuel type in the first 9.0 MWd/kgHM correlates well with the expected stepsize necessary to capture the gadolinium burnup toward the beginning of cycle. The benefit of the stepsize controller is especially realized as the gadolinium burnup peaks, as this point in time is not usually known a priori, and the stepsize may be increased while ensuring the solution accuracy.

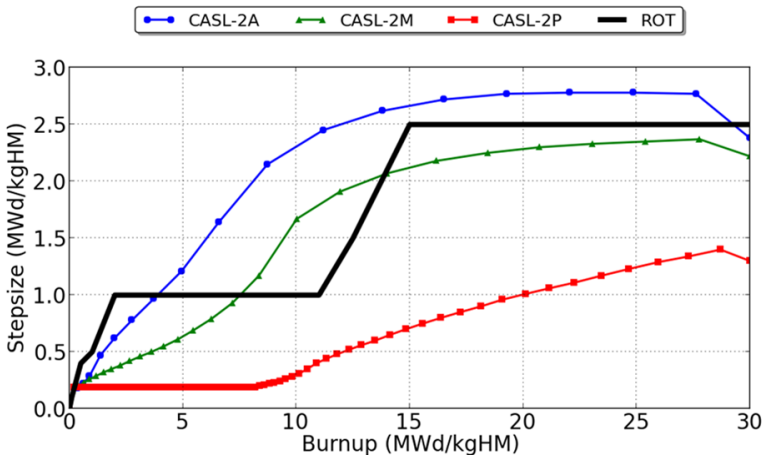


Figure 5.61: Depletion stepsize sequence predicted by the parameterized I controllers for the three lattice fuel types; rule of thumb stepsize sequence included.

The parameterized integral controller predicts a stepsize sequence that reduces the number of steps during the depletion cycle from 21 to 19 in comparison to the rule of thumb sequence for the CASL-2A benchmark. No loss of accuracy in terms of the eigenvalue is encountered. For all three of the lattice types, Table 5.27 summarizes the number of predicted depletion steps and comparisons with the very fine step reference multiplication factor. The tabulated differences are the maximum encountered during the depletion cycle. In general, the presence of strong BAs dominates, or controls, the multiplication factor of the system. In other

words, isotopic concentration errors introduced by the stepsize sequence may cancel or be less pronounced in lattices containing strong burnable absorbers.

Table 5.27: Summary of adaptive burnup stepsize predictions for each lattice fuel type with maximum $k_\infty$ differences encountered during the depletion cycle.

| Benchmark | Lattice type | Flux tolerance | $k_I$ | Number of steps | Max $\delta k_\infty$ (pcm) |
|---|---|---|---|---|---|
| ROT | no BAs | – | | 21 | -189 |
| CASL-2A | no BAs | $3 \times 10^{-4}$ | 0.10 | 19 | -185 |
| CASL-2M | IFBA | $3 \times 10^{-4}$ | 0.10 | 27 | -168 |
| CASL-2P | gad | $7 \times 10^{-4}$ | 0.03 | 74 | -114 |

Figure 5.62 (left, top) shows the infinite multiplication factor, $k_\infty$, evolution predicted while using the stepsize controller for each of the lattice fuel types. The lattice without any burnable absorbers decreases nearly linearly, while the lattices containing BAs result in very different neutron economy behavior due to the rate at which the burnable isotopes are depleted. Figure 5.62 (left, bottom) shows the multiplication factor error between the predicted stepsize sequence and the very fine step reference solution. The rule of thumb stepsize sequence solution error is also included for the CASL-2A benchmark.

Because the $L^2$ relative error norm of the one-group scalar neutron flux is used as the control variable, it is useful to plot the evolution of the norm of the reference and predicted solutions; Figure 5.62 shows the flux norm of the reference solution (right, top) and the norm of the controller predicted solution (right, bottom). Comparison of the reference solution flux norms reveals the need for loosening the flux tolerance of the parameterized stepsize controller of gadolinium-bearing fuel. Even for the reference solution, the relative error norm of the flux is half a magnitude higher than the other lattice types in the first 10.0 MWd/kgHM.

From a practical research standpoint, an automatic and adaptive burnup stepsize selection algorithm may be especially useful for novice computational lattice physics users, who are unfamiliar with burnup stepsize requirements. Furthermore, such a method may be used to improve the efficiency of performing sensitivity studies on different burnable absorber loadings, especially when the computational cost is high. Using the tolerance on the control variable to intuitively adjust the solution accuracy of the stepsize controller should be

utilized by the user. That being said, it is the author's hope that the controller parameterization and recommended flux tolerances serve as a starting point to optimize the controller parameterization process for other fuel loadings and parameter studies.

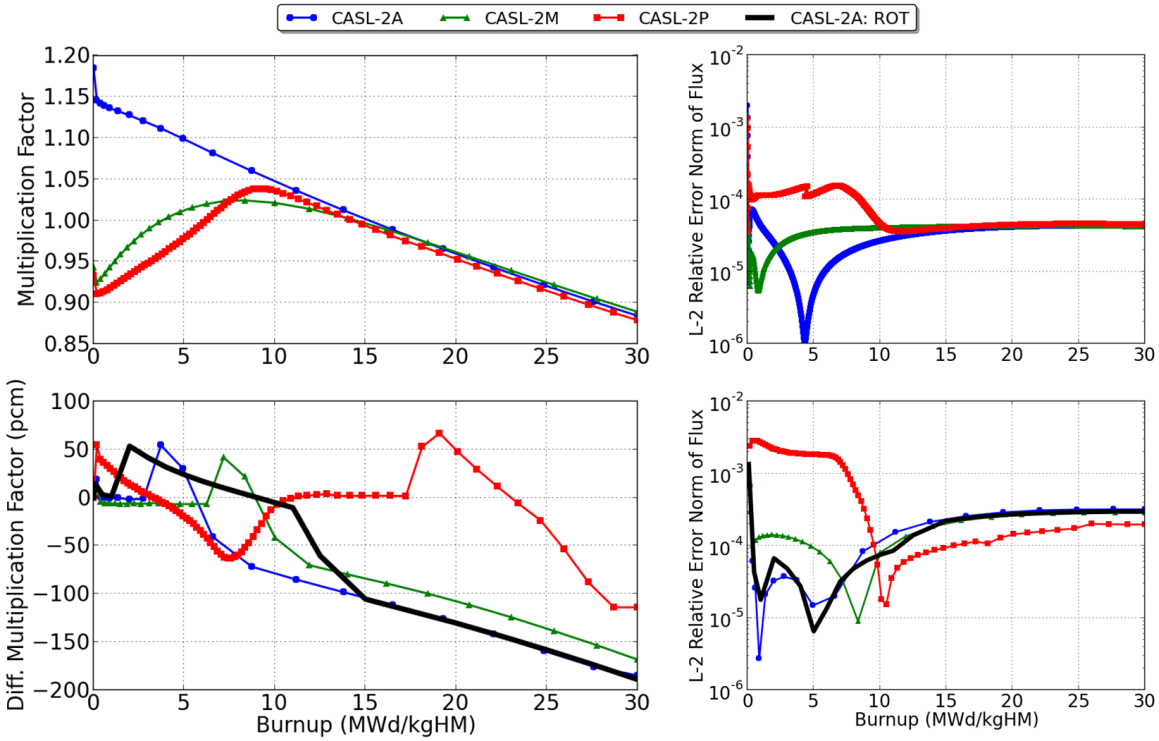


Figure 5.62: Multiplication factor (left, top) and absolute difference from fine step of 0.01 MWd/kgHM reference solution (left, bottom); $L^2$ relative error norm of scalar flux for fine step reference solution (right, top) and for I controller stepsize prediction solution (right, bottom) for three lattice types when using parameterized I controllers.

### 5.2.2 3-D fuel depletion

A full-length 3-D fuel pin cell without burnable absorbers is used to extend the 2-D fuel depletion controller parameterization. The model is documented in detail in Appendix A and has previously been used in Chapter IV to investigate the feedback mechanisms involved in multiphysics CRUD deposition simulations. The only difference from the model in Chapter IV is that the coolant boron concentration is fixed during the cycle at 1300 ppm.

### Controller parameterization

The parameterized 2-D lattice depletion controller developed in Subsection 5.2.1 and given by Equation 5.90 is used as a starting point for parameterizing a controller applicable to 3-D problems. Again, the error estimate is computed using the $L^2$ relative error norm of the one-group scalar neutron flux, as shown in Equation 5.89.

In comparison to the 2-D assembly model (CASL-2A), the relative error norm of the one-group scalar neutron flux is significantly larger in the present 3-D model because of several factors that impact the spatial variation of the flux solution:

1. the addition of the third dimension in the axial direction,
2. single high power fuel rod free of radial leakage and core heterogeneity effects,
3. equilibrium xenon calculation in three dimensions,
4. and azimuthally-dependent cross section regions are utilized to enable assignment of CRUD deposits circumferentially around the rod, thus the depletion of the fuel is also azimuthally-dependent.

Figure 5.63 compares the flux $L^2$ relative error norms of the 2-D assembly and 3-D pin cell models when using the rule-of-thumb stepsize sequence, as shown in Table 5.25.

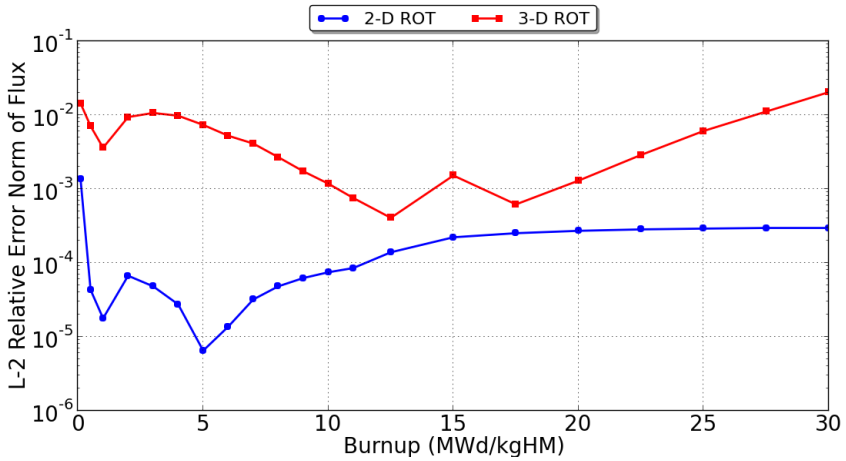


Figure 5.63: Comparison of flux $L^2$ relative error norms of 2-D assembly and 3-D pin cell solutions when using the rule of thumb stepsize sequence.

Despite comparable errors in the multiplication factor, e.g. -200 pcm at 30.0 MWd/kgHM, for the 2-D and 3-D models when using the rule of thumb stepsize sequence, the additional (axial) direction and the aforementioned reasons for a larger flux norm impact the optimal depletion stepsize sequence. To demonstrate this, a modified rule of thumb (mROT) is introduced that uses a stepsize sequence shown in Table 5.28. Figure 5.64 compares the difference in multiplication factor with respect to the reference stepsize of 0.01 MWd/kgHM (left) and the axial offset of the power distribution (right). An error in the calculated neutron flux (power) distribution of approximately 2.5% in terms of the axial offset is revealed when using the ROT sequence. The modified ROT sequence corrects the axial power distribution by reducing the maximum stepsize of 2.5 MWd/kgHM to 1.5 MWd/kgHM and by increasing the number of depletion steps by nine.

Table 5.28: Modified rule of thumb depletion stepsize sequence suggested for 3-D depletion calculations.

| Depletion step | Burnup stepsize (MWd/kgHM) | Burnup (MWd/kgHM) |
|---|---|---|
| 1 | 0.1 | 0.1 |
| 2 | 0.4 | 0.5 |
| 3 | 0.5 | 1.0 |
| 4 | 1.0 | 2.0 |
| ⋮ | ⋮ | ⋮ |
| 27 | 1.5 | 25.5 |
| ⋮ | ⋮ | ⋮ |
| 30 | 1.5 | 30.0 |

By loosening the flux tolerance from $3 \times 10^{-4}$, as used in the 2-D controller, to $1 \times 10^{-3}$, the predicted stepsizes are within the range of the modified rule of thumb stepsize sequence. The newly parameterized I controller for the 3-D problem is,

$$h_{n+1} = \left( \frac{1 \times 10^{-3}}{\hat{r}_{n+1}} \right)^{0.10} h_n. \tag{5.92}$$

The stepsize and axial offset solutions using the 2-D controller of Equation 5.90 and the

modified I controller of Equation 5.92 are compared for the 3-D pin cell cycle model in Figure 5.65. The 3-D controller provides axial offset predictions with differences of less than 0.3% by the EOC.

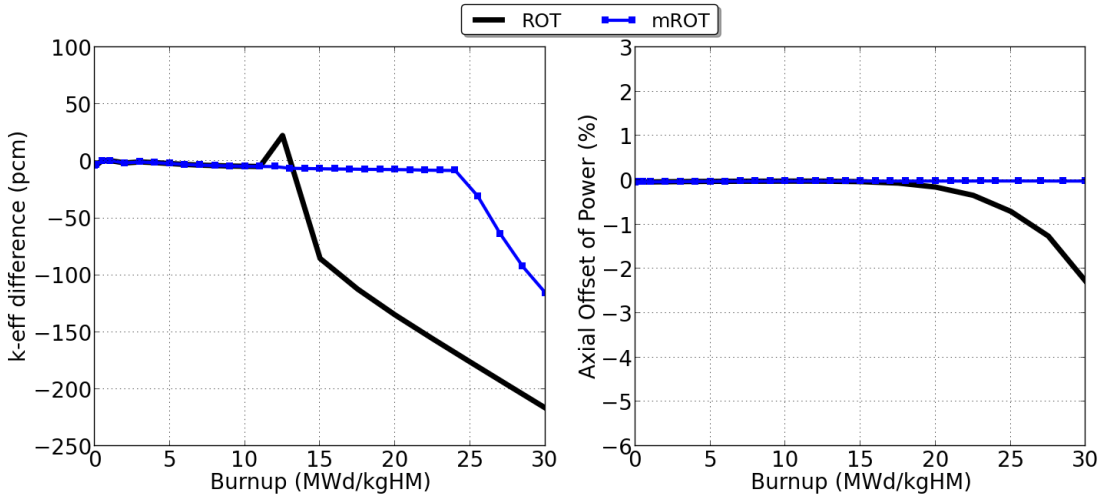


Figure 5.64: Comparison of multiplication factor error with respect to 0.01 MWd/kgHM stepsize reference (left) and axial offset of power (right) for original ROT and modified ROT stepsize sequence.

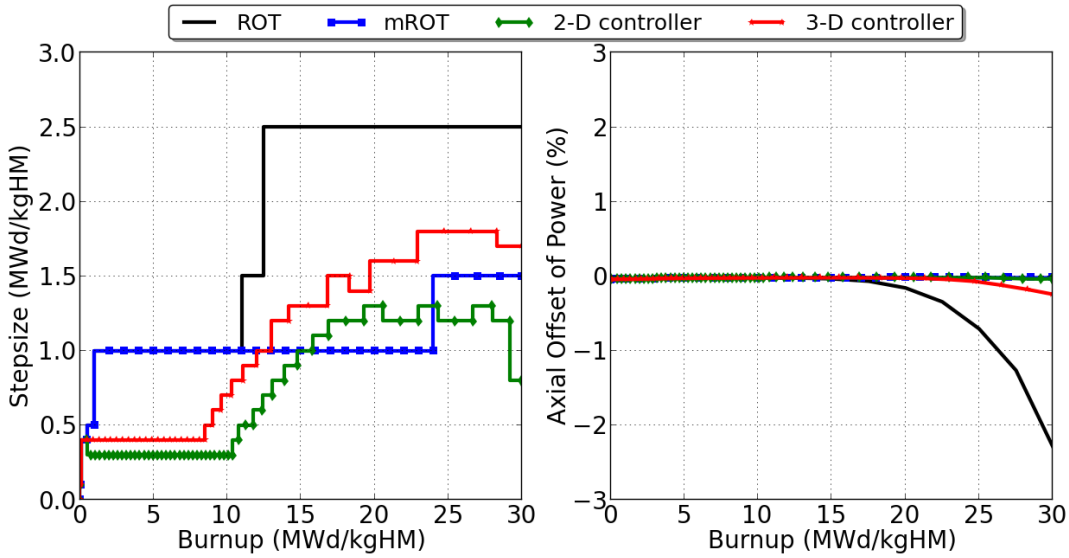


Figure 5.65: Comparison of 2-D and 3-D controller stepsize predictions (left) and axial offset of power (right) for 3-D pin cell cycle simulation; ROT and modified ROT included as well.

**CRUD deposition effects**

With a depletion stepsize controller parameterized for a 3-D pin cell containing fresh fuel, the effects of a neutron-absorbing CRUD deposit are investigated. Three temporal coupling methods for modeling CRUD deposition within a depletion cycle are considered: (i) a lagged approach, as shown in Figure 2.10, where the EOS CRUD data is fixed during the depletion calculation, (ii) a similar lagged approach, where the BOS CRUD data is used instead, and (iii) a predictor-corrector approach, where the BOS CRUD data is used on the depletion predictor step and the EOS CRUD data used on the depletion corrector step. For this comparison, a 3-D CRUD deposit containing boron hideout is precomputed in 1 day increments, and is then assigned within the neutronics mesh at each depletion step, i.e. a one-way coupling from MAMBA to DeCART is utilized. The CRUD deposition data from the 1.5 power model with fixed thermal hydraulic boundary conditions in Chapter III is used.

A fine step 0.1 MWd/kgHM (approximately 2 EFPD) solution utilizing the predictor-corrector method of modeling CRUD within neutronics/depletion is used as the reference solution. Then, for each coupling method, two stepsize sequences are compared: (i) the modified rule of thumb, and (ii) the predicted stepsize sequence when using the parameterized controller in Equation 5.92. The difference in the multiplication factor computed by the reference 0.01 MWd/kgHM stepsize solution (no CRUD) and the axial offset of the power distribution are the metrics used in the comparisons.

Figure 5.66 compares the output metrics when using the modified rule of thumb stepsize sequence. The larger stepsize of 1.5 MWd/kgHM toward the end of the depletion cycle is clearly too large to model a CRUD deposit with boron hideout. When using a predictor-corrector method to assign the CRUD composition within the neutronics domain, the power distribution dependence on the depletion stepsize is stronger; stepsizes on the order of 1.0 MWd/kgHM also appear to be too large and produce significant errors in the axial power distribution prediction.

The fluctuations in the 0.1 MWd/kgHM step reference solution of the axial offset are due to the dynamic nature of the CRUD deposition solution. Specifically, the spatial dependence of boron diffusion and precipitation within the CRUD directly affect the predicted power distribution within neutronics. Due to model size (single fuel rod), seemingly chaotic power shifts are not unrealistic because the CRUD distribution and composition is continuously

evolving. A larger model (assembly) would exhibit a smoother axial offset sequence because individual rod effects would be shadowed by the assembly-average behavior.

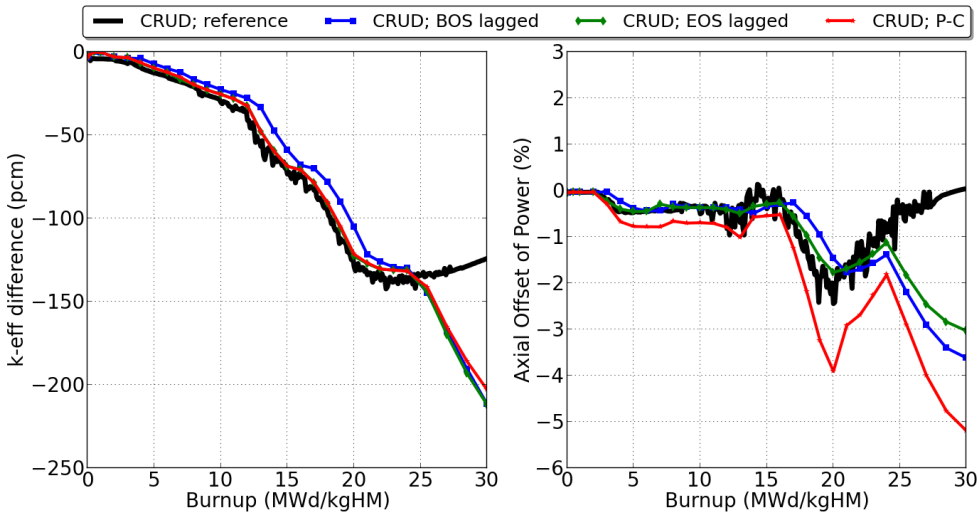


Figure 5.66: Multiplication factor error (left) and axial offset (right) comparison of temporal coupling approaches when modeling CRUD deposition within neutronics/depletion using the modified rule of thumb stepsize sequence.

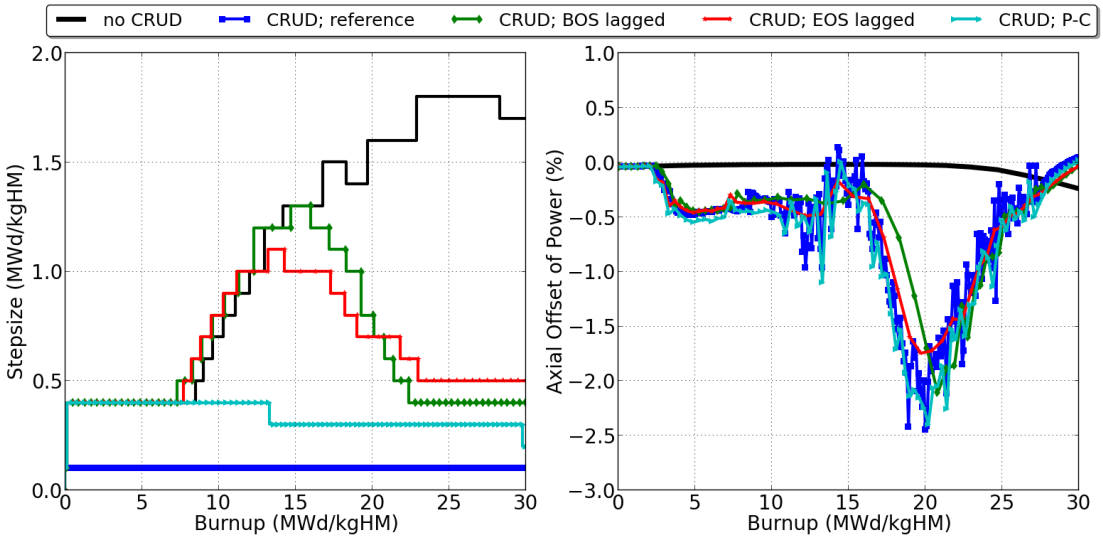


Figure 5.67: Comparison of predicted depletion stepsize (left) and axial offset (right) when using the 3-D stepsize controller for various temporal coupling approaches when modeling CRUD deposition within neutronics/depletion.

Figure 5.67 shows comparisons of the predicted depletion stepsize and the axial offset of the power when using the stepsize controller shown in Equation 5.92. When utilizing a predictor-corrector method for modeling the CRUD deposition, the predicted stepsizes are very small a relatively constant value of 0.3 to 0.4 MWd/kgHM throughout the cycle. Inclusion of two difference CRUD compositions, one on the predictor step and one on the corrector step, significantly affects the $L^2$ relative error norm of the flux distribution. On the other hand, using a lagged method with either the BOS or EOS CRUD composition fixed during the depletion step allows larger stepsizes, while maintaining solution accuracy; see Figure 5.67 (right). Therefore, a lagged approach, using the EOS CRUD composition, is adopted for the coupling of neutronics/depletion with CRUD deposition.

### 5.2.3 CFD and CRUD chemistry

The strong effect of the local thermal hydraulic boundary conditions on the CRUD deposition and boron hideout predictions has previously been demonstrated in Chapters III and IV; see Figures 3.33 and 4.51. Changes in the power distribution, due to fuel depletion and the presence of CRUD, directly affect the local cladding heat flux and coolant temperature conditions, calculated by CFD and conjugate heat transfer, which are provided to the CRUD solver.

Similar to the previous stepsize controller parameterizations for 2-D and 3-D neutronics/depletion calculations, a coupled stepsize controller is parameterized for 3-D CFD and CRUD chemistry calculations of a single fuel rod. A predictor-corrector temporal coupling approach, as shown in Figure 2.9, is utilized to enable error estimates. The boron mass is used as the control variable because it has been shown in previous chapters to be most sensitive to changes in the TH boundary conditions. The $L^2$ relative error norm of the boron mass, $m_B$, is used in the calculation of the error (per unit step) estimate,

$$\hat{r}_{n+1} = \left(\frac{1}{h_n}\right)\sqrt{\frac{\sum_V (m_{B,n} - m^p_{B,n})^2}{\sum_V (m_{B,n})^2}}. \tag{5.93}$$

In Equation 5.93, the predictor boron mass, $m^p_B$ and the end of step boron mass, $m_B$, are utilized to control the coupled stepsize (frequency of updating the TH boundary conditions).

A previous parameterization used the relative change in the integral boron mass along the fuel rod [Walter et al., 2015a]; since, it has been determined that using the $L^2$ relative error norm provides better stepsize control. Only MAMBA cells that are present in both the predictor and corrector steps are included in the norm calculation.

Coupled CRUD/CFD stepsize controllers are investigated by using precomputed power distributions to drive the TH boundary condition evolution. As with the neutronics/depletion physics, an integrating controller performs well. A controller of the form,

$$h_{n+1} = \left( \frac{3 \times 10^{-6}}{\hat{r}_{n+1}} \right)^{0.10} h_n, \tag{5.94}$$

is suggested for controlling the frequency of updating the TH boundary conditions within the CRUD solver. The 1.5 power level model using the stepsize controller in Equation 5.94 is simulated for the 500 day cycle. Figure 5.68 compares the stepsize controller solution to a 1 day reference solution for the predicted stepsize (left), boron mass (middle), and relative difference in boron mass (right). Based on the temporal coupling studies in Chapter IV, the stepsize controller behaves as expected. As boron precipitation begins, the coupled stepsize is reduced by about an order of magnitude from 25 to 2 days to sufficiently capture the chemical reaction dependence on the thermal hydraulic boundary conditions.

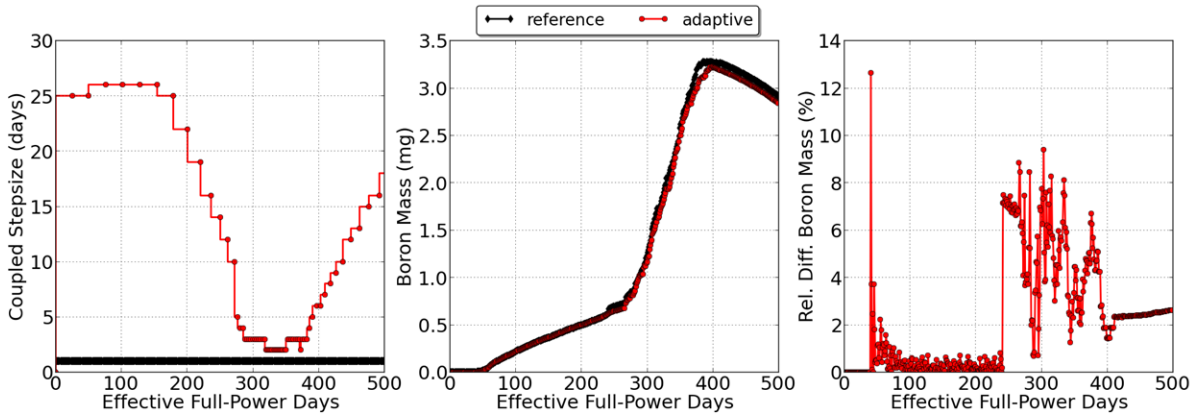


Figure 5.68: Coupled CRUD/CFD stepsize (left), integral boron mass (middle), and difference from 1 day reference (right) for 1.5 power level model.

### 5.2.4 Rendezvous scheme

Separate adaptive stepsize controllers have been developed to control the coupled solution during high fidelity multiphysics CRUD deposition simulations. Essentially, there are two stepsize controllers that must be synchronized:

1. coupled neutronics and depletion,
2. and coupled CFD and CRUD deposition.

An explicit stepsize controller between neutronics and CRUD deposition is not necessary because the power distribution predicted by neutronics is provided to the CFD and conjugate heat transfer solver. Therefore, the stepsize controller for the coupled CFD and CRUD deposition solution accounts for changes in the power distribution through the changing TH conditions (due to nuclide depletion and CRUD/boron deposition).

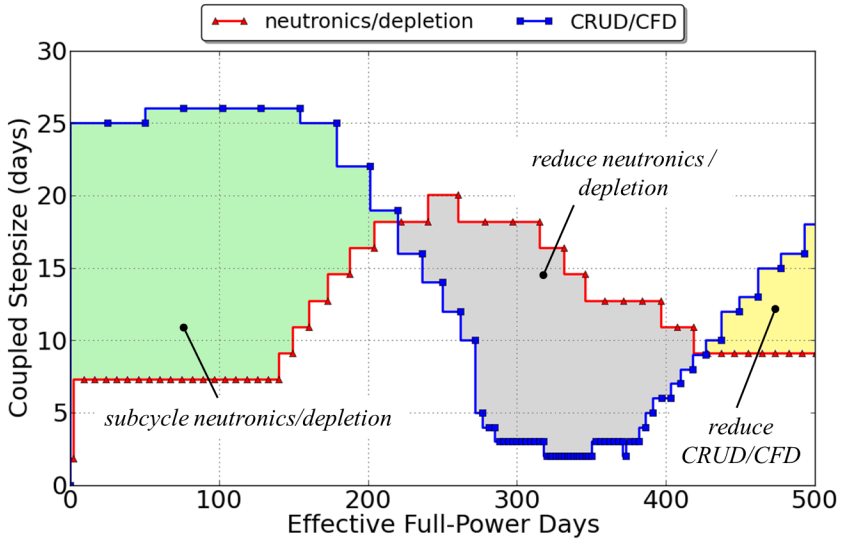


Figure 5.69: Coupled stepsize predictions for neutronics/depletion and coupled CRUD/CFD using their respective controllers for 1.5 power level model.

A useful strategy relevant to the development of a rendezvous scheme is *subcycling*, which was utilized by [Valli et al., 2008] and [Miller et al., 2013]. Subcycling refers to the process of taking smaller time steps with one physics and synchronizing the data exchanges with larger

steps taken by another physics. The term *multicycling* is also used, referring to multiple levels of subcycling, e.g. three coupled physics where physics A is subcycled with respect to physics B and physics B is subcycled with respect to physics C.

The stepsize sequence during the cycle for two separate (previously completed in Subsections 5.2.2 and 5.2.3) simulations are compared in Figure 5.69. One simulation is a depletion calculation that utilizes precomputed CRUD deposit compositions (from Figure 5.67); the other simulation is a coupled CRUD deposition and CFD calculation that utilizes precomputed power distributions (from Figure 5.68).

Consider two rendezvous approaches; the first, and the simplest, takes the smaller of the two stepsizes to use as the next stepsize for both of the physics. Using this method, the coupled stepsize is not optimal, thus the computational expense is not minimized. The second approach utilizes subcycling of the physics with smaller stepsizes with respect to the other physics; then, the two physics are synchronized at the points in time corresponding with the coarser time stepsizes. Such a subcycling approach minimizes the computational expense.

Two conclusions regarding the coupled physics of neutronics/depletion and CRUD/CFD have previously been drawn:

1. the power distribution evolution with depletion directly impacts the CRUD deposition calculations through the TH boundary conditions,
2. and the presence of CRUD deposits within the neutronics model produces significant feedback to subsequent CRUD predictions through changes in the power distribution (and TH boundary conditions).

These facts affect the rendezvous scheme in the following ways:

- despite a predicted depletion stepsize that is larger than the CRUD/CFD stepsize, the depletion stepsize should be reduced to capture the power evolution required by the TH boundary condition updates,
- and despite a predicted CRUD/CFD stepsize that is larger than the depletion stepsize, the CRUD/CFD stepsize should be reduced to sufficiently capture the neutronics effects due to CRUD deposition.

One caveat to the latter point is that toward the beginning of the cycle, little to no CRUD deposits exist; therefore, the feedback through the neutronics is negligible for a period of time and subcycling the neutronics/depletion with respect to the CRUD/CFD is utilized. Figure 5.69 illustrates the times during the cycle when subcycling or reduction of one of the physics' time stepsizes is utilized (in the present model).

The CRUD/CFD time state is synchronized with the depletion time state once the depletion time exceeds the CFD/CRUD time. For example, at synchronized time $t_n$, the depletion stepsize $h_{n+1}^{depl}$ is predicted (using $n-1$ to $n$ information), and the end of the next depletion step is $t_{n+1}^{depl}$,

$$t_{n+1}^{depl} = t_n + h_{n+1}^{depl}. \tag{5.95}$$

Similarly, the CRUD/CFD stepsize $h_{n+1}^{CRUD}$ is predicted, and the end of the next CRUD step is $t_{n+1}^{CRUD}$, where,

$$t_{n+1}^{CRUD} = t_n + h_{n+1}^{CRUD}. \tag{5.96}$$

In this approach, it is a requirement that,

$$t_{n+1}^{depl} > t_{n+1}^{CRUD}, \tag{5.97}$$

and synchronization of the CRUD/CFD solution occurs on the coupled corrector step by extending the CRUD/CFD stepsize to,

$$\tilde{h}_{n+1}^{CRUD} = h_{n+1}^{CRUD} + (t_{n+1}^{depl} - t_{n+1}^{CRUD}). \tag{5.98}$$

Using the modified CRUD/CFD stepsize, the end of the next step is now the same for both physics,

$$t_{n+1} = t_{n+1}^{depl} = \tilde{t}_{n+1}^{CRUD}. \tag{5.99}$$

This synchronization method relies on the assumption that,

$$(t_{n+1}^{depl} - t_{n+1}^{CRUD}) \ll h_{n+1}^{CRUD}; \tag{5.100}$$

regardless, a temporal inconsistency is introduced, where the predictor and corrector end-of-step times are different for the CRUD/CFD model. The dominant effect of this inconsistency is on the CRUD/CFD stepsize controller, which is parameterized for a boron mass tolerance according to temporally consistent predictor and corrector solutions. To address this issue, the end-of-step ($t_{n+1}$) corrector solution is not used in the CRUD/CFD stepsize prediction, rather the corrector step solution at $t_{n+1}^{CRUD}$ is used to generate $h_{n+2}^{CRUD}$, so that,

$$t_{n+2}^{CRUD} = t_{n+1} + h_{n+2}^{CRUD}. \tag{5.101}$$

In this way, the fact that the CRUD deposition solution is computed on a shorter time scale within MAMBA is leveraged.

Other coupling effects due to the aforementioned temporal inconsistency are negligible provided boron precipitation is not occurring. As with the stepsize controller, the $L^2$ relative error norm of the boron mass is used to indicate when to cease the neutronics/depletion subcycling and begin reducing the CRUD/CFD stepsize to that of the depletion stepsize. Currently, a tolerance of $5x10^{-6}$ is used.

## 5.3 Coupled 3-D fuel rod cycle simulation

A single pin cell 500-day cycle simulation with automated and adaptive coupled stepsize selection is performed in this section. The multiphysics model includes CRUD deposition and all of the associated feedback mechanisms suggested within the high fidelity framework.

Figure 5.69 compares the predicted stepsize sequence, where, toward the beginning of the cycle, the neutronics/depletion is subcycled with respect to the CRUD/CFD time stepping. The CRUD/CFD stepsize exhibits minor oscillations due to the rendezvous scheme. Because boron precipitation is not occurring, the solution dependence on the temporal coupling with thermal hydraulics is weak, and such stepsize oscillation is not a concern. Once the $L^2$ relative error norm of the boron mass exceeds $1 \times 10^{-6}$, the subcycling of DeCART is ceased;

this occurs at approximately 188 days in the present simulation. Subsequently, the minimum of the predicted stepsizes (from each of the two controllers) is used for the remainder of the cycle; see Subsection 5.2.4 for justification of this method.

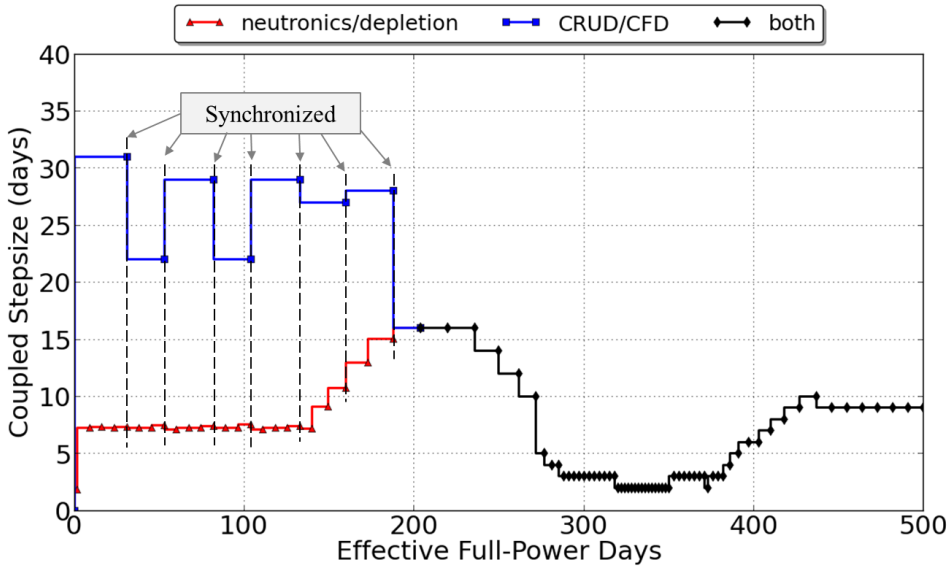


Figure 5.70: Coupled stepsize predictions for coupling neutronics/depletion and CRUD/CFD, where subcycling is utilized toward the BOC.

## 5.4 Chapter V conclusions

Leveraging predictor-corrector methods to provide an error estimate of a particular solution variable allows multiphysics convergence control through time stepsize predictions. Such an approach has been successfully applied to multiphysics CRUD deposition models, where stepsize controllers for neutronics/depletion and CFD/CRUD deposition were parameterized for a single 3-D fuel pin cell. Additionally, time stepsize controllers were parameterized for 2-D lattice depletion models containing both fresh fuel and burnable absorbers in the form of IFBA and gadolinium. Optimizing the coupled stepsize sequence minimizes the computational expense without sacrificing solution accuracy. Several benefits of an automated and adaptive depletion stepsize algorithm are realized:

- consistent accuracy of neutron flux solution,

- efficient burnable absorber design optimization,
- modeling changes in core power, e.g. load following,
- and balancing solution accuracy and computational expense of 3-D neutron transport with other coupled physics.

Depletion of a high power fuel rod showed that a typical depletion stepsize sequence was not sufficient, and the axial power distribution was incorrectly calculated. Despite accurate multiplication factor predictions, depletion stepsizes exceeding 1.8 MWd/kgHM introduced axial offset errors of more than 2%. Errors on this order are significant from a CRUD induced power shift standpoint. Moreover, the introduction of a boron-containing CRUD deposit within the neutronics model demanded a smaller depletion stepsize to maintain accurate axial offset predictions. Specifically, the number of necessary depletion steps within a 30.0 MWd/kgHM cycle increased from 39 to 54 with the presence of CRUD.

Combining adaptive stepsize controllers for neutronics/depletion and CRUD/CFD resulted in a globally adaptive temporal coupling between the physics present in this modeling framework. Subcycling the neutronics/depletion calculations with respect to the CRUD/CFD calculations toward the beginning of the cycle minimized the computational expense without sacrificing the coupled solution accuracy. Understanding the strength of the feedback mechanisms between the physics was necessary to optimize the time stepping algorithm.

# CHAPTER VI

# Seabrook plant comparison

## 6.1 Plant background

Seabrook Unit 1 is a pressurized water reactor located in New Hampshire and has been operational since 1990. Cycle 5 began in December 1995 and was identified as an *aggressive* core design when compared to previous cycles; an increased cycle length and higher rod powers were two contributing factors. The core was demonstrating CIPS with a maximum axial offset of approximately -3.3% by 260 EFPD. Soon after, fuel failures were detected; details of these failures are discussed in the following subsection.

### Failed fuel rods

Around 350 EFPD, the first fuel failures were detected in cycle 5 of the Seabrook plant. A total of five failed rods, all of which neighbored guide thimbles and contained IFBA, were discovered. The failed rods belonged to four distinct feed assemblies, each containing IFBA rods in the 128 pattern. Figure 6.71 (top) shows the core layout and assembly identifiers; the four fuel assemblies containing the failed rods are identified: G63 with rod K12, G64 with rod E12, G69 with rod M14, and G70 with rods G9 and L7. Note the symmetry in the core locations of the failed fuel assemblies. The bottom image of Figure 6.71 details the G70 rod layout with the 5x5 pin array identified, which will be used as the modeling domain in this chapter. The sub-assembly contains one failed fuel rod, designated as rod 8 in this analysis.

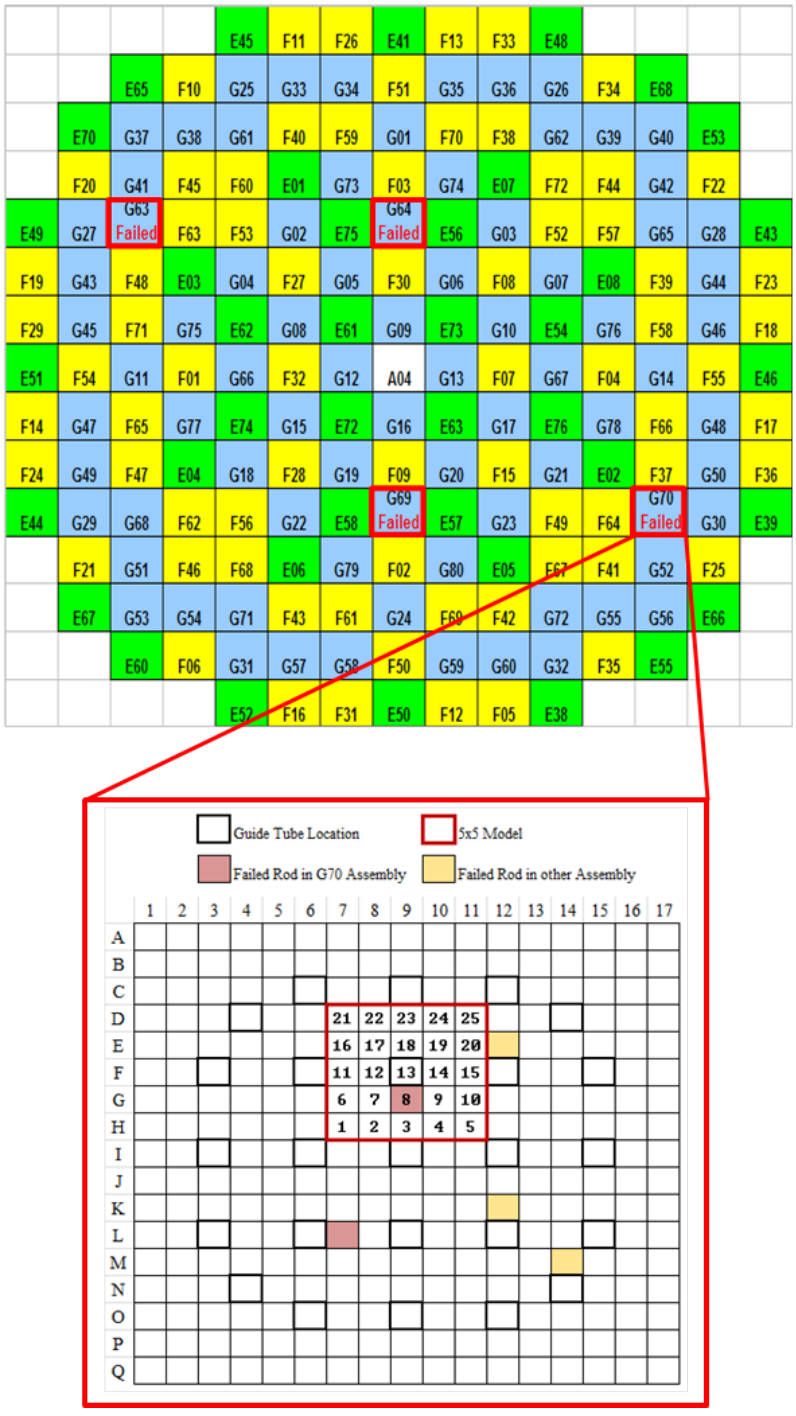


Figure 6.71: Seabrook cycle 5 core layout with assembly G70 showing rod failures and 5x5 model location.

## Core conditions

Cycle 5 operated between December 1995 and May 1997; Figure 6.72 shows the power history, axial offset, and coolant pH during the cycle. The dissolved species within the coolant, including boron, lithium, and nickel concentrations were previously shown in Section 2.4 in Figures 2.12 and 2.13.

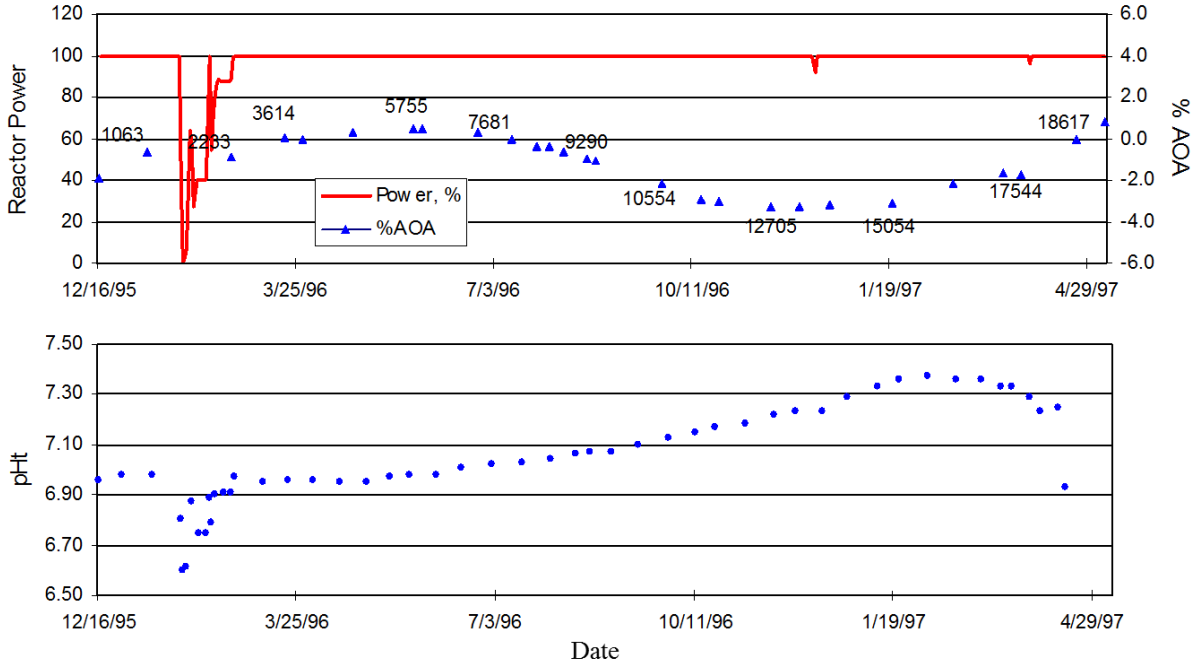


Figure 6.72: Seabrook cycle 5 core power and axial offset (top), and coolant pH (bottom).

The Seabrook core's nominal thermal power is 3,411 MW and consists of 193 assemblies, each with 264 active fuel rods. The core power density at the operating temperature is 102.87 $kW/cm^3$, corresponding to 338.27 $W/cm^3$of actual fuel power density. The failed fuel rods belonged to fresh fuel assemblies with a U-235 enrichment of 4.8 $w/o$.

Assembly G70 exhibited an average power peaking of more than 1.3 throughout the depletion cycle; Figure 6.73 (left) shows the evolution and Table 6.29 shows the rod powers at the BOC. The length of cycle 5 was 502 effective full-power days, corresponding to a core burnup of 19.242 MWd/kgHM. Figure 6.73 (right) shows the radially-integrated axial power

distributions for the assembly at select burnup states, as predicted by the nodal neutron diffusion code ANC. No radial or azimuthal variation of the power was provided by ANC.

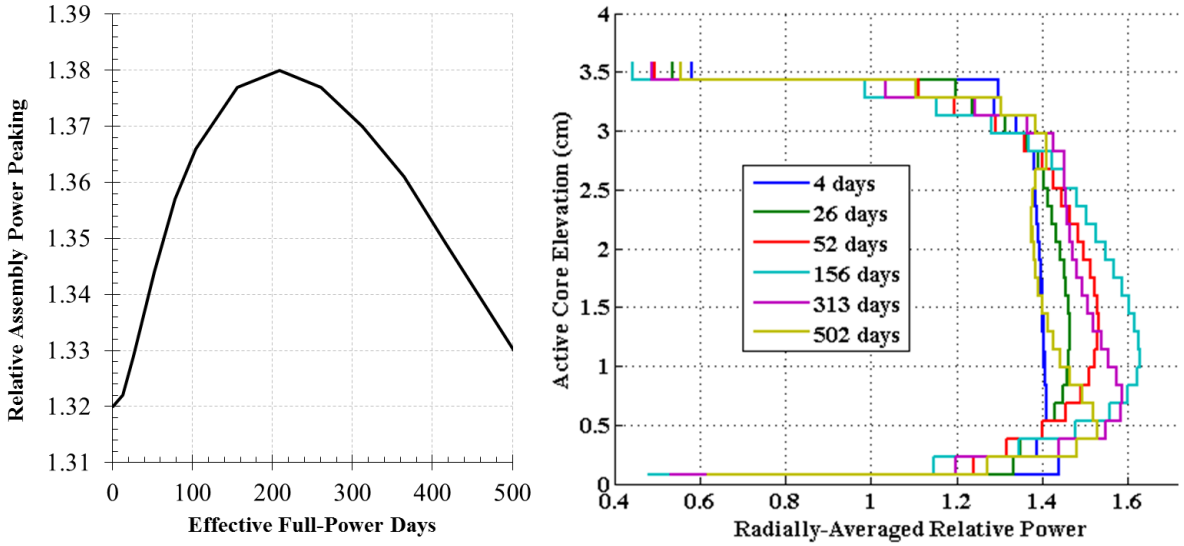


Figure 6.73: Power peaking (left) and axial power distributions predicted by ANC (right) for assembly G70 during cycle 5 of Seabrook plant.

Table 6.29: Normalized rod power distribution at beginning of cycle 5, Seabrook.

| | | | | |
|---|---|---|---|---|
| 1.354 | 1.285 | 1.401 | 1.279 | 1.341 |
| 1.308 | 1.361 | 1.336 | 1.353 | 1.293 |
| 1.423 | 1.339 | | 1.330 | 1.405 |
| 1.312 | 1.368 | 1.343 | 1.358 | 1.293 |
| 1.372 | 1.309 | 1.424 | 1.299 | 1.349 |

## Available corrosion data

Three types of data are available to use as validation of the multiphysics CRUD deposition model prediction capability:

1. CRUD samples obtained from rod scrapes,

2. visual examination to inform CRUD distributions,

3. and intact rod oxide measurements.

Measurements of the oxide thickness were performed on several failed and non-failed fuel rods [Secker, 2011]. These measurements were performed along the axial length of the rod and were repeated at several azimuthal locations. Azimuthal scans around the rods at a few selected axial heights were also performed. However, the CRUD analysis is mostly qualitative and is based primarily on visual examinations of the various faces of the rods in the upper spans (5-7) where CRUD was thickest.

Figure 6.74 shows the rod locations within each assembly where CRUD data was obtained; the assembly identifier is labeled, e.g. 63. Additional visual examinations that are not shown include, rod L7 in assembly G64, rod K12 in assembly G69, and rod G9 in assembly G69.

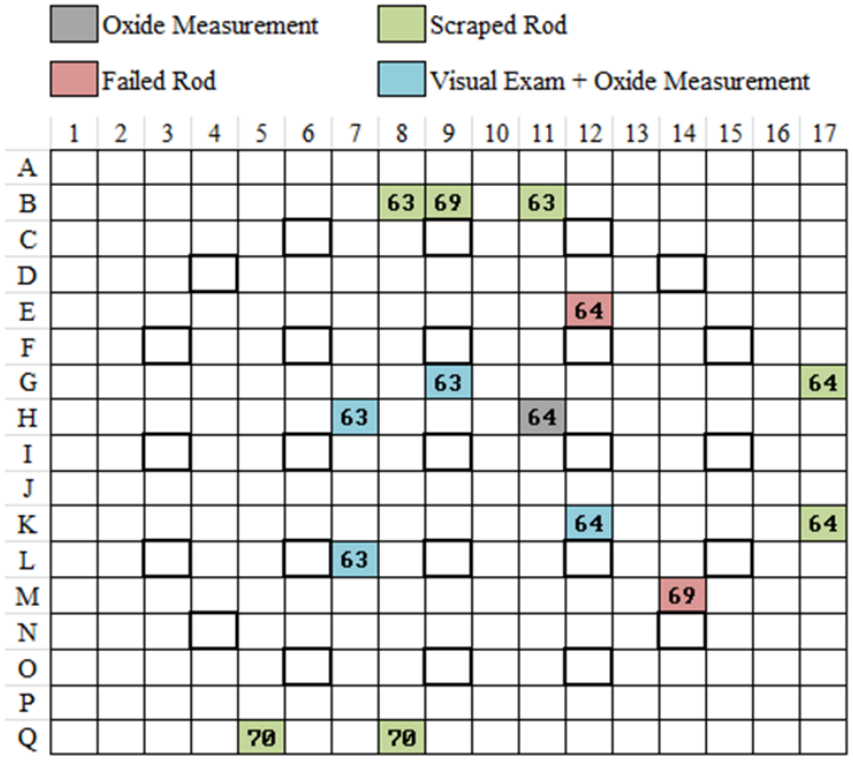


Figure 6.74: Fuel rods within Seabrook assemblies that provided CRUD data in the form of an oxide measurement, a scraped sample, or a visual examination at the end of cycle 5.

## 6.2 Multiphysics model

As previously mentioned, the computational domain consists of a 5x5 rod array with one guide thimble at the center of the sub-assembly in the rod 13 position. The CFD model includes the full heated length of 365.76 cm of the fuel rods; three spacer grids with mixing vanes at axial locations of 217.944 cm, 270.144 cm, and 322.2344 cm are modeled. Due to incomplete specifications, the orientation of grids 5 and 7 in the CFD model were incorrectly rotated with respect to the actual grids in the Seabrook core; this modeling discrepancy is addressed in Subsection 6.3.4. The CRUD deposition is performed on a rod-by-rod basis using the thermal hydraulic boundary conditions extracted from the CFD solver.

Table 6.30: Coupled time steps for 5x5 CRUD deposition cycle simulation; based on ANC depletion steps and available power distribution data.

| Time step | Burnup (MWd/kgHM) | Time (EFPD) | Stepsize (EFPD) |
|---|---|---|---|
| 1 | 0.150 | 3.91 | 3.91 |
| 2 | 0.500 | 13.0 | 9.09 |
| 3 | 1.00 | 26.1 | 13.1 |
| 4 | 2.00 | 52.1 | 26.0 |
| 5 | 3.00 | 78.2 | 26.1 |
| 6 | 4.00 | 104 | 25.8 |
| 7 | 6.00 | 156 | 52.0 |
| 8 | 8.00 | 209 | 53.0 |
| 9 | 10.0 | 261 | 52.0 |
| 10 | 12.0 | 313 | 52.0 |
| 11 | 14.0 | 365 | 52.0 |
| 12 | 16.0 | 417 | 52.0 |
| 13 | 19.2 | 502 | 85.0 |

The cycle simulation is completed via a lagged coupling of the CRUD deposition and computational fluid dynamics physics, where precomputed (radially- and azimuthally-uniform) power distributions are provided to the CFD model at each depletion state point accord-

ing to the ANC data points; see Table 6.30. Figure 2.8 (left) in Section 2.3 illustrates this method of loose temporal coupling; the end-of-step CRUD distribution in the form of a thermal resistance is provided to the thermal hydraulics solver. A tighter coupling, such as a predictor-corrector approach, with smaller coupled stepsizes is not necessary because boron precipitation is not predicted due to insufficient rod power (and heat flux). No tuning of the multiphysics model to the Seabrook plant is performed, i.e. the simulation is performed *blind* without prior access to the plant CRUD data.

A second cycle simulation is completed to assess the effects of azimuthal power variations on CRUD deposition predictions. Because ANC is unable to provide radial or azimuthal distributions of the power, azimuthal variations predicted by DeCART are applied to the axial power distributions for each fuel rod. Refer to Figure 3.40 in Subsection 3.5.3 of Chapter III for details of the normalized azimuthal power variation within a 5x5 pin array with a central water rod.

## 6.3 Cycle predictions

### 6.3.1 Thermal hydraulic characteristics

To illustrate the complex flow patterns induced by the spacer grid mixing vanes, the strong spatial dependence of the cladding temperature is shown in Figures 6.75, 6.76, and 6.77.

In Figure 6.75, the azimuthal variation of the cladding surface temperature is shown for three axial locations in the vicinity of the first space grid modeled. Upstream of the vanes, the variation is due to asymmetric cooling from the square subchannel. Downstream of the vanes, an asymmetric flow swirl develops due to differing vane orientations on the present (rod 8) and surrounding rods. Refer to Figure 7.96 in Appendix A for exact location and orientation of each mixing vane. The seemingly random cladding temperature distribution in the axial and azimuthal directions is shown for all 24 fuel rods in Figure 6.76. Again, the specific orientations of the vanes drives the heat removal rate and subsequent temperature distribution. At an elevation of 312 cm, the azimuthal distributions are extracted and shown in Figure 6.77.

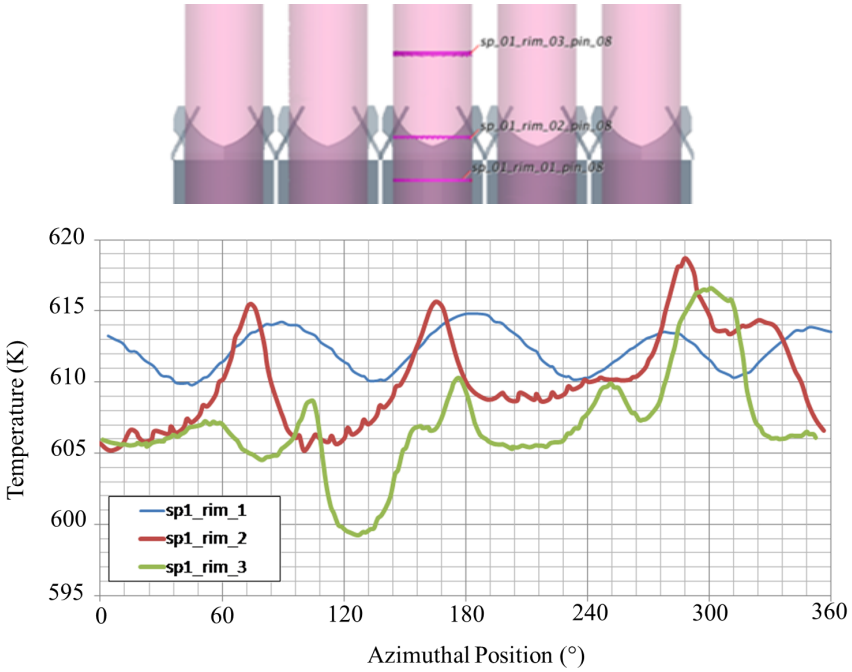


Figure 6.75: Azimuthal distribution of outer cladding temperature for rod 8 near spacer grid 5 (first grid axially in model) at BOC, Seabrook.

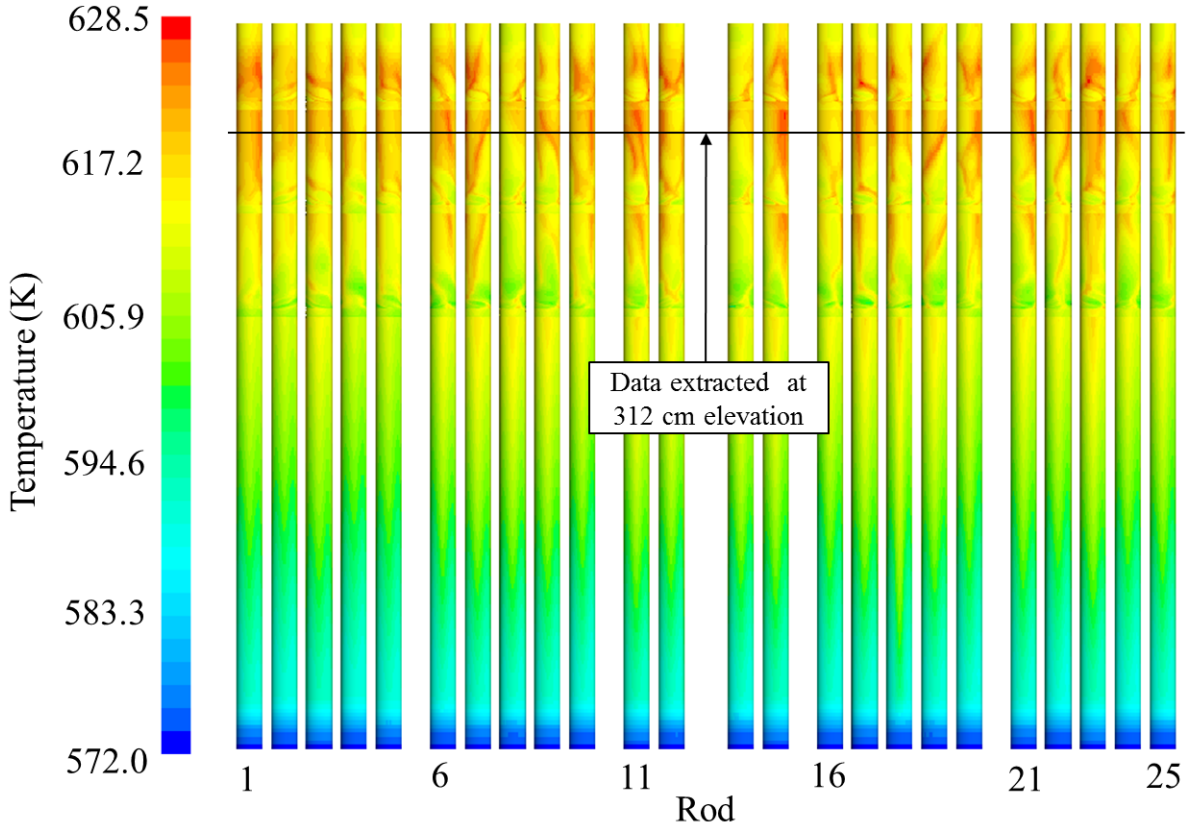


Figure 6.76: Outer cladding temperature on all fuel rods at BOC, Seabrook; 312 cm elevation labeled.

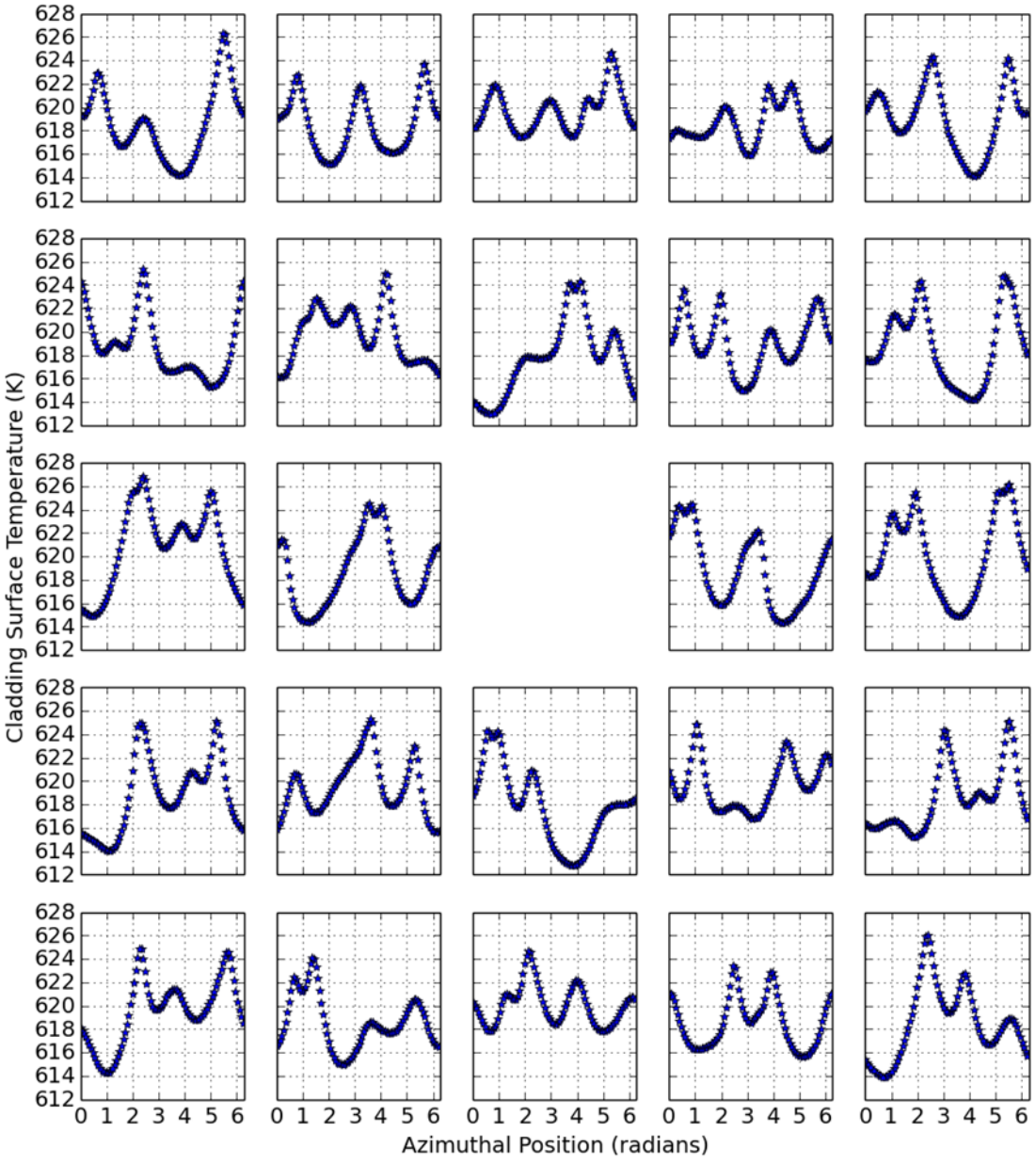


Figure 6.77: Outer cladding temperature at an elevation of 312 cm for each pin within sub-assembly of Seabrook model.

### 6.3.2 CRUD characteristics

In agreement with the plant data, there is no correlation for CRUD deposits preferred orientation with the location of the water rod, as the highest CRUD thicknesses are not necessarily observed on the rod faces adjacent to the water rod. For example, in Figure 6.78, although rod 8 is facing the water rod, it exhibits maximum CRUD thickness on the opposite face. Moreover, rod 8 has a higher power than rod 12 (see Table 6.29), despite a higher accumulated CRUD mass on rod 12. The conclusion in Chapter III that the local thermal hydraulic properties, resulting from the mixing vanes, drive the CRUD deposition distribution is reconfirmed in the present analysis. Regarding the effect of rod power level on boron precipitation, none of the rod powers are sufficient to cause boron precipitation during the 500 day cycle simulation of the Seabrook sub-assembly.

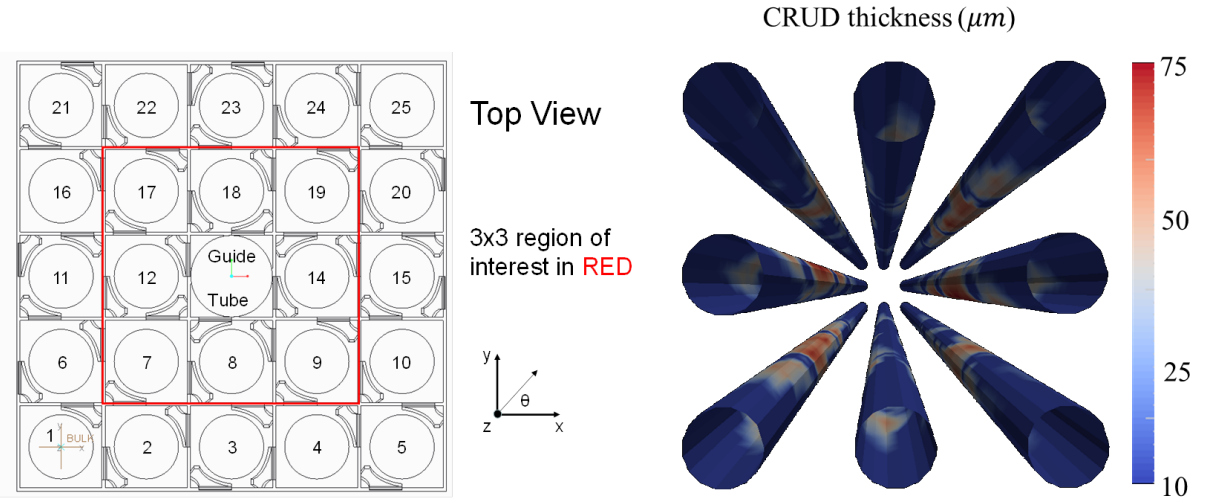


Figure 6.78: 3x3 pin array region of interest (left), and CRUD thickness distribution at the EOC (right) for Seabrook model.

Additional 3-D perspective plots of the eight rods neighboring the guide tube are shown in Figure 6.79. The swirling CRUD patterns in the upper spans are clearly visible and are correlated with the locations of the spacer grids. Figure 6.80 shows the integral CRUD mass for each fuel rod; the rods within the 3x3 region are separated from all other rods in the 5x5 array. A small jump in the mass accumulation rate is observed at 50 EFPD, due to a

temporary spike in the coolant nickel concentration (see Footnote 4), induced by a reactor shutdown and subsequent extended operation at reduced power.

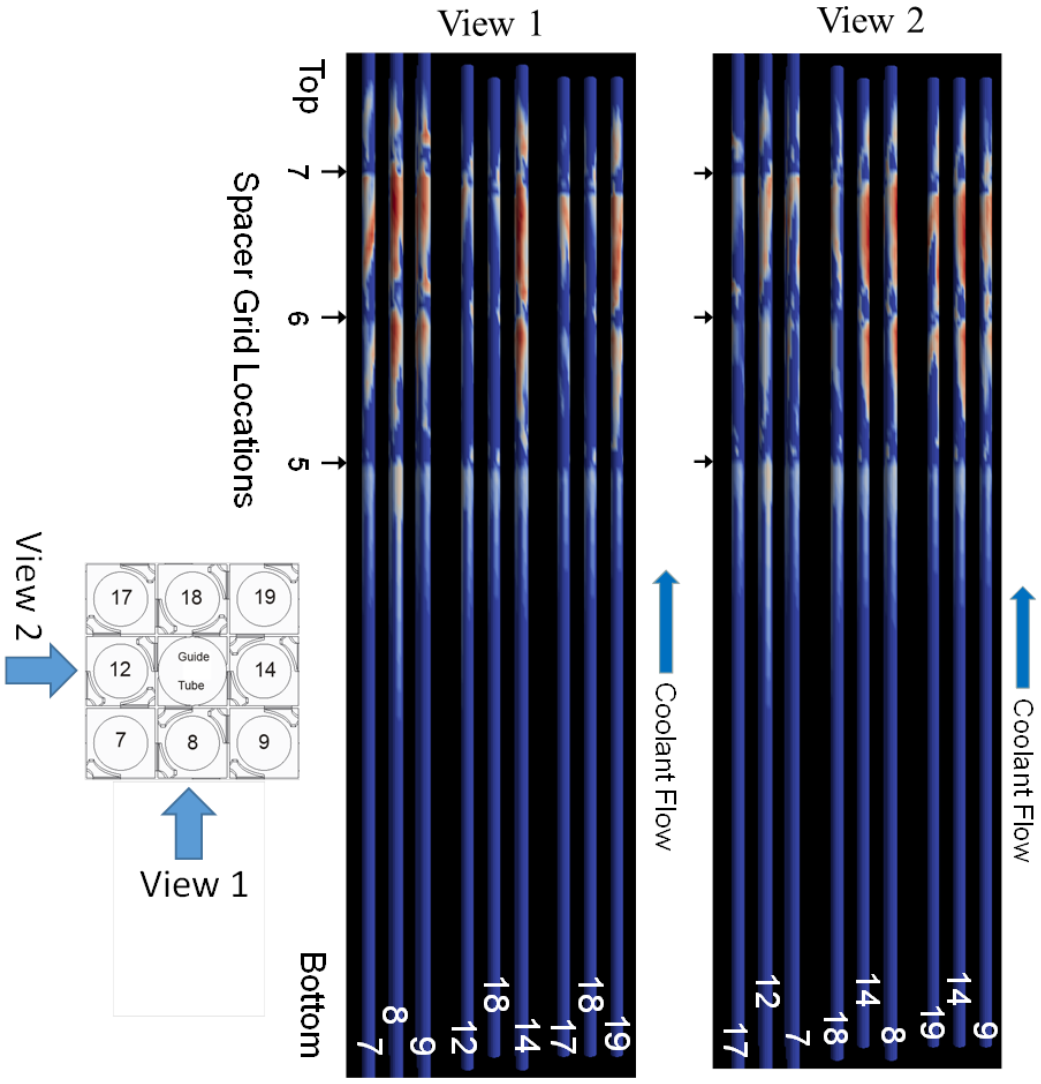


Figure 6.79: Predicted CRUD thickness on the nine fuel rods neighboring guide tube at EOC, Seabrook.

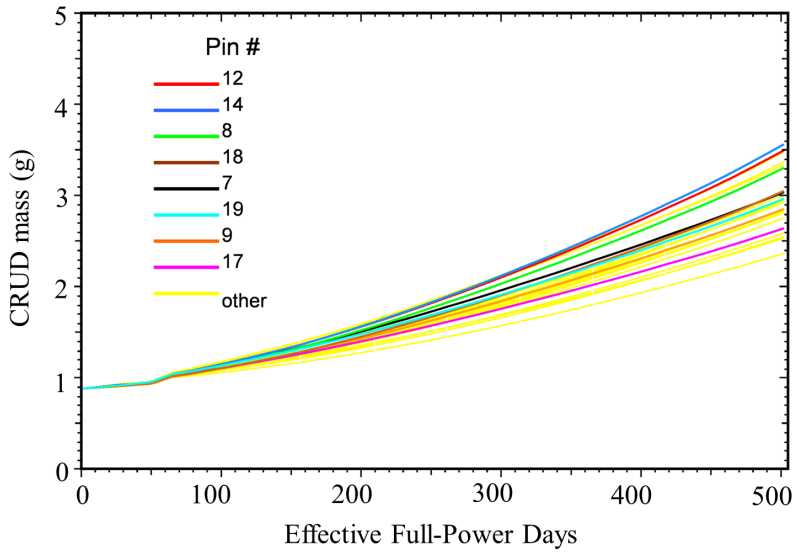


Figure 6.80: Predicted total CRUD mass on rods surrounding guide tube and all other rods during cycle 5 of Seabrook.

### 6.3.3 Azimuthal power variation

The azimuthally-uniform power distributions provided by ANC are modulated using normalized predictions by DeCART. In Figure 6.81, the effect of the azimuthal power variation on the outer cladding temperature is demonstrated. Differences on the order of a few degrees are predicted. Figure 6.82 shows the CRUD thickness in the azimuthal and axial directions for the cases with and without azimuthal power variation. Very minor differences in the distribution are predicted. Because boron precipitation is not occurring in this Seabrook model, the azimuthal power effect is negligible. This is consistent with the conclusion of Chapter III.

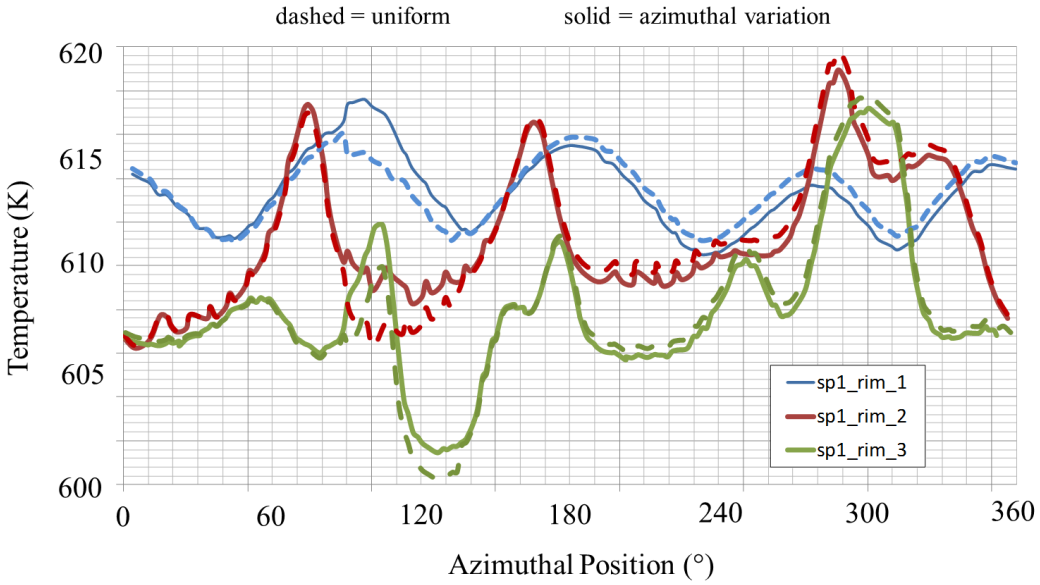


Figure 6.81: Effect of uniform and azimuthal power variation on the azimuthal distribution of outer cladding temperature for rod 8 near spacer grid 5 (first grid axially in model) at EOC, Seabrook.

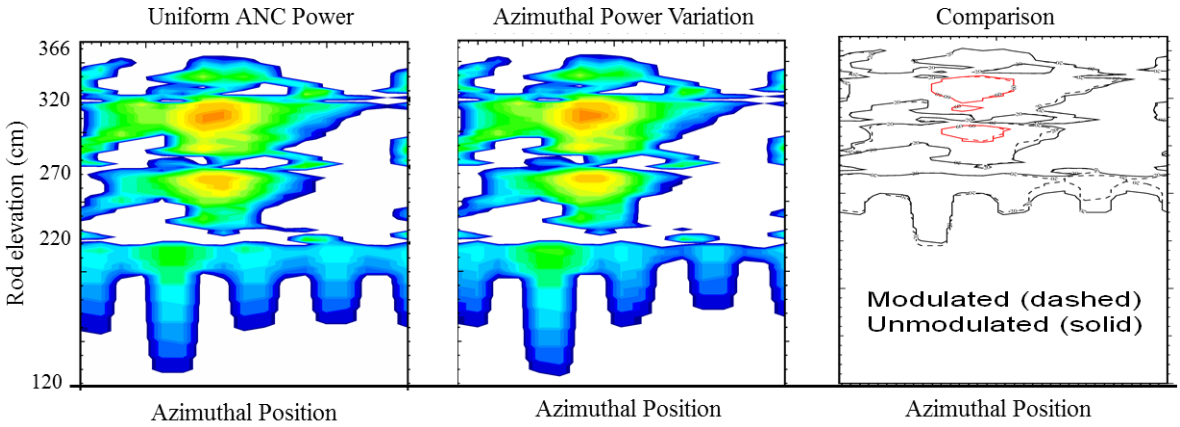


Figure 6.82: CRUD thickness predicted by MAMBA for rod 8 at EOC with and without azimuthal variations; comparison contour plot shows 60 $\mu m$ thickness in red and 20 $\mu m$ thickness in black.

### 6.3.4 Comparison with plant data

In this comparison of predicted CRUD deposits to the Seabrook plant data, the following rods are focused on:

- rod G9 in assembly G70,
- rod G9 from assembly G63
- and rod L7 from assembly G63,

where assembly G63 is the symmetric partner of assembly G70. The measured oxide thickness and MAMBA's computed CRUD thickness are compared, under the assumption that the thicker oxide layers ($> 75\,\mu m$) are most likely due to the presence of CRUD. Because there are no quantitative data on CRUD thickness, only a qualitative comparison can be made.

As previously mentioned, the orientations of grids 5 and 7 are different than those for grid 6, implying that the coolant flow patterns downstream of grid 5 and 7 will be different than downstream of grid 6. Even though the present simulation assumed the same mixing vane orientation for all three grids, initial comparisons to the plant data are possible by considering two different rods with the appropriate mixing vane orientation. Specifically, the vane orientation around rod 8 corresponds to the actual orientation of Seabrook's grid spans 5 and 6 for rod G9 in assembly G70. Moreover, the vane orientation around rod 12 (rotated by 90° into rod 8 position) corresponds to the orientation of Seabrook span 6 for rod G9.

The predicted azimuthally-averaged CRUD thickness distribution for rods 8 and 12 is compared in Figure 6.83 with the measured oxide thickness. The oxide thickness appears to correlate with the CRUD thickness; in particular, the valleys in the measured oxide thickness correspond to the top of the spacer grids, where the turbulent flow past the mixing vanes suppresses CRUD formation. The oxide and CRUD thickness are both highest in the hotter span 6, then decrease rapidly in span 7, where the heat flux is lower. Consistent with the plant data, no significant deposits are predicted at elevations below 200 cm. It should be noted that only eight azimuthal locations around the rod were measured, whereas 16 sectors are used in the MAMBA model. Additionally, the four spacer grids upstream of grid 5 were not included in the CFD model; therefore, the effects of grid 4 on the CRUD deposition are not included.

Figure 6.84 compares the oxide/CRUD thickness of rod G9 in assembly G63, which corresponds to rod 8 in the simulation model. The measured oxide thickness on this rod (at 0° in the measurement coordinate system) corresponds to an azimuthal location of 315° in the computation coordinate system. The correlation between the measured and predicted thickness distribution is excellent downstream of spacer grid 5. Upstream of grid 5 exhibits a large difference; however, neglecting spacer grid 4 in the CFD model is suspected to be the cause of the discrepancy. The predicted data at ±45° are shown in Figures 6.85 and 6.86, respectively. The measured data is the same in Figures 6.84, 6.85, and 6.86. Clearly, the CRUD pattern is strongly dependent on the azimuthal direction, and the first comparison showed at a consistent azimuthal location of 0° in Figure 6.84 shows exceptional agreement.

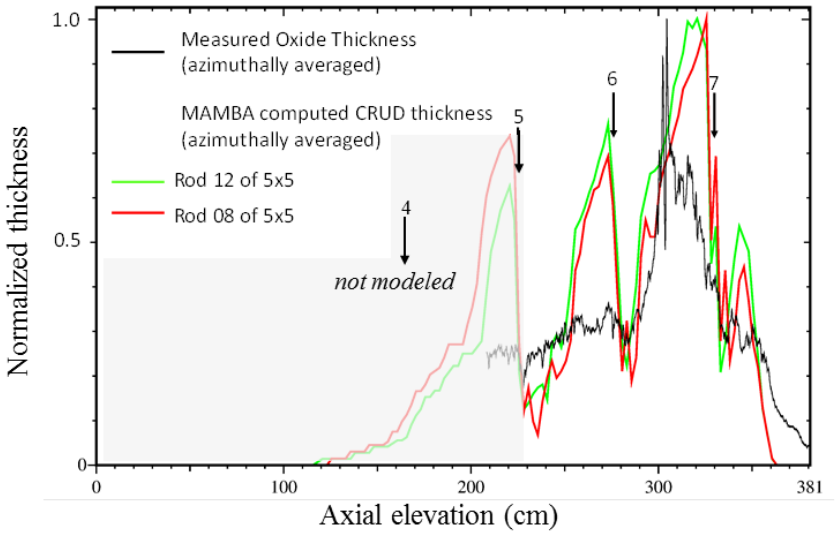


Figure 6.83: Normalized comparison of azimuthally-averaged oxide/CRUD thickness measurement along the height of rod G9 of assembly G70 and the rod 8 and 12 model predictions; grid 4 not included in CFD model.

In Figure 6.87, 2-D contour plots of the normalized CRUD thickness predicted by MAMBA and measured are compared. Because of the orientation error of grid 6 within the CFD model, only span 6 provides a consistent comparison with rod 12, and only spans 5 and 7 for rod 8. All three span comparisons correspond well, especially when focusing on the locations of highest oxide thickness measurement and highest CRUD thickness predicted. It should be noted that the measured data (as plotted in Figure 6.87) was limited to four angles for rod L7

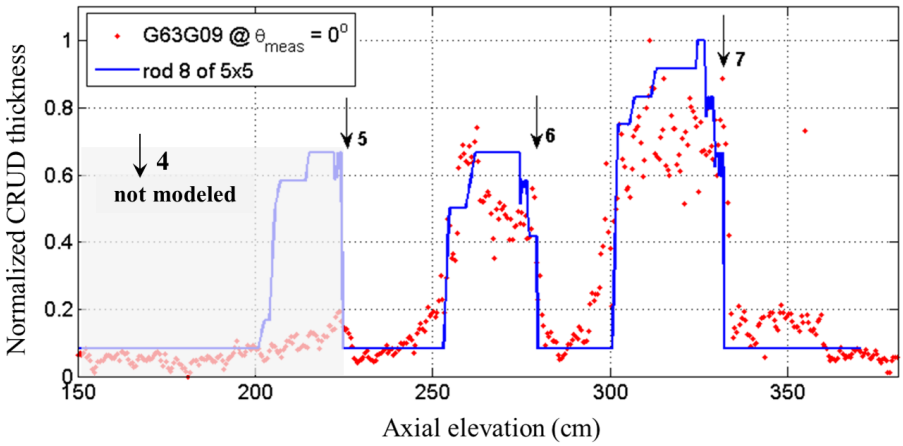


Figure 6.84: Normalized comparison of oxide/CRUD thickness along the height of rod at azimuthal location of 0° for predicted and measured data on rod G9 in assembly G63; grid 4 not included in CFD model.

in G63 and eight angles for rod G9 in G70, where as the MAMBA azimuthal discretization is 16 sectors. Due to the lower fidelity measurements, the azimuthal location of the maximum CRUD thickness within each span does not match exactly with the predictions.

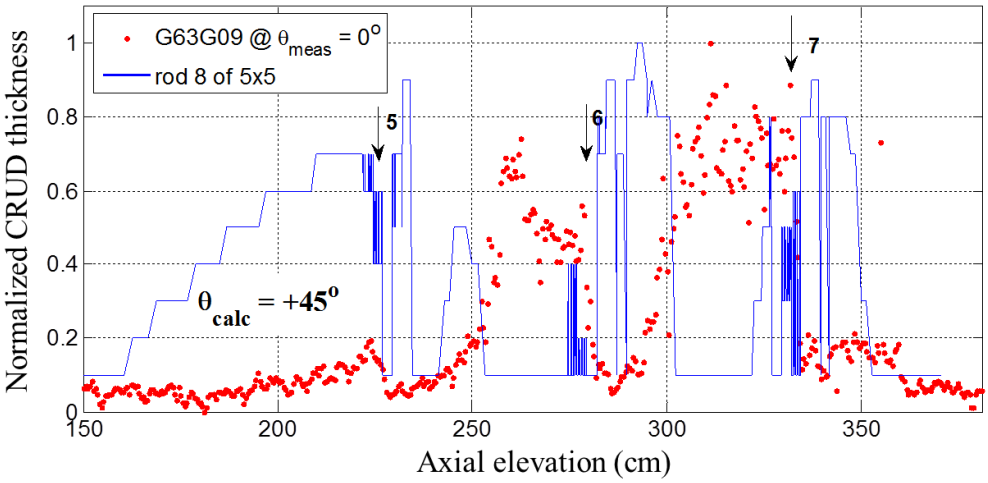


Figure 6.85: Normalized comparison of oxide/CRUD thickness along the height of rod at azimuthal location of 45° for predicted data and 0° for measured data on rod G9 in assembly G63.

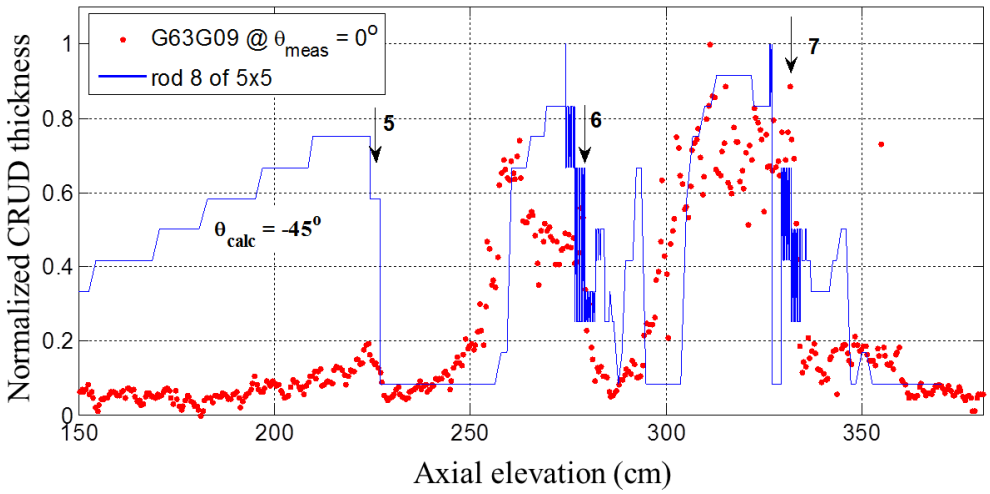


Figure 6.86: Normalized comparison of oxide/CRUD thickness along the height of rod at azimuthal location of −45° for predicted data and 0° for measured data on rod G9 in assembly G63.

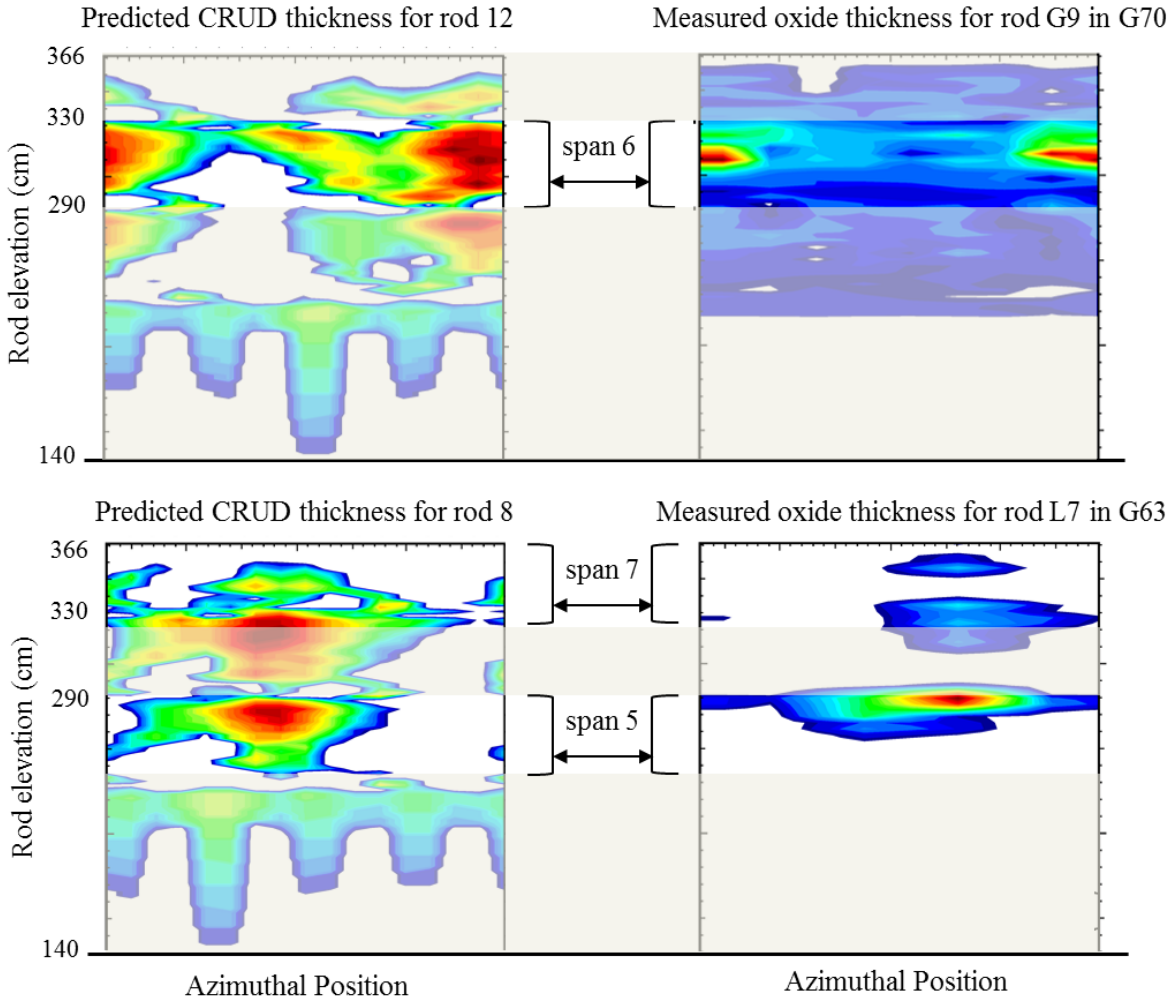


Figure 6.87: Normalized CRUD thickness predicted by MAMBA for rod 12 (top, left) compared to measured oxide thickness for rod G9 in assembly G70 (top, right); for rod 8 (bottom, left) compared to rod L7 in assembly G63 (bottom, right)

## 6.4 Chapter VI conclusions

The coupling of computational fluid dynamics and CRUD deposition physics via STAR-CCM+ and MAMBA has successfully reproduced local CRUD distributions as measured on fuel rods from cycle 5 of the Seabrook plant. No parameter optimizations were performed, and the simulations were completed prior to obtaining the plant data; thus, the agreement of the predicted and measured data is very encouraging.

In accordance with plant data, the thickest CRUD deposits do not necessarily correspond with the rods with the highest power; in fact, the dominant effect is that of the flow swirl induced by the spacer grid mixing vanes. It is concluded that to correctly predict the pattern of CRUD deposits, an accurate representation of the mixing vanes geometry and orientation is crucial. It has also been found that the mass evaporation flux and thick CRUD deposits are directly correlated. Therefore, computed mass evaporation flux maps can be used to aid in the optimization of spacer grid designs to minimize CRUD deposition.

It is noted that the rod powers (predicted by ANC and used in the coupled cycle simulation) were not high enough to result in sufficient heat flux to cause boron precipitation on any of the rods. Therefore, if the rod powers were uniformly increased to the level that would cause boron precipitation, then a greater dependence on the rod power would be revealed as demonstrated in Chapter III.

# CHAPTER VII

# Concluding remarks

## 7.1 Summary of dissertation

This dissertation details a physics-based framework for the high fidelity simulation of CRUD deposition on PWR fuel rods. The current industry-standard approach to CRUD simulation is incapable of modeling rod-level phenomena, including the identification of localized corrosion due to insulating corrosion deposits. Therefore, the coupling of higher fidelity 3-D computational tools including neutronics, nuclide depletion, fluid dynamics, heat transfer, coolant chemistry, and CRUD deposition kinetics has been established. This modeling framework has enabled significant research of the multiphysics nature of CRUD deposition, including parameter sensitivity studies of its CRUD structure property inputs, coupled boundary conditions, and plant conditions that impact corrosion product deposition.

Beyond the physics of CRUD deposition, the well-known issue of how to define the temporal discretization of loosely coupled physics is addressed through the use of control theory. First, a stepsize controller was parameterized for 2-D lattice depletion simulations; to the author's knowledge, automatic and adaptive depletion stepsize selection had previously not been researched. Then, the stepsize controller was modified for a 3-D single pin cell depletion model, where the effects of CRUD deposits within the neutronics/depletion physics were shown to impact the required stepsize. Specifically, the prediction of the axial power distribution, and axial offset value, were more sensitive to the depletion stepsize when CRUD deposits were present. A final stepsize controller was parameterized for coupled CFD and

CRUD deposition simulations, where the precipitation of boron drives the requirement for a tighter coupling between the two physics.

An initial validation of the modeling framework was completed by performing a blind simulation of a 3-D sub-assembly from the Seabrook plant. Comparisons with oxide thickness measurements showed excellent agreement. The spacer grid mixing vane locations and orientations were found to drive the distribution of the CRUD deposits.

## 7.2 Conclusions

If one conclusion is drawn from this dissertation, let it be that:

***The coolant flow patterns induced by the spacer grid and mixing vanes drive the CRUD deposition distribution through a strong spatial dependence of the heat removal rate and CRUD erosion rate.***

Furthermore, the most important conclusions drawn from each chapter are:

**III** The stand-alone inputs of particulate nickel concentration within the coolant and the CRUD porosity have the strongest correlation with the CRUD and boron hideout mass predictions.

**III** The rod power level and distribution, which evolve with fuel depletion, are coupled with the local thermal hydraulic boundary conditions provided to the CRUD deposition solver and strongly influence the boron precipitation rate.

**IV** Accurate prediction of boron precipitation is necessary to accurately predict both CIPS and CILC; specifically, with respect to CILC, as the CRUD pores fill with precipitates, convective heat removal is reduced and the CRUD's thermal resistance increases.

**IV** The strongest feedback mechanism results from the shifting of the power within the neutronics by changing the thermal hydraulic boundary conditions utilized by the CRUD deposition solver.

**V** An adaptive time stepping algorithm that leverages predictor-corrector solutions to approximate the coupled convergence residual minimizes computational expense without sacrificing solution accuracy.

**VI** CILC predictions require high fidelity cladding and coolant information that is only available through detailed computational fluid dynamics calculations.

## 7.3 Proposed future work

The challenge of modeling CRUD deposition on fuel rods is significant, and much of the work presented in this dissertation can and should be expanded. In particular, three areas are identified that seem most important to furthering the modeling effort:

1. develop a benchmark based on experiments involving CRUD deposition on a heat generating rod that includes spacer grids and mixing vanes,
2. decrease computational expense of CFD by developing correlations for enhanced heat transfer and TKE (or shear stress) to be implemented within subchannel analysis codes,
3. and ensure consistency between fluid phase modeling within the CRUD deposit and outside the CRUD deposit.

With respect to the third area of research, a two-phase flow model within CFD is necessary for accurately modeling PWRs with subcooled boiling existing on the cladding surface (not just within the CRUD) and for modeling BWRs where significant boiling occurs throughout the core. In these cases, several modeling uncertainties arise, including (i) effects of cladding surface boiling on CRUD deposition and precipitation, and (ii) enhancement of boiling due to presence of CRUD. Currently, no quantitative information exists to validate such boiling effects on CRUD deposition.

## 7.4 A similar modeling application

Using a similar high fidelity modeling approach, initial simulations of cladding hydriding phenomena have been completed by coupling computational fluid dynamics and fuel performance. Similar to CRUD deposition, cladding hydriding is strongly dependent on local temperature distributions; therefore, most of the conclusions in terms of rod power, mixing vane effects, etc. are also applicable.

Outer cladding azimuthal temperature distributions from the 5x5 Seabrook model were extracted and provided to BISON as a Dirichlet boundary condition. Because cladding hydrogen migration and subsequent precipitation of hydrides is influenced by the local temperature gradient, detailed CFD calculations in the vicinity of spacer grid mixing vanes are necessary to enable accurate predictions. 7.88 illustrates the modeling results of rod 11 from the Seabrook sub-assembly with the cladding temperature (top), hydrogen in solid solution (bottom, left), and hydride distribution (bottom, right) predicted by BISON.

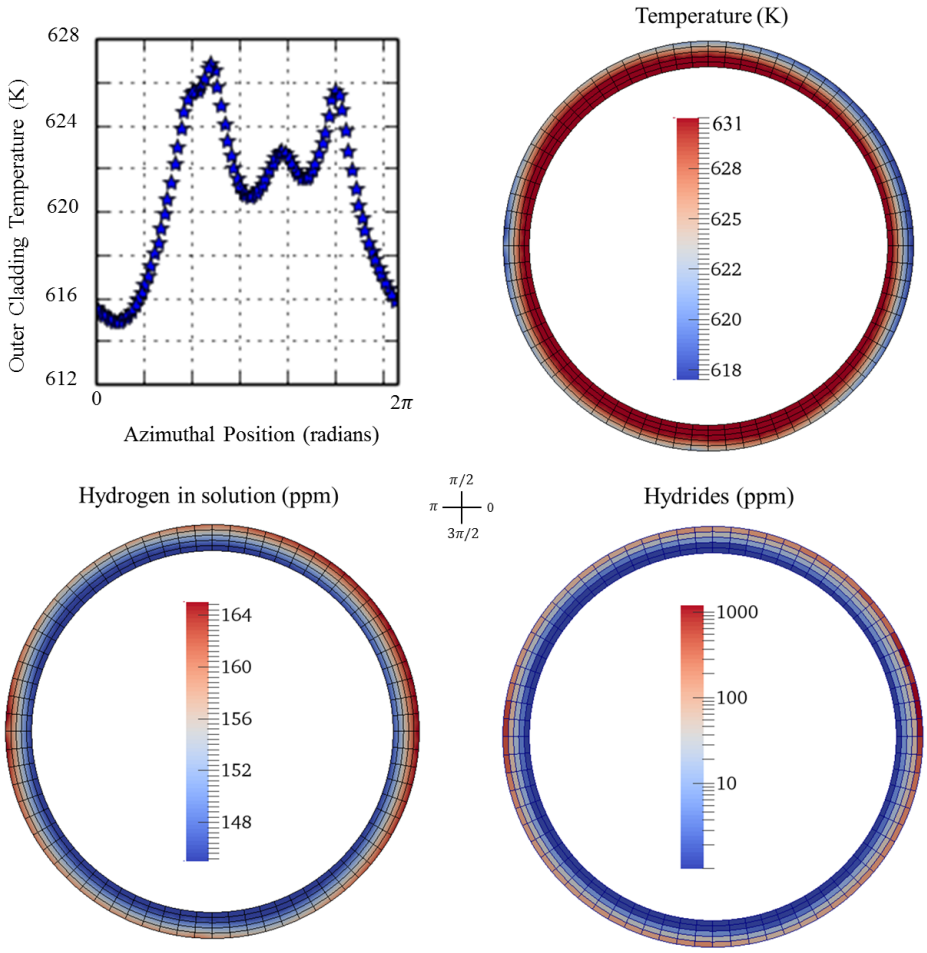


Figure 7.88: Outer cladding temperature on rod 11 of 5x5 at an elevation of 312 cm (top-left) predicted by STAR-CCM+, and BISON predictions for cladding temperature distribution (top-right), hydrogen in solution (bottom-left), and precipitated hydrides (bottom-right).

## 7.5 Publications resulting from this work

More than ten conference papers have resulted from the work reported in this dissertation. Four of those papers were expanded and published as journal articles.

### Journal articles

1. Walter, D. J., Kendrick, B. K., Petrov, V., Collins, B., Manera, A., and Downar, T. J., "Proof-of-principle of high-fidelity coupled CRUD deposition and cycle depletion simulations," *Annals of Nuclear Energy*, **85**, pp. 1152-1166 (2015)

2. Walter, D. J. and Manera, A., "CRUD, boron, and burnable absorber layer 2-D modeling requirements using MOC neutron transport," *Annals of Nuclear Energy*, **87**, pp. 388-399 (2016)

3. Petrov, V., Kendrick, B. K., Walter, D. J., Manera, A., and Secker, J., "Prediction of CRUD deposition on PWR fuel using a state-of-the-art CFD-based multi-physics computational tool," *Nuclear Engineering and Design*, in press, corrected proof (2016)

4. Walter, D. J. and Manera, A., "Adaptive burnup stepsize selection using control theory for 2-D lattice depletion simulations," *Progress in Nuclear Energy*, **88**, pp. 218-230 (2016)

### Conference proceedings

1. Walter, D. J., Collins, B., Petrov, V., Kendrick, B. K., Manera, A., and Downar, T. J., "High-fidelity simulation of CRUD deposition on a PWR fuel pin with grid spacers: a proof-of-principle using the fully-coupled MAMBA/DeCART/STAR-CCM+ code," NURETH-15 (2013)

2. Petrov, V., Kendrick, B. K., Walter, D. J., and Manera, A., "Impact of 3D spatial variations in fluid flow on the prediction of CRUD deposition in a 4x4 PWR subassembly," NURETH-15 (2013)

3. Bolesch, C., Walter, D. J., Manera, A., Petrov, V., and Kendrick, B. K., "Impact of thermal-hydraulic fidelity on the prediction of CRUD deposition on PWR fuel rods," ANS (2013)

4. LaFleur, B., Walter, D. J., and Manera, A., "Neutronic effects of nickel ferrite CRUD without boron hideout," ANS (2013)

5. Walter, D. J., Petrov, V., Franceschini, F., Manera, A., and Downar, T. J., "Impact of reactor physics parameters of 3D CFD vs. 1D T-H feedback for a 4x4 sub-assembly during depletion," TOPFUEL (2013)

6. Kendrick, B. K., Petrov, V., Walter, D. J., Manera, A., Collins, B., Downar, T. J., Secker, J., and Belcourt, K., "CASL multiphysics modeling of CRUD deposition in PWRs," TOPFUEL (2013)

7. Petrov, V., Kendrick, B. K., Walter, D. J., Manera, A., and Secker, J., "Prediction of CRUD deposition on PWR fuel using a state-of-the-art CFD-based multi-physics computational tool," CFD4NRS-5 (2014)

8. Walter, D. J., Petrov, V., and Manera, A., "Thermal hydraulic effects of 3-D power variations in a PWR fuel pin using CFD," ANS (2014)

9. Walter, D. J. and Manera, A., "CRUD and boron layer modeling requirements using MOC neutron transport," M&C (2015)

10. Walter, D. J. and Manera, A., "A control theory approach to adaptive stepsize selection for lattice depletion simulations," M&C (2015)

11. Walter, D. J., Petrov, V., Kendrick, B. K., and Manera, A., "A control theory approach to adaptive stepsize selection for coupled CFD and CRUD chemistry simulations," NURETH-16 (2015)

12. Walter, D. J., Kendrick, B. K., Petrov, V., and Manera, A., "Sensitivity of fuel rod CRUD deposition modeling: CRUD properties and boundary condition effects," PHYSOR (2016)

13. Walter, D. J., Petrov, V., Kendrick, B. K., and Manera, A., "Sensitivity of fuel rod CRUD deposition modeling: feedback effects of neutronics and thermal hydraulics," PHYSOR (2016)

# APPENDIX A
# Simulation models

## 2-D assembly

Three 17x17 fuel assembly 2-D models are used in DeCART to test the adaptive stepsize selection algorithm. The model descriptions are based on the CASL benchmark problems 2A, 2M, and 2P, which feature feed fuel without burnable absorbers, with a 10 μm IFBA layer, and with gadolinium-bearing fuel pins, respectively. The models are documented in detail within [Godfrey, 2012]. The full-length assembly power is fixed at 17.214 MW, which corresponds to a typical nominal operating power of a PWR assembly, or a core power of approximately 3,322 $MW_{th}$.

The 2-D neutron transport model domain consists of one fuel assembly with reflective boundary conditions featuring 264 fuel rods and 25 guide tubes. All material temperatures are constant at 600 K and the moderator density is 0.743 g/cm3 with a dissolved boron concentration of 1300 ppm. Figure 7.89 shows one quarter of the symmetric assembly with standard fuel pins shown in red and IFBA pins shown in light blue (left) and gadolinium pins shown in black (right).

The assembly models are verified using the reference multiplication factor and pin power solutions provided in [Godfrey, 2012]. The reference solutions were obtained with continuous energy (CE) KENO-VI [Hollenbach et al., 2004] using the ENDF-B-VII.0 library. Table 7.31 summarizes the reference solution comparisons. The difference in eigenvalue is attributed to using different cross section libraries; the reference solution is obtained using an ORNL library, while the DeCART simulations use the HELIOS 47-group library [Stamm'Ler, 2008], generated from ENDF/B-VII data.

Depletion calculation reference solutions were not provided within the benchmarks, so the cycle reference data was obtained using DeCART. A very fine burnup stepsize of 0.01 MWd/kgHM was used to generate the cycle reference solution for each of the lattice types.

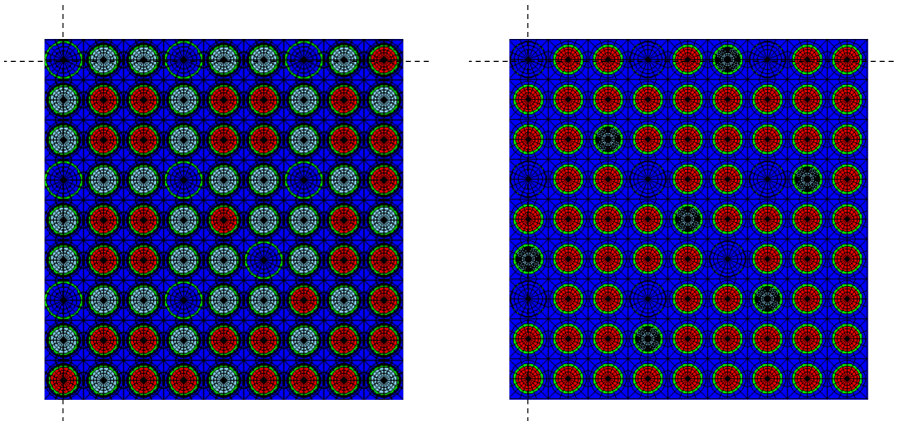

Figure 7.89: Quarter assembly lattice model with 128 IFBA pattern shown as light blue pins (left), and with gadolinium pins (right).

Table 7.31: DeCART comparison with reference solution for the multiplication factor and pin powers at the BOC.

| Benchmark | Lattice type | Reference $k_\infty$ | DeCART $k_\infty$ | $\delta k_\infty$ (pcm) | Max pin power RMS; abs. diff. (%) |
|---|---|---|---|---|---|
| CASL-2A | no BAs | 1.18496 | 1.18496 | +223 | 0.0699; 0.2000 |
| CASL-2M | IFBA | 0.94261 | 0.94261 | +315 | 0.5129; 0.9200 |
| CASL-2P | gad | 0.93309 | 0.93309 | +509 | 0.1056; 0.3000 |

# 3-D fuel pin cell

## DeCART

The DeCART model for the 3-D pin cell domain contains an active fuel height of 365.76 cm and 20 cm thick water reflectors at each end. The radial boundary conditions are reflective, while the axial boundary conditions are vacuum. The power of the fuel pin is fixed to a nominal level of 62.97 kW, which is typical for a fuel rod within a 17x17 PWR assembly. Several peaking factors of 1.3, 1.45, and 1.5 are used depending on the objectives of the model.

The fuel is composed of $UO_2$ with 3.3 wt% enriched uranium-235. A fuel-cladding gap is not

included in the model. The fuel temperature is fixed at 700 K, the cladding at 427 K, and the coolant at 292 K with a density of 0.743 $g/cm^3$. To ensure typical power distributions, thermal hydraulic feedback to the cross sections is not included; otherwise, a single pin cell model is very difficult to maintain realistic power distributions during depletion. Unless otherwise noted, the coolant boron concentration is fixed during depletion simulations according to the Seabrook plant, as shown in Figure 2.12.

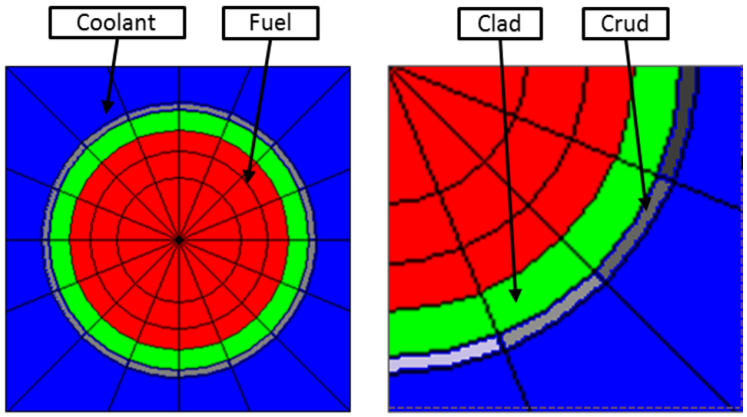


Figure 7.90: Single pin cell model in DeCART, showing cross section mesh and material regions including azimuthally-dependent CRUD assignment.

Figure 7.90 shows the pin cell geometry with the flat source (and cross section) regions: 48 within the fuel and 16 within each of the cladding, CRUD, and coolant. There is a 150 $\mu m$ thick radial region designated for CRUD deposition outside the cladding surface; in this region, CRUD is uniformly homogenized with the coolant. Refer to Appendix E for the effects of this assumption.

In the axial direction, the fuel rod is discretized into 80 planes with uniform thickness of 4.572 cm. A ray spacing of 0.03 cm with 16 azimuthal and 4 polar angles is utilized by the MOC solver. An equilibrium xenon calculation is performed for each depletion step.

## STAR-CCM+

The single pin cell CFD domain includes the solid structure containing the fuel pellets and cladding, the water domain in the subchannel surrounding the fuel pin, and three spacer

grids with mixing vanes. Only three of the eight grid spacers are included in the CFD model to reduce computation time. An inlet velocity of 5.278 m/s, inlet temperature of 556.76 K, system pressure of 15.51 MPa, and pressure boundary condition is imposed for the inlet and outlet axial planes of the coolant domain, respectively. Symmetric boundary conditions are imposed on the lateral surfaces of the water domain. No-slip conditions are imposed on the spacer grids, pin walls, and outer cladding surface. A volumetric power source is used in the fuel domain (provided by the neutronics solution). The coolant density is calculated according to the following third-order polynomial:

$$\rho_{cool}(T) = -1.16905 \times 10^{-5}T^3 + 1.225 \times 10^{-2}T^2 - 4.84697T + 1.670326 \times 10^3. \quad (7.102)$$

The $UO_2$ fuel and cladding thermal conductivity are set constant at 3.0 and 17 W/m-K, respectively. The fluid-dynamic simulation includes conjugate heat transfer for the calculation of the temperature distribution in the fuel and cladding domains.

Table 7.32: STAR-CCM+ single pin cell model mesh properties.

| Region | Cells | Faces | Vertices |
|---|---|---|---|
| Fuel | 430,803 | 2,642,496 | 2,214,928 |
| Cladding | 454,521 | 1,915,847 | 1,317,250 |
| Fluid | 776,970 | 3,401,427 | 2,283,715 |
| Total | 1,662,294 | 7,959,770 | 5,869,893 |

The CFD domain was meshed by means of polyhedral cells. The spacer grid regions, which rest at 203.28 cm, 249.00 cm, and 294.72 cm from the bottom of the active fuel, were discretized using polyhedral cells with three layers of prismatic cells at the wall, as shown in Figure 7.91. The computational mesh upstream and downstream of the grid spacers was generated by extrusion, applying the hyperbolic tangent law. Approximately 1.6 million cells makeup this model; additional mesh properties are summarized in Table 7.32. The convergence criteria were fixed at $1 \times 10^{-6}$ for continuity, z-momentum, and energy, respectively. Figure 7.91 shows the boundary conditions and the cross section mesh.

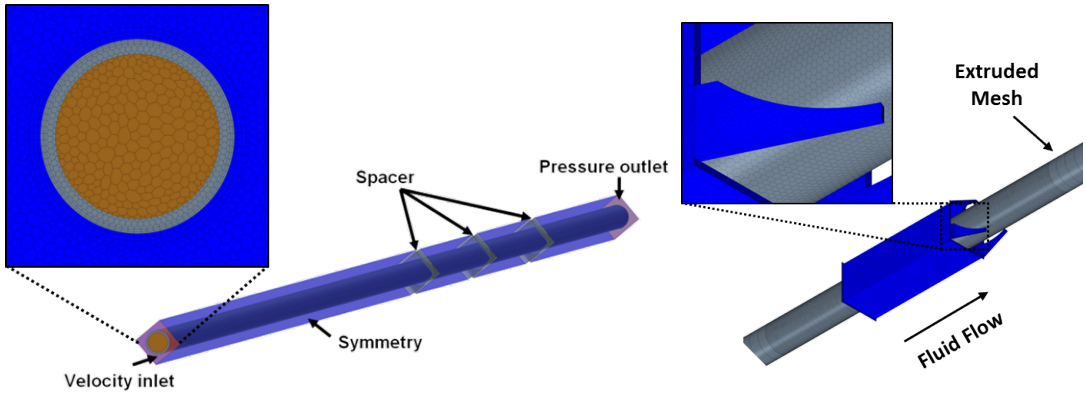


Figure 7.91: STAR-CCM+ single pin cell geometry and mesh model showing boundary conditions and spacer grid locations.

# 3-D sub-assembly

## DeCART

The DeCART model for the 3-D sub-assembly domain contains an active fuel height of 365.76 cm and 20 cm thick water reflectors at each end. The radial boundary conditions are reflective, while the axial boundary conditions are vacuum. The power of the pin array is fixed to a nominal level of 1.511 MW, which is typical for 24 fuel rods within a 17x17 PWR assembly. Several peaking factors of 1.3, 1.45, and 1.5 are used depending on the objectives of the model.

Half of the fuel rods contain IFBA (in the 128 pattern), as shown in Figure 7.92. In the axial direction, the active fuel height is discretized into 40 planes with uniform thickness of 9.144 cm. The $UO_2$ fuel rods both with and without burnable absorber are enriched to 4.8 wt% in the middle 292.608 cm of the rod; outside this region, there are 36.576 cm thick blanket regions with 4.0 wt% fuel.

A fuel-cladding gap is not included in the model. The fuel temperature is fixed at 700 K, the cladding at 427 K, and the coolant at 292 K with a density of 0.743 $g/cm^3$. Unless otherwise noted, the coolant boron concentration is fixed during depletion simulations according to the Seabrook plant letdown, as shown in Figure 2.12.

A ray spacing of 0.005 cm with 32 azimuthal and 4 polar angles is utilized by the MOC

solver. An equilibrium xenon calculation is performed for each depletion step.

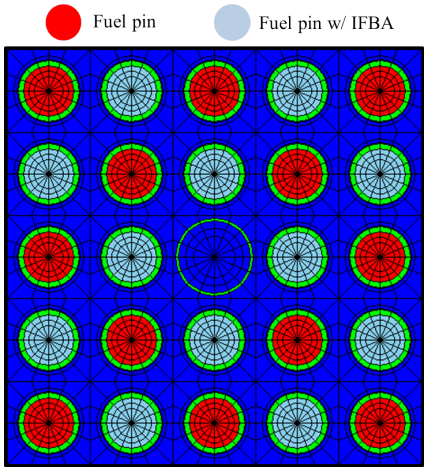


Figure 7.92: Sub-assembly DeCART model with 128 IFBA pattern.

Figure 7.93 shows the radially-integrated and normalized axial power distribution for the 5x5 pin array for select days during the depletion cycle. Figure 7.94 shows the sub-pin level power distribution at a core elevation between 283.46 and 292.61 cm with fresh fuel; pin 8 is identified with a box.

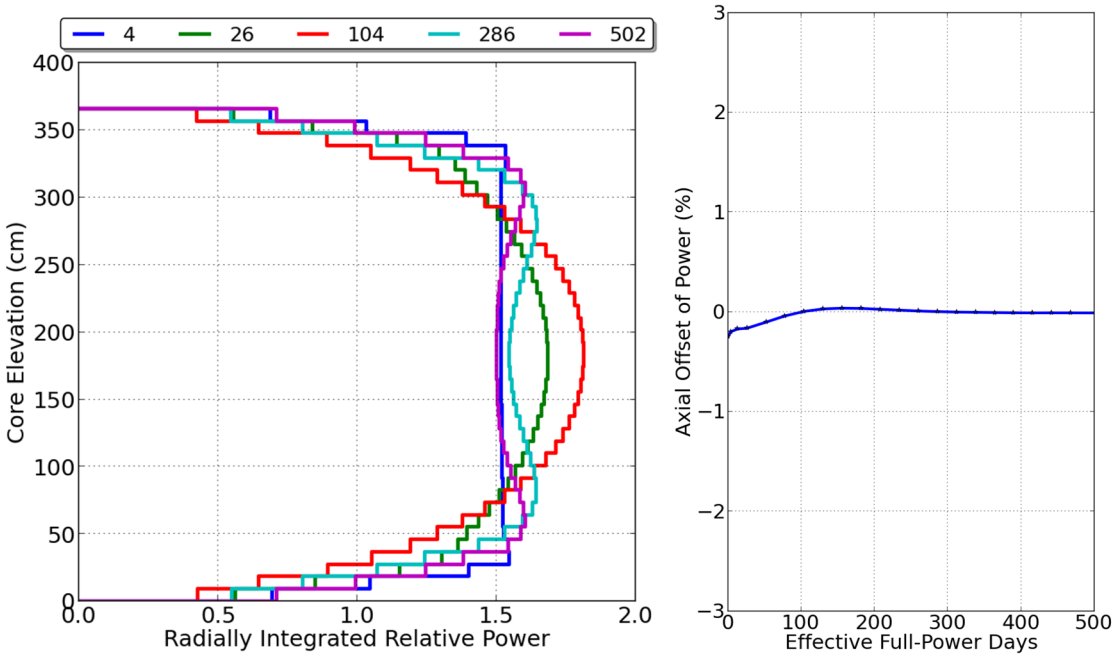


Figure 7.93: Normalized axial power distribution with 1.45 peaking calculated by DeCART at select burnup states for 5x5 pin array (left) and axial offset of power (right).

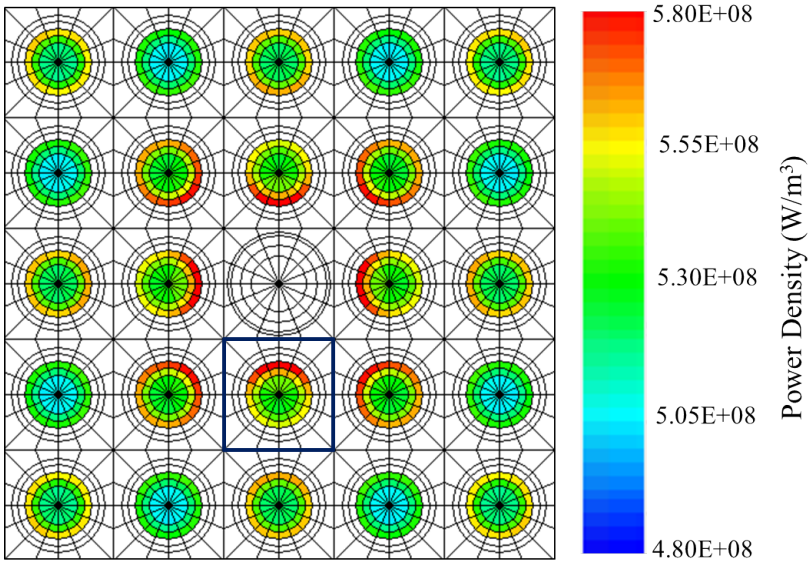


Figure 7.94: Sub-pin level power distribution calculated by DeCART with 1.45 power peaking at a core elevation spanning 283.46 to 292.61 cm for fresh fuel (left); pin 8 is identified with a box.

## STAR-CCM+

The sub-assembly CFD model includes the full heated length of 365.76 cm of the fuel rods; three spacer grids with mixing vanes at axial locations of 217.944 cm, 270.144 cm, and 322.2344 cm are modeled. The grid geometry is based on data published in [Navarro and Santos, 2011], and the orientation of the vanes was deduced from [Karoutas et al., 2012]. The axial locations of the grids was determined based on the specifications in [Godfrey, 2012].

The STAR-CCM+ computational mesh consists of over 64 million polyhedral cells. A mesh base size of 0.4 mm was adopted with four prism layers in proximity of the wall. The fuel solid region is modeled as well to solve the heat conduction within the fuel. The distribution of mesh elements among coolant, fuel, cladding and guide tubes is summarized in Table 7.33. A cross section of the mesh with zoom on a single pin and the vanes is shown in Figure 7.96. An inlet velocity of 5.239 m/s and pressure boundary condition is imposed for the inlet and outlet axial planes of the coolant domain, respectively. Symmetric boundary conditions are imposed on the lateral surfaces of the water domain. No-slip conditions are imposed on the spacer grids, pin walls and on the outer cladding surface.

A volumetric power source is used in the fuel domain. The fluid-dynamic simulation includes conjugate heat transfer for the calculation of the temperature distribution in the fuel and cladding domains. The k-$\varepsilon$ turbulence model, combined with the Two-Layer All y+ wall treatment approach is employed. Past research efforts have shown that such a model can predict the velocity field downstream of spacer grids with mixing vanes very well [Yan et al., 2014].

The convergence criteria are fixed at $1 \times 10^{-6}$ for continuity, momentum, and energy. In STAR-CCM+, the convergence criteria are calculated as,

$$R_{rms} = \sqrt{\frac{1}{n}\sum_{n} r^2}, \tag{7.103}$$

where $r$ is the absolute error in the solution of a particular variable and $n$ is the number of computational cells.

The thermo-physical properties of fuel and cladding materials are summarized in Table 7.34. All properties are assumed to be constant, with the exception of the $UO_2$ thermal

Table 7.33: STAR-CCM+ 5x5 sub-assembly model mesh properties.

| Region | Cells | Faces | Vertices |
|---|---|---|---|
| Fuel | 33,402,671 | 13,573,982 | 14,041,949 |
| Cladding | 3,081,230 | 161,728,592 | 60,538,875 |
| Fluid | 85,524,637 | 20,731,043 | 112,379,469 |
| Guide Tube | 45,224,451 | 70,251,624 | 17,608,914 |

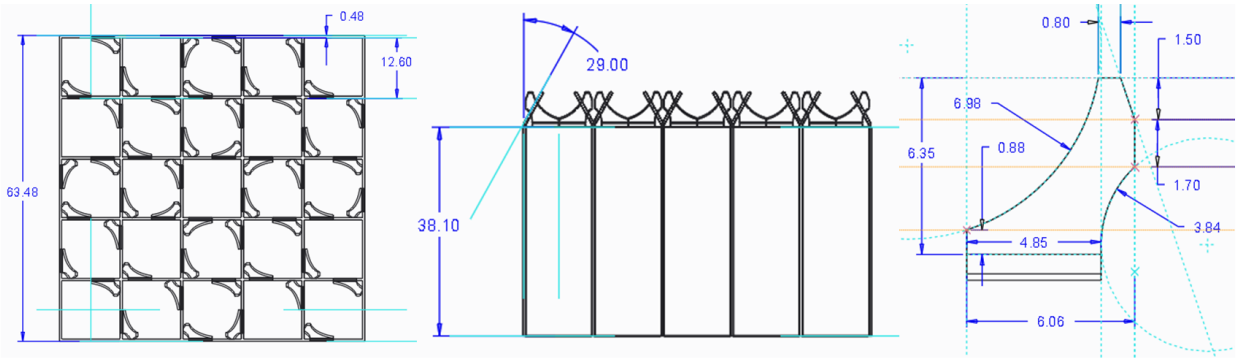


Figure 7.95: Spacer grid within mixing vanes geometry for 5x5 CFD model; dimensions in mm.

conductivity which is assumed to be a function of the local temperature:

$$k_{UO_2}(T) = 100 * \left( \frac{1}{11.8 + 0.0238 * T} + 8.775 \times 10^{-13} * T^{-3} \right). \tag{7.104}$$

Table 7.34: STAR-CCM+ 5x5 sub-assembly thermo-physical properties of materials.

| Region | Property | Value | Units |
|---|---|---|---|
| Fuel | density | 10400.0 | $kg/m^3$ |
| | specific heat | 300.0 | $J/kg-K$ |
| Cladding | density | 6500.0 | $kg/m^3$ |
| | specific heat | 350.0 | $J/kg-K$ |
| | thermal conductivity | 17.0 | $W/m-K$ |

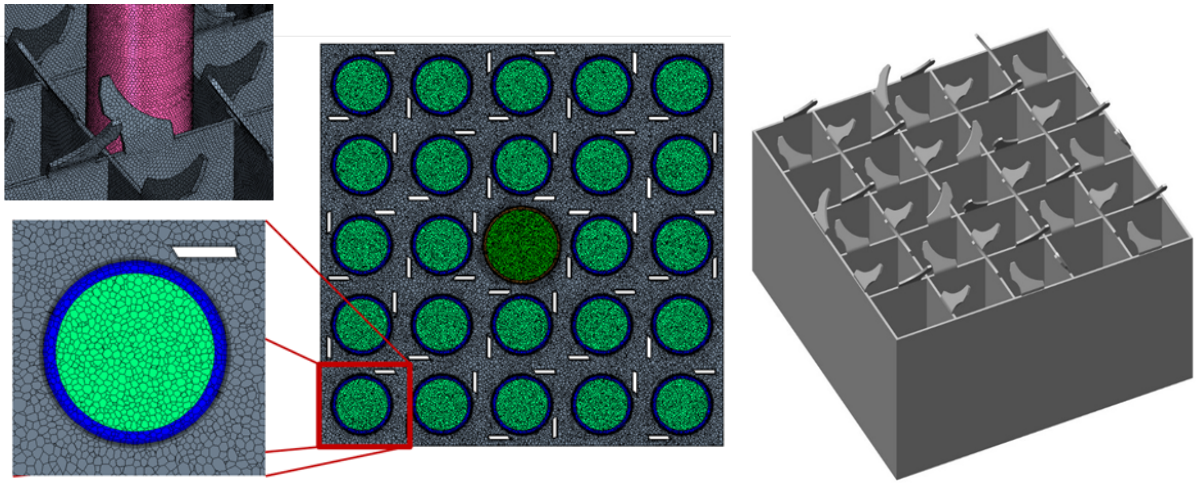

Figure 7.96: CFD mesh (left) and spacer grid geometry (right) for 5x5 sub-assembly.

The temperature-dependent fluid properties are described by:

$$\rho(T) = -1670.325859 - 4.84697 * T + 0.01225 * T^2 - 1.16905 * T^3, \tag{7.105}$$

$$\mu(T) = 3.111 + 0.03026 * T - 0.8131 \times 10^{-4} * T^2 + 0.4635 \times 10^{-7} * T^3$$

$$+1.677 \times 10^{-9} * T^4 - 0.3094 \times 10^{-12} * T^5 + 0.151 \times 10^{-15} * T^6, \tag{7.106}$$

$$c_p(T) = \frac{T - 59610}{-167.5 + 4.091 \times 10^{-4} * T^2} + 3659, \tag{7.107}$$

$$k(T) = \frac{0.1183 \times 10^{12} + 0.2419 \times 10^{9} * T}{1 - 0.4177 \times 10^{13} * T + 0.138 \times 10^{11} * T^2}. \tag{7.108}$$

# APPENDIX B
# Turbulence modeling analysis

In order to evaluate the effect of turbulence models on CRUD buildup, a sensitivity study is performed using stand-alone CFD simulations. The comparison among different turbulence models is focused on the key parameters affecting CRUD buildup and erosion: cladding temperature, turbulent kinetic energy, and wall shear stress in the proximity of the cladding surface. The turbulence model sensitivity study includes the following combinations of turbulence models and wall treatments:

- realizable k-$\varepsilon$ model [Shih et al., 1994] with high y+ treatment,
- realizable k-$\varepsilon$ two layer model [Rodi, 1991] with all y+ treatment,
- standard k-$\varepsilon$ model [Jones and Launder, 1972, Launder and Spalding, 1974] with high y+ treatment,
- standard k-$\varepsilon$ two layer model [Rodi, 1991,Jones and Launder, 1972,Launder and Spalding, 1974] with all y+ treatment,
- Reynolds stress model [Gibson and Launder, 1978],
- and quadratic k-$\varepsilon$ model [Lien et al., 1996, Baglietto et al., 2006, Shih et al., 1993] with high y+ treatment.

The values of the pressure drops across the third spacer grid obtained with the different turbulence models are compared in Table 7.35. The relative differences are tabulated with the standard k-$\varepsilon$ two-layer model with all y+ treatment as reference. As shown in Table 7.35, the deviations in pressure drop fall in the range of -2.9% to 1%, and the largest differences result from the realizable k-$\varepsilon$ model.

Table 7.35: STAR-CCM+ single pin turbulence modeling analysis pressure drops across third spacer grid.

| Turbulence model | Wall treatment | Pressure drop (kPa) | Rel. Difference (%) |
|---|---|---|---|
| realizable k-$\varepsilon$ | high y+ | 22.737 | -2.7 |
| realizable k-$\varepsilon$ | two-layer all y+ | 22.701 | -2.9 |
| standard k-$\varepsilon$ | high y+ | 23.403 | 0.1 |
| standard k-$\varepsilon$ | two-layer all y+ | 23.378 | 0.0 |
| Reynolds stress | high y+ | 23.619 | 1.0 |
| quadratic k-$\varepsilon$ | high y+ | 23.132 | -1.1 |

Moreover, the realizable k-$\varepsilon$ model exhibits flow oscillations (i.e. steady state solution does not exist) when applied to relatively tight-lattice bundles without spacer grids. Because of these flow oscillations, when a realizable k-$\varepsilon$ model is applied, a transient calculation, rather than steady state, should be performed, thus yielding significantly higher computational costs. Because the 5x5 sub-assembly and single pin cell CFD models used in the present work do not contain spacer grids or mixing vanes in the lower half of the core, flow oscillations were prone to develop when the realizable k-$\varepsilon$ model was employed. It should also be mentioned that recent studies have shown that the realizable k-$\varepsilon$ model may provide a noticeable pressure drop discrepancy with respect to experiments [Sugrue et al., 2013]. Therefore, this type of turbulence model is used for the sub-assembly or single pin cell models simulations in this dissertation.

The use of high y+ wall treatment is limited by the fact that these types of models require a y+ higher than 30, which is challenging to achieve because of the small gaps formed where the spacer grids are located. In these cases, small gaps are likely meshed too coarsely. The Reynolds stress model is much more computationally expensive because it involves the solution of additional partial differential equations for the Reynolds stresses. The quadratic k-$\varepsilon$ model appeared to be numerically unstable and required extra measures such as adjustments of the under-relaxation parameters. The azimuthal variations of cladding temperature and turbulent kinetic energy in the proximity of spacer #3 are reported in Figure 7.97, as obtained with the turbulence models listed in Table 7.35.

Overall, the turbulence models exhibit similar behavior with respect to TKE and shear

stress profiles, with the exception of the Reynolds stress model for which the TKE has higher values and the cladding temperature for rim 1 has a smaller range of variations. In order to better understand this discrepancy, an additional investigation would be required aimed at evaluating the impact of the Reynolds stress model constants. The difference among the various turbulence models will reduce when applied to models larger than the single-pin treated in this sensitivity study (e.g., 5x5 sub-assembly), because the effect of the boundary conditions on the subchannel flow will be mitigated in a larger domain. The largest differences among the turbulence models predictions are observed for the cladding temperature profiles in rim 1 (see Figure 7.97, top-left), upstream of the mixing vanes. The reason for this is that in this region, the flow is completely surrounded by the spacer walls and the effect of secondary of secondary motions is more dominant.

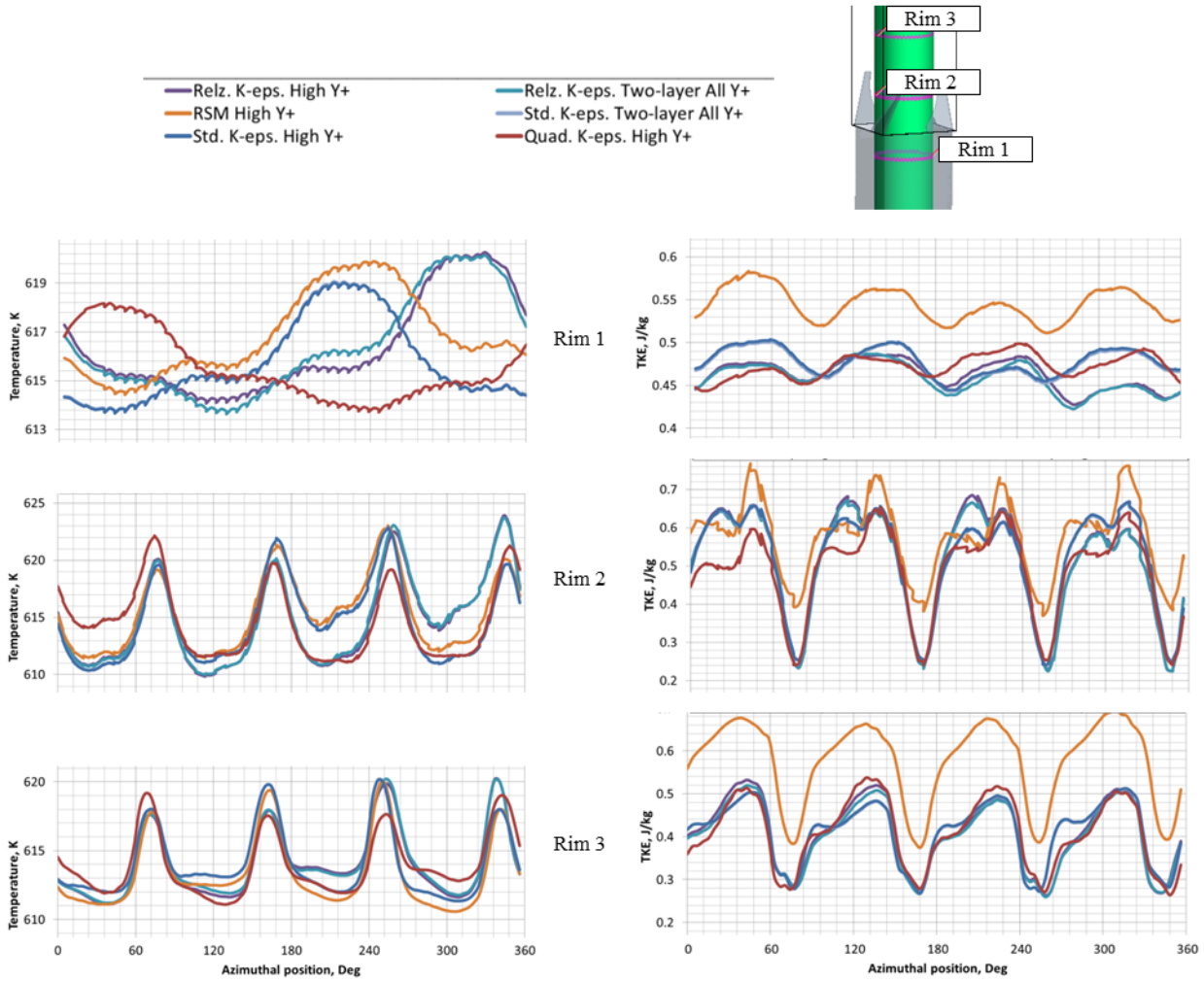


Figure 7.97: CFD turbulence model comparison of azimuthal cladding temperature (left) and TKE (right) at three axial locations in vicinity of third spacer grid in single pin cell model.

# APPENDIX C
# CFD meshing analysis

Mesh convergence studies were performed on a 4x4 sub-region including the water rod. Six different polyhedral meshes of increasing refinement in which either the number of prism layers in the wall proximity or the base size of the computational mesh was varied (see Table 7.36) for more details on the mesh parameters). A seventh mesh (*v7* in Table 7.36) was included in the study as well, characterized by the same parameters as the finest polyhedral mesh (*v6*), but employing trimmed elements instead of polyhedral. The different meshes were compared by analyzing relevant figures of merit such as the magnitude of the velocity field computed on cross-sections right above and below the mixing vanes of the grid spacers, and surface temperature. It was found that mesh *v4* was sufficient to correctly reproduce the velocity field. Therefore, these mesh parameters were used for the modeling of the 5x5 region.

Table 7.36: Details of meshes used in CFD convergence studies.

| Case | Number of cells (millions)* | Cell base size (m) | Number of prism layers | Mesh type |
|---|---|---|---|---|
| v1 | 1.9 | $6.0x10^{-4}$ | 4 | polyhedral |
| v2 | 2.5 | $5.0x10^{-4}$ | 4 | polyhedral |
| v3 | 5.0 | $3.5x10^{-4}$ | 2 | polyhedral |
| v4 | 5.6 | $4.0x10^{-4}$ | 4 | polyhedral |
| v5 | 6.7 | $3.5x10^{-4}$ | 4 | polyhedral |
| v6 | 25.4 | $2.0x10^{-4}$ | 4 | polyhedral |
| v7 | 23.4 | $2.0x10^{-4}$ | 4 | trimmed |

* for fluid domain of single spacer grid

# APPENDIX D
# Plant and WALT loop CRUD data

Tables 7.37 and 7.38 report CRUD deposit structure properties from plants and experiments, respectively. These tables are referred to in Section 3.1, Chapter III.

Table 7.37: Plant boiling chimney analysis data [Byers and Wang, 2006].

| Plant | Cycles | Pore Chimney Radius ($\mu m$) | | | Average Chimney Density ($cm^{-2}$) |
|---|---|---|---|---|---|
| | | Average | Minimum | Maximum | |
| Beaver Valley 2 | 10 | 1.75 | 0.85 | 3.9 | $9.6x10^5$ |
| Braidwood 2 | 11 | 1.25 | 0.55 | 2.8 | $1.4x10^6$ |
| Plant F | 9 | 3.65 | 0.85 | 15 | $7.8x10^5$ |
| Plant F | 10 | 15.0 | 15.0 | 15.0 | $6.6x10^5$ |
| Plant F | 13 | 1.75 | 0.75 | 3.15 | $7.1x10^5$ |
| Plant E | 11 | 1.8 | 1.0 | 2.5 | $1.2x10^6$ |
| Plant A | 5 | 2.45 | 1.9 | 4.4 | $2.5x10^5$ |
| Plant B | 10 | 1.95 | 0.95 | 3.15 | $1.0x10^6$ |
| Plant B | 11 | 1.75 | 0.95 | 3.6 | $8.7x10^5$ |
| Plant C | 8 | 2.15 | 0.95 | 4.7 | $1.1x10^6$ |
| Plant C | 9 | 1.65 | 0.95 | 3.15 | $1.8x10^6$ |

Table 7.38: WALT loop experiment CRUD properties [Wang et al., 2013].

| Rod # | Thickness ($\mu m$) | Porosity (%) | CRUD density ($g/cm^3$) | Chimney Density ($cm^{-2}$) | Median Chimney Radius ($\mu m$) | Thermal Conductivity (W/mK) |
|---|---|---|---|---|---|---|
| 110 | 66 | 72 | 5.1 | $4.8x10^4$ | 3.0 | 0.715 |
| 110 | 43 | 76 | 5.4 | $4.8x10^4$ | 3.0 | 0.718 |
| 110 | 88 | 72 | 5.3 | $4.8x10^4$ | 3.0 | 1.025 |
| 111 | 42 | 73 | 5.4 | $2.0x10^5$ | 1.5 | 0.519 |
| 111 | 49 | 70 | 5.4 | $2.0x10^5$ | 1.5 | 0.597 |
| 111 | 46 | 69 | 5.2 | $2.0x10^5$ | 1.5 | 0.54 |
| 111 | 42 | 56 | 4.4 | $2.0x10^5$ | 1.5 | 0.538 |
| 112 | 61 | 49 | 3.9 | $1.6x10^5$ | 2.0 | N/A |
| 112 | 85 | 66 | 4.9 | $1.6x10^5$ | 2.0 | N/A |
| 112 | 58 | 63 | 4.5 | $1.6x10^5$ | 2.0 | 0.665 |
| 112 | 69 | 67 | 4.9 | $1.6x10^5$ | 2.0 | N/A |
| 116 | 99 | 57 | 4.4 | $5.7x10^4$ | 4.0 | N/A |
| 116 | 66 | 66 | 5.5 | $5.7x10^4$ | 4.0 | N/A |
| 116 | 78 | 62 | 4.9 | $5.7x10^4$ | 4.0 | 1.39 |
| 116 | 54 | 67 | 5.3 | $5.7x10^4$ | 4.0 | 1.016 |
| 117 | 120 | 66 | 4.4 | $8.4x10^4$ | 1.5 | N/A |
| 117 | 76 | 60 | 5.9 | $8.4x10^4$ | 1.5 | N/A |
| 117 | 67 | 59 | 5.3 | $8.4x10^4$ | 1.5 | 0.822 |
| 117 | 70 | 61 | 5.5 | $8.4x10^4$ | 1.5 | 0.829 |

# APPENDIX E
# Modeling CRUD within MOC neutron transport

This chapter details the results published in [Walter and Manera, 2016b]. The CASL-2A and CASL-2M benchmark problems, detailed in Appendix A, are used in the subsequent investigation to develop modeling requirements for a CRUD layer within 2-D MOC transport simulations.

## CRUD distributions

Three unique 3-D CRUD distributions are extracted from coupled full-length single pin cell neutronics, CFD, and CRUD chemistry simulations. The axial dependence is eliminated by identifying a single planar section. The cases were chosen based on the amount of boron hideout (boron-10 mass) present within the CRUD layer. Two of the three distributions, denoted 2D-1 and 2D-2, were extracted from the coupled STAR-CCM+ and MAMBA cycle simulation results for rods 14 and 23 presented in Chapter VI; whereas, the third distribution, 2D-3, represents an upper limit of the amount of boron-10 that is expected to be encountered on a single fuel rod. Table 7.39 summarizes the characteristics of the planar (radially- and azimuthally-dependent) 2-D CRUD distributions. Case 2D-1 contains the least amount of boron hideout and case 2D-3 the most.

Table 7.39: Characteristics of the 2-D CRUD distributions used in neutronics modeling requirements study.

| Distribution | Thickness (um) | Boron-10 mass (mg) | $NiFe_2O_4$mass (mg) |
|---|---|---|---|
| 2D-1 | 70 | 0.0365 | 36.1 |
| 2D-2 | 95 | 0.0595 | 39.3 |
| 2D-3 | 100 | 0.147 | 24.9 |

## Radial

One-dimensional radial distributions are calculated from each 2-D distribution by performing an azimuthal homogenization of the CRUD layer within each 5 μm radial. The 1-D radial distributions of the boron-10 and nickel ferrite are shown in Figure 5 with distribution R-1 shown at the top, R-2 in the middle, and R-3 at the bottom. Uniform radial homogenization, i.e. elimination of the radial dependence, of the CRUD layer is also shown in each plot. The boron-11 mass is ignored in all cases because its significance from a neutronics standpoint is negligible. Specifically, the presence of the boron-11 in the 2D-3 distribution changed the multiplication factor by less than 1 pcm.

Table 7.40: Radial mesh refinement case descriptions.

| Radial mesh refinement case | CRUD layer description | Homogenized with coolant | Coolant radial thickness used in homogenization (μm) |
|---|---|---|---|
| a | explicit | No | 0 |
| b | homogenized | No | 0 |
| c | homogenized including coolant | Yes | 100 |
| d | | Yes | 300 |
| e | | Yes | 675 |
| f | | Yes | all coolant |

For each radial distribution, six mesh refinement cases are considered, as detailed in Table 7.40. Homogenization of the CRUD layer with various amounts of coolant is compared. Case *a* preserves the exact boron-10 and nickel ferrite radial distributions as shown in Figure 7.98. Case *b* uniformly homogenizes the explicit distribution to eliminate the radial dependence. The remaining cases include homogenization of a fixed amount of coolant with the CRUD layer. Case *c* includes a 100 μm thick radial region of coolant, case *d* a 300 μm thick region, case *e* a 675 μm thick region, and case *f* includes all of the remaining coolant within the pin cell, i.e. uniform homogenization of the CRUD layer with the coolant contained within the four subchannels surrounding each fuel pin.

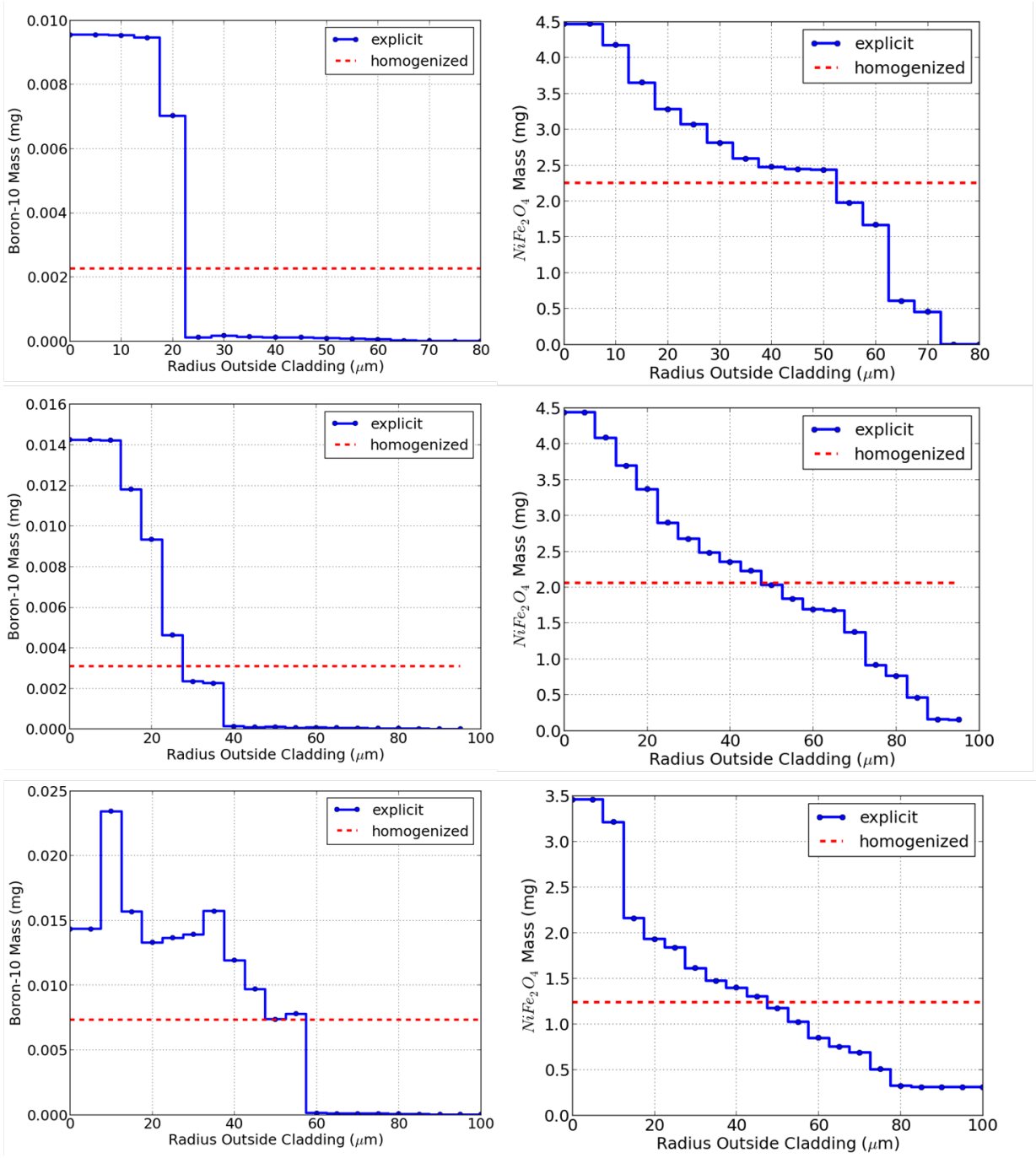


Figure 7.98: Radial CRUD distributions for boron-10 (left) and nickel ferrite (right): distribution R-1 (top), case R-2 (middle), and case R-3 (bottom).

Typically, in MOC simulations without a CRUD layer modeled, there is a single radial division in the coolant region outside of the cladding surface, but still within the pin cell boundary. Such a division of the coolant spatial domain helps resolve the neutron flux distribution in the vicinity of the fuel rod and coolant interface where neutrons are experiencing significant moderation. Case *e* places a radial 675 μm away from the cladding, which is representative of a typical pin cell discretization.

Figure 7.99 illustrates the first three mesh refinement cases for the R-1 distribution. The first case, R-1a, explicitly models the CRUD layer. The second case, R-1b, eliminates the radial dependence by homogenizing the B-10 and NiFe2O4 materials into one uniformly distributed mixture, as shown in Figure 7.99 (middle). The third case, R-1c, homogenizes the 70 μm thick mixture from case R-1b with an additional 100 μm radial region of coolant, i.e. the CRUD is homogenized within a 170 μm radial, as depicted in Figure 7.99 (right). Cases R-1d through R-1f are the same as R-1c except the CRUD is homogenized with more coolant, as summarized in Table 7.40. Cases R-1d through R-1f are not illustrated as they are similarly represented by case R-1c in Figure 7.99.

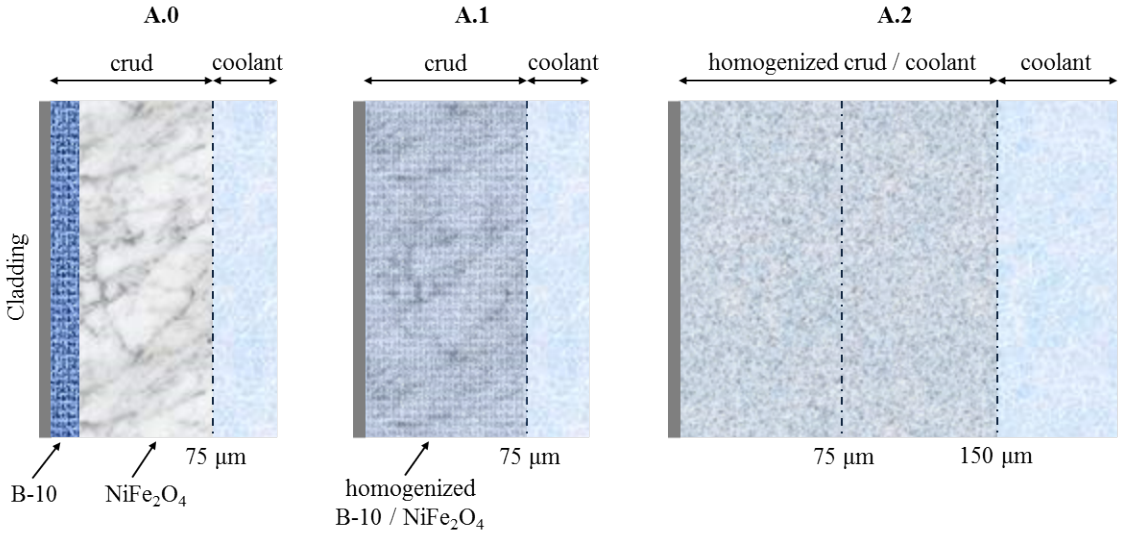


Figure 7.99: Radial mesh refinement of CRUD within neutronics mesh for cases R-1a, R-1b, and R-1c – not to scale.

## Azimuthal

To investigate the effect of azimuthal homogenization of a CRUD layer, the same 3-D distributions as previously mentioned are utilized. One-dimensional, circumferentially-varying distributions are found by identifying a single axial section and performing a radial homogenization within each azimuthal sector (16 in total). Circumferential variation of the CRUD composition is simulated using three different distributions, as shown in Figure 7.100; distributions A-1 (top), A-2 (middle), and A-3 (bottom) represent varying locations and magnitudes of nickel ferrite deposition and boron-10 precipitation. Because of localized species concentration and spacer grid mixing vane effects, the precipitation of boron-10 as lithium tetraborate exhibits strong spatial dependence. Therefore, the boron concentration within the CRUD layer may vary more than one order of magnitude in locations around the cladding surface, resulting in variations in the cladding surface temperature on the order of 10 degrees.

Table 7.41: Azimuthal CRUD mesh refinement cases.

| Azimuthal mesh refinement case | Homogenized | Number of azimuthal sectors |
|---|---|---|
| a | No | 16 |
| b | Yes | 8 |
| c | Yes | 4 |
| d | Yes | 1 |

For each azimuthal distribution, four cases that refine the mesh within the neutron transport model to assess the effects of smearing the CRUD layer are investigated. Table 7.41 summarizes the azimuthal mesh discretizations considered. Figure 7.101 illustrates the four levels of mesh refinement for an arbitrary azimuthal distribution. Case *a* explicitly models the azimuthal variation, according to 16 equal-volume sectors, of the CRUD layer. The second and third cases, *b* and *c*, remove some of the resolution by smearing the distribution into sectors of an 8- and 4-region discretization, respectively. The final mesh refinement case, *d*, removes all azimuthal dependence and is equivalent to the radial mesh refinement case *b*.

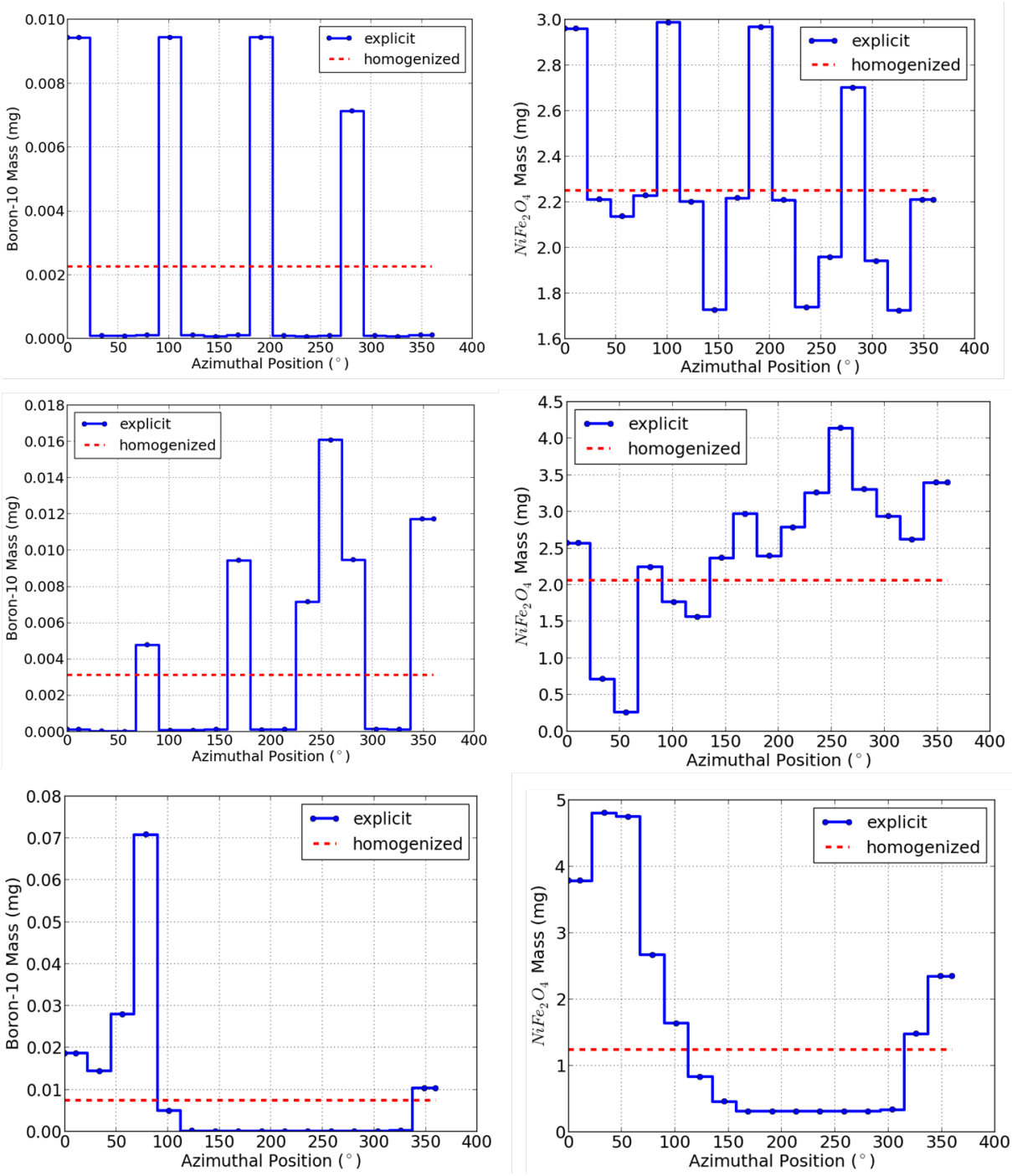


Figure 7.100: Azimuthal CRUD distributions for boron-10 (left) and nickel ferrite (right): distribution A-1 (top), case A-2 (middle), and case A-3 (bottom).

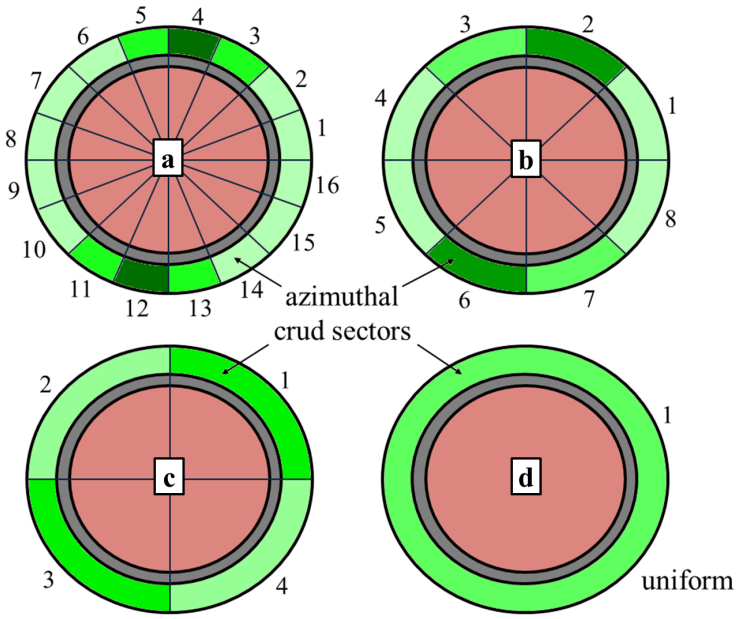


Figure 7.101: Azimuthal mesh refinement and homogenization of CRUD layer – not to scale.

# Cross section region mesh refinement

## Radial

The resolution of the neutron transport mesh required to accurately model a CRUD layer is investigated in this section. In the radial variation simulations, the ray tracing parameters to sufficiently resolve the IFBA layer are used: 50 μm spacing, 32 azimuthal angles, and 4 polar angles. Table 7.42 summarizes the solution sensitivity to smearing a 70% porous CRUD layer in the radial direction for two different coolant boron concentrations. The cases that meet the cutoff criterion are highlighted in red.

Table 7.42: Solution comparison of radial CRUD mesh refinement cases for both 1300 and 0 ppm coolant boron concentrations in combination with a 70% porous CRUD structure.

| Radial case | 1300 ppm | | 0 ppm | |
|---|---|---|---|---|
| | $k_\infty$ | $\delta k_\infty$(pcm) | $k_\infty$ | $\delta k_\infty$(pcm) |
| R-1a | 1.16835 | – | 1.33979 | – |
| R-1b | 1.16834 | -1 | 1.33978 | -1 |
| R-1c | 1.16829 | -6 | 1.33969 | -10 |
| R-1d | 1.16821 | -14 | 1.33955 | -24 |
| R-1e | 1.16809 | -26 | 1.33934 | -45 |
| R-1f | 1.16775 | -60 | 1.33873 | -106 |
| R-2a | 1.15984 | – | 1.32813 | – |
| R-2b | 1.15977 | -7 | 1.32802 | -11 |
| R-2c | 1.15969 | -15 | 1.32788 | -25 |
| R-2d | 1.15955 | -29 | 1.32766 | -47 |
| R-2e | 1.15936 | -48 | 1.32733 | -80 |
| R-2f | 1.15883 | -101 | 1.32638 | -175 |
| R-3a | 1.12985 | – | 1.28789 | – |
| R-3b | 1.12969 | -16 | 1.28765 | -24 |
| R-3c | 1.12943 | -42 | 1.28724 | -65 |
| R-3d | 1.12906 | -79 | 1.28666 | -123 |
| R-3e | 1.12857 | -128 | 1.28585 | -204 |
| R-3f | 1.12727 | -258 | 1.28364 | -425 |

The lattice model with 0 ppm coolant boron concentration shows larger reactivity effects when radially smearing the CRUD layer. This is attributed to the magnitude of the CRUD's neutron absorption ability is relatively increased when a strong neutron absorber, such as the coolant boron concentration, is reduced. In the most limiting cases associated with the R-3 distribution, case R-3c is the lowest resolution model that still meets the 100 pcm criterion. R-3c corresponds with homogenization of the CRUD layer with 100 μm of coolant.

As more coolant is used in the homogenization, the spatial self-shielding in the CRUD is decreased, resulting in enhanced neutron capture. It is also noted that the cutoff criterion of 1% maximum pin power difference remains unviolated for all of the ray tracing parameter combinations considered.

## Azimuthal

The effect of azimuthal mesh refinement is summarized in Table 7.43; again, the same ray tracing parameters of 50 μm spacing, 32 azimuthal angles, and 4 polar angles are used in the comparison. The effect of smearing the CRUD layer azimuthally is strongly dependent on the actual CRUD layer distribution. For the distributions considered, elimination of the azimuthal dependence is acceptable for the A-1 and A-2 distributions; however, due to the higher boron-10 concentration in distribution A-3, the 100 pcm cutoff is met by case A-3b when the coolant boron concentration is 0 ppm. It is also noted that the cutoff criterion of 1% maximum pin power difference remains unviolated for all of the ray tracing parameter combinations considered.

## Discussion

Approximately half of the fuel pins contained CRUD in this investigation; recall that the pins containing IFBA were replaced with pins containing a CRUD layer. As shown in Figure 7.89 (left) within Appendix A, these pins are most prevalent in the vicinity of the water rods, which is consistent with the coupled CRUD deposition results reported in [Petrov et al., 2016]. Therefore, the assembly CRUD loading, and thus the reactivity differences reported, for cases R-1, R-2, A-1, and A-2 are quite representative of a high power PWR fuel assembly. On the other hand, distributions R-3 and A-3 are worst case CRUD loadings that would only be expected to be encountered in select pins in the entire core, so this degree of CRUD on half the pins in the assembly is likely not realistic. However, if single pin cell or sub-assembly calculations are performed using boundary conditions leading to significant CRUD buildup, then the reported results would be relevant.

To better understand the effects of homogenizing a radially and azimuthally dependent CRUD deposit, the three 2-D distributions are explicitly modeled by preserving the radial

Table 7.43: Solution comparison of azimuthal CRUD mesh refinement cases for both 1300 and 0 ppm coolant boron concentrations in combination with a 70% porous CRUD structure.

| Azimuthal case | 1300 ppm | | 0 ppm | |
|---|---|---|---|---|
| | $k_\infty$ | $\delta k_\infty$(pcm) | $k_\infty$ | $\delta k_\infty$(pcm) |
| A-1a | 1.16850 | – | 1.33999 | – |
| A-1b | 1.16838 | -12 | 1.33983 | -16 |
| A-1c | 1.16834 | -16 | 1.33977 | -22 |
| A-1d | 1.16834 | -16 | 1.33977 | -22 |
| A-2a | 1.16005 | – | 1.32841 | – |
| A-2b | 1.15991 | -14 | 1.32821 | -20 |
| A-2c | 1.15982 | -23 | 1.32808 | -33 |
| A-2d | 1.15977 | -28 | 1.32801 | -40 |
| A-3a | 1.13226 | – | 1.29118 | – |
| A-3b | 1.13189 | -37 | 1.29068 | -50 |
| A-3c | 1.13145 | -81 | 1.29007 | -111 |
| A-3d | 1.12969 | -257 | 1.28764 | -354 |

and azimuthal distributions within the neutron transport solver. Table 7.44 compares the reactivity effect of separately removing the azimuthal dependence, the radial dependence, and both the azimuthal and radial dependence. Last, the spatially-independent CRUD deposit is homogenized with an additional 300 μm of coolant. The primary takeaway is that removing the azimuthal and radial dependence, as well as homogenizing with an additional 300 μm of coolant, for the 2D-1 and 2D-2 distributions is acceptable. However, for the strongest absorbing case of 2D-3, the azimuthal dependence is important and cannot be removed without a significant reactivity prediction error.

Generally, CRUD deposits are approximately 70% porous, so inclusion of the coolant within the CRUD mixture is necessary to correctly capture the reactivity effects. In the current investigation, the density of the coolant contained within the porous CRUD structure is assumed the same as the bulk coolant, despite a spatially-dependent temperature present with the deposit. The effect of the CRUD structure porosity is compared in Table 7.45 for

Table 7.44: Solution comparison of each 2-D explicit CRUD distribution to select mesh refinement cases for 70% porous CRUD structure and 1300 ppm coolant boron concentration.

| Azimuthal case | Radial homogenization | Azimuthal homogenization | Reactivity effect | |
|---|---|---|---|---|
| | | | $k_\infty$ | $\delta k_\infty$(pcm) |
| 2D-1 | no | no | 1.16874 | – |
| A-1a | yes | no | 1.16850 | -24 |
| A-1a | no | yes | 1.16835 | -39 |
| R-1b, A-1d | yes | yes | 1.16834 | -40 |
| R-1d | yes | yes | 1.16821 | -53 |
| 2D-2 | no | no | 1.16020 | – |
| A-2a | yes | no | 1.16019 | -1 |
| A-2a | no | yes | 1.15984 | -36 |
| R-2b, A-2d | yes | yes | 1.15978 | -42 |
| R-2d | yes | yes | 1.15955 | -65 |
| 2D-3 | no | no | 1.13245 | – |
| A-3a | yes | no | 1.13226 | -19 |
| A-3a | no | yes | 1.12985 | -260 |
| R-3b, A-3d | yes | yes | 1.12969 | -276 |
| R-3d | yes | yes | 1.12906 | -339 |

both of the coolant boron concentrations previously considered. Interestingly, the change in reactivity is very different for the two coolant boron concentrations because of competing effects. The first, and most obvious, effect is that of the coolant boron resulting in increased neutron absorption when included within the CRUD structure. The second effect is that of neutron moderation due to the addition of hydrogen (low mass isotopes) within the CRUD.

When the coolant boron concentration is high (1300 ppm), including the CRUD's porosity results in a decrease in the multiplication factor of approximately 50 pcm. The additional boron increases the neutron absorption and trumps the increase in moderation caused by the lighter isotopes. On the other hand, when the coolant boron concentration is reduced to 0 ppm, the addition of the hydrogen is the only effect, thus causing an increase in the

multiplication factor on the order of 100 pcm for the cases investigated.

Table 7.45: CRUD structure porosity effect on the reactivity for coolant boron concentrations of 1300 and 0 ppm.

| CRUD distribution | Coolant boron concentration (ppm) | Porosity (%) | Reactivity effect | |
|---|---|---|---|---|
| | | | $k_\infty$ | $\delta k_\infty$(pcm) |
| R-1a | 1300 | 0 | 1.16873 | – |
| R-1a | 1300 | 70 | 1.16835 | -38 |
| R-1a | 0 | 0 | 1.33901 | – |
| R-1a | 0 | 70 | 1.33979 | +78 |
| R-2a | 1300 | 0 | 1.16036 | – |
| R-2a | 1300 | 70 | 1.15984 | -52 |
| R-2a | 0 | 0 | 1.32709 | – |
| R-2a | 0 | 70 | 1.32813 | +104 |
| R-3a | 1300 | 0 | 1.13040 | – |
| R-3a | 1300 | 70 | 1.12985 | -55 |
| R-3a | 0 | 0 | 1.28692 | – |
| R-3a | 0 | 70 | 1.28789 | +97 |

# Conclusions

In this study, very thin corrosion layers were investigated to determine the spatial discretization and ray tracing requirements when using MOC neutron transport formulated with the flat source approximation. A cutoff criterion of 100 pcm in the multiplication factor is used. the ray tracing parameters may set to a spacing of 300 μm, 16 azimuthal angles, and 4 polar angles to model the CRUD layers considered. These parameter requirements are dependent on several factors: (i) the source approximation within the MOC formulation, e.g. flat vs. linear, (ii) the volume correction applied to the ray tracing track lengths, and (iii) the concentration of the neutron-absorbing material.

Overall, elimination of the radial and azimuthal spatial dependencies of the CRUD distributions results in approximately 50 pcm lower eigenvalues – see Table 7.45. Specifically, radial mesh refinement including homogenization of the CRUD layer with the coolant is acceptable, provided the amount of coolant is restricted to approximately a 300 μm thick region. If the CRUD mixture is smeared into a larger coolant region, then the effective absorption is increased and the cutoff criteria are no longer satisfied for all three distributions considered. Azimuthal mesh refinement including smearing of the CRUD layer circumferentially around the rod is acceptable for most CRUD loadings that would be encountered during reactor simulation. The most limiting distribution, A-3, resulted in errors nearing 300 pcm when eliminating the azimuthal dependence; however, such a high boron mass is only realistic for select pins within an assembly. Therefore, the reactivity effect is exacerbated in this investigation as nearly half of the fuel pins contain the CRUD deposit.

Inclusion of the CRUD structure porosity has reactivity effects ranging from -50 to +100 pcm, depending on the coolant boron concentration. Therefore, it is recommended to include the additional coolant within the CRUD structure to reduce multiplication factor prediction errors. The sensitivity of the solution to a non-uniform coolant density distribution within the CRUD layer should also be investigated.

# APPENDIX F
# Lattice depletion stepsize controller parameterization

The parameterization of the controllers presented in Chapter V for 2-D lattice depletion simulations is detailed in this appendix.

Several general controllers, including I, PI, and PID, were considered for determining the optimal lattice depletion stepsize. Parameterizing the controllers involves determining an acceptable tolerance on the flux solution (the $L^2$ relative error norm) and appropriate gain values to result in overall good dynamic behavior; additionally, the initial stepsize used to begin the depletion cycle must also be chosen. To efficiently parameterize the stepsize controller, Latin hypercube sampling (LHS) of the control parameters is utilized; the DAKOTA code package is used to perform the LHS [Adams, 2015].

A range for each control variable to be uniformly sampled is set and summarized in Table 7.46 for an I controller. Using these bounds, 130 samples are determined, and the benchmark problem CASL-2A with depletion is simulated for each sample set. The rule of thumb stepsize sequence shown in Table 5.25 is used as a baseline trend to find sample sets that behave similarly. To eliminate the sample sets that yield poor behavior, four filters are applied to the stepsize prediction time series sets:

1. the number of steps taken is not to exceed 80,
2. the stepsize is not to exceed 3.0 MWd/kgHM,
3. the maximum stepsize should exceed 0.5 MWd/kgHM,
4. the change in stepsize from one burnup state to the next is not to exceed 2.0 MWd/kgHM,
5. and the difference between the maximum stepsize and the final stepsize taken is not to exceed 0.5 MWd/kgHM.

Filters 1 through 4 are self-explanatory; filter 5 eliminates time series that have a peak mid-cycle and decrease by more than 0.5 MWd/kgHM by the end-of-cycle, i.e. eliminates overshoot. Using these filters and eliminating a few others that have redundant behavior, the 130 data sets are reduced to just seven; Table 7.47 summarizes each data set's parameter values and compares some of the multiplication factor differences. Specifically, the difference in eigenvalue due to the initial stepsize is tabulated, as is the maximum difference occurring during the cycle. Figure 7.102 compares the stepsize sequences for the filtered data sets and the rule of thumb sequence, and it compares the infinite multiplication factor differences when compared to a reference case using a very fine fixed stepsize of 0.01 MWd/kgHM.

Table 7.46: Parameter bounds used in Latin hypercube sampling of I controller for CASL-2A.

| Parameter | Lower bound | Upper bound |
|---|---|---|
| Initial stepsize (MWd/kgHM) | 0.02 | 0.50 |
| Flux tolerance | $1x10^{-5}$ | $1x10^{-3}$ |
| $k_I$ | 0.01 | 0.35 |

Regarding the effects of the control parameters on the stepsize predictions and eigenvalue errors, several behavioral traits are noted:

1. a tight flux tolerance results in more time steps (see sample 47),
2. a flux tolerance range of 1e-4 to 4e-4 gives reasonable stepsize predictions,
3. the initial stepsize affects the total number of steps taken, while only introducing a few pcm additional error (compare samples 2 and 115),
4. a higher integral gain causes larger stepsizes (see sample 19),
5. and balancing the integral gain and flux tolerance is important to avoid overshoot (see sample 45), i.e. the integral gain may be too large for the given flux tolerance and over predict the stepsize, which is followed by stepsize reductions.

Based on this parameter study, an integral controller behaves well for the problem CASL-2A. Higher stepsize predictions are correlated with higher integral gains. Sample set 19 eliminates

five of the depletion steps during the 30.0 MWd/kgHM cycle when compared to the rule of thumb sequence with 21 steps, while maintaining comparable accuracy in the eigenvalue solution. As a baseline for comparison, the rule of thumb stepsize sequences results in more than 180 pcm of error in the eigenvalue toward the end-of-cycle.

Moreover, excluding sample set 47, all other sample sets display an abrupt introduction of error in the eigenvalue sometime between 3.0 and 12.0 MWd/kgHM; in the rule of thumb case, the increase in error occurs around 1.0 MWd/kgHM. Correlating these changes in the eigenvalue error with the size of the depletion step reveals that any step greater than approximately 0.9 MWd/kgHM causes an immediate eigenvalue error of at least +50 pcm. This detail will be investigated in Section 5 by examining isotopic concentrations.

Table 7.47: Results for filtered sample sets from LHS of I controller design space for CASL-2A.

| Sample set | Initial stepsize (MWd/kgHM) | Flux tolerance | $k_I$ | Number of steps | $\delta k_\infty$ due to initial step (pcm) | Max $\delta k_\infty$ (pcm) |
|---|---|---|---|---|---|---|
| ROT | 0.10 | – | – | 21 | 15 | 184 |
| 2 | 0.11 | $1.85 \times 10^{-4}$ | 0.087 | 25 | 18 | 181 |
| 19 | 0.31 | $2.10 \times 10^{-4}$ | 0.121 | 16 | 21 | 184 |
| 45 | 0.38 | $1.33 \times 10^{-4}$ | 0.091 | 21 | 21 | 187 |
| 47 | 0.09 | $3.75 \times 10^{-5}$ | 0.029 | 77 | 11 | 11 |
| 48 | 0.22 | $1.81 \times 10^{-4}$ | 0.020 | 39 | 20 | 157 |
| 115 | 0.35 | $1.95 \times 10^{-4}$ | 0.085 | 19 | 21 | 186 |
| 124 | 0.47 | $3.89 \times 10^{-4}$ | 0.060 | 17 | 22 | 183 |

Before adding additional control components, e.g. proportional and derivative gains, the parametric study on the integrating controller is continued with the CASL-2P problem containing gadolinium burnable absorbers. Based on the parameters associated with the filtered time series shown in Table 7.47, a constrained parameter space is identified and shown in Table 7.48.

Again, the 130 sample sets are filtered using similar criteria as used for CASL-2A. Additionally, sample sets exhibiting oscillations in the stepsize are neglected, and the filtered sample

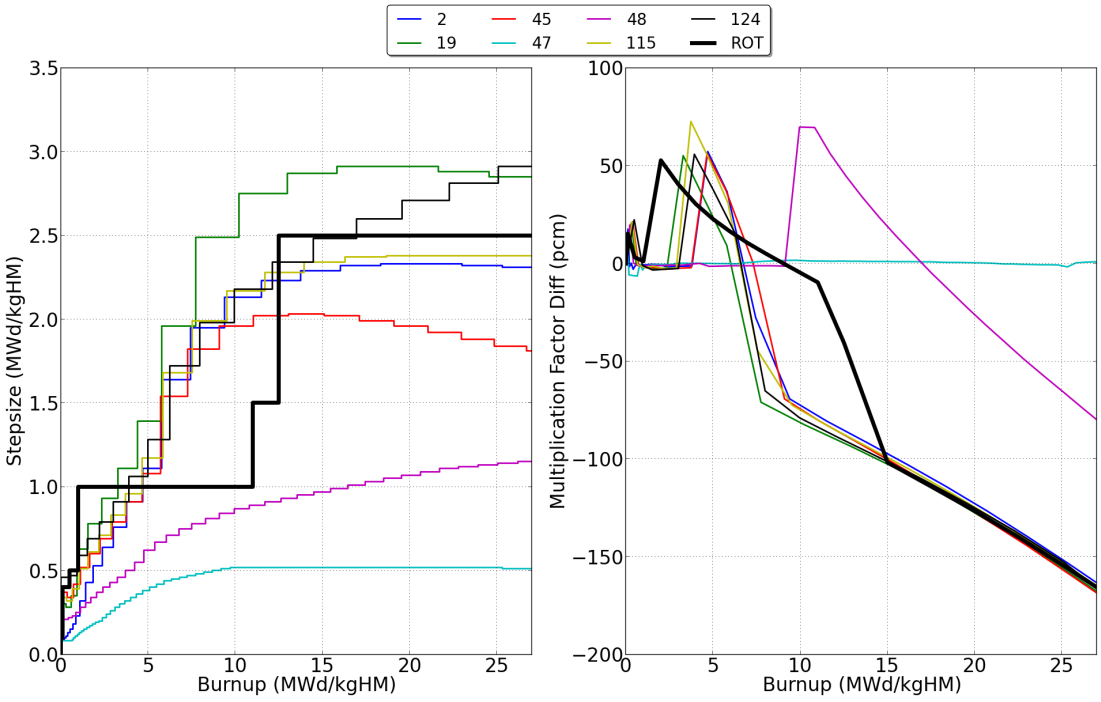


Figure 7.102: Filtered stepsize prediction sequences (left) and difference in multiplication factor from reference (right) for LHS of parameters for I controller, applied to CASL-2A.

sets are summarized in Table 7.49. Figure 7.103 compares the stepsize sequences for the filtered data sets and the rule of thumb sequence, and it compares the infinite multiplication factor differences when compared to a reference case using a very fine fixed stepsize of 0.01 MWd/kgHM. The rule of thumb sequence is expected to perform very poorly for gadolinium-bearing fuel; it is included as a baseline of comparison.

In the first 10.0 MWd/kgHM of the cycle, the stepsizes range from approximately 0.15 to 0.4 MWd/kgHM for the filtered sample sets, which is consistent with expected stepsizes for gadolinium-bearing fuel [Knott and Wehlage, 2007]. Similar to the eigenvalue error trends from the CASL-2A problem, once the gadolinium burns out of the CASL-2P lattice and the stepsize is increased, the +50 pcm error is introduced with stepsizes greater than 0.9 MWd/kgHM. Samples 92 and 128 remain below the stepsize threshold and do not introduce the eigenvalue error. Regarding the effects of the control parameters on the stepsize predictions and eigenvalue errors, several behavioral traits are noted:

Table 7.48: Parameter bounds used in Latin hypercube sampling of I controller for CASL-2P.

| Parameter | Lower bound | Upper bound |
|---|---|---|
| Initial stepsize (MWd/kgHM) | 0.09 | 0.30 |
| Flux tolerance | $1 \times 10^{-4}$ | $7 \times 10^{-4}$ |
| $k_I$ | 0.02 | 0.15 |

1. flux tolerances spanning 5e-4 and 7e-4 introduce eigenvalue errors of more than 100 pcm during the period of gadolinium burnout (see samples 50, 51, and 56),

2. stepsizes above 0.3 MWd/kgHM during gadolinium burnout produce errors of more than 100 pcm (see samples 50, 51, and 56),

3. integral gains above 0.07 introduce larger eigenvalue errors toward the EOC due to rapid increase of stepsize once gadolinium burns out, however, these errors are consistent with those introduced in the CASL-2A problem when using the rule of thumb stepsize sequence (see samples 40 and 125),

4. and a flux tolerance around 3e-4 balances solution accuracy and stepsize prediction efficiency.

Thus far, an I controller has proved to behave very well for both fresh fuel and gadolinium-bearing fuel lattices. A flux tolerance of approximately and an integral gain range of 0.02 to 0.10 gives acceptable stepsize prediction behavior. At this point, the addition of proportional and derivative control components is investigated with the objective of increasing the robustness of the controller and further optimizing the balance of solution accuracy and the number of stepsizes predicted.

First, the bounds on the control parameters, shown in Table 7.50, are used in conjunction with the CASL-2A lattice. The addition of proportional control more often introduces stepsize oscillations than the I controller; to eliminate these data sets, an additional filter of a decrease of 0.2 MWd/kgHM or more followed by an increase of the same magnitude is used. These sample sets are shown in Table 7.51 and the stepsize sequences with eigenvalue errors are shown in Figure 7.104. Overall, the PI controller does not seem to offer much

Table 7.49: Results for filtered sample sets from LHS of I controller design space for CASL-2P.

| Sample set | Initial stepsize (MWd/kgHM) | Flux tolerance | $k_I$ | Number of steps | Max $\delta k_\infty$ (pcm) |
|---|---|---|---|---|---|
| 1 | 0.10 | $4.42 \times 10^{-4}$ | 0.047 | 78 | 114 |
| 16 | 0.15 | $2.25 \times 10^{-4}$ | 0.069 | 105 | 112 |
| 40 | 0.12 | $3.54 \times 10^{-4}$ | 0.102 | 89 | 146 |
| 50 | 0.29 | $5.46 \times 10^{-4}$ | 0.031 | 58 | 115 |
| 51 | 0.25 | $6.96 \times 10^{-4}$ | 0.030 | 52 | 142 |
| 56 | 0.18 | $6.49 \times 10^{-4}$ | 0.025 | 60 | 110 |
| 92 | 0.22 | $3.02 \times 10^{-4}$ | 0.021 | 85 | 58 |
| 128 | 0.15 | $1.05 \times 10^{-4}$ | 0.035 | 126 | 25 |

improvement over the I controller. Sample set 130 shows 16 steps, which is 5 less than the rule of thumb sequence; however, the predicted sequence behaves more poorly than sample set 19 in Table 7.47 with only an integral component used.

Table 7.50: Parameter bounds used in Latin hypercube sampling of PI controller for CASL-2A.

| Parameter | Lower bound | Upper bound |
|---|---|---|
| Initial stepsize (MWd/kgHM) | 0.05 | 0.40 |
| Flux tolerance | $1 \times 10^{-4}$ | $5 \times 10^{-3}$ |
| $k_I$ | 0.01 | 0.15 |
| $k_P$ | 0.01 | 0.35 |

The previous I and PI controller parametric studies have allowed the bounds of the control variables to be tightened to a well-behaving range. The remaining control variable of derivative gain is included in a parametric study with the bounds shown in Table 7.52. Similar filters as used with the PI controller parametric study are used to eliminate ill-behaved time series; Table 7.53 shows the sample sets that remain after the filtering. Figure 7.105 compares the stepsizes sequences and multiplication factor errors. No significant benefits

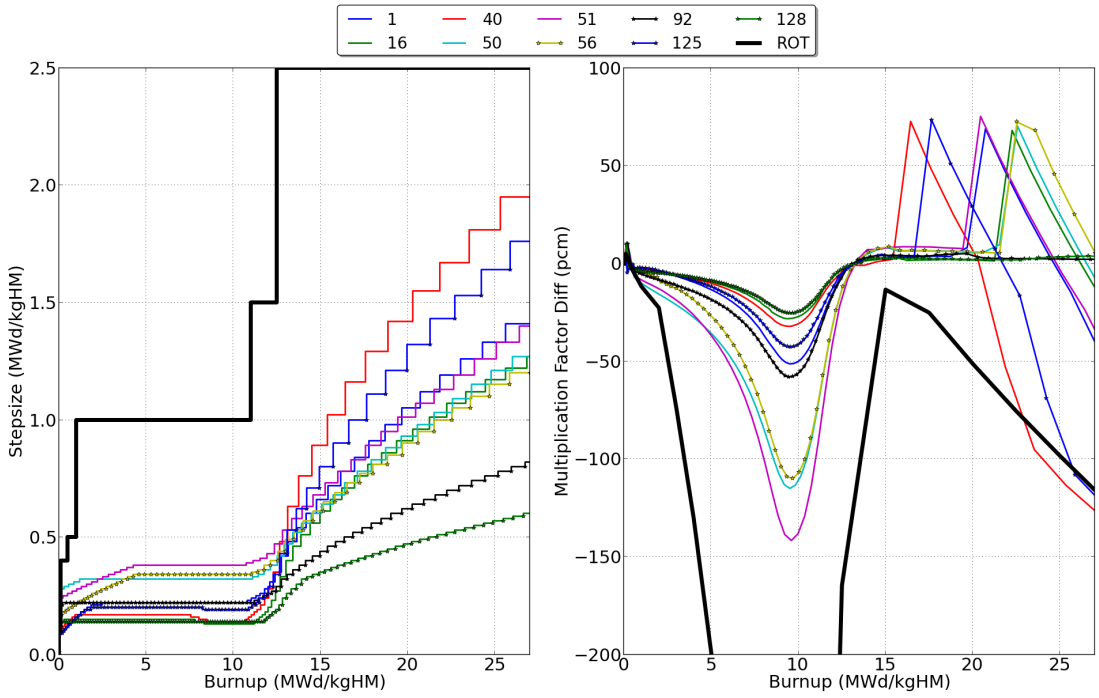


Figure 7.103: Filtered stepsize prediction sequences (left) and difference in multiplication factor from reference (right) for LHS of parameters for I controller, applied to CASL-2P.

are realized with the addition of both derivative and proportional error components for the CASL-2A problem.

The PID controller parameter space is further constrained and is tested using the CASL-2P problem. Table 7.54 summarizes the parameter ranges. Table 7.55 details the parameters associated with the filtered sample sets. In Figure 7.106, the filtered results are compared in terms of their respective stepsize sequences and their multiplication factor errors.

By inspecting the parameter space in Table 7.55, it is clear that the flux tolerance is driving the magnitude of the stepsizes and thus the number of depletion steps required for the cycle. Because the controller gains have previously been constrained to a well behaving range, it is not surprising that the overall progression of the stepsize predictions is similar in Figure 7.106 and is primarily being driven by the magnitude of the flux tolerance. When considering the results of the PID controller and that of the I controller in Table 7.49 and Figure 7.103, comparable stepsize progressions are obtained. However, there is one important feature of

Table 7.51: Results for filtered sample sets from LHS of PI controller design space for CASL-2A.

| Sample set | Initial stepsize (MWd/kgHM) | Flux tolerance | $k_I$ | $k_P$ | Number of steps | Max $\delta k_\infty$ (pcm) |
|---|---|---|---|---|---|---|
| ROT | 0.10 | – | – | – | 21 | 184 |
| 6 | 0.32 | $7.54 \times 10^{-4}$ | 0.032 | 0.220 | 22 | 176 |
| 19 | 0.25 | $1.07 \times 10^{-4}$ | 0.067 | 0.131 | 30 | 116 |
| 45 | 0.31 | $8.54 \times 10^{-4}$ | 0.030 | 0.034 | 23 | 179 |
| 55 | 0.17 | $2.20 \times 10^{-4}$ | 0.106 | 0.167 | 19 | 189 |
| 77 | 0.24 | $1.84 \times 10^{-4}$ | 0.082 | 0.023 | 21 | 183 |
| 102 | 0.10 | $2.88 \times 10^{-4}$ | 0.035 | 0.247 | 33 | 156 |
| 130 | 0.27 | $2.76 \times 10^{-4}$ | 0.111 | 0.114 | 16 | 189 |

Table 7.52: Parameter bounds used in Latin hypercube sampling of PID controller for CASL-2A.

| Parameter | Lower bound | Upper bound |
|---|---|---|
| Initial stepsize (MWd/kgHM) | 0.09 | 0.40 |
| Flux tolerance | $1 \times 10^{-4}$ | $5 \times 10^{-3}$ |
| $k_I$ | 0.02 | 0.10 |
| $k_P$ | 0.03 | 0.18 |
| $k_D$ | 0.01 | 0.35 |

the PID controller that stands out, the increase in the stepsize, once the gadolinium burns out, occurs much more quickly.

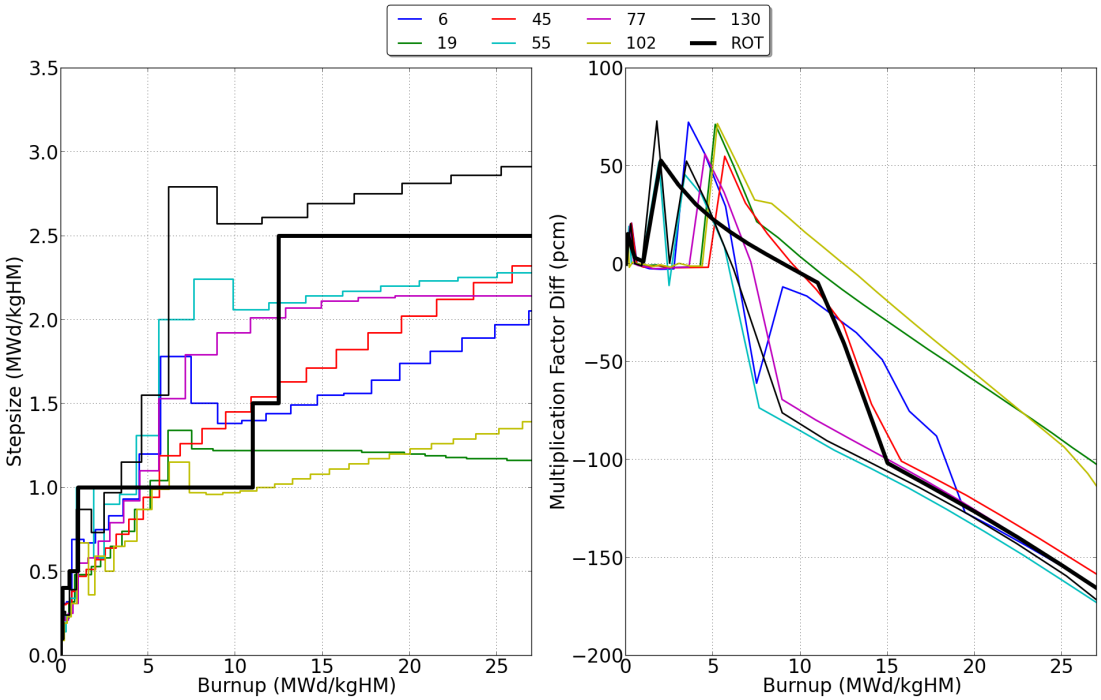


Figure 7.104: Filtered stepsize prediction sequences (left) and difference in multiplication factor from reference (right) for LHS of parameters for PI controller, applied to CASL-2A.

Table 7.53: Results for filtered sample sets from LHS of PID controller design space for CASL-2A.

| Sample set | Initial stepsize (MWd/kgHM) | Flux tolerance | $k_I$ | $k_P$ | $k_D$ | Number of steps | Max $\delta k_\infty$ (pcm) |
|---|---|---|---|---|---|---|---|
| ROT | 0.10 | – | – | – | – | 21 | 184 |
| 13 | 0.12 | $1.29 \times 10^{-4}$ | 0.026 | 0.06 | 0.057 | 33 | 178 |
| 26 | 0.26 | $2.62 \times 10^{-4}$ | 0.046 | 0.045 | 0.059 | 26 | 172 |
| 30 | 0.11 | $1.53 \times 10^{-4}$ | 0.029 | 0.084 | 0.084 | 28 | 172 |
| 47 | 0.17 | $2.42 \times 10^{-4}$ | 0.023 | 0.104 | 0.024 | 20 | 181 |
| 97 | 0.35 | $5.75 \times 10^{-4}$ | 0.088 | 0.050 | 0.036 | 19 | 179 |
| 123 | 0.16 | $6.89 \times 10^{-4}$ | 0.075 | 0.041 | 0.139 | 26 | 177 |

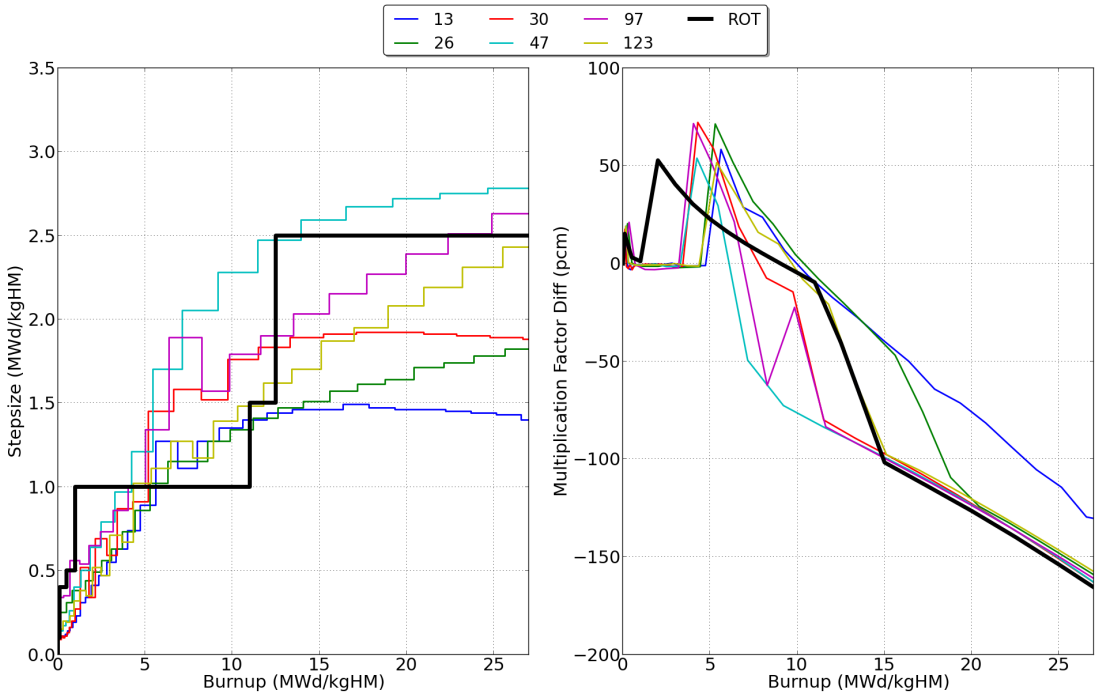


Figure 7.105: Filtered stepsize prediction sequences (left) and difference in multiplication factor from reference (right) for LHS of parameters for PID controller, applied to CASL-2A.

Table 7.54: Parameter bounds used in Latin hypercube sampling of PID controller for CASL-2P.

| Parameter | Lower bound | Upper bound |
|---|---|---|
| Initial stepsize (MWd/kgHM) | 0.09 | 0.30 |
| Flux tolerance | $1 \times 10^{-4}$ | $7 \times 10^{-4}$ |
| $k_I$ | 0.02 | 0.10 |
| $k_P$ | 0.03 | 0.13 |
| $k_D$ | 0.02 | 0.15 |

Table 7.55: Results for filtered sample sets from LHS of PID controller design space for CASL-2P.

| Sample set | Initial stepsize (MWd/kgHM) | Flux tolerance | $k_I$ | $k_P$ | $k_D$ | Number of steps | Max $\delta k_\infty$ (pcm) |
|---|---|---|---|---|---|---|---|
| 13 | 0.11 | $1.22 \times 10^{-4}$ | 0.026 | 0.050 | 0.038 | 153 | 16 |
| 62 | 0.13 | $4.81 \times 10^{-4}$ | 0.025 | 0.109 | 0.136 | 70 | 152 |
| 89 | 0.16 | $6.03 \times 10^{-4}$ | 0.059 | 0.054 | 0.046 | 58 | 139 |
| 102 | 0.14 | $2.84 \times 10^{-4}$ | 0.090 | 0.067 | 0.033 | 99 | 70 |
| 108 | 0.14 | $3.54 \times 10^{-4}$ | 0.053 | 0.123 | 0.067 | 90 | 142 |
| 116 | 0.19 | $6.96 \times 10^{-4}$ | 0.027 | 0.093 | 0.079 | 50 | 152 |
| 129 | 0.27 | $5.32 \times 10^{-4}$ | 0.070 | 0.033 | 0.074 | 58 | 118 |

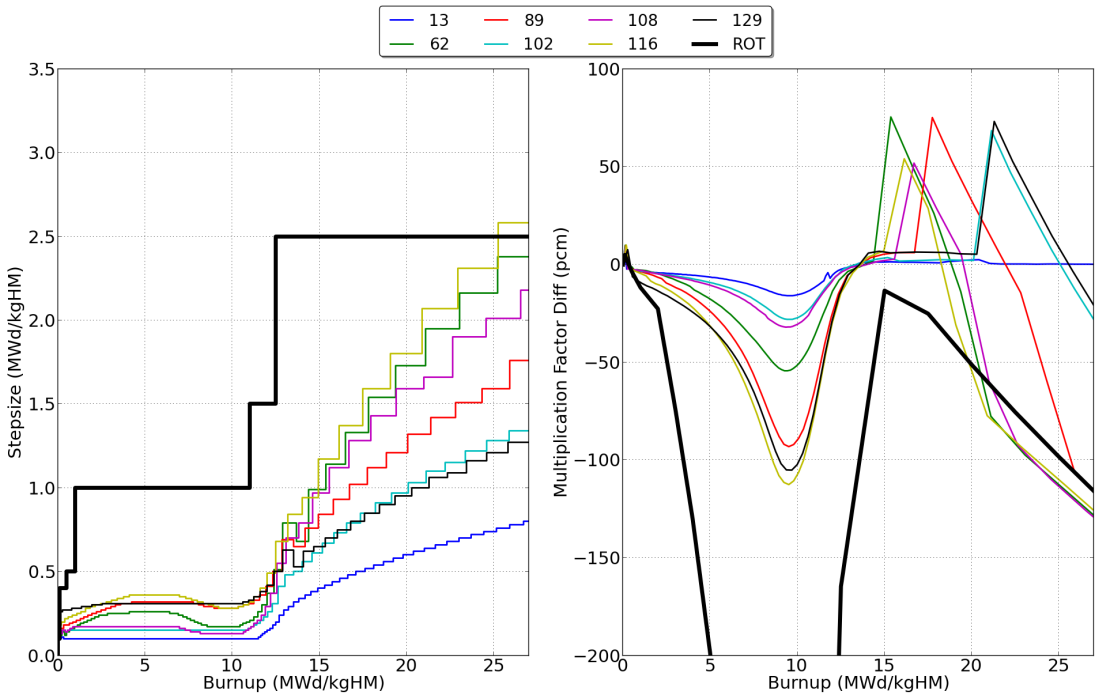


Figure 7.106: Filtered stepsize prediction sequences (left) and difference in multiplication factor from reference (right) for LHS of parameters for PID controller, applied to CASL-2P.

# Bibliography

[Adams, 2015] Adams, B. M. (2015). *Dakota, A multilevel parallel object-oriented framework for design optimization, parameter estimation, uncertainty quantification, and sensitivity analysis: version 6.2 user's manual.* Sandia National Laboratory.

[ANSYS, 2009a] ANSYS (2009a). *ANSYS CFD-Solver Theory Guide.*

[ANSYS, 2009b] ANSYS (2009b). *ANSYS FLUENT 12.0: Theory Guide.*

[AREVA, 2016] AREVA (2016). http://www.areva.com/en/operations-807/fuel-production-integrated-expertise-from-a-to-z.html. Technical report.

[Baglietto et al., 2006] Baglietto, E., H, N., and Misawa, T. (2006). Cfd and dns methodologies development for fuel bundle simulations. *Nuclear Engineering and Design*, 236:1503–1510.

[Bhatt et al., 2015] Bhatt, A., Jones, J., Swanson, R., Palzewicz, S. M., Monti, L., and Sieber, G. (2015). Application and validation of areva's advanced thermal-hydraulic methods and codes for pwr level iii crud risk assessment. In *NURETH-16.*

[Burrage et al., 2004] Burrage, P. M., Herdiana, R., and Burrage, K. (2004). Adaptive stepsize based on control theory for stochastic differential equation. *Journal of Computational and Applied Mathematics*, 170(2):317–336.

[Byers et al., 2000] Byers, W. A., Lindsay, Jr., W. T., and Kunig, R. H. (2000). Solubility of lithium monoborate in high temperature water. *Journal of Solution Chemistry*, 29(6):541–559.

[Byers and Wang, 2006] Byers, W. A. and Wang, G. (2006). Assessing zinc injection limitations in high-duty pwrs. A presentation to EPRI fuel reliability program working group 1.

[Cacuci, 2010] Cacuci, D. G., editor (2010). *Handbook of Nuclear Engineering*.

[Carpenter, 2009] Carpenter, D. (2009). A comparison of constant power depletion algorithm. In *International Conference on Mathematics, Computational Methods & Reactor Physics*.

[Carpenter and Wolfill, 2010] Carpenter, D. C. and Wolfill, J. H. (2010). The log linear rate constant power depletion method. In *PHYSOR*.

[Castelli, 2010] Castelli, R. (2010). *Nuclear Corrosion Modeling*. Butterworth-Heinemann.

[CD-adapco, 2012] CD-adapco (2012). *STAR-CCM+ Version 7.04.011 User Guide*.

[Clarno et al., 2015] Clarno, K., Pawlowski, R., Montgomery, R., Kochunas, B., and Gaston, D. (2015). High fidelity modeling of pellet-clad interaction using the casl virtual environment for reactor applications. In *M&C*.

[Cochran and Tsoulfanidis, 1999] Cochran, R. G. and Tsoulfanidis, N. (1999). *The Nuclear Fuel Cycle: Analysis and Management*. American Nuclear Society.

[Cohen, 1974] Cohen, P. (1974). Heat and mass transfer for boiling in porous deposits with chimneys. *AIChE Symposium Series*, 70:138.

[Collins et al., 2014] Collins, B., Zhu, A., Kochunas, B., and Downar, T. (2014). Demonstration of advanced pin-resolved depletion with mpact. Technical Report CASL-Z-2013-0276-001, CASL.

[Croff, 1980] Croff, A. G. (1980). *A users manual for the ORIGEN2 computer code*. Oak Ridge National Laboratory.

[CSAInc, 2015] CSAInc (2015). www.csai.com/vipre/. Technical report.

[Deshon, 2011] Deshon, J. (2011). Simulated fuel crud thermal conductivity measurements under pressurized water reactor conditions. Technical Report 1022896, EPRI, EPRI, Palo Alto, CA.

[Deshon et al., 2010] Deshon, J., Hussey, D., Kendrick, B., McGurk, J., Secker, J., and Short, M. (2010). Pressurized water reactor fuel crud and corrosion modeling. *JOM*, 63(8):64–72.

[EPRI, 1997] EPRI (1997). Rootcause investigation of axial power offset anomaly. Technical Report 108320, EPRI, EPRI, Palo Alto, CA.

[EPRI, 2003] EPRI (2003). Boron-induced offset anomaly (boa) risk assessment tool. Technical Report 1003211.

[EPRI, 2004] EPRI (2004). Pwr axial offset anomaly (aoa) guidelines, revision 1. Technical Report 1008102, EPRI, EPRI, Palo Alto, CA.

[EPRI, 2010] EPRI (2010). Boron-induced offset anomaly risk assessment tool, version 3.0. Technical Report 1021227.

[EPRI, 2014] EPRI (2014). Computational fluid dynamics benchmark of high fidelity rod bundle eexperiment: Industry round robin phase i - rod bundle with simple support grids. Technical report, EPRI.

[EPRI, 2015] EPRI (2015). Computational fluid dynamics benchmark of high fidelity rod bundle eexperiment: Industry round robin phase ii - rod bundle with mixing vane grids. Technical report, EPRI.

[Fellipa et al., 2001] Fellipa, C. A., Park, K. C., and Farhat, C. (2001). Partitioned analysis of coupled system. *Computer Methods in Applied Mechanics and Engineering*, 190:3247–3270.

[Fiorito et al., 2013] Fiorito, L., Stankovskiy, A., Van den Eynde, G., and Labeau, P. E. (2013). Development of time-dependent reaction rates to optimize predictor-corrector algorithm in aleph burn-up code. *Annals of Nuclear Energy*, 38:307–315.

[Gaston et al., 2009] Gaston, D., Newman, C., Hansen, G., and Lebrun-Grandie, D. (2009). Moose: A parallel computational framework for coupled systems of nonlinear equations. *Nuclear Engineering and Design*, 239:1768–1778.

[Gear, 1969] Gear, C. W. (1969). The automatic integration of stiff ordinary differential equations. *Information Processing*, 68:187–193.

[Geelhood et al., 2011] Geelhood, K. J., Luscher, W. G., and Beyer, C. (2011). Frapcon-3.4: A computer code for the calculation of steady-state, thermal-mechanical behavior of oxide fuel rods for high burnup (nureg/cr-7022, volume 1, pnnl-19418, volume 1). Technical report, Pacific Northwest National Laboratory.

[Geiser and Fleck, 2009] Geiser, J. and Fleck, C. (2009). Adaptive step-size control in simulation of diffusive cvd processes. *Mathematical Problems in Engineering*, 2009:1–34.

[Gibson and Launder, 1978] Gibson, M. M. and Launder, B. E. (1978). Ground effects on pressure fluctuations in the atmospheric boundary layer. *Journal of Fluid Mechanics*, 86(3):491–511.

[Godfrey, 2012] Godfrey, A. (2012). Vera core physics benchmark progression problem specifications, revision 2. Technical Report CASL-U-2012-0131-001, CASL.

[Gustafsson, 1991] Gustafsson, K. (1991). Control theoretic techniques for stepsize selection in explicit runge-kutta methods. *ACM Transactions on Mathematical Software*, 17:533–554.

[Gustafsson, 1994] Gustafsson, K. (1994). Control-theoretic techniques for stepsize selection in implicit runge-kutta methods. *ACM Transactions on Mathematical Software*, 20:496–517.

[Gustafsson et al., 1988] Gustafsson, K., Lundh, M., and Soderlind, G. (1988). A pi stepsize control for the numerical solution for ordinary differential equations. *BIT*, 28:270–287.

[Gustafsson and Soderlind, 1997] Gustafsson, K. and Soderlind, G. (1997). Control strategies for the iterative solution of nonlinear equations in ode solvers. *SIAM J. Sci. Comput.*, 18:23–40.

[Hairer et al., 1993] Hairer, E., Wanner, G., and Norsett, S. P. (1993). *Solving Ordinary Differential Equations I.* Springer-Verlag.

[Hales, 2013] Hales, J. D. (2013). *BISON Users Manual.* Idaho National Laboratory.

[Henshaw et al., 2006] Henshaw, J., McGurk, J., Sims, H. E., Tuson, A., Dickinson, S., and Deshon, J. (2006). A model of chemistry and thermal hydraulics in pwr fuel crud deposits. *Journal of Nuclear Materials*, 353:1–11.

[Hollenbach et al., 2004] Hollenbach, D. F., Petrie, L. M., and Landers, N. F. (2004). Keno-vi: A general quadratic version of the keno program. vol. ii, sect. f17 of scale: A modular code system for performing stanstandard computer analysis for licensing evaluation. Technical Report NUREG/CR-0200, Rev. 7, Oak Ridge National Laboratory.

[Hursin et al., 2008] Hursin, M., Kochunas, B., and Downar, T. (2008). *DeCART v2.05 Theory Manual.* University of Michigan.

[IAEA, 2007] IAEA (2007). Current trends in nuclear fuel for power reactors. Technical report, IAEA.

[IAEA, 2010] IAEA (2010). Review of fuel failures in water cooled reactors. Technical report, IAEA.

[In et al., 2001] In, W. K., Oh, D. S., and C, T. H. (2001). Flow analysis for optimum design of mixing vane in a pwr fuel assembly. *Journal of the Korean Nuclear Society.*

[INL, 2005] INL (2005). *RELAP5-3D Code Manual Volume 1: Code Structure, Systen models, and Solution Methods*, 2.4 edition.

[Isotalo and Aarnio, 2011a] Isotalo, A. E. and Aarnio, P. A. (2011a). Comparison of depletion algorithms for large systems of nuclides. *Annals of Nuclear Energy*, pages 261–268.

[Isotalo and Aarnio, 2011b] Isotalo, A. E. and Aarnio, P. A. (2011b). Higher order methods for burnup calculations with bateman solutions. *Annals of Nuclear Energy*, 38:1987–1995.

[Jones et al., 2013] Jones, J. H., Pop, M. G., Hove, C. M., Harne, R. L., Anghelescu, M. S., Galimov, A. Y., Palzewicz, S. M., Lydzinski, S. R., Monti, L., and Reiterer, F. (2013). Areva simulations of crud risk assessment. In *TOPFUEL.*

[Jones and Launder, 1972] Jones, W. P. and Launder, B. E. (1972). The prediction of laminarization with a two-equation model of turbulence. *Int. J. Heat and Mass Transfer*, 15:301–314.

[Joo et al., 2004] Joo, H. G., Cho, J. Y., Kim, K. S., Lee, C. C., and Zee, S. Q. (2004). Methods and performance of a three-dimensional whole-core transport code decart. In *PHYSOR*.

[Jung et al., 2013] Jung, Y. S., Shim, C. B., Lim, C. H., and Joo, H. G. (2013). Practical numerical reactor employing direct whole core neutron transport and subchannel thermal/hydraulic solvers. *Annals of Nuclear Energy*, 62:357–374.

[KAERI, 2016] KAERI (2016).

[Karoutas et al., 2012] Karoutas, Z. E., Lu, R., Yan, J., Krammen, M. A., and Sham, T.-L. (2012). Application of advanced methods to predict grid to rod fretting in pwrs. Technical report, WEC.

[Kendrick and Barber, 2012] Kendrick, B. K. and Barber, J. (2012). Initial validation and benchmark study of 3d mamba v2.0 against the walt loop experiment and boa v3.0. Technical Report MPOCRUD.P5.02, CASL.

[Kendrick et al., 2013] Kendrick, B. K., Petrov, V., Walter, D. J., Manera, A., Collins, B., Downar, T., Secker, J., and Belcourt, K. (2013). Casl multiphsyics modeling of crud depositon in pwrs. In *TOPFUEL*.

[Knott, 1995] Knott, D. (1995). *CASMO-4: A Fuel Assembly Burnup Program*. STUDSVIK.

[Knott and Wehlage, 2007] Knott, D. and Wehlage, E. (2007). Description of the lancer02 lattice physics code for single- assembly and multibundle analysis. *Nuclear Science and Engineering*, 155:331–354.

[Kochunas et al., 2013] Kochunas, B., Collins, B., Jabaay, D., Downar, T., and Martin, W. (2013). Overview of development and design of mpact: Michigan parallel characteristics transport code. In *M&C*.

[Kozlowski et al., 2004] Kozlowski, T., Miller, R. M., Downar, T. J., Barber, D. A., and Joo, H. G. (2004). Consistent comparison of the codes relap5/parcs and trac-m/parcs for the oecd mslb coupled code benchmark. *Nuclear Technology*, 146(1):15–28.

[Launder and Spalding, 1974] Launder, B. E. and Spalding, D. B. (1974). The numerical computation of turbulent flows. *Computer Methods in Applied Mechanics and Engineering*, 3(2):269–289.

[Lee and Nam, 2013] Lee, Y. and Nam, Z. C. (2013). Efficient and accurate depletion calculations via two-block decomposition of nuclide concentration vector. *Annals of Nuclear Energy*, 53:147–157.

[Lien et al., 1996] Lien, F. S., Chen, W. L., and Leschziner, M. A. (1996). Low-reynolds number eddy-viscosity modemodel based on non-linear stress-strain/vorticity relations. In *3rd Symposium on Engineering Turbulence Modelling and Measurements*.

[Mankosa et al., 2016] Mankosa, M., Walter, D. J., Ivanov, K., Avramova, M., Manera, A., Petrov, V., Williamson, R., and Novascone, S. R. (2016). Three-dimensional modeling of hydrogen and hydride distribution in zirconium alloy cladding using high-fidelity multiphysics simulations. In *PHYSOR*.

[Miller et al., 2013] Miller, B. A., Crowell, A. R., and McNamara, J. J. (2013). Loosely coupling time-marching of fluid-thermal-structure interactions. In *Structures, Structural Dynamics, and Materials and Co-located Conferences*.

[Navarro and Santos, 2011] Navarro, M. A. and Santos, A. A. C. (2011). Evaluation of a numeric procedure for flow simulation of a 5x5 pwr rod bundle with a mixing vane spacer. *Progress in Nuclear Energy*, 53:1190–1196.

[NEA, 2013] NEA (2013). Report of the oecd/nea kaeri rod bundle cfd benchmark exercise. Technical report, Nuclear Energy Agency.

[NRC, 2010] NRC (2010). *TRACE V5.0 Theory Manual: Field Equations, Solution Methods, and Physical Models*.

[Nutt and Wallis, 2004] Nutt, W. T. and Wallis, G. B. (2004). Evaluation of nuclear safety from the outputs of computer codes in the presence of uncertainties. *Reliability Engineering and System Safety*, 83:57–77.

[Pearson, 1895] Pearson, K. (1895). Notes on regression and inheritance in the case of two parents. *Proceedings of the Royal Society of London*, 58:240–242.

[Petrov et al., 2016] Petrov, V., Kendrick, B. K., Walter, D. J., Manera, A., and Secker, J. (2016). Prediction of crud deposition on pwr fuel using a state-of-the-art cfd-based multi-physics computational tool. *Nuclear Engineering and Design*.

[Piperno and Farhat, 2001] Piperno, S. and Farhat, C. (2001). Partitioned procedures for the transient solution of coupled aroelastic problems - part ii: energy transfer analysis and three-dimensional applications. *Comput. Methods Appl. Mech. Engrg.*, 190:3147–3170.

[Piperno et al., 1995] Piperno, S., Farhat, C., and Larrouturou, B. (1995). Partitioned procedures for the transient solution of coupled aroelastic problems - part i: Model problem, theory and two-dimeosional application. *Comput. Methods Appl. Mech. Engrg.*, 124:79–112.

[Pope, 2000] Pope, S. B. (2000). *Turbulent Flows*. Cambridge University Press.

[Pusa and Leppanen, 2010] Pusa, M. and Leppanen, J. (2010). Computing the matrix exponential in burnup calculations. *Nuclear Science and Engineering*, 164:140–150.

[Ragusa and Mahadevan, 2009] Ragusa, J. C. and Mahadevan, V. S. (2009). Consistent and accurate schemes for coupled nneutronic thermal-hydraulics reactor analysis. *Nuclear Engineering and Design*, 239:566–579.

[Rodi, 1991] Rodi, W. (1991). Experience with two-layer model combining the k-e model with a one-equation model near the wall. In *29th Aerospace Sciences Meeting*.

[Saadi et al., 2012] Saadi, M. K., Abbaspour, A., and Pazirandeh, A. (2012). Burnup span sensitivity analysis of different burnup coupling schemes. *Annals of Nuclear Energy*, 47:6–13.

[Salko, 2015] Salko, R. (2015). *COBRA-TF Subchannel ThermalTheoryThermal-Hydraulics Code (CTF) Theory Manual: Revision 0*. Pennsylvania State University.

[Schmidt, 2012] Schmidt, R. (2012). A description of the algorithmic steps and data transfer needs for coupling anc-vipre-boa in a time-consistent manner. Technical report, Sandia National Labs.

[Secker, 2011] Secker, J. (2011). Test problem and validation data package for crud. Technical report, CASL.

[Secker et al., 2012] Secker, J., Milanova, R., Sung, Y., Hilton, P., Coulter, B., Belcourt, K., and Schmidt, R. (2012). Coupled anc-vipre-boa multiphysics standard and fine mesh models for vogtle 1 cycles 12-14. Technical report, Consortium for Advanced Simulation of LWRs.

[Secker et al., 2011] Secker, J., Nelson, S., Hilton, P., Coulter, B., Belcourt, K., and Schmidt, R. (2011). Coupled anc/vipre/boa multi-physics results for watts bar 1 cycles 1-3. Technical report, Consortium for Advanced Simulation of LWRs.

[Shih et al., 1994] Shih, T.-H., Liou, W. W., Shabbir, A., Yang, Z., and Zhu, J. (1994). A new k-eps eddy viscosity model for high reynolds number turbulent flows: model development and validation. Technical Report 106721, NASA.

[Shih et al., 1993] Shih, T.-H., Zhu, J., and Lumley, J. L. (1993). A realizable reynolds stress algebraic equation model. Technical Report 105993, NASA.

[Short et al., 2013] Short, M. P., Hussey, D., Kendrick, B. K., Besmann, T. M., Stanek, C. R., and Yip, S. (2013). Multiphysics modeling of porous crud deposits in nucelar reactors. *Journal of Nuclear Materials*, 443(1-3):579–587.

[Soderlind, 1998] Soderlind, G. (1998). The automatic control of numerical integration. *DWI Quart.*, 11(1):55–74.

[Soderlind, 2002] Soderlind, G. (2002). Automatic control and adaptive time-stepping. *Numerical Algorithms*, 31:281–310.

[Soderlind, 2003] Soderlind, G. (2003). Digital filters in adaptive time-stepping. *ACM Trans. Math. Software*, 29(1):1–26.

[Stamm'Ler, 2008] Stamm'Ler, R. J. J. (2008). *HELIOS methods*. Studsvik Scandpower.

[Station, 2004] Station, P. V. N. G. (2004). Nuclear fuel update. Meeting with US NRC.

[Studsvik, 1995] Studsvik (1995). *SIMULATE-3 Methodology: Advanced Three-Dimensional Two-Group Reactor Analysis Code*. STUDSVIK.

[Studsvik, 2008] Studsvik (2008). *HELIOS Methods (version 1.10)*. STUDSVIK.

[Sugrue et al., 2013] Sugrue, R., Conner, M., Yan, J., and Baglietto, E. (2013). Pressure drop measurements and cfd pprediction for pwr structural grids. In *TOPFUEL*.

[Valli et al., 2002] Valli, A. M. P., Carey, G. F., and Coutinho, A. L. G. A. (2002). Control strategies for timestep selection in simulation of coupled viscous flow and heat transfer. *Communications in Numerical Methods in Engineering*, 18:131–139.

[Valli et al., 2005] Valli, A. M. P., Carey, G. F., and Coutinho, A. L. G. A. (2005). Control strategies for timestep selection in finite element simulation of incompressible flows and coupled reaction-convection-diffusion processes. *International Journal for Numerical Methods in Fluids*, 47:201–231.

[Valli et al., 2008] Valli, A. M. P., Carey, G. F., and Coutinho, A. L. G. A. (2008). On decoupled time step / subcycling and iteration strategies for multiphysics problems. *Communications in Numerical Methods in Engineering*, 24:1941–1952.

[Vijalapura and Govindjee, 2005] Vijalapura, P. K. and Govindjee, S. (2005). An adaptive hybrid time-stepping scheme for highly non-linear strongly coupled problems. *International Journal for Numerical Methods in Engineering*, 64:819–848.

[Walter et al., 2014] Walter, D., Petrov, V., and Manera, A. (2014). Thermal hydraulic effects of 3-d power variations in a pwr fuel pin using cfd. In *ANS Winter Meeting*.

[Walter and Manera, 2016a] Walter, D. J. and Manera, A. (2016a). Adaptive burnup step-size selection using control theory for 2-d lattice depletion simulations. *Progress in Nuclear Energy*, 88:218–230.

[Walter and Manera, 2016b] Walter, D. J. and Manera, A. (2016b). Crud, boron, and burnable absorber layer 2-d modeling requirements using moc neutron transport. *Annals of Nuclear Energy*, 87:388–399.

[Walter et al., 2015a] Walter, D. J., Petrov, V., Kendrick, B. K., and Manera, A. (2015a). A control theory approach to adaptive stepsize selection for coupled cfd and crud chemistry simulations. In *NURETH-16*.

[Walter et al., 2015b] Walter, D. J., Petrov, V., Kendrick, B. K., Manera, A., Collins, B., and Downar, T. J. (2015b). Proof-of-principle of high-fidelity coupled crud deposition and cycle depletion simulation. *Annals of Nuclear Energy*, 85:1152–1166.

[Wang, 2009] Wang, G. (2009). *Improved crud heat transfer model for dryout on fuel pin surfaces at PWR operating conditions*. PhD thesis, The Pennsylvania State University.

[Wang et al., 2013] Wang, G., Byers, W. A., Young, M. Y., Deshon, J., Karoutas, Z., and Oelrich, R. L. (2013). Thermal conductivity measurements for simulated pwr crud. In *ICONE21-16655*.

[Wang et al., 2010] Wang, G., Young, M. Y., Byers, W. A., and Krammen, M. A. (2010). Methods to reduce cips/cilc risk for the zero fuel failure by 2010 initiative. In *18th International Conference on Nuclear Engineering*.

[WEC, 2011] WEC (2011). Seabrook cycle 5 report. Technical report, WEC.

[Wilks, 1941] Wilks, S. S. (1941). Determination of sample sizes for setting tolerance limits. *Annals of Mathematical Statistics*.

[Yamamoto et al., 2007] Yamamoto, A., Tatsumi, M., and Sugimura, N. (2007). Numerical solution of stiff burnup equation with short half lived nuclides by the krylov subspace method. *Journal of Nuclear Science and Technology*, 44:147–154.

[Yamamoto et al., 2009] Yamamoto, A., Tatsumi, M., and Sugimura, N. (2009). Projected predictor-corrector method for lattice physics burnup calculations. *Nuclear Science and Engineering*, 163:144–151.

[Yan et al., 2014] Yan, J., Yuan, P., Smith, L. D., Karoutas, Z. E., and Joffre, P. (2014). Pwr fuel sub-channel thermal mixing cfd model development and validation. In *CFD4NRS*.

[Zhang et al., 1998] Zhang, J., Bajorek, S. M., Kemper, R. M., Nissley, M. E., Petkov, N., and Hochreiter, L. E. (1998). Application of the wcobra/trac best-estimate methodology to the ap600 large-break loca analysis. *Nuclear Engineering and Design*, 186(1-2):279–301.

[Zhong et al., 2004] Zhong, Z., Downar, T. J., Joo, H. G., and Cho, J. Y. (2004). Benchmark analysis of the decart moc code with the venus-2 critical experiment. In *PHYSOR*.

[Ziemniak et al., 2007] Ziemniak, S. E., Gaddipati, A. R., Sander, P. C., and Rice, S. B. (2007). Immiscibility in the nickel ferrite-zinc ferrite spinel binary. *Journal of Physics and Chemistry of Solids*.